

INFORMATION TO USERS

This reproduction was made from a copy of a document sent to us for microfilming. While the most advanced technology has been used to photograph and reproduce this document, the quality of the reproduction is heavily dependent upon the quality of the material submitted.

The following explanation of techniques is provided to help clarify markings or notations which may appear on this reproduction.

1. The sign or "target" for pages apparently lacking from the document photographed is "Missing Page(s)". If it was possible to obtain the missing page(s) or section, they are spliced into the film along with adjacent pages. This may have necessitated cutting through an image and duplicating adjacent pages to assure complete continuity.
2. When an image on the film is obliterated with a round black mark, it is an indication of either blurred copy because of movement during exposure, duplicate copy, or copyrighted materials that should not have been filmed. For blurred pages, a good image of the page can be found in the adjacent frame. If copyrighted materials were deleted, a target note will appear listing the pages in the adjacent frame.
3. When a map, drawing or chart, etc., is part of the material being photographed, a definite method of "sectioning" the material has been followed. It is customary to begin filming at the upper left hand corner of a large sheet and to continue from left to right in equal sections with small overlaps. If necessary, sectioning is continued again—beginning below the first row and continuing on until complete.
4. For illustrations that cannot be satisfactorily reproduced by xerographic means, photographic prints can be purchased at additional cost and inserted into your xerographic copy. These prints are available upon request from the Dissertations Customer Services Department.
5. Some pages in any document may have indistinct print. In all cases the best available copy has been filmed.

**University
Microfilms
International**

300 N. Zeeb Road
Ann Arbor, MI 48106

8409371

Crutchfield, James Patrick, Jr.

NOISY CHAOS

University of California, Santa Cruz

PH.D. 1983

University
Microfilms
International 300 N. Zeeb Road, Ann Arbor, MI 48106

Copyright 1983

by

Crutchfield, James Patrick, Jr.

All Rights Reserved

PLEASE NOTE:

In all cases this material has been filmed in the best possible way from the available copy. Problems encountered with this document have been identified here with a check mark .

1. Glossy photographs or pages
2. Colored illustrations, paper or print _____
3. Photographs with dark background
4. Illustrations are poor copy _____
5. Pages with black marks, not original copy _____
6. Print shows through as there is text on both sides of page _____
7. Indistinct, broken or small print on several pages
8. Print exceeds margin requirements _____
9. Tightly bound copy with print lost in spine _____
10. Computer printout pages with indistinct print _____
11. Page(s) _____ lacking when material received, and not available from school or author.
12. Page(s) _____ seem to be missing in numbering only as text follows.
13. Two pages numbered _____. Text follows.
14. Curling and wrinkled pages _____
15. Other _____

University
Microfilms
International

UNIVERSITY OF CALIFORNIA

SANTA CRUZ

Noisy Chaos

A Dissertation submitted in partial satisfaction
of the requirements for the degree of

DOCTOR OF PHILOSOPHY

in

PHYSICS

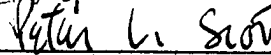
by

James Patrick Crutchfield, Jr.

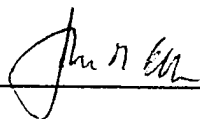
September 1983

The dissertation of
James Patrick Crutchfield, Jr.
is approved:









Dean of the Graduate Division

Noisy Chaos



Copyright 1983 James P. Crutchfield, Jr.

ABSTRACT

Deterministic dynamics often leads to complex, unpredictable behavior. This randomness or chaos produces information and limits one's ability to predict future events. There are two components to this imposed ignorance. The first arises in a mathematical context from highly convoluted orbit structures in state space. These allow a system to rapidly visit many regions of state space. In a physical context, the second comes from the coupling of the system-under-study to other systems that provide information to it. Extrinsic information sources preclude the exact determination of the system's state. By the mechanism of their complex orbits, chaotic systems amplify this uncertainty into unpredictable macroscopic behavior. The physical study of chaotic dynamical systems is incomplete without an appreciation of how external fluctuations affect their predictability.

Using information theory we describe how to measure the unpredictability of (i) deterministic chaotic systems (without extrinsic noise), and (ii) nondeterministic chaotic systems (coupled to extrinsic noise). Scaling concepts are invaluable tools in this. Scaling reveals that extrinsic noise acts as a disordering field for chaos. Furthermore, even for systems with extrinsic noise, scaling captures fundamental features of chaotic behavior. It provides a unified framework for the topological, metric, and Renyi dimensions and entropies.

The physical relevance of these concepts lies in their ability to analyze noisy chaotic signals. The information theoretic approach to

temporally complex behavior is applied to chaotic signals from two hydrodynamic experiments. In addition, the dynamic aspects of pattern evolution and the possible breakdown of (naive) dynamical systems theory is discussed for experiments with an image processing system.

The first appendix contains descriptions of algorithms for dynamical systems studies. The second discusses a movie on the geometric structure of chaotic driven oscillators using animated Poincare sections.

And thus spoke Zarathustra to the people: "The time has come for man to set himself a goal. The time has come for man to plant the seed of his highest hope. His soil is still rich enough. But one day this soil will be poor and domesticated, and no tall tree will be able to grow in it. Alas, the time is coming when man will no longer shoot the arrow of his longing beyond man, and the string of his bow will have forgotten how to whir!

"I say unto you: one must still have chaos in oneself to be able to give birth to a dancing star. I say unto you: you still have chaos in yourselves."

Friedrich Nietzsche, *
Thus Spoke Zarathustra

* translated by W. Kaufmann, Penguin Books, New York, 1978.

Contents

Preface	v
Acknowledgements	ix
1. Unpredictability	1.1
2. Information Flow	2.1
3. Measurement Dynamics	3.1
4. Scaling	4.1
5. Entropies of Chaos	5.1
6. Noisy Chaos	6.1
7. Solid State Turbulence	7.1
8. Hydrodynamic Chaos	8.1
9. Complexity in Spatially Extended Systems	9.1
Appendices	
A. Algorithms for Dynamical Systems	A.1
B. Chaotic Attractors of Driven Oscillators:	
The Movie	B.1

Preface

Chaos arises naturally in a completely classical universe. No appeals need be made to quantum uncertainty as the ultimate source of ignorance. Indeed, my premise in the following discussion is that the world is completely deterministic. This extends even to the "fluctuations" often introduced to describe physical processes. Fluctuations, or external sources of randomness, can be simply constructed using strictly deterministic dynamics.

Given this deterministic world view, how do surprise, creativity, and beauty appear? The possibility now presents itself that they arise as products of the world's complex dynamics. To be more precise, they result from our observation of this complexity. Innately, we make "sense" of our observations. We learn about the world and summarize this knowledge by constructing "models".

Our models of the world's complex processes are both explicit and implicit. Implicitly and unconsciously we build mental pictures imbued with their own dynamics. We base our future actions on these world models. We experience, learn, construct models, simulate, and predict. This process seems to spontaneously occur in all life. Some believe it can happen in structures that we now call inanimate, such as computers. Explicitly as gregarious cultural beings, we construct mythology, religion, and then science as tentative, collective explanations of the

world's workings.

We are now in a position to comprehend our construction of these models as we take the first steps in developing the requisite tools to access their full range of complexity. With this, we move closer yet to understanding nature in its own terms. Without this, we would never see the how and why of learning and evolution. If surprise, creativity, and beauty truly exist as consequences of the world's dynamics as captured in our models, we will no longer have to presuppose some transcendent source of complexity. Complexity and interaction will be warp and woof of reality.

The study of chaos is but one small step in this direction. Nevertheless, it provides an important and hopeful metaphor for further understanding. The picture I have tried to present is of chaos as constrained randomness. Chaotic dynamics is the constraint that amplifies uncertainty. Randomness represents our ignorance of the world external to our considerations. It is also a mirror of our finite capacities and so too represents our inability to probe the world with arbitrary precision.

The first portion of the dissertation presents an observational theory of chaos. After this introduction the reader can skip around. A list of chapter interdependencies is provided to facilitate this following a description of the overall organization.

The first three chapters briefly lay out an information theoretic model of physical processes that includes their observation. The

existence of deterministic, information-producing (chaotic) dynamical systems forces this approach (Chapter 1). Shannon's analysis of information flow through a communication channel provides a basis for this model (Chapter 2). The average amount of information gained upon making a measurement knowing the entire history of a system is seen to quantify its predictability (Chapters 3 and 5).

Chapter 4 introduces the notions of scaling from critical phenomena theory that are very useful in summarizing the essential features of chaos. Indeed, I propose that chaos be defined solely in terms of its scaling properties. The measurement techniques for unpredictability use scaling and are discussed subsequently in chapter 5. Scaling appears again in chapter 6 to explain how external fluctuations, or external sources of information, act as a "disordering field" that enhances chaotic behavior.

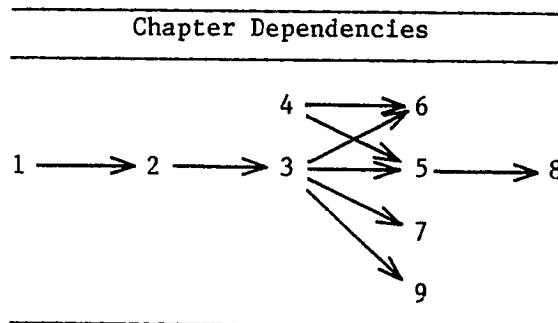
The final three chapters indicate some of the richness of complex dynamics occurring in the physical world: in solid state (chapter 7) and hydrodynamic systems (chapter 8) and in an image processing system (chapter 9). Each chapter discusses how the complexity may be characterized and what difficulties may arise in the application of dynamical systems.

The use of computing machines to analyze chaotic behavior in idealized simulations and in physical experiments has resulted in recent rapid progress. As a consequence, computer programs thus have become a medium for exchange of ideas. Much of the current understanding of

chaos and dynamical systems has been rendered into algorithms. Appendix A includes a few algorithms relating to the topics of the foregoing chapters.

Chaotic attractors often take the form of complex and beautiful objects in state space. Appendix B describes a movie that studies their structure using animated Poincare sections.

The reader can pick and choose after reading the first three chapters. In this case the reader can use the following dependency diagram. Chapter B requires A if the arrow points from A to B.



References not explicitly given in the text can be found in the reprinted papers.

Acknowledgements

"Invention it must be humbly admitted, does not consist in creating out of the void, but out of chaos."

Mary Shelley

Many people and places have contributed to the chaos. They made nurturing environments for the percolating fluctuations that became my thoughts. I would like to thank a special few.

My parents Jim Crutchfield and Marilyn Grether have provided unquestioning support of my pursuits. Alice Roos was the essential support in the production of this dissertation. She kept the project from collapsing in upon itself.

Undoubtedly, the chaotic core consists of Doyne Farmer, Norman Packard, and Rob Shaw. As time and the external world dismantled the Dynamical Systems Collective, we all wondered what awaited us as a group. I am very grateful these fluctuations have seen to it that we will be able to continue to work together, if no longer side by side.

I have Doyne to thank for my financial solvency this past year. His invitations to Los Alamos came at crucial times. His hospitality and energy benefited me greatly during these visits. I still do not know from where he derives his tremendous enthusiasm. It is surely a

wonderful asset.

I thank Norman for the most satisfying working relationship that formed out of the chaos. It is largely responsible for the ideas on symbolic dynamics, entropy, and scaling contained herein. I very much enjoyed our intense, lively discussions and shared philosophy on chaotic dynamics. Norman's understanding nature was a effective antidote to my compulsiveness.

Rob has been a chaotic mentor for a number of years. Through his eyes I began to see the beauty of the classical world. I have him to thank for an unwarranted, but very useful, confidence in tackling problems, whether mundane or esoteric. I learned from him mostly by osmosis rather than by discourse and argument. This is a method to which I still have not adapted, although I have gained much by it.

Ralph Abraham and Bill Burke ran professional interference for us during our first days as a group. Just by their early interest and support they made the going a lot smoother. Ralph's "Big Picture", couched in abstract dynamical systems, seems to be bearing substantial fruit in the physical world these days. I thank him for his willingness to contribute this in the beginning.

When the weight of technical chaos bears down I remind myself of Otto Rössler's humble remark that "science is play". Those who disavow this simple truth frighten me. As Zarathustra extolls,

"I would believe only in a god who could dance. And when I saw my devil I found him serious, thorough, profound, and solemn: it was the spirit of gravity -- through him all things fall."

Some of my most enlightening exchanges have been with Otto. Hinting at the larger context, these gave me the heart to continue. I thank him for these moments and his willingness to share his desire to learn.

I would like to thank the Center for Nonlinear Studies, Los Alamos National Laboratory, for its generous support during my winter visit that made the writing of this dissertation possible.

The Physics Board of Studies has been a tolerant agent of my (non)studenthood for a good many years. It was here, with the faculty's and staff's good will, that the largest and most subtle fluctuations arose to guide me. The financial support of the Theory Group and Regents fellowships provided times of concentrated research for which I remain very grateful.

In and around the Physics Board, there are a number of people I wish to thank: Bill and Pat Burke for their hospitality during the final writing of this dissertation; Mike Nauenberg for urging me to turn into a bonified graduate student; Joe Rudnick for his quiet and consistent support; Peter Scott for taking up my cause several times when I ran afoul of the administration and for his direct, warm encouragement of my work; Jeanne Vandiver and Candi Arnott for their help over the years behind the facade of science; Jim Warner for his tireless help in the hardware and software wars that became so much chaos.

I have benefited from discussions and correspondence with, and criticisms and suggestions from the late Gregory Bateson, Michael Berry, Jean-Pierre Eckmann, David Fried, Joe Ford, John Gukenheimer, Bernardo Huberman, Erica Jen, Gottfried Mayer-Kress, and David Ruelle.

CHAPTER 1

Unpredictability

1.1. Introduction

Strictly deterministic dynamics can be unpredictable. This fact is not recently discovered. At the turn of this century, Poincaré's studies of celestial mechanics led him to an appreciation of deterministic sources of complex behavior. Subsequently, both Birkoff and Hopf continued this initial development. Simple examples of unpredictable dynamics can be found in their early work. The modern understanding of unpredictability, however, began with Kolmogorov's suggestion during the 1950's that Shannon's information theory could be used to compare the complex dynamics of abstract systems. In the early 1960's, Lorenz, a student of Birkhoff's, numerically studied unpredictability in the first system derived (somewhat brutally) from hydrodynamic equations. The problem that concerned Lorenz was why the weather is difficult to predict. In his work, he was the first to provide a clear physical explanation of the deterministic mechanism underlying unpredictability. This mechanism is now called chaos. Lorenz not only appreciated the possibility of complex temporal dynamics, but equally significant, the possibility of arbitrarily complex variation in behavior with changes in system control parameters. Kolmogorov's abstract approach and Lorenz's physical understanding found a synthesis during the late 1970's in Shaw's observational picture of chaos producing information.

In a similar spirit, the present work proposes a conceptual model for deterministic unpredictability in the physical world of fluctuations. To this end the following chapters present three themes. The first is that chaos occurs in the real world and dynamical systems theory provides the necessary descriptive language. The second is that the effect of fluctuations is essential to a physical appreciation of chaos. Finally, that the unpredictability due to both deterministic dynamics and fluctuations can be quantified using information theory.

These themes are developed from the perspective that chaos is constrained randomness. Roughly speaking, there are three sources of observed unpredictability. The first is observational noise due to measurement errors, for example. The second is extrinsic noise associated with the system-under-study's coupling to external sources of information and energy. The results of these couplings are often labeled "fluctuations". The final source is intrinsic noise that arises from the deterministic dynamics of the system-under-study itself. The last noise source is called chaos.

The global dynamics constrains, or molds, the fluctuations as it amplifies them into macroscopic unpredictable behavior. Additionally, fluctuations make it impossible to observe small-scale, short-term deterministic dynamics. This picture of constrained randomness will be laid out more concretely in the following chapters. The remainder of this chapter presents a brief overview of dynamical systems theory and then introduces the concept of information as it applies to dynamics.

1.2. Deterministic Dynamical Systems Theory

The context of all discussion of dynamics is the state space. It is the powerful, yet very simple idea that the state of a system can be summarized by a set of numbers. The usefulness of this abstraction already has been demonstrated in the statistical mechanical foundations of thermodynamics. In comparison, dynamical systems theory may be thought of as a more detailed consideration of the dynamics upon which statistical mechanics itself is based.

Each configuration of a system corresponds to a single point in the state space. In other words, the state space represents all possible "microscopic" system configurations. The time evolution of the system as it changes from configuration to configuration, traces out an orbit that moves from point to point in the state space. The physical forces and constraints that determine the system's time evolution form the dynamic that governs the sequence of states visited by the system's orbit. The dynamic is thus a rule that given a state produces the successor state.

There are two broad categories of dynamic: conservative and dissipative. Conservative dynamics preserve state space volumes in time. Physically the associated system conserves energy. Dissipative dynamics describe the behavior of systems through which energy flows. They shrink state space volumes. The following discussion concentrates on dissipative dynamics although it could be easily generalized to conservative systems.

1.4

The shrinking of state space volumes due to dissipation brings certain simplifying features into the description of possible behavior. In time orbits of a dissipative system become restricted to relatively small regions of state space. These regions are called the system's attractors. They represent a type of global stability for the system: once perturbed, the system will return to its attractor. All those points that evolve to a single attractor are said to be in the attractor's basin of attraction. For a given dynamic then, the state space is partitioned into some number of basins each with its own attractor.

In addition, attractors can be classified into three types. The first is called a fixed point attractor: all initial states evolve toward a single final state. This is the analog of the physicist's notion of an equilibrium state. The second attractor type describes stable oscillations in a system; it is called a limit cycle. In the state space a limit cycle is an orbit that repetitively visits a sequence of states. Multiple stable oscillations also can be combined to give a hierarchy of torus attractors. These also are considered to be the second attractor type. All these attractors, from fixed point to torus, describe predictable behavior. Knowledge of the system's state and the dynamics allow one to predict the future evolution of the system.

The next broad class of attractor describes unpredictable behavior. These are the chaotic attractors. Like the foregoing types, they are globally stable. However, once on the attractor, an orbit's evolution is

unpredictable beyond some time.* Chaotic attractors exponentially amplify fluctuations with time. Any arbitrarily small error in determining the system's state leads in a finite time to general ignorance about its location on the attractor. This can also be expressed in computational terms. Even given an infinitely precise determination of the chaotic system's state at some time, only a machine that computes with infinite precision can predict the system's future evolution. For example, the size of a finite computer must grow without bound to predict within a given error the evolution of a chaotic system successively further into future. The next chapter will return to this aspect of chaotic behavior.

Dynamical systems theory also considers how attractors change from one type to another with the variation of some control parameter. This models an experimentalist's control over his experiment. A bifurcation occurs when there is a qualitative alteration of an attractor's structure with the smooth variation of a control parameter. Bifurcations occur in many different ways: an attractor may change from one type to another at a single parameter setting, continuously with control variation, or on a Cantor set of parameter values. Thus not only does dynamical systems theory anticipate chaotic behavior at set control parameters, but also the arbitrarily complex variation between chaotic attractors.

* Chaotic attractors may have some periodic or predictable component. I will ignore this possibility in the following discussion.

My thesis will be that a chaotic system's unpredictability is its most fundamental physical property. As will be seen, this property can be expressed precisely. The next and final sections introduce information, the basic concept that will lead to a quantitative description of unpredictability.

1.3. Information

Shannon used information in his communication theory to quantify an observer's surprise at the outcome of a measurement. He presented convincing arguments that the information observed in an event is given by the negative of the logarithm of its probability. Unpredictable systems are surprising. Predicting the future state based on a previous measurement leads to the surprise, or information, that the prediction and the next measured state do not always agree.

Of course, the observer's surprise rests on his expectations. Thus in the definition of information there must always be, explicitly or implicitly, a context dependence. This context represents the accumulated knowledge about the system's behavior. For example, initially an experimentalist does not know what detailed behavior to expect and so a reasonable assumption is that all measurement outcomes are equally probable. Relative to this ignorance the occurrence of a given measurement outcome gives the experimentalist a certain average amount of information about the system's state. After some time, though, the experimentalist learns the relative probabilities of the outcomes. His accumulated knowledge alters his expectations, and so too the

-

information context of future measurements.

Within this new context, the natural question is, given a particular outcome, how accurately can one predict the next? In other words, how much does the information that the system is in a given state tell one about the system's future state? The answers to these questions quantify the system's unpredictability. For periodic behavior the information about the system state serves to determine the future states: prediction is possible. For chaotic systems, this is not generally the case. Because of their global structure, chaotic systems do exhibit some order. They are not completely unpredictable, but rather display varying degrees of predictability.

The late Gregory Bateson gives the most elegant definition of information in the glossary to his Mind and Nature (E.P. Dutton, 1979). Information is "any difference that makes a difference." This concisely expresses the context dependence of information as an essential part of information itself. A deviation from the ordinary provides information to an observer. This deviation thus produces an effect in the observer. It makes a difference. The subtler aspect of his definition is that it shows appreciation for the creation of different logical levels in the observation of information producing systems. It captures this in its equivocal use of "difference". Information is not the system or its measurement, but quantifies our observation of it.

The burden of the following chapters is to detail how unpredictability arises and how the spectrum of chaos can be quantified.

Before delving into this a few general remarks about information dynamics are in order.

1.4. Information Dynamics

There are three "laws" of information dynamics that emerge in any description of unpredictable systems. The laws are working assumptions that are used implicitly by many in the application of information theory. The laws cannot be proven, but rather summarize experience and represent useful fundamental concepts. They are hypotheses to be validated and modified in their application to interpreting experiments. I will list them first as a group and then discuss each in turn, mentioning some analogies with thermodynamics.

- (1) Total information is conserved.
- (2) An observer's information about the state of a chaotic system can only decrease.
- (3) An observer cannot obtain infinite information about a system's state.

In the first law the total information refers to the entire observer-experiment system. The observer and the system-under-study are subsystems of a larger, encompassing system. This larger system can be called the universe. (See figure 1.1) The total information context is the universe. If information appears not to be conserved, then the boundaries of the universe are not sufficiently large. Thus, like the first law of thermodynamics, information conservation can be made to

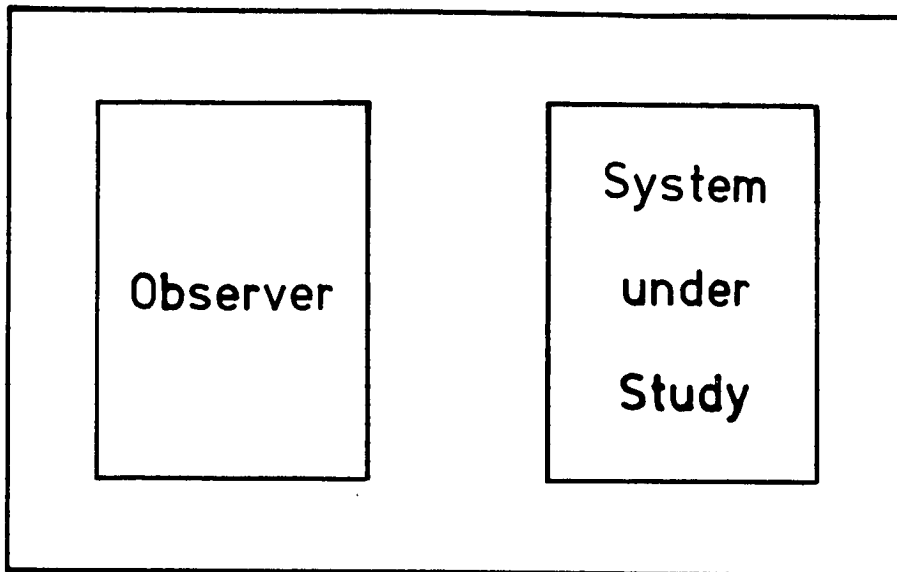


Figure 1.1.

The universe of discourse for information dynamics.

hold trivially.

The second law reflects an observer's inability to predict the future evolution of a chaotic system. A measurement reveals that the system is in some small region of state space. As long as there is any error in this determination, however, the observer will be unable to predict the chaotic system's behavior beyond some finite time, due to the chaotic dynamics. The measurement uncertainty means that any model for prediction cannot be put into a state identical to the system's.

Even assuming that the model completely describes the system's dynamics, the deviation of the model's behavior from the system's will grow exponentially. When the deviation is as large as the system's attractor the behavior is no longer predictable.

The second law is analogous to that in thermodynamics which says the entropy of an isolated system increases. The entropy can be formulated in terms of "missing information" about the state of a thermodynamic system once a macroscopic state function, such as energy, is specified. According to Boltzmann, thermodynamic entropy is the logarithm of the number of microscopic states giving rise to the same value of the macroscopic state function. The total number N of microscopic states associated with a macroscopic state gives the latter's probability N^{-1} . The thermodynamic entropy of a macroscopic state is proportional to the information that the system is in that state.

Preparing a thermodynamic system in a small ensemble of microscopic states with fixed energy (say) corresponds to having low entropy, or a large amount of information about the system's macroscopic state. Subject to energy conservation, however, the system evolves toward equilibrium visiting larger regions of state space than initially. It appears more disordered, the entropy increases, and the observer's initial information can be used with decreasing effectiveness to determine the system's current microscopic state.

From information conservation, the system produces information that "displaces" the observer's. As time goes on, the observer is less able to predict the system's microscopic state. The observer "loses" information.

The third law is equivalent to the impossibility of the observer to make infinitely precise measurements about a system's state. It is analogous to the third law of thermodynamics that says a system cannot be prepared in states of zero entropy, such as zero temperature. Zero entropy corresponds to perfect knowledge of a system's state. There is no missing information because an infinitely precise measurement yields a complete determination of the system's state.

Dissipative chaotic systems, although purely classical, obey the above third law because they exponentially amplify fluctuations.* The third law applies to the observer's measurements of a chaotic system as it continually receives information from other parts of the universe, including the observer. Consequently, the state of the observer must be included in the classical complete determination of the system-under-study.

An estimate of the effect of external fluctuations on chaotic behavior will illustrate their importance when observing chaotic systems. This will provide a quantitative motivation for including the observer and the rest of the universe in a complete (infinitely precise

* The "fluctuations" here, and introduced in later discussions, are also to be thought of as coming from deterministic dynamics.

) state-determination of a chaotic system. Consider the gravitational effect of an electron at the "edge" of the universe (~17 billion light years) on a game of billiards. Assume, for simplicity, that the billiards is energy conserving over half an hour and that the balls are hit sufficiently hard to cause a few collisions each second. The unpredictability of such a billiard can be conservatively estimated as an information loss rate of approximately 1 bit per second. The uncertainty caused by the existence or non-existence of the electron at the edge of the universe leads to total unpredictability in about six minutes. An electron at the edge of the solar system does so in four minutes, and if they move around, the billiard players do so in about one half minute. Similarly, an erratic dripping kitchen faucet (chapter 8) becomes unpredictable in less than half a minute if the uncertainties are produced by the neighbor's cat prowling in the garden. Such is the sensitivity of chaos to fluctuations. This comes about by its exponential amplification of uncertainty, noise, and error. These examples demonstrate the necessity of considering the observer in an arbitrarily accurate determination of a chaotic system's state.

The observer's complete determination of the system-under-study leads to a determination of the entire universe of which the observer is part. Thus the observer must observe and measure himself. This produces an infinite regression of necessary measurements and requires the storage of information of the universe's state within a subsystem. The process of storage itself involves the measurement and manipulation of further subsystems' states. The infinite regression thus requires the

storage of an infinite amount of information. Regardless of the size of the universe, this self-observation and internal self-coding is impossible. Thus one concludes that arbitrarily precise measurements of a chaotic system's state are not possible. The third law of information dynamics seems forced upon us by the sensitivity of chaos to external information sources.

This result and its argument remind one, somewhat uncannily, of the paradoxes associated with Godel's incompleteness theorem. Godel's theorem states that in a formal system of sufficient structure there are true statements expressible in the system's syntax that are not provable using the system's rules. Thus the formal system cannot "know" (prove) everything implicit in its structure. The third law of information dynamics represents a similar "measurement" incompleteness for chaotic dynamics.

With these general considerations in mind, the next two chapters set up a more explicit picture of dynamical systems in the physical world. This will lead in chapter 5 to quantitative measurements of a chaotic system's unpredictability.

CHAPTER 2

Information Flow

2.1. Information Production

Chaos, in its unpredictability, produces information. This distinguishes chaos from other behavior types. This is its most fundamental physical property. To measure information production requires an accounting of the information flow between subsystems in the universe. These subsystems necessarily include the system-under-study and any information sources external to it including the observer and his measuring apparatus.

This chapter presents a conceptual model for the dynamic flow of information between these subsystems. This model forms the basis of the observational theory of chaotic behavior. The model represents the information flow in a small number of pathways between the universe's subsystems. In preparation for quantifying unpredictability, the next chapter describes in more detail information flow within a subset of these pathways.

Shannon's picture of information flow through a noisy communication channel provides the analytic basis for understanding each pathway. The next section reviews this approach. The information flow model for chaos is then presented. The chapter concludes with a few remarks on how information production precludes the construction of predictive models

of chaotic behavior.

2.2. Shannon's Noisy Communication Channel

Shannon's noisy communication channel is an idealization of the processes that affect information as it moves from its source to a destination. Figure 2.1 illustrates this. The analysis of this process makes no reference to chaotic behavior as such.

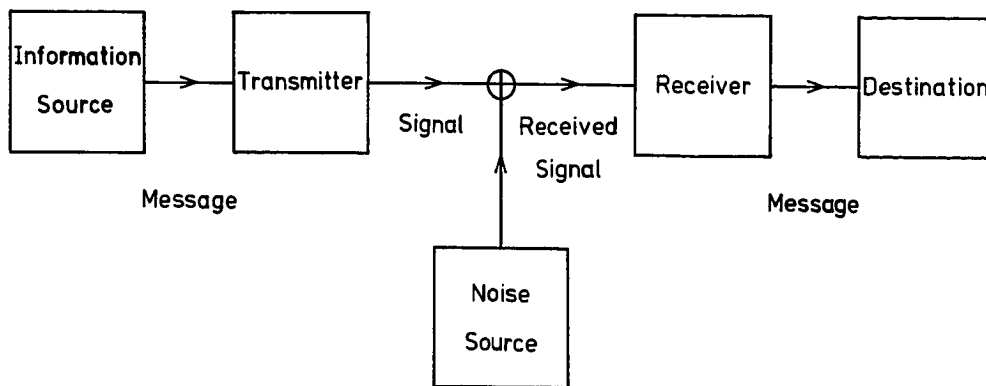


Figure 2.1.

Shannon's noisy communication channel.

2.3

The information source represents a system that produces information such as a television camera, a bird, or a waterfall. The source produces a message that is encoded into a signal by the transmitter: a picture is broadcast as radiowaves; the bird gives a mating call that spreads through the forest as air pressure waves; the waterfall splashes producing a representative pattern of electromagnetic radiation. During the transmission distortion of the signal occurs that degrades its original information content. This is represented by a noise source. The signal is then received, reconstructed into a message, and presented to the destination. The television signal is received with snow or ghosts in the picture; the bird's call is lost among thousands of others; the splash is barely visible behind the waterfall's mist.

It is important to note that in describing this communication process, energy is certainly not the quantity that is transmitted. Indeed, each stage may dissipate tremendous amounts of energy for the short term maintenance of information stored as the stable states of some subsystem. Information arises as the natural quantity describing the communication process.

A given channel may be part of a larger flow of information. For example, the television camera itself is an entire communication channel. Its information source is the photons incident on its pickup tube; its distortion is electronic noise and the raster dissection of the picture; its destination the output of an electronic signal. Any physical system considered as a channel thus can be seen as a

composition of channels, depending on the scale of description.

2.3. Observing Chaos

Dynamics that produces information demands accounting for the flow of this information. This is especially important if the dynamics' unpredictability is to be given a quantitative measure. Furthermore, this information bookkeeping allows a precise statement of the measurement problem of chaos. This can be stated roughly as follows, given a data set of observed states of a noisy physical system, how much can one deduce about the underlying dynamics? In particular, how much of the unpredictability is due the deterministic chaos and how much to external fluctuations? A concrete statement of this problem is given at the end of this section, but first the overall picture of information flow in the observation of chaotic physical systems must be described.

Figure 2.2 presents a "gedanken" diagram for the observation process. There are four subsystems, namely the extrinsic noise, the system-under-study, the measuring instrument, and the observer. Information flows in the pathways between these subsystems.

The goal in this observation process is to understand as much as possible about the system-under-study. I will assume that its dynamics produce information. Independent of extrinsic information sources, it is characterized by its information production rate. This property is reflected in several measures of chaos from dynamical systems theory. These are defined in chapter 5, but are listed here for the sake of discussion: the spectrum of Lyapunov characteristic exponents $\{L_i\}$, and

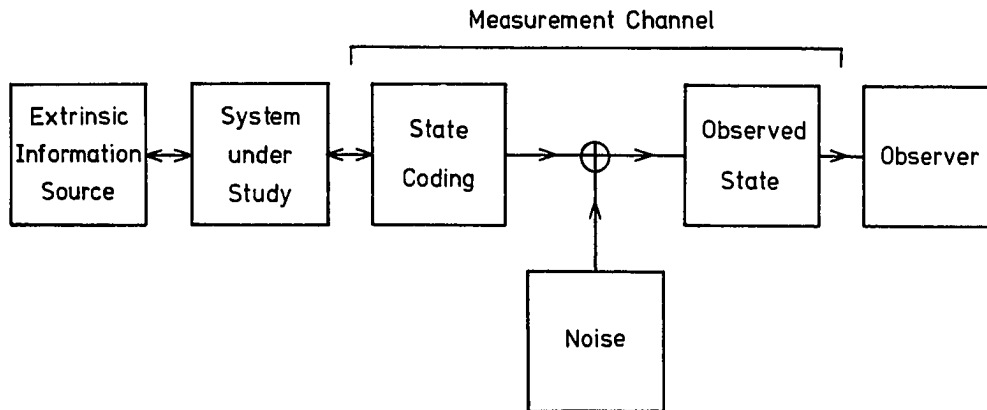


Figure 2.2.

Information flow in the observation of chaotic physical processes.

the topological and metric entropies, h and h_u respectively. I will concentrate on the metric entropy h_u , that for now can be interpreted as the closest representative of a deterministic chaotic system's information production rate.

The diagram assumes that classical and completely deterministic processes govern the physical world's dynamics. The inclusion of "extrinsic noise" represents the observer's a priori decision that certain dynamics is uninteresting or unknowable in detail. The extrinsic

information source affects the system-under-study's dynamics. The "noise" increases or decreases the observed information production rate. Its dynamics are statistically summarized by a general noise level σ_x . It corresponds to couplings of the system-under-study to other degrees of freedom in the universe that are considered separate from the system. This occurs practically because extrinsic information sources cannot be measured and/or controlled. Such a statistical characterization of the extrinsic information is tantamount to assuming it comes from a totally unpredictable information source, such as delta-correlated noise. In the language to be developed in the next chapters, the dynamics producing these external fluctuations is assumed to have infinite metric entropy. The system-under-study then acts as a "filter" for the fluctuations.

The system-under-study also is an information source for the external fluctuation dynamics. It loses information and dissipates energy by interacting with these external dynamics.

The measuring instrument produces the observed state after a sequence of idealized steps called a noisy measurement channel: (i) projecting the physical degrees of freedom onto some observables; (ii) partitioning the state space of observables into a finite and discrete set of symbols; (iii) erring in the assignment of a given symbol to a measured state. The first two processes are called state coding in analogy with the transmitter function in Shannon's channel. This stage takes the "signal" from the system-under-study and codes it into a symbol selected from some "alphabet". Possible errors in this coding process and the transmission or storage of the measured state are

summarized by the addition of a measurement noise source with noise level ϵ_m^- .

In measuring the information production properties of deterministic chaotic systems, the noisy measurement channel's information-carrying capacity R may limit the reconstruction of the dynamics by the observer. To guarantee accurate reconstruction, the noisy measurement channel's capacity must be greater than the system-under-study's information production rate, i.e. $R > h_u$.

Similar reasoning leads to an observational definition of extrinsic noise. Consider an ideal measurement channel with a prescribed measurement resolution $I_m = -\ln(\epsilon)$ and sampling rate \dagger_m . Also, assume for simplicity that the channel is noiseless, $\epsilon_m^- = 0$. This instrument acquires information at a rate of $\dot{I}_m \sim \dagger_m I_m$.^{*} Extrinsic noise, then, comes from dynamics whose information production rate h_{u_x} is greater than the measurement channel's information acquisition rate, i.e. $h_{u_x} > \dot{I}_m$.

The observer uses the measurement channel to collect a time series of observed states. The observer's data analysis consists in reconstructing the dynamics from the time series and subsequently determining its unpredictability. The measurement problem of chaos now can be stated within this framework. The problem has several components. First is a theoretical question, given h_u , $\{L_i\}$, ϵ_x^- , ϵ_m^- , \dagger_m , and I_m ,

^{*}Naturally, if $\epsilon_m^- > 0$, then \dot{I}_m is lowered.

how accurately can the observer reconstruct the dynamics of the system-under-study? Second, given the above quantities and complete knowledge of the governing dynamics for the system-under-study, how predictable is the observed behavior? Finally, and most importantly for experimental interpretation, given a time series how accurately can h_u , $\{L_i\}$, and σ_x be estimated knowing σ_m , τ_m , and I_m ?

To address these questions, the nature of chaotic dynamics as information producers must be understood.

2.4. Dynamical Systems as Feedback Communication Channels

As mentioned in the first section, components of a communication channel are also communication channels. This section illustrates how a dynamical system itself is a communication channel. There is one significant difference with Shannon's original picture. Dynamical systems are channels with feedback. Figure 2.3 illustrates this. In a dynamical system the current state is operated on ("encoded") to produce the successor state. This successor state then becomes the current state by "feedback in time". The information here is the current state out of the domain of possibilities. Dynamical systems "communicate information from the present into the future", as Shaw expresses it. The dynamics is a possibly nonlinear encoder or transmitter that takes in the current state and generates the successor state. The extrinsic information source is pictured as producing deviations from the "true" successor state.

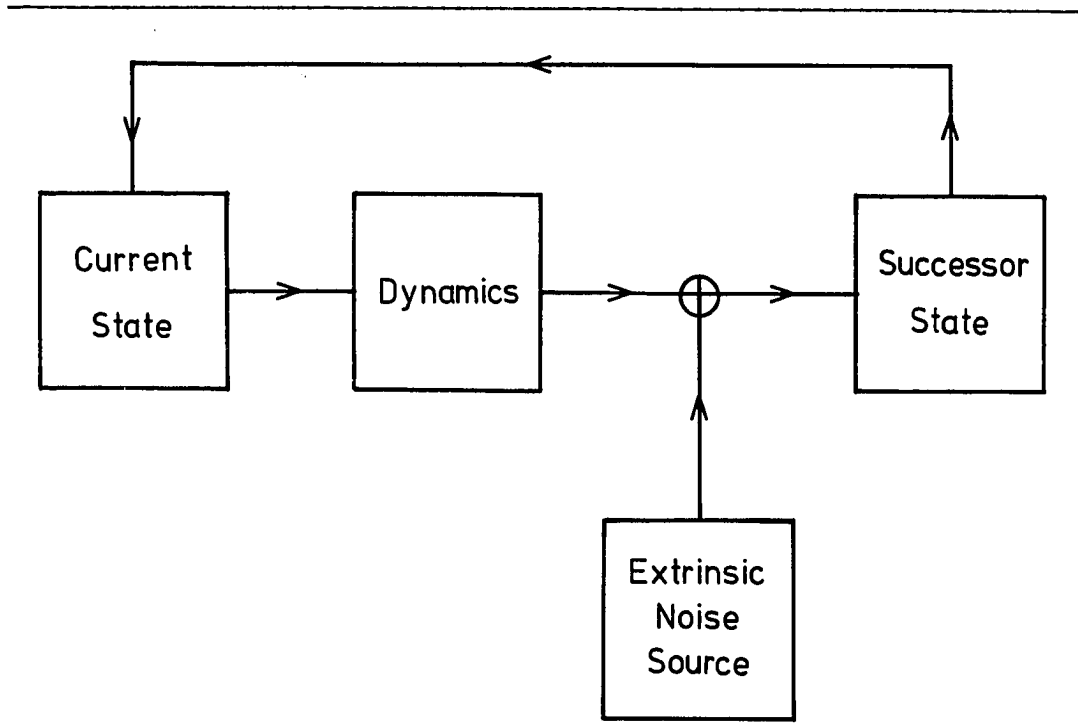


Figure 2.3.

A dynamical system as a feedback communication channel.

In the next chapter, this picture will provide the basis for the quantitative measurement of unpredictability. The last remarks in this chapter address the modeling of observed chaotic behavior from an algorithmic information viewpoint.

2.5. Modeling Chaos

The existence of deterministic unpredictable behavior forces a re-evaluation of the scientific modeling process, as conventionally conceived. To see how this comes about, the modeling of predictable

behavior must be appreciated first. The following discussion is premised on the traditional scientific algorithm, as pictured by Norman Packard. (See figure 2.4)

The scientific method for developing models of physical processes assumes that they are predictable. In the method a model of the dynamics governing the system is postulated and an initial observation of the system-under-study is made. Using this measured state and the postulated dynamics the next measurement outcome is predicted. The

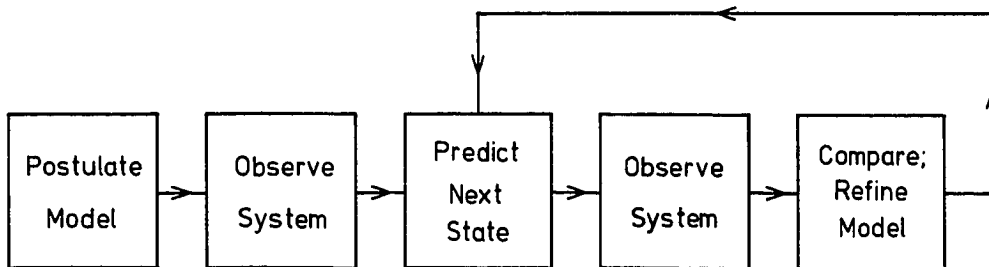


Figure 2.4.

The scientific algorithm. (after N.H. Packard)

system is then actually measured and the predicted and observed states compared. Based on the deviation of the predicted outcome from the observed state, the model is refined: parameters adjusted, terms added or dropped, and so on. For predictable behavior this process can be iterated to give an accurate model of the observed dynamics that is commensurate with the measurement accuracy and external noise in the system. The deviation of the model system orbit from the observed behavior is meaningful for predictable behavior. That is, this difference provides information upon which the model can be refined and its predictions made more accurate. The modeling of predictable behavior "converges" in this sense.

Chaotic dynamics, in direct contrast to this, exponentially amplifies any uncertainty or deviation between the observed and actual states. The model refinement process no longer converges. Chaos breaks the feedback loop in the scientific algorithm. Detailed predictions of the system's behavior cannot be made in this case. All that can be gleaned from this process are geometric and statistical characterizations of the behavior. The deviation between the model's predictions and the observed behavior cannot be reduced below that set by the system's information production rate.

The language of algorithmic information theory lends precision to the notion of constructing models of chaotic behavior.* A model is an

* See the first three papers included in chapter 5 for further discussion and references.

algorithm that produces an output x_t from an observed state x_0 after a time t has elapsed. A predictive model is an algorithm that predicts the future states to within some fixed error for all time. The size of the algorithm is a measure of the behavior's complexity. It can be expressed in several ways: first, as the number of arithmetic steps in the algorithm; or second, as the number of bits in the smallest computer program that implements the algorithm. Kolmogorov showed that the particular method of measuring the algorithm's size is unimportant if one considers the growth rate of its size with increasing prediction time. This growth rate is called the algorithmic complexity. Furthermore, under reasonable physical assumptions, the algorithmic complexity is equal to the system's information production rate.

There is an equivalent, but different formulation of these ideas from an observational viewpoint. The system-under-study produces a sequence of symbols: the observed states. The complexity of a symbol sequence is given by the smallest algorithm necessary to produce that sequence. The growth rate of this algorithm's size with increasing measurement sequence length is also the algorithmic complexity. For example, an infinitely long, but periodic sequence can be reproduced by a finite-size algorithm by storing one record of the periodic portion of the sequence and simply repeating it. A truly random sequence cannot be so reduced and stored. It can only be reproduced by the algorithm that simply stores the entire sequence. In this case, the size of the algorithm grows with the sequence length and the sequence's algorithmic complexity is non-zero.

A chaotic system produces a sequence of measurements that has positive algorithmic complexity, according to Kolmogorov. Therefore, no finite-size algorithm exists that can predict the system's behavior for all time. Chaos admits no predictive models.*

The general framework for predictability in physical systems has been developed in these first two chapters. The next addresses specific questions of quantifying unpredictability.

*These considerations can be extended to the non-deterministic case of added extrinsic fluctuations.

CHAPTER 3

Measurement Dynamics

3.1. Toward an Observation Theory of Chaos

The preceding chapters adopted an empirical viewpoint to account for information flow in observing chaos. In probing the world an observer only has measurements from which to construct models. These measurements are of finite precision for all practical purposes, or perhaps even in principle.

To make the preceding general considerations more concrete, this chapter develops an observation theory of chaos. This corresponds to a subset of figure 2.2's information flow diagram. In particular, the following discussion ignores noise in the measurement channel. This is a separate, simpler problem that can be straightforwardly analyzed with Shannon's original theory. Indeed, understanding the effect of measurement noise requires no knowledge of chaotic dynamics.

The observation theory describes how the system-under-study's information production can be determined from the information content of measurement sequences. It focuses especially on the finite nature of measurements. A state transition matrix captures the system-under-study's dynamics by describing its orbit as transitions along a sequence of states in a reconstructed "measurement" space. The following sections present this picture in detail and describe the structure of the

measurement space. This chapter concludes the general consideration of observing noisy chaos. The following chapter introduces scaling theory. The subsequent chapter then details methods using scaling theory for computing a system's unpredictability from the information contained in measurement sequences.

3.2. Dynamics and Shannon's State Transition Picture

From a sequence of measured states an observer reconstructs a dynamical picture of the system-under-study's temporal behavior. The observed dynamic ϕ acts on a space Σ of possible measurement sequences, producing a new measurement outcome each sample time. Using feedback communication channels, the observation of a dynamical system can be depicted as in figure 3.1. The diagram illustrates the information flow during one observation interval or sample time \uparrow .

The upper portion of the diagram essentially comes from figure 2.3. The system-under-study's dynamic f acts on a point $x(t)$ in the state space M leading to the next state $x(t+\uparrow)$. Extrinsic noise may also affect this process. The measurement process π , assumed noiseless for simplicity, assigns the system-under-study's state $x(t)$ to a particular measurement outcome P_i . A measurement partition $P = \{P_i : i = 0, \dots, q-1\}$ is used for this state coding. The elements P_i of the measurement partition P are labeled, for convenience only, with integer symbols $S = \{s_i : s_i = i, i = 0, 1, \dots, q-1\}$. The system-under-study's time evolution becomes coded into a measurement sequence s of outcomes, e.g. $s = (2, 5, 1, 0, 3, \dots)$.

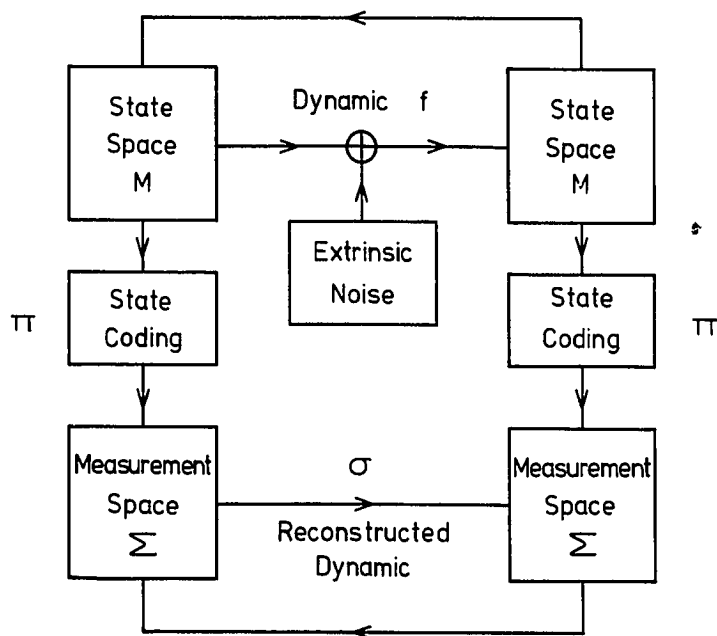


Figure 3.1.

Dynamic flow of information during one observation interval.

The collection Σ of measurement sequences s is the measurement space. The actual order in which the symbols occur allows the observer to reconstruct the observed dynamic σ . The success of the reconstruction in capturing the actual dynamics depends entirely on the nature of the measurement partition and the observation interval. Together these two choices constitute a partitioning of space-time into a lattice of observed states as illustrated in figure 3.2.

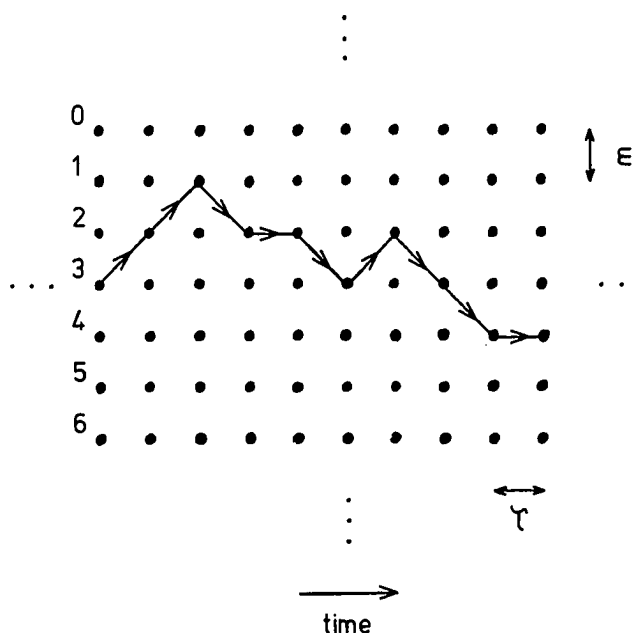


Figure 3.2.

The space-time partition induced by a choice of partition P and observation interval τ . The partition pictured is uniform with $q = \epsilon^{-1}$ elements of size ϵ . The arrows represent a realization of the reconstructed dynamic ϕ and the measurement sequence $\{3, 2, 1, 2, 2, 3, 2, 3, 4, 4, \dots\}$.

This process is summarized by Shannon's state transition picture for a communication channel. (See figure 3.3) The state transition matrix $T = (t_{ij})$ gives the probabilities t_{ij} of transitions from one observed state i to the next j ($i, j = 0, \dots, q-1$), during one observation interval. This summarizes the action of the original dynamic f acting on M for the same time interval.

3.5

In any discrete transition matrix description of dynamical processes there are three transition structures that occur. The first is a simple renaming in which a state i goes to only one other j and conversely state i is j 's only predecessor. In the second type several states lead to a single state. Shannon called this the equivocation because of the ambiguity in determining the predecessor. For a given k -to-1 structure, its equivocation is k . The third structure is the temporal opposite of equivocation: a single state goes to a number k of resultant states. I call k the indeterminacy. A renaming has an equivocation and an indeterminacy of 1. Any transition matrix T is composed of these structures. The total indeterminacy of T , for example, is the sum of the individual indeterminacies divided by the number of predecessor states.

For a transition matrix representing an attractor's dynamics, the total equivocation is equal to the total indeterminacy. This follows by contradiction. If they are not equal, then there is some state that will not be visited or is inaccessible, and so by definition it cannot be on the attractor. The exponential divergence of trajectories in a deterministic chaotic system is mirrored in the transition matrix by indeterminate transition structures. The global folding and local contraction are reflected in equivocal transition structures.

In the presence of extrinsic noise, the dynamics must be described by a continuous conditional probability distribution $P(x_{t+\tau} | x_t)$ that gives the probability of finding the orbit at $x_{t+\tau}$ knowing that at an earlier time t it was at x_t . It represents the state transitions

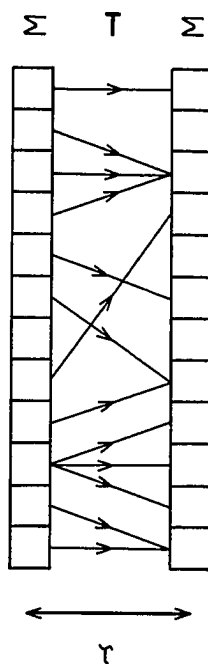


Figure 3.3.

Shannon's state transition picture. The transition matrix $T = (t_{ij})$ gives the probabilities t_{ij} of transitions from one observed state i to another j during one observation interval.

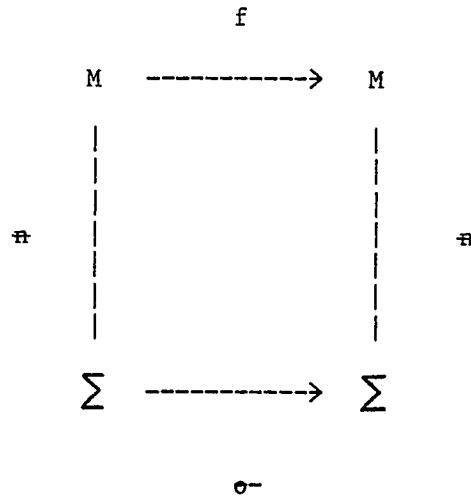
governed by the "noisy dynamic": f plus extrinsic noise. The state transition matrix T itself is a discrete conditional distribution approximation of this consisting of the single-time-step probabilities of making a transition from one observed state to its successors. Both the reconstructed dynamic ϕ and the state transition matrix T are used (Chapter 5) to quantify the system-under-study's unpredictability.

The effect of noise has a simple geometric description in terms of the state transition matrix's structure. Consider a family of partitions P_ϵ with $q = \epsilon^{-1}$ elements of size ϵ . The temporal evolution of a dynamical system observed using P_ϵ is summarized by a transition matrix $T_\epsilon = (T_{ij})$, $i, j = 0, \dots, q-1$, that takes q states to q states. With no extrinsic noise, the total indeterminacy $K(\epsilon)$ of T_ϵ remains constant with decreasing ϵ . This constant is the average spreading rate of the dynamic f . In the presence of fluctuations with noise level σ_x , $K(\epsilon)$ remains constant initially, until a resolution $\epsilon_c(\sigma_x)$ is reached at which the fluctuations themselves create indeterminate (and equivocal) transitions. The total indeterminacy then increases with decreasing resolution, diverging in the limit $\epsilon \rightarrow 0$. Below resolution ϵ_c a given state visits the successors in a state space region of size ϵ_c . The indeterminacy is then $\frac{\epsilon_c}{\epsilon}$, which diverges as ϵ vanishes. The resolution ϵ_c is thus a measure of the observed noise level. Properties of the transition matrix T_ϵ will be used in chapter 5 to measure the dimension of the attractor.

3.3. Symbolic Dynamics and Measurement Space

The observation theory of chaos considers only the structure of measurement sequences and transitions between measurement outcomes. The sequences are codified into symbol sequences for convenience. Thus the theory describes the dynamics of symbols and so is often referred to as symbolic dynamics. To accurately represent the actual dynamic f the theory requires an appropriate measurement partition and sampling time.

The observation of a dynamical system can be summarized compactly in a "commutating diagram" very similar to the forgoing figure's,



The objects in this mathematical representation are essentially the same as those already introduced. The dynamic f takes a point x in its domain M to other points in M , this is denoted $f : M \dashrightarrow M$. The projection operator \mathfrak{A} , signifying the measurement process, assigns a symbol s_i from an alphabet $S = \{0, 1, \dots, q-1\}$ to each element P_j of the measurement partition $P = \{P_j : j = 0, 1, \dots, q-1\}$. The event of an orbit falling into a partition element P_j at time i produces the symbol $s_i (= j)$. The entire evolution of an orbit is translated in this manner into a sequence of symbols $s = \{\dots, s_{-1}, s_0, s_1, s_2, \dots\}$. The reconstructed dynamic σ^- is called the shift operator, it merely reindexes the time origin of a sequence: $\sigma^-(s) = s'$ where $s'_i = (\sigma^-(s))_i = s_{i-1}$.

The space of all possible symbol sequences $\Sigma = \{s\}$ is an infinite discrete lattice of all possible symbols: $\Sigma = \dots \times S \times S \times S \times \dots = S^{\mathbb{Z}}$, where S is the alphabet of possible symbols and the integers \mathbb{Z} index time. An admissible sequence is one that is actually observed for a particular system. The elements of an admissible sequence satisfy $f^i(x_0) \in P_{s_i}$. The set of admissible sequences Σ_f is a closed, invariant subset of Σ .

A finite sequence of n symbols $(s_0^n, \dots, s_{n-1}^n)$ defines an n -cylinder $s^n = \{s: s_i = s_i^n, i = 0, 1, \dots, n-1\}$. s^n is the open subset of Σ_f consisting of all sequences whose first n elements agree with s_i^n . Due to the partition's identification of symbols with regions of state space, an n -cylinder codes for the set of orbits that are close for n measurements in the sense that they fall in the same n partition elements.

In other words, an n -cylinder labels the region of M in which these orbits begin being close. Different n -cylinders label different regions of M . Thus the set of all n -cylinders labels elements of a refined partition P^n of M . The longer the sequences the finer the induced partition P^n becomes.

The requirement necessary to guarantee the accuracy of the symbolic dynamics representation is that sufficiently long symbol sequences uniquely label orbits of f . This is the requirement of a "generating" partition. A generating partition is a partition of state space that yields symbol sequences which tend with increasing length to identify

unique orbits of f . When a generating partition is used the preceding diagram depicting the observation process commutes: $f(\pi(s)) = \pi(\sigma(s))$. The projection operator then satisfies

$$\pi(s) = \bigcap_{i=-\infty}^{\infty} f^{-1} P_{s_i} ,$$

for all observed sequences s .

The original dynamic f is approximated by a sequence of transition matrices T_n that give the transition probabilities between successive measurement sequences s^n of length n . That is,

$$T_n = (P(s_i^n | s_j^n)) , i = 0, \dots, q^n - 1 , \quad (3.1)$$

where the i -th sequence s_i^n is followed by s_j^n . The transition matrix describes transitions from q^n states to q^n states. The previous one-step matrix T is simply T_1 . As each n -cylinder labels an element of the refined partition P^n , T_n describes the transition probabilities between this partition's elements. With no extrinsic fluctuations, T_n becomes a better representation of the actual dynamics f with increasing sequence length n . When extrinsic fluctuations are present, the identification of n -cylinders and orbits breaks down. T_n then describes the "noisy dynamic" of f plus fluctuations.

T_n is all that an observer can know about the actual dynamics. Fortunately, it is sufficient for measuring the physically relevant properties of a chaotic system. The effects of extrinsic fluctuations

will be discussed in detail when quantitative measures of chaos are introduced.

The papers included in chapter 5 illustrate the application of these concepts to simple chaotic dynamical systems. In particular, they include pictures showing the Cantor set structure of the probability distributions $P(s_i^n)$ of n -cylinders s^n . Before developing the information theory of measurement dynamics, the next chapter introduces the ideas of scaling theory that are useful in understanding the features of information production.

CHAPTER 4

Scaling

4.1. Introduction

Many objects in the natural world and in the mathematical realm are scale invariant. This means that they reveal similar structure upon closer scrutiny. This chapter introduces the basic ideas of scaling theory that are used to describe this property and outlines some of the mathematical consequences. The intention is to set up a geometric picture of scaling phenomena that is independent of any particular physical or dynamical systems interpretation. This is done in order to bring out its generality as it is applied, in later chapters, to a range of different problems in dynamical systems. The discussion follows Stanley, Introduction to Phase Transitions and Critical Phenomena, Oxford University Press, 1971.

The original development of scaling ideas began with the study of how materials, such as fluids or magnets, change from one phase (gaseous, unmagnetized) to another (liquid, magnetized) with variation in the system's environment (temperature). The central hypothesis in describing these phase transitions is that just at the transition, or critical point, the systems are scale invariant. This property so constrains the system's possible states that the process by which the transition occurs can be quantitatively described. More remarkably, the quantitative description does not depend on the particular details

4.2

within some class of systems. This consequence is called universality, and those systems that exhibit similar transitions fall into the same universality class.

Scaling theory is also useful in describing the transition to chaos and, indeed, the nature of chaos itself. Scaling properties appear abundantly in dynamical systems. At the end of this chapter the specific applications of scaling theory appearing in the following chapters will be summarized.

4.2. Ferromagnetic Critical Behavior

A common example of scaling theory is the description of ferromagnetic phase transitions. The idealized ferromagnet is a lattice of up/down magnetic spins. These spins prefer to be aligned to reduce the total energy. The experimental control parameters are the temperature T and an external magnetic field H . High temperatures tend to disorder aligned spins and the external field tends to align them. The observable of interest or order parameter is the magnetization M , the average density of (say) up spins.

With no external field and at high temperature the magnet is completely disordered, $M = 0$. At some lower critical temperature T_c , the preference for spin alignment overcomes the disordering tendency of the thermal fluctuations and the magnet makes a transition to a magnetized phase with $M > 0$. At $T = 0$, all spins are aligned and the magnetization is a maximum. Near the phase transition the magnetization's growth is a power law in the temperature: $M \sim (T_c - T)^b \sim t^b$. The reduced temperature

$t = \frac{(T_c - T)}{T_c}$ measures the closeness to the transition temperature. The critical exponent b summarizes the rate of the magnetization's growth just below T_c ; typically, $b \sim .4$.

Increasing the external magnetic field H increases the magnetization by aligning spins, even at high temperatures. At T_c the magnetization's increase with H is also governed by a power law: $M \sim H^{\frac{1}{d}}$; typically, $d \sim 4$. The external field destroys the sharp temperature dependence of the transition. The transition as a function of temperature becomes smoothed out. Non-zero magnetization extends, in principle, out to arbitrarily high temperatures. An effective critical temperature t^* can be defined as that temperature at which the magnetization equals the applied external field: $t^* = \{t: M(t, H) = H\}$. The effective critical temperature can be considered as the observable transition temperature. Larger external fields increase t^* . For low fields, the increase behaves as a power law: $t^* \sim H^W$.

These three power laws appear to be rather independent features of the ferromagnet's behavior. In fact, they completely describe its response to all possible variations in temperature and external field. The magnetization M , considered as a function of t and H , is a two-dimensional surface. The invariance of the shape of this surface with changes in scale of the temperature and external field near the transition serves as the necessary constraint to relate the power laws.

The following sections develops this geometric picture of scaling. The next section briefly defines critical exponents and discusses power law behavior. The fourth section details the mathematical description of scaling. The fifth then summarizes the relationships between the critical exponents.

4.3. Exponents, Power Laws, and Limits

The critical exponents summarize the order parameter's behavior near the critical point in terms of simple power laws. Generally, though, this behavior is not a simple power law away from the transition. And so, a definition that takes this into account is necessary. The following discussion uses reduced variables as dimensionless measures of the distance from criticality.

A critical exponent k for a function $f(\epsilon)$ near its critical point, $\epsilon = 0$, is given by

$$k = \lim_{\epsilon \rightarrow 0} \frac{\ln f(\epsilon)}{\ln(\epsilon)} \quad (4.1)$$

assuming the limit exists. Asymptotically, this is often expressed as a power law $f(\epsilon) \sim \epsilon^k$. The definition does not imply this for all ϵ . For example, definition (4.1) does not distinguish between $f(\epsilon) = A\epsilon^k$ and $f(\epsilon) = A\epsilon^k(1 + B\epsilon^b + \dots)$, $b > 0$. Sufficiently near criticality the leading term dominates and a plot of $\ln(f)$ versus $\ln(\epsilon)$ exhibits a straight line region whose slope is the critical exponent.

In this regime many of the system-specific details become unimportant. The experimentalist finds a range of physical systems with very similar critical exponents. Thus the critical exponents parametrize systems into different universality classes of similar transition behavior.

Another useful definition of critical exponents that describes the large ϵ behavior is

$$L = \lim_{\epsilon \rightarrow \infty} \frac{\ln f(\epsilon)}{\ln(\epsilon)} \quad (4.2)$$

assuming this limit exists. The latter type of critical exponent definition will be used extensively in chapter 5.

For the ferromagnet the function f is the magnetization and the variable ϵ the temperature or external field. The corresponding critical exponents follow from definition 4.1.

4.4. Scaling Geometry

A scale-invariant function is a homogenous function. This section presents a mathematical description of homogeneity from a geometric viewpoint. The immediately succeeding section then ties the power laws and scaling behavior together.

A scaling function remains the same after a change in the scale of its independent variables. This invariance typically requires that the range of the function be scaled, too. Homogeneous functions are defined

by the following functional constraint that represents a change of scale

$$f(x) = g^{-1}(s) f(sx) \quad (4.3)$$

where x is a variable, s the scaling factor, and g is an unspecified function. If $f(x) = kx^{1/2}$, then $f(sx) = s^{1/2}f(x)$ and $g(s) = s^{1/2}$.

Scaling appears in more general forms than simple rescaling of the variables. In particular, there may be some arbitrary transformation T of the function that after rescaling reproduces the function. This leads to the following functional constraint on f

$$f(x) = g^{-1}(s) T f(sx)$$

A well-known example of this is the scaling structure of period-doubling bifurcation sequences. In this case, the functional equation is $f(x) = -f^2(x/a)/a$ for a one-dimensional map $x_{n+1} = f(x_n)$ at the onset of chaos. The constant a represents the spatial scaling of the attractor's structure. In these introductory remarks, I will not dwell on this more general functional form of scaling.

The constraining property of homogeneous functions given by Eq. 4.3 is that the value of f at some point x_0 and the functional form of $g(s)$ determine $f(x)$ everywhere. The value of $f(x)$ is related to that of $f(x_0)$ by a (nonlinear) change of scale

$$f(x) = f(sx_0) = g(s) f(x_0)$$

4.7

Furthermore, the functional form of Eq. 4.3 constrains the rescaling function to be of the form $g(s) = s^p$, with p some constant. This follows from composing two scale changes s and r

$$f(r(sx)) = g(r) f(sx) = g(r) g(s) f(x) .$$

This should be compared with

$$f((rs)x) = g(rs) f(x) ,$$

from which we see that

$$g(rs) = g(r) g(s) , \quad (4.4)$$

and that g too is a homogeneous function.

Assuming g is differentiable, it is straightforward to show that it is a simple power law. Differentiating Eq. 4.4 with respect to r ,

$$s g'(rs) = g'(r) g(s)$$

Setting $p = g'(1)$ and $r = 1$, we find

$$\frac{g'(s)}{g(s)} = \frac{d}{ds} \ln g(s) = \frac{p}{s}$$

or

$$\ln g(s) = p \ln(s) + \text{constant} .$$

Upon integrating and using $p = g'(1)$, we have

$$g(s) = s^p,$$

as claimed.

Homogeneous functions can be generalized in two ways. The first is to any number of scaling variables $\bar{x} = (x_1, x_2, \dots, x_n)$ with the functional equation

$$f(s\bar{x}) = s^p f(\bar{x}).$$

Consider, for example, the function $f(x,y) = x^2 + y^2$, with $p = 2$. Scale the variables by letting $x \rightarrow sx$ and $y \rightarrow sy$, then the original surface $f(x,y)$ is obtained from $f(sx,sy)$ by scaling its vertical coordinate by s^2 . As before, because s is arbitrary, knowing $f(\bar{x})$ along any path encircling $\bar{x} = 0$ determines $f(x,y)$ everywhere.

The second form of scaling is specified by generalized homogeneous functions that satisfy

$$f(\bar{s}\bar{x}) = s f(\bar{x})$$

where $\bar{s} = (s^{p_1}, s^{p_2}, \dots, s^{p_n})$ with (p_1, p_2, \dots, p_n) . The p_i are called scaling parameters. This scaling form is used to describe scaling by different factors in different variables. A two-dimensional example of this is $f(x,y) = x^2 + y^3$, with $p_1 = 1/2$ and $p_2 = 1/3$. Rescaling yields $f(s^{1/2}x, s^{1/3}y) = s f(x,y)$. Homogeneity does not specify the scaling

parameters, rather they are determined by the form of the scaling function f .

The "surfaces" described by a homogeneous function have the notable property that they can be collapsed to a function of a single variable. The homogeneity constraint implies an inter-dependence between the scaling variables, so that they can be combined into a single variable. This can be seen by considering the two variable case

$$f(s^a x, s^b y) = s f(x, y) .$$

Set $s^b = y^{-1}$, then we have

$$f(xy^{-a/b}, 1) = y^{-1/b} f(x, y) .$$

Define the function of a single variable $F(z) = f(z, 1)$ and we have

$$f(x, y) = y^{1/b} F(xy^{-a/b}) . \quad (4.5)$$

Thus under suitable rescaling, f can be expressed as a function of one variable. Conversely, if a function has the form of Eq. 4.5, then it is a homogeneous function. There is another possible choice for the function F obtained by setting $s^a = x^{-1}$,

$$f(x, y) = x^{1/a} F(yx^{-b/a}) . \quad (4.6)$$

The homogeneous forms in Eqs. 4.5 and 4.6 are preferred expressions of scaling as they make no explicit reference to the factor s . They

illustrate that homogeneity and scaling invariance are intrinsic properties of the function. In order to verify that the scaling or homogeneity hypothesis holds for an observed transition, one plots $y^{-1/b} f$ versus $z = xy^{-a/b}$, for example. This also reveals the shape of the function $F(z)$. In the preceding example with $f(x,y) = x^2 + y^3$, $z = xy^{-3/2}$ and $F(z) = z^2 + 1$.

4.5. Critical Exponents and Sum Rules

The scaling parameters \bar{p} determine the critical exponents. Either set of numbers summarizes the geometry of the "surface" f near criticality. This section explicitly shows for the two-dimensional case how the critical exponents describe the asymptotic properties of a homogeneous function and how they are determined by the scaling parameters.

In analogy with the ferromagnet, the following power laws can be used to describe the behavior of a function $f(x,y)$ that displays critical behavior,

$$f(x,0) \sim x^b \quad (4.7)$$

$$f(0,y) \sim y^{1/d} \quad (4.8)$$

$$x^*(y) \sim y^w \quad (4.9)$$

$x^*(y)$ gives the dependence of x on y for $f(x,y) = 0$. Assuming that f is homogeneous, the relationship between the exponents and scaling

parameters can be derived. Consider the following homogeneous form for f ,

$$f(x,y) = y^{1/q} F(xy^{-p/q}) \quad (4.10)$$

with the scaling parameters p and q . The power laws can then be successively applied to Eq. 4.10.

Eq. 4.7 requires that

$$\lim_{y \rightarrow 0} f(x,y) = \lim_{y \rightarrow 0} y^{1/q} F(xy^{-p/q}) = x^b \quad (4.11)$$

$F(z) \sim z^b$ satisfies this, and we have

$$y^{1/q} F(xy^{-p/q}) = x^b y^{\frac{1-bp}{q}}.$$

Condition 4.11 thus demands that $1 - bp = 0$, or $p = b^{-1}$. Power law 4.8 applied to Eq. 4.10 leads to

$$\lim_{x \rightarrow 0} f(x,y) = \lim_{x \rightarrow 0} y^{1/q} F(xy^{-p/q}) = y^{1/q}.$$

From which one concludes that $q = d$. The most general condition on Eq. 4.10 for f to vanish is that $F(z)$ remains constant. This specifies a particular $z = z_0$ at which $xy^{-p/q} = z_0$. Considering x to be a function $x^*(y)$, we find

$$x^*(y) = y^{p/q}$$

or from power law 4.9 that $w = p/q$.

4.12

Putting together these relationships between critical exponents and scaling parameters, the exponents are seen to be related by

$$b d w = 1 . \quad (4.12)$$

Such relationships are generally referred to as sum rules. These are to be expected as there are only two scaling parameters for a two-dimensional homogeneous function. Eq. 4.12 shows that the homogeneity assumption constrains the function's geometry so that there are only two independent critical exponents. Many other critical exponents can be defined and other sum rules can be derived to show their inter-relatedness.

4.6. Scaling in Dynamical Systems

A physical theory of chaos can be defined solely in terms of its scaling features. This circumvents the use of unphysical notions, such as infinitely precise points and infinitely long aperiodic orbits. Such a theory can be naturally extended to describe the effects of extrinsic noise that by definition destroy the above mathematical abstractions. The current literature on dynamical systems is rife with the analysis of microscopic dynamics: Smale's horseshoes, Axiom-A basic sets, homoclinic orbits, and so on. These concepts are unphysical to the extent that their stability and scaling features in the presence of noise is as yet unproven. An appreciation of the scaling behavior of these structures may lead to a theory for observable chaos.

A previous section mentioned the application of scaling ideas to period-doubling bifurcations to chaos. In the following chapters scaling will be used in quite different ways to describe (i) noise as an external "disordering" field for chaos; (ii) the entropies as disorder parameters describing the unpredictability of a chaotic system; (iii) the homogeneity relationship between entropy and dimension; (iv) the convergence of entropy and dimension estimates; and (v) the effect of extrinsic noise on the entropies and dimensions. The next chapter uses information theory to introduce the entropies of chaos as the quantifiers of unpredictability.

CHAPTER 5

Entropies of Chaos

The general considerations of scaling and information dynamics are applied in this and the following chapters to quantify the unpredictability of chaotic behavior. This chapter introduces various types of "entropy" to measure information production in different contexts. Special attention is given to the effects of extrinsic noise on the entropies and how these effects also can be quantified. Emphasis is placed on how the definitions and formulae can be used to analyze chaotic signals. Scaling theory elucidates the relationship between an attractor's entropies and dimensions.

The four reprints at this chapter's end present a more rigorous introduction to the entropies, including example calculations for prototypical dynamical systems. For technical considerations and for detailed references the reader should consult these papers. In contrast to the presentation in the papers, the following discussion presents the entropies and dimensions from an observational viewpoint. Where possible connections with Shannon's theory are indicated. Additionally, these sections include more recent numerical calculations on several questions not addressed in the papers. All logarithms will be to the base 2 and all information quantities are measured in bits.

5.1. Topological and Metric Entropies

During the late 50's and early 60's the topological entropy h and the metric entropy h_u were introduced to classify dynamical systems according to their temporal complexity. The mathematical literature since then gives very little indication that these quantities come simply and directly from Shannon's theory. The usefulness of Shannon's approach lies not only in its accessibility, but especially in its straightforward consideration of observing information sources. With little modification, it can be applied to the observation of chaotic dynamical systems. This section introduces the topological and metric entropies from Shannon's viewpoint.

The observation of a chaotic signal corresponds to Shannon's discrete communication channel. The measurement outcomes are then symbols that are communicated by the measurement channel to the observer. As before, the measurement channel itself will be assumed to produce no errors. After some time an observer will collect a long sequence of measurements. Any finite block of measurements is a message that contains information about the source's dynamics.

Within this framework Shannon defines the capacity C of a discrete channel by

$$C = \lim_{n \rightarrow \infty} \frac{\ln N(n)}{n}$$

where $N(n)$ is the number of observed length n sequences of q -symbols.

If $N(n)$ is the order parameter of the communication process and the total number q^n of possible sequences the scaling variable, then the channel capacity appears as a critical exponent. It measures the asymptotic growth rate of the number of observed sequences. Physically, it gives a measure of the temporal complexity. Observing periodic behavior for sufficiently large n , the number of sequences will eventually become constant.* For chaotic behavior new sequences still appear with increasing sequence length. This results in a non-zero growth rate or channel capacity.

If the outcomes or symbols are produced using an appropriate measurement partition P^* , then the channel capacity $C(P^*)$ of the measurement sequences for that partition is the topological entropy h of the attractor, $h = C(P^*)$. The existence of such a partition is thus a very important element in the observation of chaotic behavior. The next section will address this.

With a sufficiently long measurement sequence an observer can begin to estimate the probabilities $P_i(s^n)$, $i = 0, \dots, q^n - 1$, of subsequences $\{s_i^n\}$ of length n . The natural estimator $\bar{P}(s_i^n)$ of these probabilities is given by the sequences' frequencies of occurrence, namely

$$\bar{P}(s_i^n) = \frac{N(s_i^n)}{N(n)}$$

The length n^ at which this occurs is a measure of the "finite complexity" of the periodic behavior. This is used in "Symbolic Dynamics of One-Dimensional Maps" to study the complexity of orbits in finite-precision approximations to chaotic systems.

where $N(s_i^n)$ is the number of times the particular sequence s_i^n is observed.

Shannon defines the information associated with the observation of a particular sequence s_i^n as $I_i(n) = \ln P(s_i^n)$. The average information $I(n)$ contained in length n sequences is

$$I(n) = \sum_{\{s_i^n\}} P(s_i^n) I_i(n) . \quad (5.1)$$

The information production rate I of the source is the growth rate of the average information with increasing sequence length,

$$I = \lim_{n \rightarrow \infty} \frac{I(n)}{n} . \quad (5.2)$$

I is the average amount of information observed with each symbol.

Shannon actually considers the information loss rate or entropy $H = -I$ of the source. The average entropy of length n measurement sequences is $H(n) = -I(n)$. Again assuming a measurement partition P^* that maximizes H , the entropy of the measurement sequence is the metric entropy h_u of the attractor producing the sequence, i.e. $h_u = H(P^*)$. This result is due to Kolmogorov. In the same sense as for the channel capacity, the entropy h_u is the critical exponent for the average entropy "order parameter". Asymptotically, the average entropy grows like

$$H(n) = V^{h_u} ,$$

5.5

where $V = q^n$ is the volume of measurement space occupied by length n sequences of q -symbols.

There are several estimates of the entropy suggested by Shannon. These will be useful in later computations of the metric entropy and are given here without proof. Each method has its benefits and disadvantages depending on the nature of the underlying dynamics. After presenting them all, their trade-offs will be discussed.

Method 1:

The entropy can be estimated directly from Eqs. 5.1 and 5.2 using the natural estimator for the sequence probabilities.

Method 2:

The growth rate of the total entropy can be directly computed per symbol. Define the n -sequence estimate $\bar{H}(n)$ of the entropy growth rate as

$$\bar{H}(n) = H(n) - H(n-1) .$$

This estimate also limits to the entropy,

$$H = \lim_{n \rightarrow \infty} \bar{H}(n) .$$

The natural estimators are used for the sequence probabilities in $H(n)$.

Method 3:

The structure of the distribution of sequence probabilities leads to an interesting entropy estimate as follows. Make an ordered set of sequence probabilities that lists them in order of decreasing probability. Let $N(\epsilon, n)$ be the number of length n sequences, starting with the most probable, required to accumulate a total probability ϵ . The quantity $B(n) = \ln N(\epsilon, n)$ is the average number of bits necessary to specify the $N(\epsilon, n)$ most probable sequences s^n . The growth rate of this quantity is given by

$$b = \lim_{n \rightarrow \infty} \frac{B(n)}{n}$$

or by

$$b = \lim_{n \rightarrow \infty} b(n)$$

where $b(n) = B(n) - B(n-1)$ is the n -sequence approximation to the per-symbol growth rate. The quantity b measures the average number of bits required to specify each symbol or measurement outcome. When ϵ is not zero or one, Shannon shows that $H = b$. Thus by considering only the "reasonably probable" sequences, the entropy can be estimated regardless of the interpretation of "reasonably probable". A practical consequence of this is that in a number of situations, there are V^H long sequences, each of probability V^{-H} , where V is the signal space volume for length n sequences of q -symbols.

Computing entropy estimates efficiently requires rapid convergence. Method 1 estimates the entropy as the slope of a line that passes through the origin and intersects the total entropy at $H(n)$. This typically leads to very slow convergence of the estimates. Method 2 estimates the entropy by a "two-point" slope of the total entropy $H(n)$. As discussed in the first three papers at the chapter's end, this leads to rapid convergence. Due to this and its simple implementation, it is the preferred method of entropy computation. Preliminary computations indicate that the convergence of estimates made by method 3 lie somewhere between those of the other two methods. Method 3 depends strongly on the nature of the information source. The "per-symbol" estimate used with method 3 gives better convergence for the same reasons as discussed for method 2.

Methods 1 and 2 can be applied verbatim to estimate the topological entropy. The papers discuss this and related problems in detail.

The second paper included in this chapter shows that entropy convergence is governed by scaling. Scaling can be used to improve entropy estimates and more importantly, characterize different types of chaotic dynamics. The effect of extrinsic noise on entropy estimates is also described by a scaling theory. The noise level and signal space volume are the scaling variables. The excess entropy above the zero-noise entropy is the (dis)order parameter for convergence.

Before presenting numerical computations of the metric entropy, a few analytical examples are in order. The following three model systems

will be useful in understanding the effects of of extrinsic noise on chaotic systems. The discussion follows Packard (1982).

Example 1

If successive symbols in a measurement sequence are independent, then the symbolic dynamical system is Bernoulli. For these systems the probability of a given length n sequence s^n factors into the product of each of its symbols $(s^n)_i$

$$P(s^n) = \prod_{i=0}^{n-1} P((s^n)_i) .$$

It then follows that the total entropy is $H(n) = nH(1)$ and so $h_u = H(1)$. As all possible sequences of q -symbols occur the topological entropy is at its maximum $h = \ln(q)$.

Example 2

For an m -state Markov process a given symbol s depends on the preceding m symbols. The dependence is summarized by the conditional probabilities $P(s|s^m)$. The symbols are independent of those preceding s^m , that is

$$P(s|s^n) = P(s|s^m) , n > m ,$$

where $s^m = (s_{n-m-1}, \dots, s_{n-1})$. Consequently, the entropy estimates have converged for sequences the same length as or longer than m ,

$$h_u(m) = h_u(n) , n > m .$$

The entropy estimates $h_u(n)$ decrease until $n = m$, at which sequence length and beyond they are constant. The length m is called the entropy convergence knee.

Example 3

For an infinite state Markov process, m is infinite and the entropy estimates $h_u(n)$ decrease monotonically to an asymptotic value.

Figure 5.1 illustrates the entropy estimate convergence as a function of sequence length for these examples.

5.2. Effective generating partitions

The preceding section assumed that an appropriate measurement partition was employed so that the information properties of the measurement sequences accurately reflected the underlying chaotic dynamics. As defined in chapter 3, such a partition is called generating if sufficiently long measurement sequences obtained by using it uniquely identify states of the dynamical system observed. Kolmogorov showed that in the space of all partitions $\{P\}$ the generating partitions P^* give maximum entropy $H(P)$. This is the dynamical system's metric entropy, $h_u = H(p^*)$.

Generating partitions are essential for the interpretation of entropy computations. For the sake of discussion, there are two types of generating partitions. Minimal partitions are those with a small number

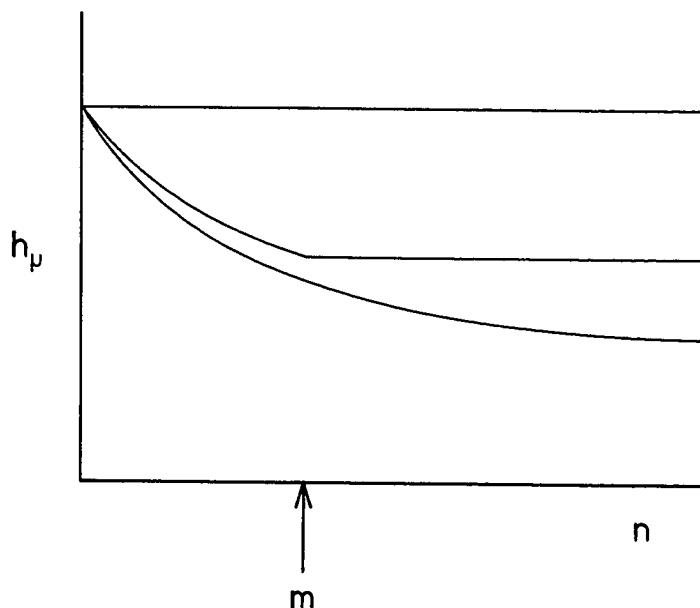


Figure 5.1.

Entropy convergence for (a) a Bernoulli system, (b) an m -state Markov process, and (c) an ∞ -state Markov process. The arrow labeled with m indicates the entropy convergence knee for the second example.

of elements and large cell size in state space. Fine partitions are those with many small elements. To be more specific in this distinction, consider a generating partition P with q elements. Minimal partitions have $q \sim 2^{h_u}$ elements, each of which is of size $\epsilon \sim 2^{-h_u}$, assuming the attractor in question is of unit size and has entropy h_u . Fine partitions, in contrast, have a very large number $q \gg 2^{h_u}$ of elements of small size $\epsilon \sim q^{-1}$.

All other considerations equal, fine partitions are vastly more difficult to use in estimating the entropy. There are two reasons for this: the first regarding the required computation and the second the required data acquisition.

The signal space volume for length n q -symbol sequences is $V \sim q^n$. A moderately large n is required for accurate entropy estimates because the growth rate is measured. With large n , V becomes extremely large with increasing number of partition elements. For entropy computation this leads to large storage requirements since the amount of storage is proportional to the signal space volume. However, since the entropy was assumed relatively small compared with the maximum possible $\ln(q)$ for q -symbols, this storage difficulty can be circumvented. Not all measurement sequences obtained from a fine partition are observed and so not all of the signal space volume is accessed during computation. To take advantage of this, clever storage algorithms with some form of efficient measurement sequence coding are necessary. For example these employ sorting, hashing, and binary trees. The algorithms become quite complex and demand vast amounts of computation time.

The data acquisition problem stems from using the natural estimator for the probabilities. As q is taken larger the signal space volume increases which reduces the number of occurrences of any given sequence. This then degrades the frequency estimate required for the probabilities and consequently lowers the entropy estimates.

Minimal generating partitions avoid these difficulties by definition. Certainly for very high dimensional attractors minimal partitions are necessary. Unfortunately, for an arbitrary dynamical system, there is no "first principle" method for finding one.

Minimal partitions for one and two dimensional maps have been studied extensively. (See the papers included here for example.) There appears to be a moderately efficient algorithm for finding them. It is based on the (unproved) observation that in the space of all partitions a generating partition is a local maximum. Improvements in the following algorithm are certainly possible, although the basic iterative nature of the algorithm will probably remain.

- (1) Choose the number q of partition elements and select a parametrized subset of partitions;
- (2) Set the symbol sequence length n to 1;
- (3) Compute the n -sequence entropy estimate as a function of partition parameters;
- (4) Reduce the partition parameter range to those "near" that giving maximum entropy;
- (5) increment n ;
- (6) go to step (3) and repeat until changes in the entropy estimates are below some set error.

The nature of the algorithm can be understood by noting that the first partition chosen is that giving equal probability to all the elements. Indeed, maximizing the entropy at each sequence length effectively chooses partitions that distribute probability as equally as possible among the measurement sequences.

As shown in the included papers, the effect of external noise on this procedure is actually beneficial. Noise tends to "smooth out" the entropies' dependence on partition so that the larger local maxima can be found unambiguously.

With such external noise, however, there are problems in the very definition of generating partitions. This is due to the fact that fluctuations render the notion of a unique orbit of a dynamical system meaningless. Generating partitions are based on the association of a given sequence with a unique orbit. With extrinsic noise the entire picture of dynamics must be generalized with probabilistic concepts. For example, orbits are replaced with constrained diffusion processes. Ruelle has developed the foundation of such a theory of noisy attractors.

To remedy this difficulty in a practical way the maximum entropy characterization of generating partitions can be used as the basis of a new partition type. An effective generating partition is one (i) all of whose elements are larger than the extrinsic noise level and (ii) yielding maximum entropy of the measurement sequences. This is a purely observational definition: the maximum entropy over all partitions of the

observed states is the observed dynamics' unpredictability. The above partition search algorithm can be applied directly to find effective generating partitions in actual data and so used to determine the unpredictability.

The remaining question is just what this entropy has to do with the deterministic dynamics of the system-under-study. In other words, how much unpredictability is due to the deterministic dynamics and how much to the extrinsic noise? This question can be answered in part by studying the entropy convergence with increasing measurement sequence length. This is the subject of the next section.

5.3. Markov Partitions and Noise

Within the class of generating measurement partitions there is another type, called a Markov partition, that has certain desirable properties. A Markov partition $P = \{P_i : i = 0, 1, \dots, q-1\}$ is generating, and so successively longer measurement sequences tend to identify unique orbits of a dynamical system. Furthermore, with a Markov partition the entropy of the dynamical system is that of the corresponding q -state Markov process. The Markov process is described by a transition matrix containing the probabilities of transitions made by the dynamical system between partition elements.

Markov partitions are especially useful in describing extrinsic noise effects on dynamics. Extrinsic noise of a given level σ_x induces a q -state Markov partition. Naturally, the number of states q depends directly on the noise level σ_x . As will be shown below, there are

approximately $q \sim 2^{h_u n_c}$ partition elements of average size $\epsilon_c \sim q^{-1}$, where n_c is the noise-induced convergence knee and h_u is the metric entropy of the observed sequences. Partition elements smaller than ϵ_c merely measure the unpredictability of the extrinsic noise. And so, there is no need to use smaller element partitions to compute the entropy. The extrinsic noise thus limits the useful observational resolution to approximately ϵ_c . This can be stated as the amount of information I_0 the dynamical system may contain in a "noisy state" for a given extrinsic noise level. Furthermore, the dependence of I_0 on the noise level is described by a critical exponent called the noise convergence exponent.

The information I_0 contained in a noisy state and the associated scaling theory are discussed in detail in the second and third papers in this chapter. I will briefly outline the arguments given there and provide a simple estimate of I_0 . The method outlined uses minimal generating partitions that with length n_c sequences become refined into Markov partitions. Fine partitions may also be used in the following arguments, but they require much more computation time and data for similar results.

The goal is to estimate the "noise level" as it affects the dynamical system. This noise level will be the size scale at which extrinsic noise begins to destroy short-term predictability. For minimal partitions this can be obtained from the entropy convergence properties. For fine partitions this follows from the convergence of the

information dimension, which is defined in a later section. The discussion will return to the trade-offs between these types of partition in the last section on the scaling relationship of entropy and dimension.

For notational simplicity, the following arguments will only consider one-dimensional maps, but the reader should be aware that the arguments can be easily generalized to higher dimensional dynamics. With a deterministic system the average refined partition element size for length n sequences is reduced by a factor of 2^{-L} from that of length $(n-1)$ sequences. L is the Lyapunov characteristic exponent and 2^{-L} estimates the average slope of the map. Assuming the attractor's size is normalized, then the length n sequence induced partition P^n has elements with size $\epsilon(n) \sim 2^{-Ln}$, for large n . As the Lyapunov exponent is observed to be equal to the metric entropy then the estimate becomes $\epsilon(n) = 2^{-h_u n}$.

In the presence of extrinsic noise, the partition elements are described as probability distributions $P_{s^n}(x)$ of those points x that result in a given sequence s^n . For sequences shorter than the noise convergence knee n_c , the element size-scaling holds as if there were no noise. Beyond n_c the partition elements are smeared by the extrinsic noise and are no longer reduced in size for longer measurement sequences. Precisely stated the probabilities for each succeeding symbol beyond n_c are independent of the preceding sequence:

$$P(s_i | s^n) = P(s_i | s^{n_c}), \quad i = 0, \dots, q-1, \quad \text{for } n > n_c. \quad \text{This is the sense in}$$

which extrinsic noise induces a finite-state Markov partition. The number of states in the induced Markov process is $2^{h_u n_c}$. This is reflected in the convergence by a leveling off of the entropy estimates.

The partition element distributions $P_{s_n}(x)$ are Gaussian.

Consequently, the partition element distributions at the convergence knee n_c have an average width $\epsilon_c \sim 2^{-h_u n_c}$. The information an observer gains by observing the particular sequence s_i is

$$I(s_i) = \int dx P_{s_i}(x) \ln \frac{P_{s_i}(x)}{\bar{P}(x)} \quad (5.3)$$

where $\bar{P}(x)$ is the asymptotic probability distribution on the attractor. The average of this quantity over all the observed sequences of length n_c gives the average information contained in a "noisy state" I_o .*

$$I_o = \sum_{\{s^{n_c}\}} P(s^{n_c}) I(s^{n_c}) . \quad (5.4)$$

By labeling the partition element distributions $P_{s_n}(x,y)$ by their mean position y another formulation of this quantity is possible. First, the information gained by the observation of the sequence s coming from the distribution $P_s(x,y)$ is given by

* This quantity is referred to as the "information contained in an initial condition" in "Symbolic Dynamics of Noisy Chaos" at the end of this chapter.

$$I(y) = \int dx P_S(x,y) \ln \frac{P_S(x,y)}{\bar{P}(x)} . \quad (5.5)$$

The noisy state information I_0 is then the average of this quantity with respect to the asymptotic distribution,

$$I_0 = \int dy \bar{P}(y) I(y) . \quad (5.6)$$

A simple estimate of I_0 can be derived as follows. At the convergence knee, the Gaussian-shaped partition element distributions $P_S(x,y)$ can be approximated by a uniform distribution of width ϵ_c centered at position y . Extrinsic noise smooths the detailed structure of the attractor's asymptotic distribution on size scales the order of ϵ_c . As a reasonable approximation then, the asymptotic distribution can be taken uniform over the attractor. Assuming the attractor has unit size and ϵ_c is measured relative to it, one finds the simple estimate from the above expression of the information contained in a noisy state

$$I_0 \sim -\ln(\epsilon_c) \quad (5.7)$$

where the noise-induced resolution ϵ_c can be estimated from the entropy convergence as outlined above. Using this one finds the noisy state information is given by

$$I_0 = h_u n_c .$$

5.4. Numerical Examples

To illustrate the dependence of the entropies on partition and extrinsic noise level the metric entropy was computed for several prototypic chaotic systems. The first examples come from the family of one-dimensional maps of the unit interval introduced in the first paper at the chapter's end, namely

$$x_{n+1} = a(1 - |2x_n - 1|^{1+\epsilon}) + \sigma I_n. \quad (5.8)$$

The parameter a controls the map's height from 0 to 1 and ϵ is the order of the map's maximum. I_n is a zero mean, uniformly distributed random variable of unit width. σ parametrizes the noise level of the added fluctuations. As ϵ ranges from 1 to -0.5 the map changes from the logistic map ($\epsilon = 1$) to the piecewise linear tent map ($\epsilon = 0$) to the Lorenz cusp map ($\epsilon < 0$). For $\epsilon > 0$ the slope at the maximum vanishes. The point on the interval at which the slope vanishes is called the critical point. For $\epsilon \leq 0$ the maps can be everywhere-expanding (slope > 1) on their attractors. As discussed in the papers the critical point and expanding regimes have important implications for entropy convergence.

The first numerical result presented here is that the shape of the entropy maximum depends on the order of the map's maximum. Figure 5.2 illustrates the metric entropy computed with binary partition $\{[0,d],[d,1]\}$ for the logistic and tent maps. The partition elements are labeled with symbols $S = \{0,1\}$. The entropy is graphed as a

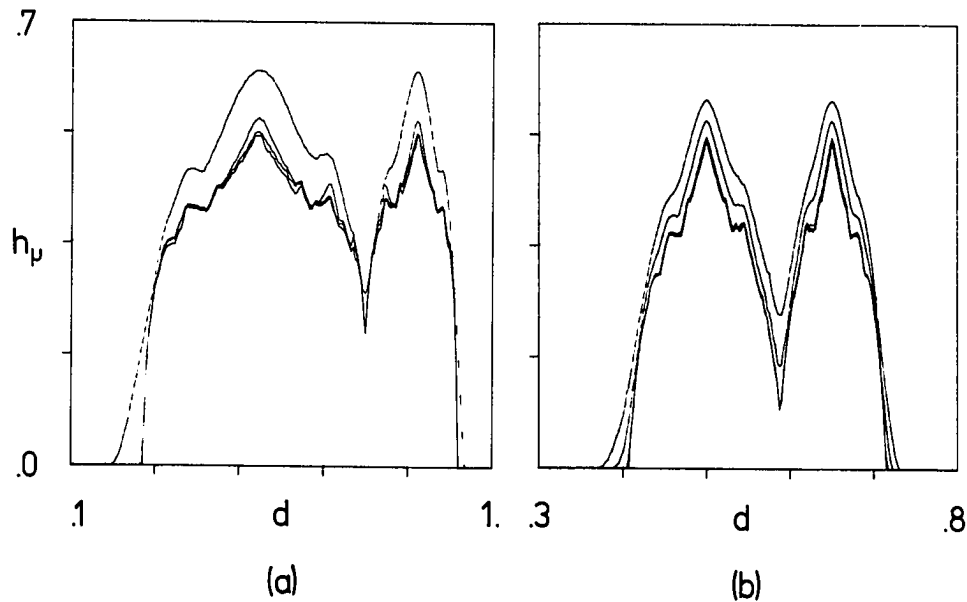


Figure 5.2.

Metric entropy h_p versus decision point d for (a) the logistic map at $a = .925$ and $\epsilon = 1^u$ and (b) the tent map at $a = .715$ and $\epsilon = 0$. The entropy curves for each map generally increase with higher noise level. The noise levels are $\epsilon = \{0, 10^{-4}, 10^{-3}, 10^{-2}\}$.

function of binary decision point d for a range of noise levels. The lowest curve in each example corresponds to no added noise. With increasing noise level the entropy at each decision point grows. Extrinsic noise is thus seen to increase the observed unpredictability. Noise also smooths out the metric entropy's dependence on decision point.

Figure 5.3 shows a detailed comparison of this dependence for the logistic, tent, and cusp maps with the decision point near the effective generating partition. Two cases, with and without noise, are shown. The expanding maps (tent and cusp) exhibit nearly piecewise linear dependence on the decision point near the generating partition. Whereas, the critical point map (logistic) has a smooth dependence. The addition of noise in all cases smoothes this dependence.

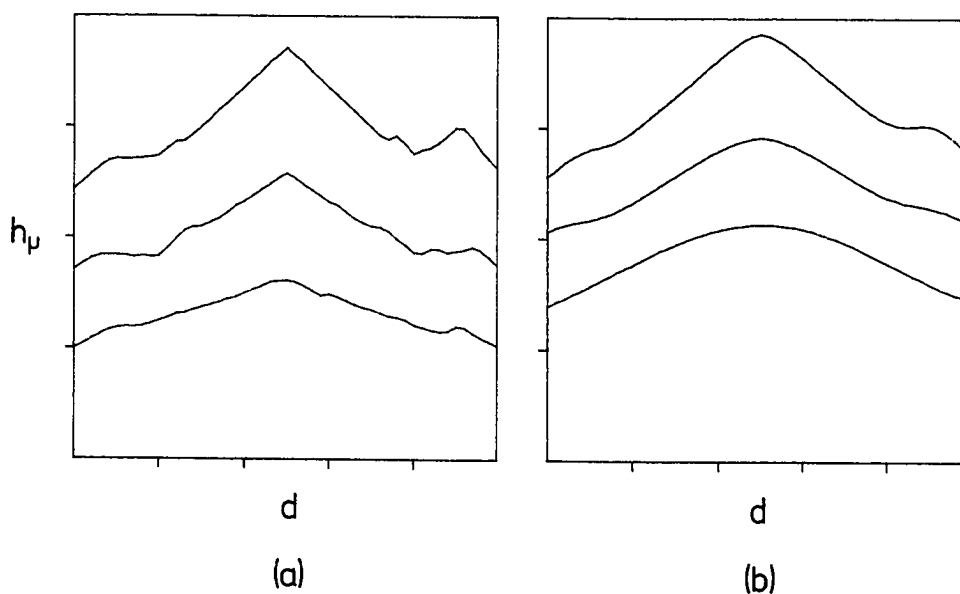


Figure 5.3.

Detail near the effective generating partition with (a) $\epsilon = 0$ and (b) $\epsilon = .01$. In each figure the curves from top to bottom correspond to the cusp map ($a = .72$, $\epsilon = -.1$), the tent map ($a = .715$, $\epsilon = 0$), and the logistic ($a = .925$, $\epsilon = 1$), respectively.

A second group of examples come from an analogous family of two-dimensional maps:

$$x_{n+1} = y_n + 1 - ax_n^{1+\epsilon} + \sigma z_n \quad (5.9)$$

$$y_{n+1} = bx_n + \sigma w_n$$

ϵ varies in the same range as before. $\epsilon = 1$ corresponds to the Henon map, $\epsilon = 0$ to the piecewise linear Lozi map, and $\epsilon < 0$ to cusp maps. The other parameters are the nonlinearity control a and the dissipation b . The added noise is given by σ as before.

The metric entropy was computed using two-element partitions $\{ P_1 \Leftrightarrow x < d, P_2 \Leftrightarrow x > d \}$.^{*} Figure 5.4 illustrates the metric entropy dependence on binary decision point d at various noise levels. Very similar, but not identical, behavior near an effective generating partition is observed.

The preceding examples calculated the metric entropy using a minimal measurement partition. This allows for rapid and accurate entropy estimates of the resulting sequences. In the case of one-dimensional maps with two monotone pieces and no added noise the sequence entropy gives the metric entropy of the dynamics. This can be checked by comparing the entropy values with the Lyapunov characteristic exponent. It has been conjectured and numerically verified for one-

^{*} Curry (1982) has made similar estimates of the Henon map's metric entropy. These are discussed in the papers.

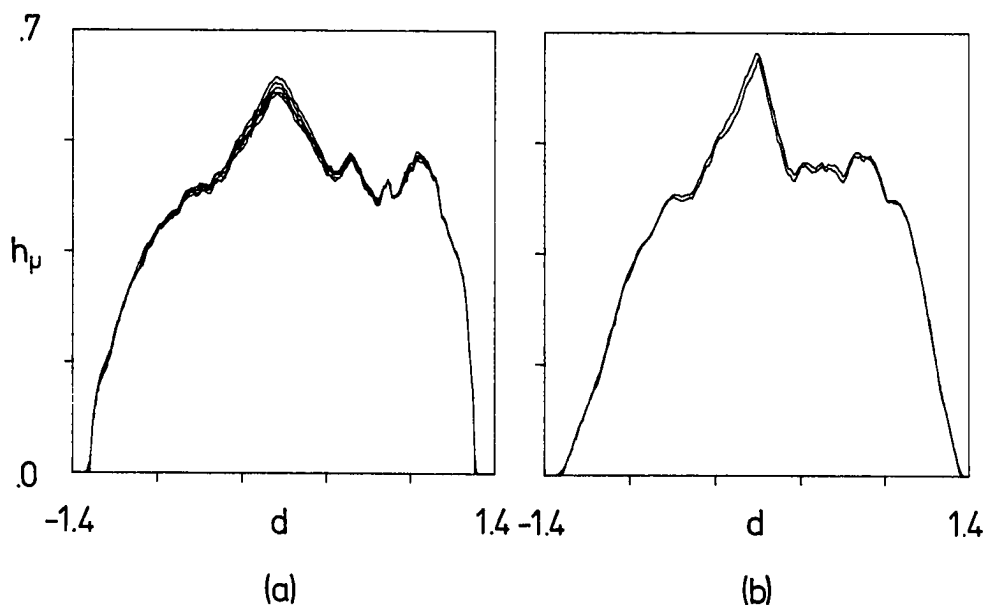


Figure 5.4.

Metric entropy h_μ versus decision line d for (a) the Henon map with $a = 1.43$ and $b = .3$, and $\epsilon = 1$; and (b) the Lozi map with $a = 1.7$, $b = .4$ and $\epsilon_3 = 0$. The noise levels are $\sigma = \{0, 3.125 \times 10^{-4}, 6.25 \times 10^{-4}, 1.25 \times 10^{-3}, 2.5 \times 10^{-3}\}$ for the Henon map and $\sigma = \{0, 10^{-2}\}$ for the Lozi map.

dimensional maps that the Lyapunov characteristic exponent is equal to the metric entropy.

As Curry (1982) found for the Henon map, the binary partition appears to be inadequate for two-dimensional maps. The computed "metric entropy" seems to remain a few percent below the Lyapunov exponent. Interestingly, this deviation is less than a percent for expanding maps, such as Lozi's. Assuming the conjectured equality between metric entropy

and Lyapunov exponent is generally correct one suspects the errors are due to not using a generating partition. However, one may conclude in these cases that binary partitions yield estimates of the metric entropy which are certainly adequate for experimental situations with added noise exhibiting simple chaotic behavior.

To understand a bit more about the structure of partition space and the resultant entropy dependence, this section concludes with sample calculations of the metric entropy computed with various three element partitions for the logistic one-dimensional map. These partitions are determined by two decision points d_1 and d_2 . The first element corresponds to $x \in [0, d_1]$, the second to $x \in [d_1, d_2]$, and the third to $x \in [d_2, 1]$. This is a two-parameter family of partitions and the entropy $h_u(d_1, d_2)$ is a surface above the (d_1, d_2) -plane. By invariance of the entropy under simple relabeling of the partition elements, one need only consider the case $d_1 < d_2$.

With this co-dimension two subspace of partitions, several questions can be addressed. What is the structure of the set $\bar{d} = \{d_1^*, d_2^*\}$ that yields maximum entropy? Specifically, are there other generating partitions than those with $d_1 = .5$ and/or $d_2 = .5$? Figure 5.5 graphs the metric entropy as a function of this partition family to answer these questions. Somewhat surprisingly, there appear to be no other generating partitions than those with d_1 or d_2 on the binary generating partition divider $d = .5$. There is no other inter-dependence between d_1 and d_2 that yields maximum entropy. The graph shows for either $d_1 = 0$ or $d_2 = 1$ the same dependence of the metric entropy on binary decision

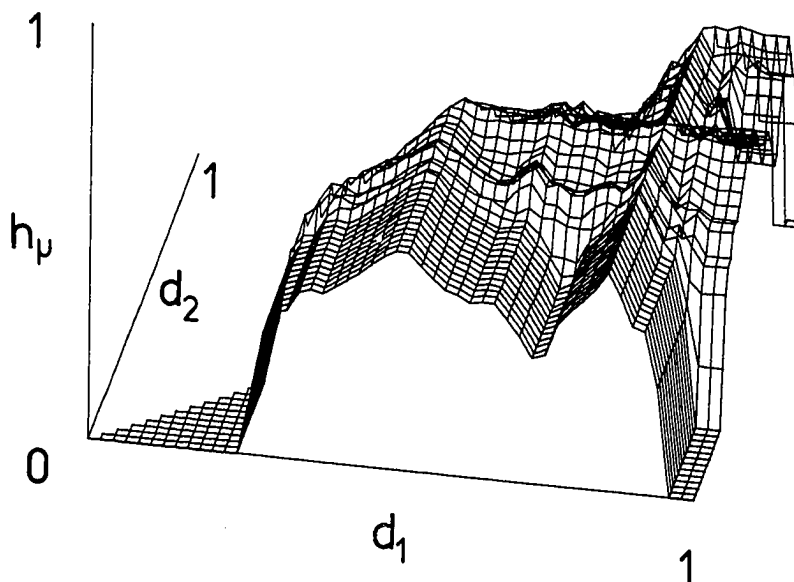


Figure 5.5.

Metric entropy computed with the three element partition $P = \{[0, d_1], (d_1, d_2], (d_2, 1]\}$. The surface is plotted only for $d_1 < d_2$.

point d_2 or d_1 , respectively, as seen in the first examples presented. This behavior also occurs when $d_1 = d_2$.

This rather simple behavior makes one somewhat hopeful that generating partitions can be found. For example, the preceding algorithm could be modified to increase the number of partitions elements once an acceptable entropy convergence is found for a partition with smaller number of elements. The addition of noise to the map has the same smoothing effect as for the binary partitions. This is also an important

indicator that the proposed generating partition algorithms will be applicable to experimental data with extrinsic noise.

For two-dimensional maps, the entropy computations are not improved much by using three-element partitions similar to those used for the logistic map. A small deviation of the maximum entropy from the Lyapunov exponent is still observed. Thus these two-dimensional maps are good candidates for the minimal generating partition algorithms. An alternative approach is to use fine partitions with many small elements.

5.5. Renyi Entropies

The topological and metric entropies are quantities in an infinite parametrized family of entropies. Renyi (Probability Theory, North-Holland, 1970) defined this family h_α , calling a member "the gain of information of order α ", where $\alpha = 0, 1, 2, \dots$.^{*} These may be simply referred to as α -order entropies. After defining this family, the topological and metric entropies will be shown to be h_0 and h_1 , respectively. Then numerical examples will be presented to illustrate the computation of several α -order entropies. In contrast with recent claims, the main result of this section is that the metric entropy is the best measure of unpredictability, especially for systems with mixed chaotic and periodic components for which the other entropies do not converge.

^{*} P. Grassberger, private communication.

Using the notation of the preceding sections, the α -order average entropy is defined

$$H_{\alpha}(n) = \frac{1}{1-\alpha} \ln \sum_{\{s^n\}} P^{\alpha}(s^n), \quad \alpha = 0, 1, 2, \dots, \quad (5.10)$$

where $P(s^n)$ is the probability of observing the measurement sequence s^n .

The α -order entropy h_{α} is then

$$h_{\alpha} = -\lim_{n \rightarrow \infty} \frac{H_{\alpha}(n)}{n} \quad (5.11)$$

Note that the α -order entropy appears to be singular at $\alpha = 1$ and to vanish at $\alpha = 0$.

The metric entropy is simply the first order entropy. To see this rewrite the α -order average entropy as

$$H_{\alpha}(n) = \frac{1}{1-\alpha} \ln \sum_{\{s^n\}} P(s^n) 2^{(\alpha-1) \ln P(s^n)}.$$

To obtain the limit as α approaches unity from above apply L'Hopital's rule, assuming H_{α} is differentiable in α ,

$$H_1(n) = \lim_{\alpha \rightarrow 1^+} H_{\alpha}(n) = - \sum_{\{s^n\}} P(s^n) \ln P(s^n)$$

and so $H_1(n) = H(n)$. Consequently, the first order entropy h_1 is the metric entropy h_u .

Similarly, the topological entropy h corresponds to h_0 . Consider the 0-order average entropy

$$H_0(n) = \lim_{\alpha \rightarrow 0^+} H_\alpha = \ln \sum_{\{s^n\}} \lim_{\alpha \rightarrow 0^+} P^\alpha(s^n) .$$

Note that

$$\lim_{\alpha \rightarrow 0^+} P^\alpha = \begin{cases} 1 & \text{if } P > 0 \\ 0 & \text{if } P = 0 . \end{cases}$$

The limit turns $P^\alpha(s^n)$ into the indicator function of the measurement sequence s^n . Consequently, one has

$$\sum_{\{s^n\}} \lim_{\alpha \rightarrow 0^+} P^\alpha(s^n) = N(n) ,$$

where $N(n)$ is the number of observed sequences of length n . Thus

$$h_0 = \lim_{n \rightarrow \infty} \frac{\ln N(n)}{n} = h ,$$

as claimed. This correspondence gives some sense of what the α -order entropies measure.

The correlation entropy h_2 can be defined for $\alpha = 2$ with

$$H_2(n) = \ln \sum_{s^n} P^2(s^n) \tag{5.12}$$

as the limit

$$h_2 = \lim_{n \rightarrow \infty} \frac{H_2(n)}{n} \tag{5.13}$$

where $P^2(s^n)$ is the probability that two orbits fall into the partition element and consequently produce the measurement sequence s^n .^{*} It can be computed more efficiently using

$$h_2 = \lim_{n \rightarrow \infty} H_2(n) - H_2(n-1) . \quad (5.14)$$

As a final remark, h_α is a monotone decreasing function of α : $h_\alpha > h_{\alpha'}$, if $\alpha' > \alpha$. This follows from term by term comparison and noting that for each term the probabilities are between zero and one and, therefore, $P^\alpha(s^n) > P^{\alpha'}(s^n)$ if $\alpha' > \alpha$. Thus the correlation entropy gives a lower bound on the metric and topological entropies.

The usefulness of the ($\alpha > 1$) entropies depends on their convergence characteristics and their response to noise. The following numerical examples indicate they are of dubious value.

For reference, the prototype systems are the logistic and tent maps already introduced. The entropies were computed using length 12 sequences of binary symbols. Typically 10^6 iterations were used to guarantee good statistical convergence for the sequence probabilities. To see if the higher order entropies are useful in searching for generating partitions, figure 5.6 graphs h_α for $\alpha = 0, 1, 2, 3, 4$ as a function of binary decision point. The entropy curves decrease with increasing α . As already seen for the logistic map, the topological ($\alpha = 0$) and metric ($\alpha = 1$) entropies clearly indicate the location of

^{*}This entropy is analogous to the correlation dimension of P . Grassberger and I. Procaccia, Phys. Rev. Lett. 50, (1983) 346.

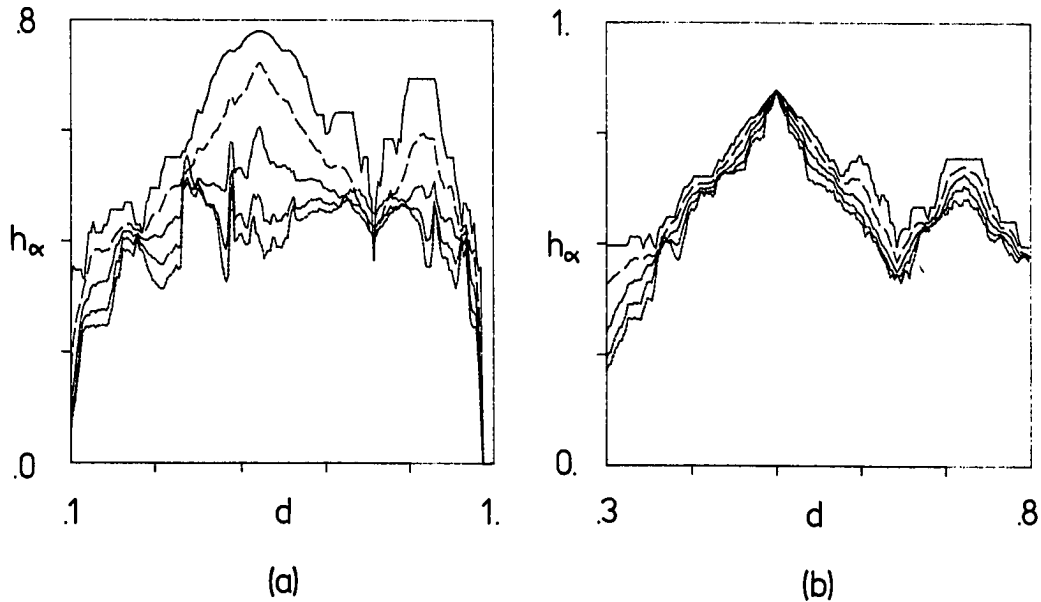


Figure 5.6.

Renyi entropies versus decision point d with $\alpha = 0, 1, 2, 3, 4$ for (a) the logistic map at $a = .925$ and (b) the tent map at $a = .715$. The corresponding entropy curves decrease with increasing α . The more broken lines correspond to larger α .

generating partitions.

The correlation entropy does this too, but much less clearly. The higher order entropies fail altogether in this. For the piecewise linear tent map, all entropies clearly indicate the generating partition. The tentative conclusion from these examples would be that the metric and topological entropies are to be preferred. In the particular case of maps with critical points the higher order entropies

should be avoided.

If noise is added to the logistic map, the situation improves markedly for the higher order entropies. (See figure 5.7.) All entropies clearly indicate the effective generating partition, although none do so as clearly and smoothly as the metric entropy.

Closer scrutiny of these figures reveals some non-monotonic behavior with increasing α for the higher order entropies. These are

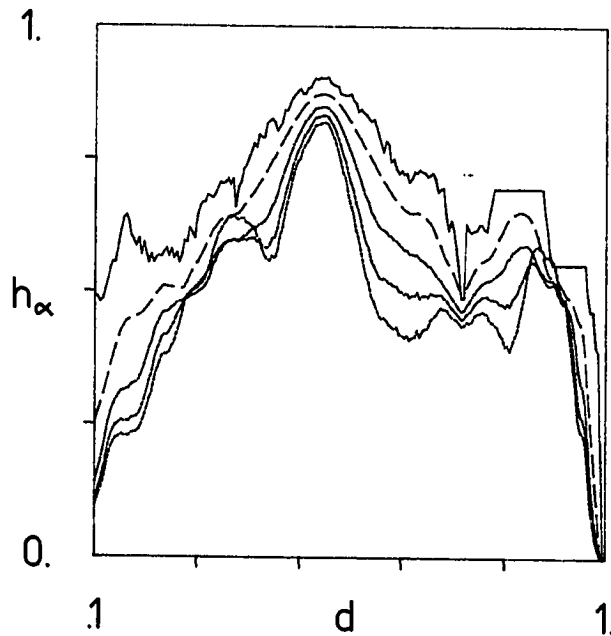


Figure 5.7.

Renyi entropies versus decision point d for the logistic map as in the last figure with noise level $\epsilon = 10^{-2}$.

due to oscillations in the entropy estimates with increasing sequence length. Using a generating partition, the entropy convergence was studied up to length 16 sequences using $\sim 10^7$ iterations.

Figure 5.8 illustrates the entropy convergence at two heights of the logistic map. For the lower height large oscillations appear in the topological, correlation, and higher entropies. This is due to the occurrence at $a = .925$ of strong period two components in the symbol

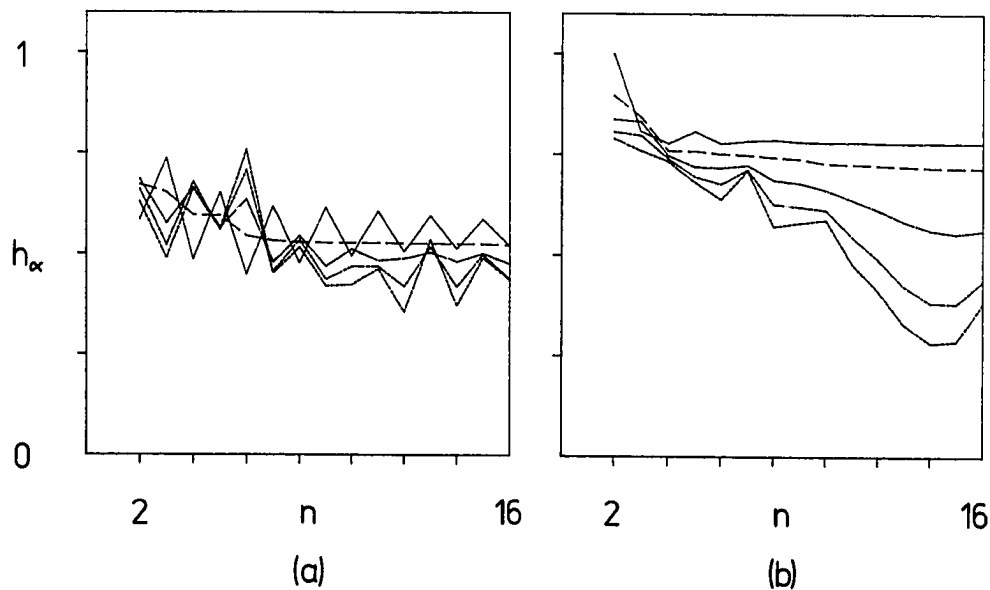


Figure 5.8.

Renyi entropy convergence for the logistic map at (a) $a = .925$ and (b) $a = .975$. The entropies are labeled as in the previous figures.

sequences. This height is just above a "band-merging". At the higher value $a = .975$ the oscillations are no longer so pronounced, but the higher order entropies exhibit peculiar, large dips at length 14 sequences. This is completely unsatisfactory behavior for entropy estimators.

A similar set of convergence graphs for the tent map at two different heights is shown in figure 5.9. At the lower height $a = .715$ all entropies but the metric entropy exhibit large oscillations. However, at the higher value $a = .9$ the oscillations almost die out by about length 10 sequences.

The general conclusion from these calculations is that the $\alpha > 1$ order entropies are very poorly converging estimators of unpredictability. The existence of critical points seems to give peculiar convergence features, even in regimes without periodic components. Like the topological entropy, these entropies also seem particularly sensitive to periodic structure in the symbol sequences. In all cases the metric entropy appeared to be the best estimator of unpredictability.

Given this and the metric entropy's direct interpretation as the observed information production rate, it should be the preferred quantity to measure in experiments. The computation of higher order entropies seems highly questionable in light of the above results.

These conclusions carry over to the next section's discussion of an attractor's dimensions. The analog of the metric entropy is the

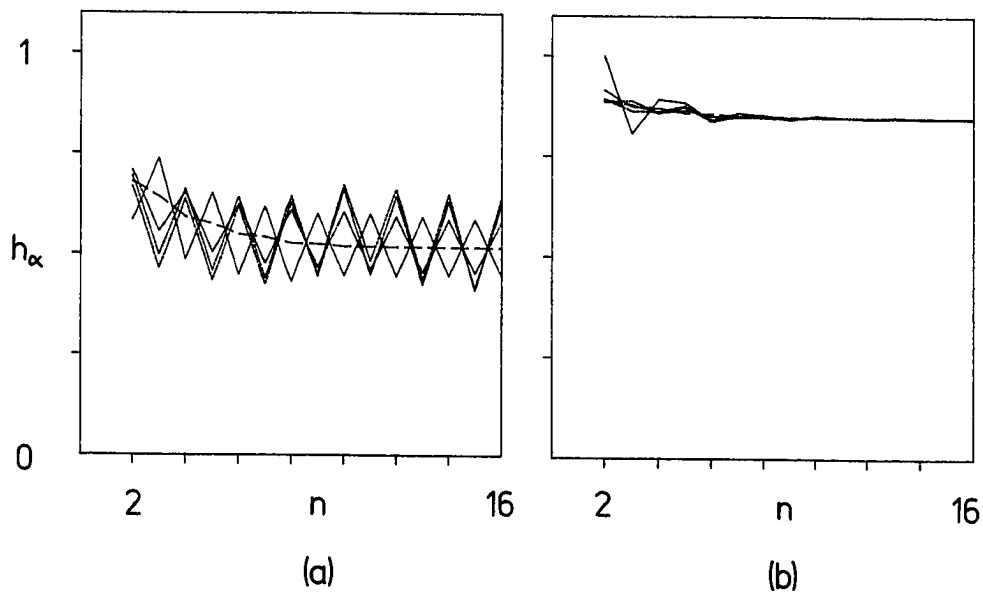


Figure 5.9.

Renyi entropy convergence for the tent map at (a) $a = .715$ and (b) $a = .9$.

information dimension. And so one would conclude that out of the possible dimensions one might measure, the information dimension is preferred.

5.6. Dimensions of attractors

An attractor's dimension indicates the number of active "modes" underlying its structure. Roughly speaking, it is the number of coordinates required to uniquely specify a state on an attractor. Like entropy, there are several different types of dimension that can be

computed. This section briefly reviews several of these dimensions, in preparation for the following discussion of their scaling relationship to the entropy. Farmer (1982) gives a more detailed introduction to dimension. Following arguments for the metric entropy in the preceding section, Farmer's "information dimension" will be seen to be the most physically relevant measure of dimension.

To determine an attractor's dimensions it is simply pictured as an object existing in a reconstructed k -dimensional space. No consideration of its dynamics is necessary. The space is partitioned into balls of volume $V = \epsilon^k$. As before the length scale ϵ should be thought of as the measurement resolution. The attractor's fractal dimension describes the ϵ -scaling of the number of balls containing portions of the attractor. It is given by

$$d_f = \lim_{\epsilon \rightarrow 0} \frac{\ln N(\epsilon)}{-\ln(\epsilon)}, \quad (5.15)$$

where $N(\epsilon)$ is the number of ϵ -balls covering the attractor. $N(\epsilon)$ is the attractor's volume measured using ϵ -ball volume units. Asymptotically then, $N(\epsilon) \sim \epsilon^{-d_f}$ and d_f appears to be the critical exponent for the ball-counting order parameter $N(\epsilon)$. It is worth noting at this point that the topological entropy is the fractal dimension of the observed sequences in measurement space. This follows from the fact that ϵ -balls in measurement space are measurement sequences.

The metric entropy also has a corresponding information theoretic dimension. Course grain the attractor's asymptotic probability

distribution \bar{P} into a discrete distribution $P(\epsilon) = \{P_i(\epsilon): P_i(\epsilon) = \text{probability contained in the } i\text{-th } \epsilon\text{-ball}\}$. The average entropy of the distribution \bar{P} at this resolution is

$$H(\epsilon) = - \sum_{\{i:\epsilon\text{-balls}\}} P_i(\epsilon) \ln P_i(\epsilon) . \quad (5.16)$$

The information dimension d_u is the growth rate of the average entropy, namely

$$d_u = \lim_{\epsilon \rightarrow 0} \frac{H(\epsilon)}{-\ln(\epsilon)} .$$

Asymptotically then, $H(\epsilon) \sim \epsilon^{-d_u}$. The information dimension is also a critical exponent, but for the average entropy contained in the attractor's probability distribution observed at measurement resolution ϵ . It is also clear now that the metric entropy is the information dimension of observed sequences in measurement space.

The Renyi entropies can also be generalized to α -order dimensions d_α as follows. Define the total α -order entropy of the distribution $P(\epsilon)$

$$H_\alpha(\epsilon) = \frac{1}{1-\alpha} \ln \sum_i P_i^\alpha(\epsilon) . \quad (5.17)$$

Then the α -order dimension is simply

$$d_\alpha = \lim_{\epsilon \rightarrow 0} \frac{H_\alpha(\epsilon)}{-\ln(\epsilon)} . \quad (5.18)$$

The fractal and information dimensions are d_0 and d_1 , respectively. The

d_α are each critical exponents for the average α -order entropy of the coarse-grained distribution.

To understand the effect of extrinsic noise on the convergence of dimension estimates, recall the partition family P_ϵ with $q = \epsilon^{-k}$ elements of volume $V = \epsilon^k$. k is the embedding dimension of the attractor in question, or simply, the dimension of the ambient reconstructed state space. For a moderate extrinsic noise level σ_x^- , the dimension estimates initially converge toward the deterministic dimension. At some resolution $\epsilon_c(\sigma_x^-)$, however, the dimension begins to scale at the ambient dimension k due to the fluctuations smearing the attractor's structure below ϵ_c . Thus the resolution at which this occurs is an observable measure of the noise level σ_x^- as it affects the attractor. This determination of ϵ_c can be used to estimate the noisy state information as outlined in a previous section.

5.7. Scaling Theory for Dimension and Entropy

From the preceding section's remarks, one suspects that there is a simple relation between an attractor's dimension and entropy. Each reflects the scaling behavior of a single information-like quantity with the change of a scaling variable. Table 5.1 summarizes the symmetric relationship between dimension and entropy. In the table the entropies and dimensions are seen to be similar scaling concepts, but applied in different spaces to different objects. As will be shown in this section an entropy reduces to its corresponding dimension for measurement sequences of unit length.

Table 5.1
Entropies and Dimensions of Chaotic Signals

	Topological	Information Theoretic	Probabilistic
entropy	topological entropy h	metric entropy h_u	correlation entropy h_2
dimension	fractal dimension d_f	information dimension d_u	correlation dimension d_2
order parameter	number of events ($N(n), N(\epsilon)$)	entropy of distribution ($H(n), H(\epsilon)$)	coincidence probability ($H_2(n), H_2(\epsilon)$)

This section presents a scaling theory as a framework for unifying the concepts of dimension and entropy. One useful consequence of this is that the effect of extrinsic noise can be understood systematically. From this one can compute, for example, the information contained in a noisy state, and how this quantity scales with extrinsic noise level. For an attractor, the dimension and entropy and their convergence properties actually determine its response to extrinsic noise. Furthermore, the homogeneous function that exhibits this scaling allows for the classification of chaotic behavior into universality classes. Indeed, this scaling theory provides a strong argument that the essential characteristics of chaos are its scaling features. The scaling theory allows one to understand chaos in a physical way. independent of unrealistic concepts such as infinitely precise points, infinitely long aperiodic orbits, and other artifacts of current

mathematical descriptions. The scaling theory will first be outlined for two scaling variables: measurement resolution and sequence length. Then the addition of a third variable, the extrinsic noise level, will be discussed.

Consider the space-time partition induced by a measurement resolution ϵ and a sample time τ . Assume for simplicity that the attractor or its signal has unity extent and that the partition elements are of uniform size ϵ . A single measurement locates the system in a state space volume $V = \epsilon^{-k}$. There are then $q = \epsilon^{-k}$ partition elements if the attractor is embedded in a k -dimensional state space. The dependence on the embedding dimension k will be suppressed henceforth. Additionally, the dynamics will be assumed discrete so that the sample time can be taken as unity $\tau = 1$.

The scaling variables of interest are first, the measurement resolution $V = q^{-1}$, and second, the measurement space volume $N = 2^n$ for length $\frac{n}{\ln(q)}$ measurement sequences. It will be more convenient to work with two related scaling variables, namely the measuring instrument's dynamic range $r = -\ln(V)$ and the length n of measurement sequences. The dynamic range r is the number of bits obtained in a single measurement and n is the number of bits in a sequence of q -symbols.

The following development will consider only information quantities by restricting attention to the information dimension and the metric entropy. The scaling theory can be easily extended to the corresponding quantities in Renyi's hierarchy. The order parameter of interest then is

the average entropy $H(n,r)$ contained in length n sequences s^{nr} obtained from a measurement partition with dynamic range r . This is given by

$$H(n,r) = - \sum_{\{s^{nr}\}} P(s^{nr}) \ln P(s^{nr}) , \quad (5.19)$$

where $P(s^{nr})$ is the probability of the sequence s^{nr} .

The information dimension d_u and the metric entropy h_u are critical exponents describing different scaling regimes of this order parameter.

The information dimension is given by

$$d_u = \lim_{r \rightarrow \infty} \frac{H(1,r)}{r} , \quad (5.20)$$

where $H(1,r)$ is the average entropy of the coarse-grained asymptotic distribution $P(s^{1r}) = \bar{P}(V=2^{-r})$. The sequences $\{s^{1r}\}$ are length 1 symbol sequences from a partition with $q = 2^r$ elements.

Assuming a generating measurement partition, the metric entropy is given by

$$h_u = \lim_{n \rightarrow \infty} \frac{H(n,r_0)}{n} , \quad (5.21)$$

where $H(n,r_0)$ is the average entropy of symbol sequences from the generating partition of dynamic range r_0 .

To study the relationship between the information dimension and the metric entropy, define the following entropy estimate

5.41

$$h_u(n,r) = \frac{H(n,r)}{n+r} . \quad (5.22)$$

In terms of the original scaling variables, this estimate is

$$h_u(N,V) = \lim_{N,V \rightarrow \infty} \frac{H(N,V)}{\ln(N/V)} . \quad (5.23)$$

The ratio in the denominator of Eq. 5.23 is the product of the measurement space volume and the state space volume, measured in units of V^{-1} . The denominator in Eq. (5.22) gives the information in bits to specify a point in the space-time lattice induced by a choice of measurement partition and sampling time. The entropy estimate's behavior as a function of n and r is shown in figure 5.10.

Requiring that the entropy estimates are within some error of the metric entropy puts a constraint on the scaling variables n and r , or equivalently N and V . Another critical exponent can be defined to describe this behavior. Let $N^*(V)$ be the measurement space volume necessary to obtain a given entropy estimate $h_u(N,V) = \text{constant}$. Then the convergence exponent w is given by

$$w = \lim_{V \rightarrow 0} \frac{\ln N^*(V)}{\ln(V)} .$$

The following three power laws and critical exponents summarize the scaling properties of the order parameter $H(N,V)$

$$H(N,V_0) \sim N^{h_u} = 2^{h_u n} \quad N \gg 1, n \gg 1, \quad (5.24)$$

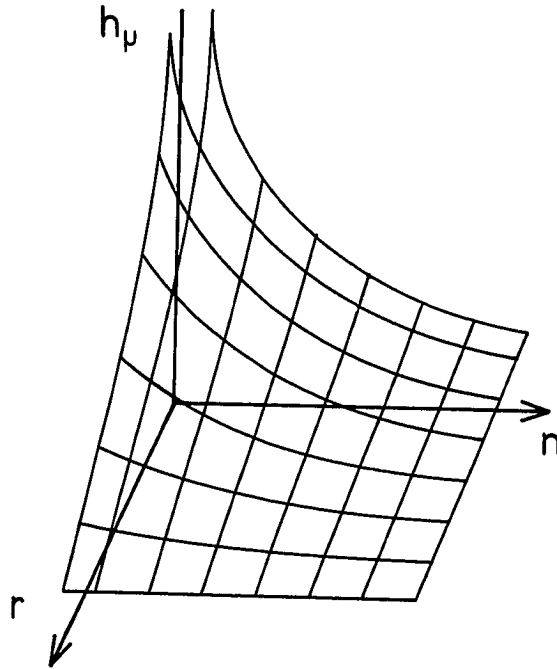


Figure 5.10.

Schematic diagram of entropy convergence. The entropy estimates $h_u(n, r)$ are graphed versus the dynamic range r and the number n of bits^u in a measurement sequence.

$$H(1, V) \sim V^{-d_u} = 2^{\frac{d_u r}{u}} \quad V \ll 1, r \gg 1, \quad (5.25)$$

and

$$N^*(V) \sim V^w = 2^{-wr} \quad V \ll 1, r \gg 1. \quad (5.26)$$

The relationship between the metric entropy and the information dimension can now be stated as a scaling hypothesis: that the average

entropy is a homogeneous function of the two scaling variables N and V , with critical exponents h_u , d_u , and w . This will also hold for the entropy estimate $h_u(n,r)$. This is equivalent to the requirement that the average entropy take the following form*

$$H(N,V) = V^{-d_u} F(NV^{d_u/h_u}), \quad (5.27)$$

where $F(z)$ is a function of the single variable $z = NV^{d_u/h_u}$. This form expresses the scaling invariance of the entropy by a rescaling in the measurement partition resolution V . It can be simply rewritten in terms of n and r as follows,

$$(n+r) h_u(n,r) = 2^{d_u r} F(2^{n-r(d_u/h_u)}). \quad (5.28)$$

To verify the scaling hypothesis the function $F(z)$ must exist. The function can be revealed by plotting $V^{d_u} H$ versus NV^{d_u/h_u} , or $(n+r)2^{-d_u r} h_u(n,r)$ versus $z = 2^{n-r(d_u/h_u)}$. More simply, by taking the logarithm, $\ln F(z)$ can be seen by graphing $\ln(n+r) - d_u r + \ln h_u(n,r)$ versus $(n - r(d_u/h_u))$.

Homogeneity results in an interdependence between the three critical exponents h_u , d_u , and w . From the above considerations, this is given by the following "sum rule":

* Only one of the two possible forms is considered here.

$$d_u = w h_u .$$

Thus the information dimension is determined by the convergence exponent w and the metric entropy h_u . Knowing any two exponents yields the third. An important consequence of this is that the convergence properties of the average entropy and the entropy estimates follows from the ratio of the information dimension to the metric entropy. The convergence properties summarized by the critical exponents take on new significance in light of this scaling theory. In particular, the exponents can be used to parametrize chaotic systems into universality classes of different convergence characteristics.

This type of scaling theory for metric entropy convergence is discussed in detail in the second and third papers at the chapter's end. To date, this theory is numerically verified for a range of one-dimensional and two-dimensional maps. The convergence theory can also be extended to the above entropy estimates. The extension uses the excess entropy \bar{h}_u defined as

$$\bar{h}_u(n,r) = \frac{h_u(n,r) - h_u}{h_u} . \quad (5.29)$$

The excess entropy measures the relative deviation of the entropy estimates from the metric entropy.

For the scaling theory proposed here extensive numerical verification beyond that given in the papers is underway. A very recent analytic result* for generalized Baker's transformations by Takens is an

example of this theory.

The dynamical systems considered are multi-dimensional Baker's transformations that can be thought of as higher dimensional analogs of the piecewise linear tent map. For example, a two-dimensional Baker's transformation takes the unit square into itself. An example is given by

$$x_{n+1} = \begin{cases} \frac{x_n}{2} & , \quad x_n < .5 \\ \frac{x_n}{2} + .5 & , \quad x_n > .5 \end{cases} \quad (5.30)$$

$$y_{n+1} = 2y_n \pmod{1}$$

for $(x_n, y_n) \in [0,1] \times [0,1]$. In words, for one iteration it stretches a square along one coordinate, cuts it, and shrinks the pieces along the other coordinate so that they can be put back into the square. The amount of stretching and the cutting point are parameters that give the family of generalized Baker's transformations. In certain symmetric cases, the topological and metric entropies are equal as well as the fractal and information dimensions.

Takens looks at the topological entropy estimate

$$h(n,r) = \frac{\ln N(n,r)}{n+r} , \quad (5.31)$$

where $N(n,r)$ is the number of length n measurement sequences obtained

* This was communicated to me by N.H. Packard.

from a partition with resolution $\epsilon = 2^{-r}$. The topological entropy h is then the limit

$$h = \lim_{n \rightarrow \infty} h(n, r), \quad (5.32)$$

assuming a generating partition. The fractal dimension d_f is similarly given

$$d_f = \lim_{r \rightarrow \infty} h(1, r). \quad (5.33)$$

By taking simultaneous limits in some direction ϕ in the (n, r) plane, Takens has shown that the quantity

$$h(\phi) = \lim_{x \rightarrow \infty} \frac{h(x, \phi)}{x} \quad (5.34)$$

is given by $h(\phi) = d_f \cos(\phi) + h \sin(\phi)$, where $x = \sqrt{n^2 + r^2}$ and $\phi = \tan^{-1}(\frac{r}{n})$. The function $h(\phi)$ is linear and so it is clearly a homogeneous function of ϕ . Takens' result concerns only the asymptotic x case. The question still to be answered is whether this ϕ -homogeneity extends to all of x .

Along these same lines, the scaling relationship between dimension and entropy can be easily extended to a third scaling variable of physical importance, namely the extrinsic noise level σ_x . The second two papers in this chapter present a noise scaling theory for the metric entropy. Exactly the same arguments can be carried over to the information dimension.

The resultant theory of entropy and dimension in the presence of extrinsic noise allows one to state precisely the effect of extrinsic noise on chaotic dynamics and to calculate the information contained in a noisy state. The scaling variables are the volume N of measurement space, the partition resolution V , and the extrinsic noise level σ_x . The important results of this theory stem from a quantitative description of how extrinsic noise affects the convergence (or lack thereof) of entropy and dimension estimates. This is particularly important for the computation of these quantities from experimental data, as well as for the theoretical justification for using metric entropy when noise is present. In principle, the metric entropy diverges with increasingly finer partitions in the presence of extrinsic fluctuations. The scaling theory allows for a systematic description of this with a noise convergence critical exponent. Consequently, it leads to the extension of "deterministic entropy" to systems with extrinsic noise. Within this theory noise is seen to be a useful experimental probe of chaos. Indeed, chaos is the geometry that constrains fluctuations. Imposing different amounts of external noise allows one to study how chaos constrains fluctuations and so to determine the critical exponents. The complete theory will be presented in future publications.

5.8. Symbolic Dynamics of One-Dimensional Maps

Symbolic Dynamics of One-Dimensional Maps: Entropies, Finite Precision, and Noise

J. P. Crutchfield and N. H. Packard

Physics Board of Studies, University of California, Santa Cruz, California 95064

Received May 7, 1981

In the study of nonlinear physical systems, one encounters apparently random or chaotic behavior, although the systems may be completely deterministic. Applying techniques from symbolic dynamics to maps of the interval, we compute two measures of chaotic behavior commonly employed in dynamical systems theory: the topological and metric entropies. For the quadratic logistic equation, we find that the metric entropy converges very slowly in comparison to maps which are strictly hyperbolic. The effects of finite precision arithmetic and external noise on chaotic behavior are characterized with the symbolic dynamics entropies. Finally, we discuss the relationship of these measures of chaos to algorithmic complexity, and use algorithmic information theory as a framework to discuss the construction of models for chaotic dynamics.

1. INTRODUCTION

We will consider the role of computation in modeling the temporal behavior of (classical) physical systems from the vantage point of dynamical systems theory. The object of any such modeling attempt is to match the behavior of some physical system with the behavior of a model comprised of some other representative system. This model may be another, simpler physical system, an abstract mathematical system, or an algorithm executed on a digital computer. It is this latter example of a model that we will focus upon. Our discussion of this modeling process relies on ideas developed by Rob Shaw (1980), to whom we are indebted for the guidance of his perspective.

If a physical system executes "regular" behavior, i.e., fixed point or periodic motion in its state space, a "good" model may be constructed to give excellent correspondence between the physical behavior and simulated model behavior, so that the model can serve a *predictive* role in understanding the physical phenomena. If one measures the physical system's state, a

model simulation can then be used to determine the future state of the physical system to within some *acceptable* error.

A large class of systems are not so well behaved: they display "irregular" motion in their state space. We will define a *turbulent* physical system as one which is inherently unpredictable in the sense that the information obtained from making a measurement on the system is lost after some finite time t . That is, an observer's knowledge of the system's state goes to zero at t .¹ This definition of a turbulent physical system is very general, and highly dependent on the measurement process used by the observer. Observed turbulent behavior may be due to one of a number of different causes: observational uncertainty, inability to resolve many degrees of freedom (as in the case of observing Brownian motion), or deterministic chaos, the latter having been added to the list only recently (Lorenz, 1963).

The case where deterministic chaos underlies the observed turbulent behavior is of special interest, and the one with which we concern ourselves here. The term *strange attractor* was coined by Ruelle and Takens (1971) to refer to the geometric structure in the state space responsible for the chaotic behavior in dissipative dynamical systems.² A strange attractor is, first of all, an attractor because a wide range of initial conditions (all those in its *basin of attraction*) approach it asymptotically, and, second of all, strange because orbits on the attractor execute neither fixed point nor periodic motion, but instead wander erratically and randomly over the attractor.³ Dynamical systems theory provides several characterizations of chaos in such systems, and so allows for the interpretation of deterministic models of the unpredictable behavior. For these systems, the unpredictability can be quantified and given an information theoretic interpretation: Nearby orbits on a strange attractor diverge exponentially in one or more directions. This process rapidly amplifies uncertainties in determining the system's state. The positive Lyapunov characteristic exponents quantify the average asymptotic rate of divergence, and can be interpreted as the strange attractor's information production rate, or alternatively, the rate at which the information contained in a measurement is lost (Shaw, 1980).

The modeling of turbulent physical systems with some underlying strange attractor presents special problems due to this inherent amplifica-

¹Phase-coherent chaotic systems present a special case; see Farmer et al. (1979).

²We refer the reader to the many excellent reviews for the relevant technical definitions of dynamical systems and strange attractors: see, for example, Chillingworth (1976), Guckenheimer et al. (1980), Collet and Eckmann (1980).

³Technical definitions of a strange attractor may be found in Ruelle and Takens (1971); in this paper we will use the physically motivated notion presented in the text, ignoring a few subtleties.

tion of measurement uncertainty. Since uncertainties are introduced because the physical system cannot be measured with infinite precision, there is no hope of using chaotic models to predict physical behavior for times longer than t . The criteria for a "good" model must now be generalized: instead of requiring exact correspondence between the physical system and the model, we must be content with a correspondence between geometric and statistical characterizations of the dynamics, giving up the idea that our deterministic model will provide us with any long-range predictive capability.

A general procedure for constructing a model for a physical system from a series of observations has yet to be developed, but progress is being made (Packard et al., 1980; Froehling et al. 1981; Takens, 1980). In the present work we will not consider this problem, but instead address certain problems that occur once a model has been chosen. We will describe quantities which characterize the chaotic behavior of a strange attractor, with particular emphasis on how these quantities may be computed numerically. We will then show how these quantities are affected by the fact that the simulation is implemented on a machine with a finite number of states, and discuss the similarities and differences between roundoff errors and errors introduced by added noise fluctuations. Though we will analyze specific models, many of the numerical techniques may be applicable to the problem of directly analyzing the turbulent behavior of a physical system.

Interest in chaotic dynamical systems has prompted other work on the reliability and interpretation of numerical results obtained by simulating such systems (Benettin et al., 1978; Erber et al., 1979). We hope the present work will extend and complement this previous work.

2. CONSTRUCTION OF SYMBOLIC DYNAMICS

There are many motivations for using the techniques of symbolic dynamics in the study of chaotic dynamical systems.⁴ The first, most physically compelling reason is that the (classical) measurement process can be viewed as producing an approximate representation of a physical system's evolution. This representation consists of a sequence of symbols, where each symbol corresponds to the output of a measuring instrument at discrete times. Any measuring instrument has finite resolution, hence the range of possible symbols is finite, with each symbol representing a different numerical value of the quantity being observed.

One of our original motivations for studying symbolic dynamics was to search for algorithms to compute an attractor's dimension and entropy from

⁴For a review of symbolic dynamical techniques, see Alekseyev and Yakobson (1981).

a time series. Of course, some algorithms already exist (Packard et al., 1980; Froehling et al., 1981; Takens, 1980; Farmer, 1981), but symbolic dynamics gives some hope of circumventing their severe precision and large data base requirements.

Symbolic dynamics also forms the cornerstone of the only rigorous treatments that exist for chaotic dynamical systems. And so, there are significant theoretical motivations for its study. Bowen (1975), Bowen and Ruelle (1975), and Sinai (1972) use symbolic dynamics to develop a fairly complete theoretical characterization of systems which satisfy Smale's axiom-A (Smale, 1967). One important aspect of this theory is the development of a "thermodynamic formalism" using the symbolic dynamics associated with an axiom-A system to prove the existence of an ergodic invariant measure which is an "equilibrium" or Gibb's state. It is not yet clear how the rigorous results concerning axiom-A systems will carry over to the many dynamical systems whose attractors are not in this class. This provides yet another reason to look at numerical results of symbolic dynamics computations of some simple non-axiom-A systems.

A dynamical system $f: M \rightarrow M$ can have many symbolic representations, each obtained by partitioning the state space M into a finite number of sets S_j , $j=1, \dots, p$, and labeling each element of this partition $S = \{S_j\}$ with a symbol s_i . The time evolution of the dynamical system is translated into a sequence of symbols

$$s = \{\dots, s_{-1}, s_0, s_1, s_2, \dots\}$$

and f itself is replaced by a *shift* operator σ , which reindexes a symbol sequence; that is,

$$\sigma(s) = s'$$

where for each symbol in the sequence s ,

$$s'_i = (\sigma(s))_i = s_{i-1}$$

Thus the shift σ merely moves the time origin of a symbol sequence one place to the right.

In the space of all possible symbol sequences

$$\Sigma = \{s = (\dots s_{-1}, s_0, s_1, \dots)\}$$

admissible sequences are those which satisfy $f^i(x_0) \in S_{s_i}$. We shall take $x_0 \in M$ as a point on the attractor of the dynamical system. The set of admissible sequences is a closed invariant set in Σ , just as are the points on

the original system's attractor. The set of admissible sequences Σ_f , along with the shift σ_f restricted to this set, is called a *subshift*. This space with the shift σ_f is the symbolic dynamical system induced by f using the *measurement partition* S . We will be mostly concerned with the space of one-sided sequences

$$\Sigma_f = \{s = (s_0, s_1, \dots)\}$$

obtained by observing which partition element is visited by the points of an f orbit $\{x_0, x_1, \dots\}$, where $x_{n+1} = f(x_n)$. The action of f on M then induces a one-sided shift on the space of admissible symbols Σ_f .

The usefulness of the symbolic dynamics construction is that if the dynamical system associated with f is ergodic, then the induced symbolic dynamical system is a faithful representation, that is, the following diagram commutes:

$$\begin{array}{ccc} \Sigma_f & \xrightarrow{\sigma_f} & \Sigma_f \\ \pi \downarrow & & \downarrow \pi \\ M & \xrightarrow{f} & M \end{array}$$

with the projection operator

$$\pi(\dots s_{-1}, s_0, s_1, \dots) = \bigcap_{i=-\infty}^{\infty} f^{-i} S_{s_i}$$

One can then study the simpler, albeit abstract, symbolic dynamical system in order to answer various questions about the original dynamical system. Within this construction, every point on the attractor will have at least one symbol sequence representation. There are a few ambiguities in the labeling of orbits by symbol sequences that prevent π from being invertible, but they will not affect our numerical calculations.

Speaking now in the context on one-sided admissible sequences, a finite sequence of symbols $(s_0^n, \dots, s_{n-1}^n)$ defines an n -cylinder $s^n = \{s: s_i = s_i^n, i = 0, \dots, n-1\}$ which is a subset of Σ_f consisting of all sequences whose first n elements match with those of s_i^n . With the identification between symbol sequences and orbits above, we see that an n -cylinder corresponds to a set of orbits that are "close" to one another in the sense that their initial conditions and first $n-1$ iterates fall in the same respective partition elements. Since these orbits must follow each other for at least

$n - 1$ iterations, they must all have initial conditions that are close, belonging to some set $U \subset M$. To a different n -cylinder will correspond a different set of orbits whose initial conditions are contained in some other set $U' \subset M$. Continuing with the set of all n -cylinders, M will become partitioned into as many elements as there are n -cylinders. As n is increased, the n -cylinder-induced partition of M will become increasingly refined.

3. SYMBOLIC DYNAMICS FOR ONE-DIMENSIONAL MAPS

In this paper, our numerical experiments will use very simple example systems, namely, maps of the unit interval onto itself (one-dimensional maps). Unless otherwise stated, we will consider the quadratic logistic equation $x_{n+1} = rx_n(1 - x_n)$ as our prototypical chaotic dynamical system. As an example of the asymptotic behavior of this system, Figure 1 shows the probability density constructed from a histogram of 10^7 iterations of the logistic equation at $r = 3.7$.⁵

We will partition the interval $[0, 1]$ into two subintervals $[0, d)$ and $[d, 1]$. Although, we will consider only two-element partitions, others are clearly possible. The symbols we shall use will be 0 for $[0, d)$, and 1 for $[d, 1]$. Changing the decision point d clearly generates a different set of admissible sequences, just as it generates different n -cylinder-induced partitions. Figure 2 illustrates the n -cylinder-induced partition with the decision point $d = 0.5$, and shows how the dividing points for the n -cylinder-induced partition are simply the collection

$$\{d, f^{-1}(d), f^{-2}(d), \dots, f^{-(n-1)}(d), \dots\}$$

whenever the specified inverse images exist. Whenever the map is not everywhere two onto one, some of the inverse images will not exist, corresponding to the fact that some n -cylinders are nonadmissible.

The space of one-sided symbol sequences can easily be metrized by mapping each symbol sequence to a power series

$$\phi(x) = \sum_{i=1}^{\infty} \frac{S(f^i x)}{2^i}$$

where $S(x)$ is 0 or 1 depending whether $x < d$ or $x \geq d$. This map identifies every sequence with a binary fraction whose value lies in $[0, 1]$. We will

⁵All logarithms in this paper are computed to the base 2.

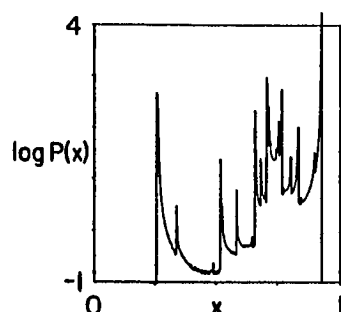


Fig. 1. Binary logarithm of the asymptotic probability distribution for the logistic equation $f(x) = rx(1-x)$ at $r = 3.7$, using 2×10^7 iterations sorted into 10^3 bins.

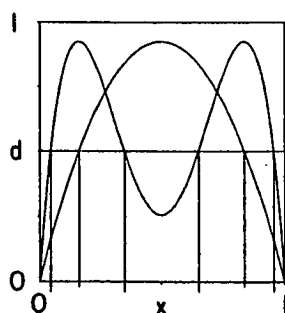


Fig. 2. Construction of the partition induced by taking n symbols (i.e., specifying an n cylinder) with a given decision point d . Illustrated is the case $d = 0.5$, and the 1-cylinder-, 2-cylinder-, and 3-cylinder-induced partitions are shown with successively longer tick marks on the x -axis.

conveniently confuse s^n with its binary fraction representation unless the distinction is necessary.⁶

The Cantor set structure of the symbol sequences of the chaotic logistic equation is revealed in Figure 3 by a sequence of probability distributions for n -cylinder binary fractions: with the increase in length of n -cylinder the distributions show successively more, although narrower, peaks. An even more graphic demonstration of the Cantor set structure is the graph of the distribution of symbols s (truncated to a finite n -cylinder with $n = 12$) versus position x , illustrated in Figure 4.

⁶Milnor and Thurston (1977) show how to form a slightly more sophisticated "invariant coordinate" which is monotonic. Our entropy calculations do not require this feature, so we use the computationally simpler binary fraction.

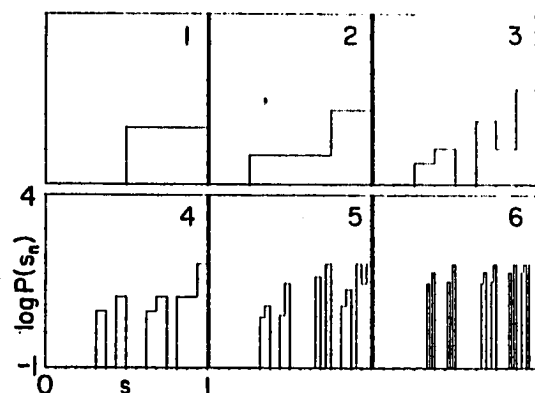


Fig. 3. The Cantor set structure of the subshift Σ_f , where f is the logistic equation with $r = 3.7$, is shown in this sequence of probability distributions for n cylinders where each n cylinder has been mapped onto the unit interval by using its binary fraction.

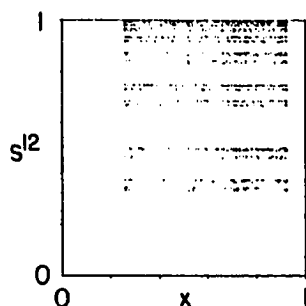


Fig. 4. Two-thousand iterations of the logistic equation with $r = 3.7$, showing in more detail the Cantor set structure of the distribution of binary fractions s^n (with $n = 12$) vs. the distribution of points x on the attractor.

We will now embark on the task of characterizing the chaotic behavior in a dynamical system using topological and metric entropies in that order. After giving their definitions, we will show various illustrative computations that will lay the groundwork for our discussions of noise and finite precision effects.

4. TOPOLOGICAL ENTROPY

Heuristically, the topological entropy of a dynamical system measures the asymptotic growth rate of the number of resolvable orbits whose initial

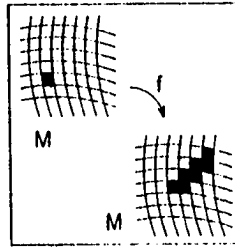


Fig. 5. Under the action of a chaotic dynamical system, points in a small region spread apart from each other exponentially, overlapping other regions, and eventually covering an attractor. The grid in each picture represents the measurement partition. The size of each element illustrates the limit of determining the system's state.

conditions are all close. Equivalently, the topological entropy quantifies the average time rate h of spreading a subset over nearby subsets (see Figure 5). This process is most easily illustrated by considering a collection of subsets which form a "cover" of the phase space, as shown schematically in Figure 5. In the figure, the dynamic f has spread the single cover element over other elements after some time t . The number of new cover elements $N(t)$ visited by points in the original cover element can be written

$$N(t) \sim e^{ht}$$

where $h > 0$ for chaotic dynamical systems. With this geometric motivation, we will now consider a more formal definition of the topological entropy h (Adler et al., 1965).

For a compact topological space M , with an open cover U , let $N(U)$ be the number of sets in a subcover of minimal cardinality. Two covers U and V may be "combined" to form a refinement W by

$$\begin{aligned} W &= U \vee V \\ &= \{A \cap B \mid A \in U \text{ and } B \in V\} \end{aligned}$$

Now if $f: M \rightarrow M$ is a continuous map, the *topological entropy* of f with respect to the cover U is defined as

$$h(f, U) = \lim_{n \rightarrow \infty} \log \frac{N(U \vee f^{-1}U \vee \dots \vee f^{1-n}U)}{n}$$

The topological entropy $h(f)$ of the map itself is then simply the supremum of $h(f, U)$ over all open covers U .

In the space of symbol sequences Σ_f , each n cylinder s^n is an open set (in the discrete topology, or in the topology generated by the metric mentioned above), and the class of all n cylinders is an open cover. As n increases, the open cover becomes more refined, and

$$\lim_{n \rightarrow \infty} \frac{\log[N(n)]}{n} \rightarrow h(\sigma_f)$$

where $N(n)$ is the number of admissible n cylinders.⁷ $N(n)$ is easily obtained numerically, so this formula presents us with a readily computable algorithm for the topological entropy.⁸ Although h is the asymptotic slope of $\log[N(n)]$, it turns out, for reasons of convergence that will be discussed shortly, that the most practical way to compute $h(\sigma_f)$ from $N(n)$ is to fit a slope to $\log[N(n)]$ for $n = 12, \dots, 16$, for example.

We have numerically computed the topological entropy of the shift induced by the binary partition $\{[0, 0.05], [0.5, 1]\}$ for the logistic equation $x_{n+1} = rx_n(1 - x_n)$. Figure 6 shows the increase of $\log[N(n)]$ with n for two parameter values $r = 3.7$ and 4.0 , and Figure 7 shows the slope of this curve, $\log[N(n+1)] - \log[N(n)]$, for two parameter values, $r = 3.9$ and 3.7 . Figure 8 shows that this numerical estimate of the topological entropy converges when a sufficient number of iterations are used. In Figures 6–8 the quantities relating to the topological entropy are shown with dashed lines; solid lines refer to the metric entropy, which will be discussed below.

Figure 7 presents several questions about the convergence and rate of convergence of the above expression for the topological entropy. Figure 7 shows how the slope of $\log[N(n)]$ begins to oscillate as r is lowered toward the value where one chaotic band splits into two bands, $r = 3.67857351 \dots$ ⁹ At the band joinings, the “two-point slope” $\log[N(n+1)] - \log[N(n)]$ oscillates indefinitely, causing $\log[N(n)]/n$ to converge rather slowly. This is illustrated in Figure 9. Convergence to $h = 0$ at the period-doubling accumulation point also is especially problematic.¹⁰

⁷For the case of symbolic dynamics, this formula for the topological entropy was first introduced by Parry (1964).

⁸There are other algorithms to compute the topological entropy of a map f based on representing the dynamics as a branching process with a deterministic transition matrix. For certain cases, they allow one to analytically calculate the topological entropy and so to study the convergence of the topological entropy directly. These techniques are based on the kneading calculus of Milnor and Thurston (1977).

⁹For a review of the phenomenology of the quadratic one-dimensional map, see Collet and Eckmann (1980) and Crutchfield et al. (1981).

¹⁰We will discuss the convergence at the period-doubling accumulation parameter value r_c in terms of the structure of the symbol sequence at r_c in a future paper.

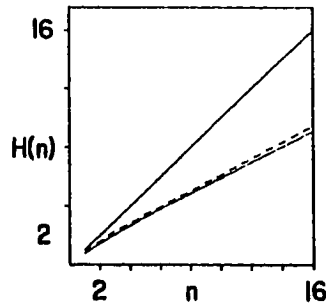


Fig. 6. Entropy convergence as a function of symbol length for the logistic equation. Top solid line is $H(n)$ and $\log[N(n)]$ for $r=4.0$ (2×10^6 iterations); the dashed line and lower solid line are $\log[N(n)]$ and $H(n)$, respectively, for $r=3.7$ (5×10^5 iterations). The topological entropy and metric entropy are the slopes of these two curves.

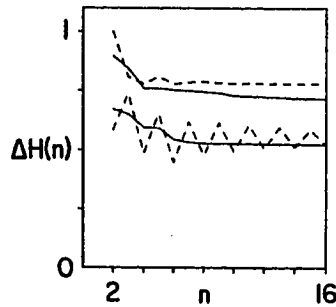


Fig. 7. Entropy convergence as a function of symbol length. Dashed lines are $\log[N(n)] - \log[N(n-1)]$ solid lines are $H(n) - H(n-1)$ for $r=3.9$ (upper set) and $r=3.7$ (5×10^5 iterations).

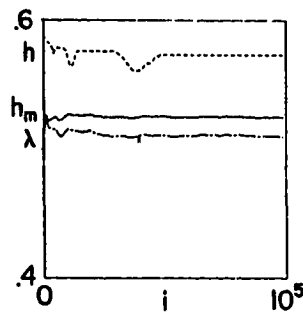


Fig. 8. Entropy convergence as a function of number of iterations i . Upper dashed curve shows topological entropy approximated by $\log[N(16)] - \log[N(15)]$, solid curve shows metric entropy $H(16) - H(15)$, and included for reference is the convergence of the Lyapunov exponent λ .

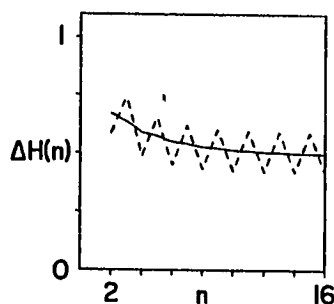


Fig. 9. Entropy convergence as a function of symbol length (as in Figure 7) at $r = 3.67857351\dots$, where two bands merge into one.

As mentioned before, changing the decision point will alter the set of admissible symbol sequences, and so the topological entropy of the shift σ_r . For example, if the decision point is on the far edge of the attractor, there will be a vast majority of one of the symbols. A graph of the topological entropy as a function of decision point is shown as the upper curve in Figure 10. From this figure we see that the measurement partition $\{[0, 0.5], [0.5, 1.0]\}$ yields a maximum value of $h(\sigma_r)$, indicating that the supremum over all partitions has been reached. In this case, we find that $h(\sigma_r)$ is identical to $h(f)$ computed using the kneading calculus of Milnor and Thurston (1977). Indeed, by the argument at the end of Section 2, each n cylinder corresponds to a particular element S_j of the cover of $[0, 1]$ comprised of the n -cylinder induced partition. Thus, for the proper partition, $h(\sigma_r) = h(f|_{\text{attractor}})$. In effect, the symbolic dynamics computation

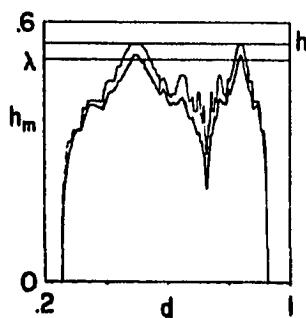


Fig. 10. Topological entropy (upper curve) and metric entropy (lower curve) of the shift induced by choosing different decision points d . The upper horizontal line is the topological entropy calculated to one part in 10^6 with the kneading determinant. The lower horizontal line is the Lyapunov characteristic exponent calculated to within 0.1%. The parameter r is 3.7.

provides a labeling scheme for the elements of the induced partition on $[0, 1]$.

5. METRIC ENTROPY

In presenting the topological entropy before metric entropy we have purposely reversed their historical order because there is a sense in which the metric entropy is a generalization of the topological entropy: the metric entropy also measures the asymptotic growth rate of the number of resolvable orbits having close initial conditions, but weighting each orbit with its probability of occurrence.

The definition of metric entropy for the dynamical system (M, f) requires an invariant measure μ and a σ algebra of measurable subsets of M : more structure than needed for the definition of topological entropy. For symbolic dynamical systems, this will not prove to be much of a problem, however, since the same n cylinders that formed elements of the open covers are also measurable subsets of Σ_f .

The structure of the attractors for the logistic equation can be quite complicated (Jonker and Rand, 1980), and the existence of many different asymptotic measures (i.e., measures whose averages of continuous functions coincide with time averages) raises serious questions concerning the validity of numerical calculations (Bennetin et al., 1978, 1979; Erber et al., 1980). Numerical evidence suggests, however, that a single asymptotic measure is selected by the simulated dynamics. The existence of such an "observable" asymptotic measure is also suggested by theoretical results that tell us when a small amount of noise is added to axiom-A systems a unique asymptotic measure is selected (Kifer, 1974).

If $P = \{P_i\}$ is a finite measurable partition of M with p elements, we define the entropy of P as

$$H_\mu(P) = \sum_{i=1}^p \mu(P_i) \log[\mu(P_i)]$$

Given two partitions P and Q , their refinement is

$$P \vee Q = \{P_i \cap Q_j \mid \text{for all } P_i \in P \text{ and } Q_j \in Q\}$$

The metric entropy of f with respect to the partition P is defined by

$$H_\mu(f, P) = \lim_{n \rightarrow \infty} H_\mu(P^n)$$

where

$$P^n = P \vee f^{-1}P \vee \dots \vee f^{1-n}P$$

Finally the metric entropy of f itself is

$$h_\mu(f) = \sup_P H_\mu(f, P)$$

where the supremum is taken over all partitions P .

For the numerical computation of metric entropy, the latter is not a very useful definition, but there is a theorem due to Kolmogorov¹¹ that helps: if P is a *generator*, i.e., the partition P^n becomes arbitrarily fine as $n \rightarrow \infty$, then we have

$$h_\mu(f) = H_\mu(f, P)$$

Unfortunately, there is no way to determine in general whether any given partition is a generator for a dynamical system. This is not a problem for symbolic dynamical systems, however, because generating partitions abound: the simplest ones being the set of all 1-cylinders. We must emphasize here that even though an n -cylinder partition of Σ_f may be a generator for the shift σ_f obtained using some measurement partition on (f, M) , this does *not* necessarily mean that the n -cylinder-induced partition on M (see Section 2 above) is a generator for f . The metric entropy computed for σ_f will be the same as the metric entropy of f *only* when this is so. In any case, the metric entropy of f is the supremum over all partitions, so it is at least as large as the entropy of the symbolic dynamical system induced by choosing some measurement partition. That is,

$$h_\mu(\sigma_f) \leq h_{\mu'}(f)$$

where μ and μ' are the asymptotic invariant measures on Σ_f and M , respectively.

We will now narrow the discussion to the special case of symbolic dynamical systems. Let $S = S^1 = \{s^1\}$ denote the partition of all 1-cylinders and S^n the partition of all n cylinders. Then, if we let $H_\mu(n) = H_\mu(\sigma_f, S^n)$,

$$h_\mu(\sigma_f) = \lim_{n \rightarrow \infty} \frac{H_\mu(n)}{n}$$

¹¹This theorem as well as the original definition of metric entropy are presented in Kolmogorov (1958).

This formula allows the numerical computation of the metric entropy for the shift σ_f , where the invariant measure μ used to compute $H_\mu(n)$ is accumulated empirically with a frequency histogram.¹² Shimada (1979) was the first to compute the metric entropy using this formula, applying it to a shift induced by the Lorenz attractor.

As in the case of topological entropy, the metric entropy is the asymptotic slope of $H(n)$ as a function of n , but this asymptotic slope is obtained numerically most readily from the "local" slope $H_\mu(n+1) - H_\mu(n)$ [or even a fit of the slope of $H_\mu(n)$ for $n_1 < n < n_2$] rather than $H_\mu(n)/n$. The quantity $H_\mu(n+1) - H_\mu(n)$ may also be written as a conditional entropy (Shimada, 1979; Billingsley, 1965), and it has a compelling informational interpretation: the metric entropy of the shift σ_f is exactly the average gain in information for each new symbol, obtained by an observer using the measurement partition \mathcal{S} , as the number of symbols gets large.

From the above definition of the metric entropy, it is easy to see that $h > h_\mu$, since $H_\mu(f, P^n)$ is maximized when each element of P^n is equally probable [i.e., $\mu(P_i^n)$ is the same for all i]. In this case, the formula for metric entropy reduces to that for the topological entropy. This is also evident from Dinaburg's theorem, which states that

$$h = \sup_\mu h_\mu$$

where the supremum is taken over all invariant measures μ (Dinaburg, 1970).

We have numerically computed the metric entropy of the shift induced by the binary partition $\{\{0,0.5\},\{0.5,1\}\}$ for the logistic equation. Figure 6 shows $H_\mu(n)$ vs n , and Figure 7 is a graph of this curve's slope, which approaches the metric entropy as n gets large. Figure 8 shows that this expression converges after enough iterations. Figure 9 shows that there is no problem with the convergence at band joinings as for the topological entropy. Although the convergence of the metric entropy still presents a problem near the accumulation points r_c of the period-doubling bifurcation sequences, away from r_c , convergence to within 5% is obtained using 13 symbols and 2×10^5 iterations. Using more symbols requires more iterations to fill out the histograms sufficiently.

As in the case of the topological entropy calculations, the choice of measurement partition used for the symbolic dynamics can make a large

¹²We assume that there exists an asymptotic invariant measure whose averages are equal to time averages for continuous functions as well as the characteristic functions on the bins of the frequency histogram. This latter feature implies that the frequency histogram should converge to a "coarse-grained" approximation of the invariant measure.

difference in the entropy of the induced shift. Figure 10 shows how the metric entropy of the shift varies with the binary partition $\{[0, d], [d, 1]\}$ as d is varied. We see that the metric entropy is maximized when $d=0.5$ and $d=0.635\dots$ (one of the inverse images of 0.5). This numerical evidence, in turn, suggests that these two decision points form generating partitions.

6. DIMENSION

When Σ_f is endowed with a metric (as described above) so that each one-sided symbol sequence is mapped to a binary fraction, the fractal dimension¹³ D_c of the set of all admissible binary fractions is given by the same formula as the topological entropy. Since increasing the length of an n cylinder is equivalent to increasing the resolution with which one specifies an element in Σ_f , the fractal dimension is given by

$$D_c = \lim_{n \rightarrow \infty} \frac{\log[N(n)]}{n}$$

So we see that the topological entropy of the subshift σ_f , and so of the map f , is equal to the fractal dimension of the binary fraction representation of the Cantor set Σ_f .

If, instead, we weight the count of n cylinders with their respective probabilities, we can define another dimensionlike quantity, the *information dimension* (Rényi, 1959; Farmer, 1981; Kaplan and Yorke, 1981),

$$D_f = \lim_{n \rightarrow \infty} \sum_{i=1}^n \mu(S_i^n) \log[\mu(S_i^n)]$$

which we see is identical to the metric entropy of σ_f . Fractal and information dimensions can also be defined for the attractors of the original dynamical system. To avoid confusion in this regard, we should emphasize that these are not the same quantities as the corresponding dimensional quantities computed for the associated symbolic dynamical system.¹⁴

¹³Properly speaking the defined quantity is the capacity of the Cantor set Σ_f . For a more detailed description of these notions of dimension, see Mandelbrot (1977).

¹⁴For a more complete overview of the information dimension concept, see Farmer (1981).

7. ENTROPIES AND LYAPUNOV CHARACTERISTIC EXPONENTS

We pause now to introduce Lyapunov characteristic exponents as another measure of chaos, and to discuss their relationship to the entropies described above. The Lyapunov characteristic exponents measure the average asymptotic divergence rate of nearby trajectories in different directions of a system's state space (Benettin et al., 1980; Shimada and Nagashima, 1979). For our one-dimensional examples, $f: I \rightarrow I$, there is only one characteristic exponent λ . It can be easily calculated since the divergence of nearby trajectories is simply proportional to the derivative of f (Shaw, 1980):

$$\lambda = \lim_{N \rightarrow \infty} \frac{1}{N} \sum_{n=1}^N \log |f'(x_n)|$$

Or equivalently, if a continuous ergodic asymptotic invariant measure μ exists, then the characteristic exponent is given by

$$\lambda = \int_0^1 \log |f'(x)| d\mu$$

We shall assume that such a measure exists, and moreover that

$$\mu_N(x) = \frac{1}{N} \sum_{n=1}^N \delta_{f^n x}$$

converges to μ as $N \rightarrow \infty$ for almost every initial condition (Oono and Osikawa, 1980).

If M is an axiom-A attractor, there is a prescription for constructing a partition which is generating, and the equality of the metric entropy h_μ and the sum of the positive Lyapunov characteristic exponents can be proven (Bowen and Ruelle, 1975). In fact, whenever an absolutely continuous invariant measure exists, a theorem due to Piesin (1977) shows that the metric entropy of a diffeomorphism is equal to the sum of the positive exponents.¹⁵ Ruelle (1978) has shown the same equality for any map that has an absolutely continuous invariant measure, and Ledrappier (1981) has

¹⁵In the general case, the exponents are a function of initial condition, so the sum must be integrated over the attractor, but we will consider only the case of an ergodic attractor where the exponents are constant almost everywhere with respect to the asymptotic invariant measure.

constructed a proof of this for the logistic equation. Shimada obtained good agreement between the characteristic exponent and the metric entropy for the Lorenz attractor and its induced symbolic dynamics using only nine symbols, and Curry (1981) has computed a metric entropy slightly lower than the positive Lyapunov characteristic exponent for a two dimensional diffeomorphism (Henon's map).

The surprising result of our numerical experiments for the logistic equation is that for most parameter values, the metric entropy of the shift induced by certain measurement partitions converges extremely slowly (from above) to the Lyapunov exponent. Naturally, the metric entropy is always less than the topological entropy. This slow convergence is clearly illustrated in Figures 8 and 10, where we see an apparent discrepancy of $\sim 5\%$ for $r = 3.7$ and $n = 16$. This slow convergence does not appear in the symbolic dynamics calculation of the topological entropy. Using 16 symbols we find it rapidly converges (to within 0.1%) to the topological entropy computed using the kneading calculus of Milnor and Thurston (1977).

The validity of the symbolic dynamics entropy calculations is supported by the fact that we find excellent agreement (to within 0.1%) between the topological entropy of the shift and the topological entropy of the map, computed using the kneading calculus of Milnor and Thurston.

We also note that, to within numerical accuracy ($< 0.1\%$), at $r = 4.0$, both entropies (computed using 16 symbols) and the Lyapunov characteristic exponent converge to 1.0. At $r = 3.6785735\dots$ where two bands merge into one, Ruelle (1977) has shown that there exists an absolutely continuous invariant measure, so that the metric entropy must be equal to the Lyapunov exponent (Ruelle, 1978). Our calculations using 16 symbols and 5×10^6 iterations, yield a topological entropy of 0.5000 ± 0.0001 , a metric entropy of 0.497 ± 0.001 , and a Lyapunov characteristic exponent 0.491 ± 0.0005 . Thus, after 16 symbols, the metric entropy has converged to within 1% of the Lyapunov exponent. Similar slow convergence was found at other parameter values (e.g. $r = 3.7$). These calculations are thus consistent with Ruelle's and Ledrappier's results mentioned above. The calculations also provide numerical evidence for the existence of an absolutely continuous invariant measure for a wide range of parameter values.

8. OTHER ONE-DIMENSIONAL MAPS

In light of the slow convergence of the metric entropy to the Lyapunov exponent, one natural question is how universal this result is. Shimada has already found good agreement between the symbolic dynamics entropy and the characteristic exponent for the cusp return map of the Lorenz attractor. To compare our results with Shimada's, we will now consider a map which

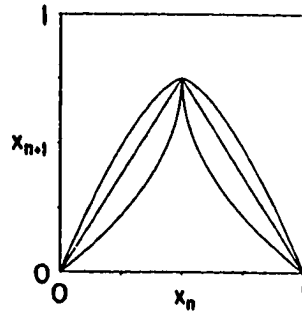


Fig. 11. Graph of $f(x) = a(1 - |2x - 1|^{1+\epsilon})$ for $\epsilon < 0$ (cusp), $\epsilon = 0$ ("tent," or piecewise linear), and $\epsilon > 0$ (hump) and $a = 3.7/4.0$.

changes under the continuous variation of a parameter from a map having a cusp, Lorenz-type maximum to one with a rounded, hump maximum. The map's functional form is

$$f(x) = a(1 - |2x - 1|^{1+\epsilon})$$

This map has a differentiable maximum ($f' = 0$) for $\epsilon > 0$, a cusp maximum for $\epsilon < 0$, and is a piecewise linear tent map for $\epsilon = 0$; $a \in [0, 1]$ determines the height of the map. Thus, $\epsilon = 1$ corresponds to the logistic equation studied in the previous section. Figure 11 shows three typical maps of this family with different values of ϵ . The results displayed in Figure 12 show that for sufficiently positive values of ϵ ($\sim > 0.8$) there is the same discrepancy between the metric entropy and the characteristic exponent as seen in the logistic equation. Whereas for all $\epsilon \sim < 0.4$, we see good agreement

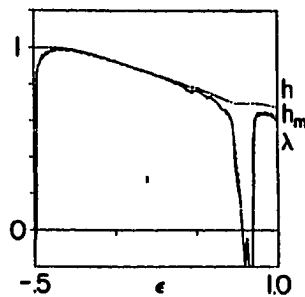


Fig. 12. Topological entropy (upper unevenly dashed line), metric entropy (dashed line), and Lyapunov exponent (solid line) for maps from cusps maps to smooth maximum maps, $\epsilon = -0.5$ to 1.0. The entropies were calculated using the kneading calculus for the topological entropy and $H(16) - H(15)$ for the metric entropy, with 5×10^5 iterations.

between them. Shimada's results for the Lorenz attractor appear then to correspond to this latter regime, as one expects. As a reference, the upper curve in the figure is the topological entropy calculated from the kneading determinant of Milnor and Thurston (1977), to an accuracy of one part in 10^6 . For ϵ in the approximate regime $[-0.3, 0.25]$ there is good (always $< 0.5\%$) agreement between all three quantities using 13 symbols. Below this regime, the topological entropy diverges from the other quantities which decrease rapidly to zero as $\epsilon = 0.4736\dots$ is approached. This particular parameter value corresponds to that at which the slope of a portion of the cusp map becomes less than one. Within this regime the origin is a stable attracting fixed point, although initial conditions may wander chaotically in portions of the map where the slope is greater than 1, before "decaying" into the attracting origin (Yorke and Yorke, 1979).

The tent map ($\epsilon = 0$) displays the same band-merging bifurcation sequence as the logistic equation, but not period-doubling bifurcations. The symbolic dynamics entropy algorithm also has the same convergence problems near the critical parameter value where the slope is everywhere 1. As the slope of the tent map increases, both the topological and metric entropies converge quite readily to the characteristic exponent. One can show that these quantities are given by the logarithm of the tent map's slope and when calculated using symbolic dynamics they agree to within 0.1%.

The tent map limit $\epsilon = 0$ is a symmetric map, for which the topological and metric entropies are equal. We also examined asymmetric piecewise linear maps for which the entropies are not equal. In these cases we find that there is good agreement ($\sim 0.1\%$) between the metric entropy and the Lyapunov exponent. Our numerical results indicate that any map that is *strictly hyperbolic*, i.e., one for which the absolute value of the first derivative is everywhere greater than 1, displays rapid convergence of the metric entropy to the Lyapunov exponent. This may be related to the fact that these maps have no infinite singularities in their asymptotic invariant probability distributions (Lasota and Yorke, 1977).¹⁶ In contrast to these systems, the logistic equation has a quadratic maximum that produces square root singularities in its asymptotic invariant probability distribution, and also displays the slow convergence.

From a practical perspective, these results indicate that a certain amount of caution must be used in the computation of the metric entropy from some experimental data set. If the underlying dynamics has singularities in its asymptotic distribution, then one might expect an overestimation of the metric entropy, and its slow convergence to the Lyapunov characteristic exponent.

¹⁶This fact may be seen from the Perron-Frobenius algorithm used to obtain the probability distribution; see, for example, Shaw (1980).

9. SYMBOLIC DYNAMICS IN THE PRESENCE OF FLUCTUATIONS

With these various theoretical results outlined, we now turn to more practical concerns: the effects of fluctuations and of finite precision on the application of symbolic dynamics to physical systems and their models. We shall address the first concern in this section and the latter in the next.

As discussed in the Introduction, symbolic dynamics appears to offer methods that circumvent the need for high-measurement resolution. Indeed, in the case of the one-dimensional maps discussed above, the measurement requirement was only 1 bit of resolution for the two-element partition $\{(0, d), [d, 1]\}$. We should point out, in contrast to this encouraging prospect, that the data base requirements can be quite substantial. For the calculation of the n -cylinder probability distributions the required memory increases as 2^{hn} , where h is the topological entropy. In comparison with other similar techniques, this is not an unusual requirement—in fact, it is typical. A second and more troubling feature of the application of symbolic dynamics to experimental systems is the requirement of a generating partition if one is to measure the “true” entropies. Such a partition is not given *a priori* to an experimentalist and, therefore, this requirement presents a significant theoretical limitation of experimental symbolic dynamics. On the practical side, however, if one keeps in mind the effects of varying the partition on the calculated entropies as shown in Figure 10, one could alter the partition to look for a maximum in the entropies. Such a procedure would be computationally intractable if the partition elements were of high dimension, but for simple low-dimensional chaotic behavior, at least, it is straightforward and feasible.

A further consideration is that the information acquisition rate must be greater than the metric entropy. That is, if the *a priori* information gain per measurement is I and the sample rate is R , then we must have $IR > h_\mu$ in order to resolve the deterministic chaotic dynamics. For example, using a binary partition at each iteration of a one-dimensional map, one cannot measure an entropy greater than one bit per iteration. We shall leave these problems, of data base, generating partition, and sample rate requirements, for future consideration and discuss the effect of fluctuations, or external noise, on the experimental application of symbolic dynamics.

Every experimental system is immersed in a “heat bath”; in other words, there will always be couplings between the system of interest and external degrees of freedom that are beyond observation by an experimentalist. To model this situation, we introduce the stochastic logistic equations which contains an explicit noise term,

$$x_{n+1} = rx_n(1 - x_n) + \tau_n$$

where τ_n is a uniform random variable with zero mean and standard deviation s . We shall call s the *noise level* of the fluctuations. The general effects of fluctuations on the logistic equation and the period-doubling bifurcation have been discussed elsewhere (Crutchfield and Huberman, 1980; Crutchfield et al., 1981; Haken and Mayer-Kress, 1981). We shall only briefly allude to these results and, instead, concentrate on the effects of fluctuations on the symbolic dynamics at a few parameter values of interest.

The values of the topological and metric entropies of the shift induced by the map in the presence of fluctuations depend on the manner in which the fluctuations alter the n -cylinder probability distributions. Changes in the characteristic exponent depend in similar way on the distribution $P(x)$ of iterates on the interval (recall Figure 1). Fluctuations smooth out the square root singularities in $P(x)$ and, for $r = 3.7$, affect the characteristic exponent very little ($< 1\%$) over a wide range in noise level: $s \in [0.0, 10^{-3}]$ (Crutchfield et al., 1981). The sequence of n -cylinder probability distributions of Figure 13 shows a similar mild change in Cantor set structure up to $n = 6$. This figure should be compared to Figure 3. We should point out that the fluctuations do *not* truncate the Cantor set structure, but only produce more admissible symbols. In order to see any alteration in this sequence, it was necessary to use the relatively large noise level of $s = 10^{-2}$. At $n = 6$, new admissible symbols appear, which in turn should result in increased entropies. Indeed, Figure 14 shows that the fluctuations increase $H(n)$ and $\log[N(n)]$ monotonically at $r = 3.7$ over three noise levels: $s = 0.0, 10^{-3}, 10^{-2}$. The metric and topological entropies, which are the slopes of these curves, clearly increase with increasing noise level, but converges to values less than one.

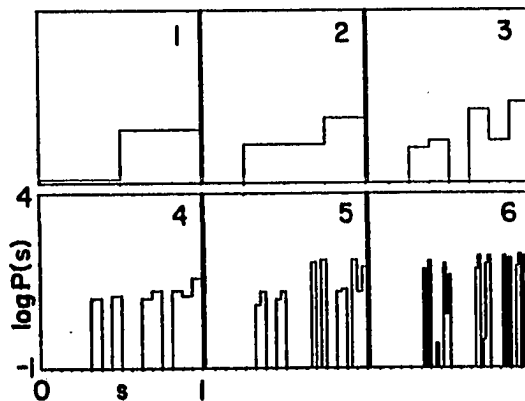


Fig. 13. n -Cylinder probability distribution (as in Figure 3) for the stochastic logistic equation with noise level $s = 10^{-2}$ at $r = 3.7$.

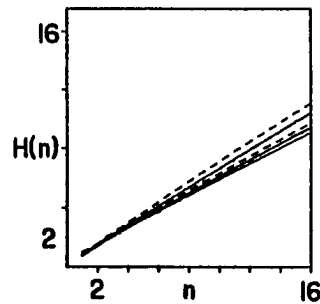


Fig. 14. Entropies $H(n)$ (solid line) and $\log\{N(n)\}$ (dashed) as a function of symbol length at $r=3.7$ for three noise levels: $s=10^{-2}$ (upper pair of dashed and solid lines), 10^{-3} (middle pair), and 0.0 (lowest pair). Note that $\log\{N(n)\}$ for $s=0.0$ overlaps $H(n)$ for $s=10^{-3}$. 2×10^5 iterations were used.

Figures 15 and 16 compare the effect of increased noise level at the parameters where four bands merge into two and at a period-4 orbit, respectively. For low noise levels $H(n)$, and so h and h_μ , differs substantially between these two parameters. At larger noise levels, however, the measured entropies are quite similar. In fact, at some noise level they would be completely indistinguishable: the period-4 orbit would appear as four bands (Crutchfield and Huberman, 1980).

The effects of external noise on the period-doubling bifurcation sequence can be described by a scaling theory and renormalization group approach (Crutchfield et al., 1981; Schraiman et al., 1981). These effects are reminiscent of an external magnetic field acting on a ferromagnet: noise acts as a disordering field on the chaotic dynamics. The characteristic exponent and the topological and metric entropies are the disorder parameters of the chaotic system, which scale in a manner similar to the magnetization order parameter for magnetic systems. In particular, the entropies in

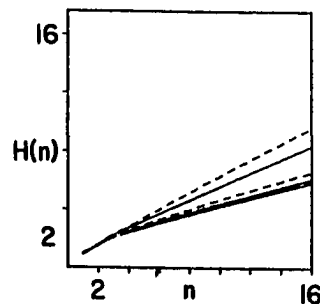


Fig. 15. Same details as Figure 14 except at the bifurcation from four bands to two, $r=3.59257218\dots$

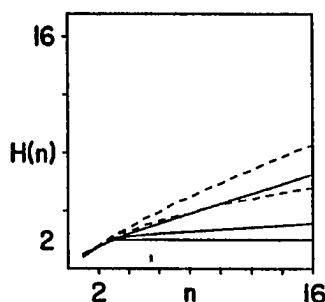


Fig. 16. Same details as Figure 14 except at period-4 orbit, $r=3.52$.

the presence of fluctuations provide a stronger analogy to the magnetization in the presence of an external field than does the Lyapunov exponent. Just as the magnetization has a nonzero tail above T_c at finite field, the entropies are nonzero in the periodic regime with noise added. The Lyapunov exponent, however, is negative in the periodic regime.

Adding external noise also increases the rate of convergence of the entropies. As an example of this, recall that at the merging of two bands into one, the topological entropy $h(\sigma_f)$ oscillates indefinitely, when calculated as the two-point slope $H_\mu(n) - H_\mu(n-1)$. When noise is added, the oscillation is "damped" and the topological entropy readily converges, albeit to a larger value than found with no noise added. A comparison of the zero noise case and that with $s=10^{-2}$ is shown in Figure 17. As the metric entropy decreases, the observer gains information about correlations between the observed symbols. When noise is added, these correlations decay, and so the metric entropy converges more rapidly.

In summary, the effects of additive fluctuations on symbolic dynamics calculations can be consistently described and so taken into account in the application of symbolic dynamics to experiments whose dynamics may be described by one dimensional maps. The entropies calculated from the n -cylinder distributions follow the deterministic values up to some n , above which the external noise causes $H(n)$ and $\log[N(n)]$ to increase at a rate greater than the zero noise case. Rather than considering this fact as compromising the usefulness of symbolic dynamics, one might suggest the use of symbolic dynamics entropies as measures of level of external fluctuations to which an experimental system is coupled.

One might conclude that, insofar as the effects of fluctuations can be described, turbulent physical systems subject to external fluctuations can be modeled by chaotic dynamical systems with added noise. This modeling process often involves the use of computer simulations which require the discretization of the model dynamics. In contrast to the apparently tractable case of external fluctuations, the effects of discretizing chaotic dynamics are

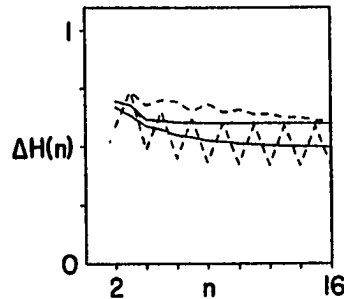


Fig. 17. Topological entropy approximated by $\log[N(16)] - \log[N(15)]$ (dashed line), and metric entropy approximated by $H(16) - H(15)$ (solid line), as a function of symbol length. The lower pair of curves corresponds to the deterministic case ($s=0$) and the upper pair to $s = 10^{-3}$. 2×10^3 iterations were used.

not so well understood. We shall address questions related to finite-state simulations of chaotic dynamical systems and symbolic dynamics in the following section.

10. EFFECTS OF FINITE PRECISION

Simulations of chaotic systems are often carried out on finite-state machines. This raises questions about the relationship between the observation of turbulent physical behavior and the chaotic behavior observed in a finite precision simulation used for a system's representation. In particular, the finite number of states available for the simulation implies that any simulated orbit will be ultimately periodic. We will now address the question of how chaotic behavior may be successfully quantified in spite of this periodicity. The simulated orbits, in fact, retain many of the statistical properties of the "ideal" continuous system (Erber et al., 1980).

In most simulations of chaotic dynamical systems one assumes that the errors introduced by a finite-state computer's roundoff will play a role analogous to fluctuations (e.g., thermal fluctuations). When comparing model simulations to observed behavior, though, one must be careful to distinguish between the resolution of a measuring instrument, the noise level of external fluctuations, and the internal precision with which the simulations are carried out. We will be concerned in this section with the latter topic. We will investigate several deterministic rounding algorithms and present a model that allows a continuous transition between a deterministic algorithm and a totally random rounding algorithm which is equivalent to adding noise of a specified magnitude. With each of these models we will compute the entropies described above, examining the effects of finite precision on their values.

We begin with the simplest version of a roundoff algorithm: truncation. For these and all the calculations presented below we have reduced the unit interval state space to 2^k points by using k bits of precision. The iteration of the one-dimensional map was done with much greater precision (floating point), but after every iteration the state was rounded to one of the 2^k discrete states. For the case of truncation, this is accomplished by always rounding down to the next lower state.

Figure 18 displays $\log[N(n)]$ (dashed) and $H(n)$ vs n for a range of different precisions: 10, 15, 20, 25, and 30 bits. We naively might expect the graph to level off when the number of symbols n reaches the precision being used, since the orbit then necessarily becomes periodic with a period less than 2^n , and this is indeed what we see in the figure. The case $k = 10$ might seem a bit puzzling since $H(n)$ remains so low, while $\log[N(n)]$ increases, but this is due to the probability distribution being composed of two delta functions with skirts which correspond to infrequently occurring symbols.

The monotonicity of $H(n)$ with increasing precision is due to a fortuitous choice of precisions. Figure 19 shows $H(12)$ and $\log[N(12)]$ as a function of precision, and we see quite a bit of nonmonotonicity with increasing precision, due to the existence of stable, relatively low period orbits. We also see that the topological entropy converges sooner, and is less affected by the finite precision.

The second rounding procedure we try is deterministic round off: after the map is iterated once, the result is rounded down if the fractional part of $2^k f(x)$ is less than 0.5, and rounded up otherwise. Figure 20 shows that this procedure yields the same nonmonotonic results as illustrated for truncation in Figure 19, but with slightly different features.

To study the relationship between the deterministic rounding algorithms described above and the effects of random fluctuations as described in the previous section, we will now look at a "hybrid" rounding algorithm.

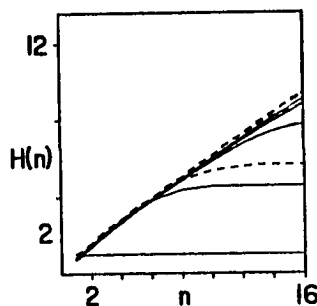


Fig. 18. Entropies $H(n)$ (solid) and $\log[N(n)]$ (broken) vs. n for truncation algorithm at various precisions, $k = 10, 15, 20, 25, 30$ bits; with the lowest line of each corresponding to 10 bits. $r = 3.7, 10^5$ iterations.

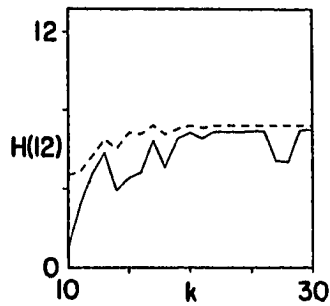


Fig. 19. $H(12)$ and $\log[N(12)]$ as a function of precision k , using truncation. $r=3.7$, 10^3 iterations.

Now the result of an iteration $f(x)$ will be rounded up or down exactly as in the deterministic round off algorithm unless the fractional part falls in a window about 0.5, in which case a random number is used to make the rounding decision. If the window width is zero, the result is equivalent to deterministic roundoff; if the window width is 1, the result is equivalent to adding a random fluctuation of magnitude 2^{-k} . The results of varying window width are illustrated in Figure 21, where we graph $H(n)$ and $\log[N(n)]$ vs n for different window widths, using a constant 20 bits of precision.

It is worth noting here that flipping the twentieth bit at random (i.e., using a window width of 1 at a precision of 20 bits) allows one to measure $H(16)$ as well as is possible using much higher precision (e.g., double-precision floating point). This point is further illustrated by Figure 22, where we see that $H(12)$ and $\log[N(12)]$ quickly converge to a constant value as the precision is increased for the window width of 1. These entropy values agree to within 1% of the double-precision floating point results.

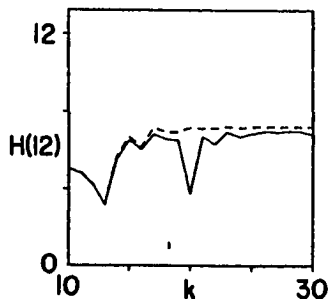


Fig. 20. Same as Figure 19 except for deterministic roundoff.

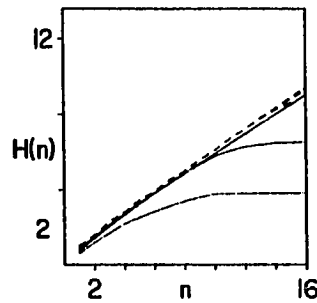


Fig. 21. $H(n)$ (solid) and $\log[N(n)]$ (dashed), vs. n using random roundoff algorithm at various window widths: 10^{-3} , 10^{-2} , 10^{-1} , 1.0, using 20 bits of precision. For each width, the $\log[N(n)]$ dashed curves remain close to each other, as do the $H(n)$ curves for widths 10^{-1} and 1.0, at the top of the figure. The lowest curve corresponds to $H(n)$ for a width of 10^{-3} , the next higher 10^{-2} , $r = 3.7$, 10^5 iterations.

Our results lead us to the practical suggestion that simulations of dynamical systems should include noise at the lowest bit of precision in order to effectively increase the precision and yield the physically relevant behavior. A simple example of this will illustrate its utility. Consider the tent map

$$x_{n+1} = \begin{cases} 2x_n, & x_n < 0.5 \\ 2(1-x_n), & x_n > 0.5 \end{cases}$$

which is equivalent to a binary shift of the initial condition x_0 . If x_0 is specified to k bits, then after k iterations of the tent map all of the initial condition has been removed and the truncation (or deterministic roundoff) algorithm has replaced the lost bits with 0's. The net effect is that after only k iterations the orbit has trivially converged to 0, making the simulation remarkably unrepresentative. A numerically accumulated probability distribution of this map would be a delta function at the origin, although the map

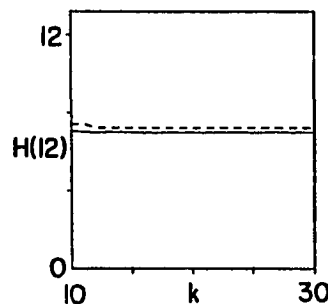


Fig. 22. Same as Figure 19 except for random roundoff algorithm with a window of 1.0.

is provably chaotic with positive entropies and characteristic exponent. Admittedly, this is an extreme example, but similar effects due to finite precision with deterministic roundoff should be expected in simulation of chaotic dynamical systems. To render such a finite-state simulation useful, we propose that the roundoff decision be made randomly. One would then observe the chaotic dynamics implicit in the mathematical specification of the map and also the behavior which most closely models real physical systems. The addition of this random degree of freedom to finite-state computers renders them effectively infinite-state machines.¹⁷

11. ENTROPY AND ALGORITHMIC COMPLEXITY

Both the topological and metric entropies described above characterize, in some sense, the "randomness" of a chaotic dynamical system. We shall now discuss the relationship between these concepts of randomness and another developed in the early 1960s independently by Solomonoff (1964),¹⁸ Chaitin (1966), Kolmogorov (1965), and Martin-Lof (1966). Their essential idea is to define the *algorithmic complexity* $A(s^n)$ of a string of symbols $s^n = (s_1, \dots, s_n)$ as the minimum size of a computer program required to generate the string. Without going into the subtleties of how to make this definition precise, we will present a heuristic discussion of how this concept may be related to chaotic dynamical systems. A summary of the technical details involved is given by Alekseyev and Yacobson (1981).

For a chaotic dynamical system $f: M \rightarrow M$ with a generating measurement partition S , we showed in Section 2 that to each orbit (x_0, x_1, x_2, \dots) there corresponds a symbol sequence (s_0, s_1, s_2, \dots) , where

$$x \in \bigcap_{i=0}^{\infty} f^{-i}(S_{s_i})$$

The algorithmic complexity $A(x_0, f)$ of this orbit may then be defined as

$$A(x_0, f) = \lim_{N \rightarrow \infty} \frac{A(s^N)}{N}$$

We then have the results that the algorithmic complexity is bounded by the

¹⁷The source of this random decision could be any of a number of chaotic electronic circuits and so be easily implemented in the current generation of LSI arithmetic processors. In such a dynamical systems processor one would, of course, want to switch between deterministic roundoff and random roundoff to aid in software error checking.

¹⁸For the first presentation of Solomonoff's ideas see Minsky (1962).

topological entropy (Brudno, 1978; Zvonkin and Levin, 1970; Kamae, 1973):

$$A(x_0, f) \leq h(f)$$

and that, for any invariant measure μ , it equals the metric entropy,

$$A(x_0, f) = h_\mu(f)$$

for all x_0 (except some measure zero set). These results justify the use of algorithmic complexity as a measure of randomness for a chaotic dynamical system, and allows us to set $A(f) = h_\mu(f)$ if f is ergodic.

There may seem to be a paradox: even if the map f is chaotic, an n cylinder s^n may be obtained simply by iterating the map n times and observing the sequence of partition elements visited ... a very simple algorithm indeed! This algorithm for generating the n cylinder s^n is simple in the sense that to generate a longer n cylinder, only the parameter which specifies the number of iterations need be changed. Thus, the algorithm's length $A(s^n)$ grows like $\log(n)$ so that

$$\lim_{n \rightarrow \infty} \frac{A(s^n)}{n} \rightarrow 0$$

contradicting $A(f) = h_\mu(f) > 0$. We must realize, however, that the algorithm must also contain a specification of the initial condition, and if the map is chaotic, the amount of information contained in the observed symbol sequence is proportional to the amount of information contained in the specification of the initial condition. Thus, the size $A(s^n)$ must grow with n .

We may now use algorithmic information theory to formalize the notions of modeling mentioned in the Introduction. Again, we will consider an observer who makes a sequence of measurements (s_0, s_1, \dots) on a physical system with some instrument whose output is one of finitely many symbols. In this context, we may define a *predictive model* as an algorithm A which would produce the string $s^n = (s_0, \dots, s_n)$ for any n . As a simple example, we see that if the system is executing periodic motion, the symbol sequence of successive measurements will also be periodic, so that a simple program could predict which symbol would be observed at any time in the future. The result that the algorithmic complexity $A(s^n)$ of n observations of a chaotic dynamical system grows like n (i.e., $A(f) > 0$) is then a concise statement of the inability of the observer to construct such a predictive model, since there is always some n for which $A(s^n)$ is larger than the size of any proposed predictive model A .

12. CONCLUDING REMARKS

One of our primary concerns here has been an elucidation of the *modeling process*, by which we mean a comparison between the observed temporal behavior of some physical system and the temporal behavior of a model comprised of some other representation system. If the physical system behaves periodically, a model can be constructed, in principle, that serves a *predictive* function.

In modeling turbulent physical systems with simple chaotic dynamical systems certain problems arise since one cannot, in principle, obtain exact correspondence between the observed physical behavior and the output of the model. Nevertheless, the chaos displayed by chaotic dynamical systems admits certain geometrical and statistical characterizations which must then be used in the modeling process as the new criteria for a model's validity.

The construction of symbolic dynamics, for example, enables a comparison between the statistical properties of a physical system and those of a model by providing measures of temporal complexity. At the same time, though, by projecting large portions of the state space onto a discrete set of symbols most, if not all, geometrical information is lost. The construction of symbolic dynamics reduces the dynamics of a physical system to a dynamical system comprised of a trivial dynamic (the shift) on a complicated state space. All the complexity of the temporal behavior of the physical system is contained in the structure of the symbol state space Σ_f . This complexity admits not only a dynamical quantification via the metric entropy¹⁹ but also an *algorithmic* quantification.

The algorithmic interpretation considers the physical system as a finite-state machine, with the original dynamics corresponding to an algorithm for a Turing machine, say. If the observed dynamics are chaotic, the minimal algorithm needed to specify any subsequence in Σ_f grows with the length of the subsequence. And the rate of this growth is equal to the metric entropy of the induced shift on Σ_f . If the observed dynamics are not chaotic, however, Σ_f reduces to a periodic lattice which can be specified in its entirety with a finite algorithm.

Turing machines were invented as conceptual tools to make precise the notion of computability. Mathematical propositions were then recast as Turing machine algorithms and a proposition's decidability could be shown to be equivalent to its algorithm's computability. Thus an equivalence was established between the notions of computability and decidability. Via algorithmic information theory, then, symbolic dynamics appears as a link between turbulent physical dynamics and the notions of decidability, often

¹⁹With appropriate restrictions on the measurement partition, this will also be the metric entropy of the observed physical system.

associated with Godel's theorem. Shaw (1980) suggested a similar connection between the unpredictability arising from chaotic dynamics and the undecidability of propositions about a chaotic system's state after the information obtained from a measurement has been lost. Here we have attempted to point out that symbolic dynamics provides a common language for the discussion of these ideas.

As mentioned in the Introduction, the existence of deterministic, unpredictable behavior obviates the hope of "closed-form" descriptions, and so allows only for statistical and geometric characterizations. For chaotic dynamical systems, the explicit prediction of behavior is no longer possible, and we are led to reconsider the criteria for the appropriateness of models of turbulent phenomena. Chaos, in this sense, necessitates a generalization of the modeling process.

Underlying these conceptual motivations, there are many practical questions concerning the construction of symbolic dynamics. We addressed some of these by examining the conditions under which digital computations can successfully approximate chaotic dynamics of a continuous system driven with "thermal" fluctuations. We also discussed the applicability of symbolic dynamics techniques to experimental data analysis. Our research along these lines has also uncovered certain theoretical questions, such as why we observe a slow convergence of the metric entropy to the Lyapunov characteristic exponent for the logistic equation. We have been able to indicate, only in a preliminary way, the usefulness of dynamical systems and symbolic dynamics in describing observed unpredictable behavior.

In the early literature on the topics we have discussed here, there appears to have been a general appreciation of the connection between information theory, algorithms, and dynamics. Such a broad perspective, which flourished during the days of the first computers, seems to have motivated much of Shannon's information theory, and subsequently Kolmogorov's ideas on dynamical systems. In the present work we have discussed chaotic dynamics within this context in an effort to rekindle the apparently diffused understanding of the intimate connection between the physics of dynamics and computation.

ACKNOWLEDGMENTS

We are grateful to Doyne Farmer, Joe Ford, David Fried, John Guckenheimer, David Rand, and Rob Shaw for stimulating discussions and correspondence on these topics. The authors also wish to thank J.-P. Eckmann, F. Ledrappier, M. Misiurewicz, and others for useful discussions on the relationship between the metric entropy and Lyapunov characteristic exponents. JPC was supported by a UC Regents Fellowship. This work has been supported by NSF grant No. 443150-21299.

REFERENCES

- Adler, R. L., Konheim, A. G., and McAndrew, M. H. (1965). "Topological Entropy," *Transactions of the American Mathematical Society*, 114, 309.
- Alekseyev, V. M., and Yakobson, M. V. (1981). "Symbolic Dynamics and Hyperbolic Dynamic Systems," *Physics Reports*, to be published.
- Benettin, G., Casartelli, M., Galgani, L., Giorgilli, A., and Strelcyn, J.-M. (1978). "On the Reliability of Numerical Studies of Stochasticity," *Nuovo Cimento*, 44B, 183; 50B, 211.
- Benettin, G., Galgani, L., Giorgilli, A., and Strelcyn, J.-M. (1980). "Lyapunov Characteristic Exponents for Smooth Dynamical Systems and for Hamiltonian Systems; A Method for Computing All of Them, Parts I and II," *Meccanica*, 21.
- Billingsley, P. (1965). *Ergodic Theory and Information*. John Wiley and Sons, New York.
- Bowen, R. (1975). "Equilibrium States and the Ergodic Theory of Anosov Diffeomorphisms," *Lecture Notes in Mathematics*, 470, Springer Verlag.
- Bowen, R., and Ruelle, D. (1975). "Ergodic Theory of Axiom-A," *Inventiones Mathematicas*, 29, 181.
- Brudno, A. A. (1978). *Uspekhi Matematicheskikh Nauk*, 33, 207.
- Chaitin, G. J. (1966). "On the Length of Programs for Computing Binary Sequences," *J. Assoc. Computing Machinery*, 13, 547; See also "Randomness and Mathematical Proof," *Sci. Amer.* May 1975, 47.
- Chillingworth, D. R. J. (1976). *Differential Topology With a View to Applications*. Pitman, San Francisco, California.
- Collet, P., and Eckmann, J.-P. (1980). *Iterated Maps of the Unit Interval as Dynamical Systems*. Birkhauser, Cambridge, Massachusetts.
- Crutchfield, J. P., Nauenberg, M., and Rudnick, J. (1981). "Scaling for External Noise at the Onset of Chaos," *Physical Review Letters*, 46, 933.
- Crutchfield, J. P., and Huberman, B. A. (1980). "Fluctuations and the Onset of Chaos," *Phys. Lett.*, 77A, 407.
- Crutchfield, J. P., Farmer, J. D., and Huberman, B. A. (1981). "Fluctuations and Simple Chaotic Dynamics," *Physics Reports*, to appear.
- Curry, J. H. (1981). "On Computing the Entropy of the Hénon Attractor," *Inst. des Hautes Etudes Sci.* preprint.
- Dinaburg, E. I. (1970). "The Relation Between Topological Entropy and Metric Entropy," *Sov. Math.* 11, 13.
- Erber, T., Everett, P., and Johnson, P. W. (1980). "The Simulation of Random Processes on Digital Computers with Chebyshev Mixing Transformations," preprint.
- Farmer, J. D. (1981). "Order Within Chaos," UCSC dissertation.
- Froehling, H., Crutchfield, J. P., Farmer, J. D., Packard, N. H., and Shaw, R. S. (1981). "On Determining the Dimension of Chaotic Flows," *Physica* 3D, 605.
- Guckenheimer, J., Moser, J., and Newhouse, S. E., (1980). *Dynamical Systems*. Birkhauser, Cambridge, Massachusetts.
- Haken, H., and Mayer-Kress, G. (1981). "The Effect of Noise on the Logistic Equation," *J. Stat. Phys.* to appear.
- Jonker, L., and Rand, D. (1980). "Bifurcations in One Dimension," *Inventiones Mathematicas*, 62, 347.
- Kamae, T. (1973). "On Kolmogorov's Complexity and Information," *Osaka Journal of Mathematics*, 10, 305.
- Kaplan, J., and Yorke, J. (1981). Private communication.
- Kifer, Ju. I. (1974). *USSR Izvestija*, 8, 1083.
- Kolmogorov, A. N. (1958). *Doklady Akademii Nauk*, 119, 754.

- Kolmogorov, A. N. (1965). "Three Approaches to the Quantitative Definition of Information," *Problems of Information Transmission (USSR)*, 1, 1.
- Lasota, L., and Yorke, J. (1976). "On the Existence of Invariant Measures for Transformations with Strictly Turbulent Trajectories," *Bull. Acad. Pol. Sci.*, 25, 233.
- Ledrappier, F. (1981). "Some Properties of Absolutely Continuous Invariant Measures on an Interval," *Ergod. Theo. Dyn. Sys.*, 1, 77.
- Lorenz, E. N. (1963). "Deterministic Non-Periodic Flow," *Journal of Atmospheric Science*, 20, 130.
- Mandelbrot, B. (1977). *Fractals: Form, Chance, and Dimension*. W. H. Freeman, San Francisco, California.
- Martin-Löf, P. (1966). "The Definition of Random Sequences," *Information Control*, 9, 602.
- Milnor, J., and Thurston, W. (1977). "On Iterated Maps of the Interval, I and II," Princeton University preprint.
- Minsky, M. L. (1962). "Problems of Formulation for Artificial Intelligence," in *Mathematical Problems in the Biological Sciences, Proceedings of Symposia in Applied Mathematics XIV*, R. E. Bellman, ed. American Mathematical Society, Providence, Rhode Island.
- Oono, Y., and Osikawa, M. (1980). "Chaos in Nonlinear Difference Equations I," *Progress in Theoretical Physics*, 64, 54.
- Packard, N. H., Crutchfield, J. P., Farmer, J. D., and Shaw, R. S. (1980). "Geometry from a Time Series," *Phys. Rev. Lett.*, 45, 712.
- Parry, W. (1964). "Intrinsic Markov Chains," *Transactions of the American Mathematical Society*, 122, 55.
- Piesin, Ya. B. (1977). "Characteristic Lyapunov Exponents and Smooth Ergodic Theory," *Uspeki Matematicheskikh Nauk*, 32, 55.
- Rényi, A. (1959). "On the Dimension and Entropy of Probability Distributions," *Acta Math. Hung.*, 10, 193.
- Ruelle, D. (1977). "Applications Conservant une Mesure Absolument Continue par rapport a dx sur $[0, 1]$," *Communications in Mathematical Physics*, 55, 47.
- Ruelle, D., and Takens, F. (1971). "On the Nature of Turbulence," *Communications in Mathematical Physics*, 20, 167.
- Ruelle, D. (1978). "An Inequality for the Entropy of Differentiable Maps," *Bull. Soc. Brasil Math.*, 9, 331.
- Schraiman, B., Wayne, C. E., and Martin, P. C. (1981). "Scaling Theory for Noisy Period-Doubling Transitions to Chaos," *Physical Review Letters*, 46, 935.
- Shaw, R. (1980). "On the Predictability of Mechanical Systems," UCSC dissertation.
- Shaw, R. (1981). "Strange Attractors, Chaotic Behavior, and Information Flow," *Zeitschrift fuer Naturforschung*, 36a, 80.
- Shimada, I. (1979). "Gibbsian Distribution on the Lorenz Attractor," *Progress in Theoretical Physics*, 62, 61.
- Shimada, I., and Nagashima, T. (1979). "A Numerical Approach to Ergodic Problems of Dissipative Dynamical Systems," *Progress Theoretical Physics*, 61, 1605.
- Sinai, Ya. (1972). "Gibbsian Measures in Ergodic Theory," *Russian Mathematical Surveys*, 27, 21.
- Smale, S. (1967). "Differentiable Dynamical Systems," *Bulletin of the American Mathematical Society*, 13, 747.
- Solomonoff, R. J. (1964). "A Formal Theory of Inductive Control," *Information Control*, 7, 224.
- Takens, F. (1980). "Detecting Strange Attractors in Turbulence," preprint.
- Yorke, J. A., and Yorke, E. D. (1979). "Metastable Chaos: The Transition to Sustained Chaotic Behavior in the Lorenz Model," *Journal of Statistical Physics*, 21, 263.
- Zvonkin, A. K., and Levin L. A. (1970). "The Complexity of Finite Objects and the Development of the Concepts of Information and Randomness by means of the Theory of Algorithms," *Russian Mathematical Survey*, 25, 83.

5.9. Noise Scaling of Symbolic Dynamics Entropies

NOISE SCALING
OF
SYMBOLIC DYNAMICS ENTROPIES

James P. Crutchfield and Norman H. Packard
Physics Board of Studies
University of California
Santa Cruz, California 95064

1. Introduction

An increasing body of experimental evidence supports the belief that random behavior observed in a wide variety of physical systems is due to underlying deterministic dynamics on a low dimensional chaotic attractor. The behavior exhibited by a chaotic attractor is predictable on short time scales and unpredictable (random) on long time scales. The unpredictability, and so the attractor's degree of chaos, is effectively measured by the entropy. Symbolic dynamics is the application of information theory to dynamical systems. It provides experimentally applicable techniques to compute the entropy, and also makes precise the difficulty of constructing predictive models of chaotic behavior. Furthermore, symbolic dynamics offers methods to distinguish the features of different kinds of randomness that may be simultaneously present in any data set: chaotic dynamics, noise in the measurement process, and fluctuations in the environment.

In this paper, we first review the development of symbolic dynamics given in [1]. In the later sections, we report new results on a scaling theory of symbolic dynamics in the presence of fluctuations. We conclude with a brief discussion of the experimental application of these ideas.

2. Dynamics of Measurement

When observing some physical system with a measuring instrument, every time we make a measurement we find that our measured quantity takes one of a finite number of possible values. We will label each of these possible measured values with a symbol $s \in \{1, \dots, q\} \equiv S$. All possible sequences of measurements (equally spaced in time, we shall imagine) can then be represented by symbols on a lattice, $S^Z = \sum$, where Z is the integers. If we imagine a sequence of measurements beginning at some time and continuing indefinitely into the future, Z would be replaced by the non-negative integers. A state of this system corresponds to a particular sequence, or configuration of symbols on the lattice, $s = (s_0, s_1, \dots)$. \sum may be considered as the state space of this symbolic dynamical system, with the temporal evolution of the state given by a shift σ of all the symbols: $(\sigma s)_i = s_{i+1}$. \sum has various names in various fields; in the theory of communication, for instance, it is called signal space: the space of all possible messages.

The properties of the sequences of symbols obtained from a series of observations will inevitably mirror properties of the system being observed. If the system is executing some sort of periodic motion, for example, the symbol sequences will also be periodic. We will, however, be interested in more complicated behavior, namely random, chaotic behavior. Information theory, invented by SHANNON [2] in the field of communication theory, provides a framework to make precise and to quantify the notion of randomness. KOLMOGOROV [3] first used SHANNON's ideas in the field of dynamical systems, and SHAW [4] began the application of information theory to randomness observed in physical systems, identifying the measurement process with SHANNON's communication through a channel.

Our development of symbolic dynamics is designed to serve two purposes: (i) to augment the existing data analysis techniques to detect and characterize low dimensional deterministic randomness from experimental data [5] and (ii) to explore the relationship between "typical" chaotic attractors that are seen in the simulation of various low dimensional models, and the systems that have a fairly complete rigorous characterization (e.g. Axiom-A dynamical systems). In the following we will review the concepts introduced by SHANNON to describe random behavior, with special attention to the distinction between randomness produced by deterministic processes and that produced by nondeterministic processes.

Before discussing the quantification of randomness, we will point out a few more or less technical features and assumptions regarding the symbolic dynamics lattice. The lattice has an intuitive notion of distance between different sequences: two sequences are "close" if they match for a long time. We can measure the distance between two sequences by

$$d(\bar{s}, \bar{s}') = \sum_{i=0}^{\infty} \frac{|s_i - s'_i|}{2^i} . \quad (1)$$

This distance function also generates a topology for the lattice, and we will sometimes call the open sets (the set of all sequences that match for n symbols)

$$s^n = (s_0^n, \dots, s_{n-1}^n) = \{\bar{s} \mid s_0 = s_0^n, \dots, s_{n-1} = s_{n-1}^n\}$$

n-cylinders.

Another attribute the lattice must have is some notion of the likelihood of observing different sequences. Mathematically this means we must have a measure u on Σ . We will assume this measure to be invariant (under the shift) and ergodic over the set of all observed sequences. We will also assume an "ergodic hypothesis", i.e. that time averages of any bounded measurable function on Σ are equal to "ensemble averages" using the measure u . In particular, if we consider the characteristic function on a given n -cylinder s^n , ergodicity implies that the frequency with which s^n occurs after a long time of observation is given by $u(s^n)$. This enables the computation of averages over symbol sequences by using frequency histograms to approximate u .

In making the observations that form a symbol sequence, it may turn out that interdependencies of the measurements exclude certain sequences from being observed. In this case the set of observed sequences Σ_0 is a subset of the set of all possible sequences Σ , and (Σ_0, σ) is sometimes called a subshift. The first measure of randomness is obtained from counting the number of sequences of length n observed, then measuring the asymptotic growth rate of this number. Defining $N(n)$ as the number of observed sequences of length n , we have

$$h = \lim_{n \rightarrow \infty} \frac{\log(N(n))}{n} . \quad (2)$$

If the growth rate is exponential, then $h > 0$ and the system is random. SHANNON called h the channel capacity; h is also the topological entropy [6] of (Σ_0, σ) considered as a dynamical system with the topology mentioned above. Note that if all sequences occur for all n , the topological entropy is $\log(q)$.

The second, more refined notion of randomness takes into account not only whether or not a given sequence occurs, but also how likely its occurrence is. SHANNON gives us a convincing argument that a good measure of the randomness of an event qualitatively corresponds to the "surprise" of an observer observing the event, and is given quantitatively by something he called entropy:

entropy (event) = $-\log$ probability(event) .

SHANNON then defines the average randomness to be the average entropy per event, where the average is taken over all observed events.

$$H(\text{events}) = - \sum_{\text{events}} P(\text{event}) \log P(\text{event}) .$$

For the case of symbolic dynamics, an event corresponds to a particular sequence of n measurements yielding one out of the $N(n)$ possibilities, so the n symbol entropy $H(n)$ may be written as

$$H(n) = - \sum_{\{s^n\}} u(s^n) \log u(s^n) . \quad (3)$$

The metric entropy of (Σ, σ, u) is then defined as the asymptotic value of the n symbol entropy per unit symbol:

$$h_u = \lim_{n \rightarrow \infty} \frac{H(n)}{n} . \quad (4)$$

Comparing this with (2), we see that the metric entropy is also a measure of the growth rate of observed sequences, weighting each sequence with its relative probability.

An interesting aspect of the topological entropy h and the metric entropy h_u is that they not only specify the chaotic properties of the lattice of observations Σ_u , but they also specify two different notions of the dimension of the space Σ_0 . Heuristically, the fractal dimension [7] of a space is the growth rate of the number of open sets needed to cover the space as the diameter of the cover is decreased. The open sets of Σ_0 are n -cylinders, so the fractal dimension D_f of Σ_0 is exactly the topological entropy h of (Σ_0, σ) . Another dimensional quantity that describes Σ_0 not only counts the growth rate of the number of sets required to cover Σ_0 , but weights them with their relative probability. FARMER [8] coined the term information dimension for this dimension. As in the definition of metric entropy, weighting the count of the open sets with their relative probability is accomplished by replacing $\log(N(n))$ in the expression for D_f with $H(n)$. Thus, the information dimension D_I of Σ_0 is given by $D_I = h_u$.

Another interesting interpretation of the metric entropy is as the growth rate of the average algorithmic complexity $A(s^n)$ of n -cylinders. By algorithmic complexity we mean the length of the shortest algorithm required to reproduce the n -cylinder. We may use algorithmic information theory to formalize the modeling an unpredictable, chaotic system. We consider an observer who makes a sequence of measurements (s_0, s_1, \dots) on a physical system with some instrument whose output is one of finitely many symbols. In this context, we may define a predictive model as an finite algorithm A which would produce the string $s^n = (s_0, \dots, s_n)$ for any n . As a simple example, we see that if the system is executing periodic motion, the symbol sequence of successive measurements will also be periodic, so that a simple program could predict which symbol would be observed at any time in the future. In this case, $A(s^n)/n \rightarrow 0$, and a predictive algorithm exists. However, the algorithmic complexity $A(s^n)$ of a typical series s^n of n observations of a random, or a chaotic, dynamical system f grows like n . That is, $A(s^n)/n \rightarrow A(f) > 0$. This is then a concise statement of the inability of the observer to construct a predictive model, since there is always some n for which $A(s^n)$ is larger than the size of any proposed predictive model A . This line of thought is developed more fully in [1]; also see [9].

3. Computation of the Entropies

We will now present a few useful features of the topological entropy h and the metric entropy h_u [2]. We will use binary logarithms throughout the following. It is easy to see that $H(n) \leq \log(N(n))$, with equality if all the s^n are equally probable. This implies the inequality $h_u \leq h$. The asymptotic slope $H(n)/n$ is approximated even better by

$$h_u = \lim_{n \rightarrow \infty} h_u(n), \text{ where } h_u(n) = H(n) - H(n-1). \quad (5)$$

Eq. (5) can be used to compute the metric entropy, given the $u(s^n)$, which can be accumulated with frequency histograms. To be more specific, given I observations of n -cylinders $\{s^n\}$, any given n -cylinder might be observed k times, so $u(s^n)$ can be estimated by k/I .

Having defined the topological and metric entropy of the symbolic dynamics lattice system obtained from a set of observations of some physical system, we will say that the physical system is chaotic with respect to the measuring instrument being used if and only if these entropies are greater than zero. Of course, computation of the $h_u(n)$ entails approximating u with frequency histograms for $u(s^n)$, and so there will be severe data base requirements for large n , making it difficult to detect long periodicities. Typically it is feasible to take $15 < n < 25$ for binary symbols.

Up to this point, we have considered the measurement process in a "black box" fashion. We will now consider the case of obtaining measurements from the observation of a deterministic dynamical system. We will consider time to be discrete, and the dynamical system to be a map f from a space of states M into itself, $f: M \rightarrow M$. We assume f has some ergodic invariant measure \tilde{u} (the \sim is to distinguish it from the measure u on the symbolic dynamic lattice Σ). If f has an attractor, we will restrict our attention to the attractor, and assume that almost all (with respect to Lebesgue measure m) initial conditions approach the attractor and have trajectories that are asymptotically described by the measure \tilde{u} on the attractor.

A dynamical system $f: M \rightarrow M$ can have many symbolic representations, each obtained by using a measurement partition, $P = \{P_1, \dots, P_q\}$, to divide the state space M into a finite number of sets each of which will be labeled with a symbol $s \in \{1, \dots, q\} = S$. The time evolution of the dynamical system $f: M \rightarrow M$ is then translated into a sequence of symbols labeling the partition elements visited by an orbit $s = \{s_0, s_1, s_2, \dots\}$ and f itself is replaced by the shift operator σ . In the space of all possible symbol sequences Σ the observed or admissible sequences are those which satisfy $f^i(x_0) \in P_{s_i}$. The set of admissible sequences Σ_f is an invariant set in Σ , just as are the points on the original system's attractor. (Σ_f, σ) is the symbolic dynamical system induced by f using the measurement partition P .

In a sense, the symbol sequences of Σ_f are a coding for the orbits of $f: M \rightarrow M$. An n -cylinder corresponds to a set of orbits that are "close" to one another in the sense that their initial conditions and first $n-1$ iterates fall in the same respective partition elements. Since these orbits must follow each other for at least $n-1$ iterations, they must all have initial conditions that are close, belonging to some set $U \subset M$. To a different n -cylinder will correspond a different set of orbits whose initial conditions are contained in some other set $U' \subset M$. Continuing with the set of all n -cylinders, M will become partitioned into as many subsets as there are n -cylinders. As n is increased, this n -cylinder partition will become increasingly refined. The refinement caused by taking an increasing number of symbols is illustrated in Fig. 1, where M is the unit interval $[0,1]$, and f is the quadratic logistic equation, $x_{n+1} = f(x_n) = rx_n(1-x_n)$, with $r = 3.7$, and where we have used the measurement partition formed by cutting the interval in half at the maximum, or critical point of f . We see from the Fig. 1 that the dividing points for the n -cylinder partition are simply the collection

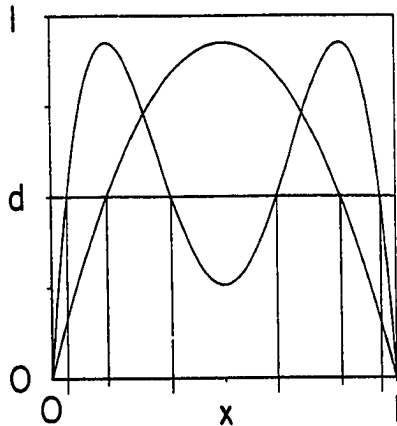


Fig. 1. Construction of the partition by taking n symbols (i.e. specifying an n -cylinder) with the measurement partition $P = \{[0, .5], (.5, 0]\}$. The 1-cylinder, 2-cylinder, and 3-cylinder, partitions are shown with successively longer tic marks below the x -axis. For example, the 3-cylinder $s_3 = (0, 1, 0)$ corresponds to the fourth subinterval from the left

$$\{d, f^{-1}(d), f^{-2}(d), \dots, f^{-(n-1)}(d) \dots\},$$

whenever the specified inverse images exist. Whenever the map is not everywhere two onto one, some of the inverse images will not exist, corresponding to the fact that some n -cylinders are non-admissible. These "gaps" cause Σ_f to have a Cantor set structure that may be visualized (as in Fig. 2) by mapping symbol sequences into $[0, 1]$ using (1).

If the n -cylinder partition becomes arbitrarily fine as $n \rightarrow \infty$, there is essentially a unique correspondence between symbol sequences and orbits. A measurement partition that has this property is called a generating partition. The correspondence is given by the map π :

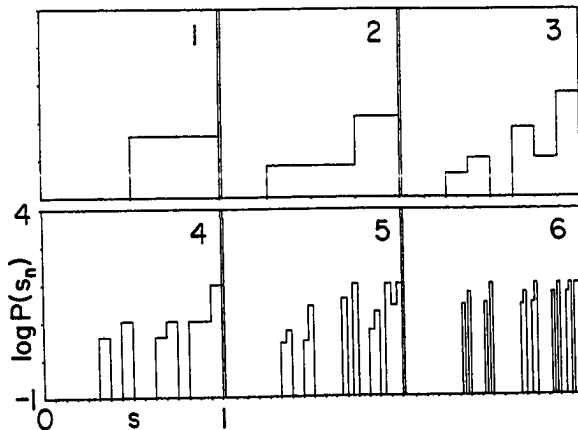


Fig. 2. The Cantor set structure of the subshift Σ_f , where f is the quadratic logistic equation with $r = 3.7$, is shown in this sequence of probability distributions for n -cylinders, $n = 1, \dots, 6$. Each n -cylinder has been mapped onto the unit interval by using its binary fraction

$$\pi(s_{-1}, s_0, s_1, \dots) = \sum_{i=0}^{\infty} f^{-i}(p_{s_i}).$$

Generating partitions are particularly useful in the computation of entropy, as we shall see later. There is no general way to find generating partitions for arbitrary dynamical systems, and this will present a problem for applying symbolic dynamics to experimental data. We will, however, present numerical evidence that it is easy to find generating partitions for simple chaotic dynamical systems (e.g. piecewise monotone, one-dimensional maps).

Assuming that the measurement partition is generating, the correspondence between points on the attractor, orbits on the attractor, and symbol sequences allows us to study the simpler, albeit abstract, symbolic dynamical system in order to answer various questions about the original dynamical system. Within this construction, every point on the attractor (and each orbit that starts from each point) will have at least one symbol sequence representation. There are a few ambiguities in the labeling of orbits by symbol sequences that prevent π from being invertible, but they will not affect our numerical calculations. One example of such ambiguity is the existence of symbol sequences that label the same point on an attractor, but are nowhere equal: .10000... = .01111....

We will now embark on the task of characterizing the chaotic behavior in a deterministic dynamical system using topological and metric entropies, in that order. We will give only heuristic descriptions of these quantities, motivating their computation using the symbolic dynamic entropies described above. For complete definitions of the entropies for a deterministic system and the relationship of these definitions to the algorithms used to compute them, see [1].

The topological entropy of a dynamical system measures the asymptotic growth rate of the number of resolvable orbits using a particular measurement partition. Since the symbol sequences simply label the resolvable orbits, the topological entropy of f with respect to a particular measurement partition is given by the topological entropy of (\sum_f, σ) , using (2). The topological entropy of f is then defined as the supremum of $h(\sum_f, \sigma)$ over all possible measurement partitions.

The metric entropy also measures the asymptotic growth rate of the number of resolvable orbits (using a given measurement partition), but weighting each orbit with its probability of occurrence. The metric entropy with respect to the measurement partition that yields the set of observed sequences \sum_f is then given by $h_u(\sum_f, \sigma)$ in (4). The metric entropy of f is then defined as the supremum of $h_u(\sum_f, \sigma)$ over all measurement partitions, but if the measurement partition is generating, KOLMOGOROV has proven that $h_u(\sum_f, \sigma) = h_u(f)$.

Figure 3 shows a graph of entropy convergence for the logistic equation at several parameter values. The measurement partition used for these calculations was $P = \{[0, .5], [.5, 1]\}$ with symbols $\{s_i\} = \{0, 1\}$. The graph shows $h(n) = \log(N(n)) - \log(N(n-1))$ for the topological entropy and $h_u(n) = H(n) - H(n-1)$ for the metric entropy. Note the oscillation in $h(n)$ for $r = 3.7$. This is due to the existence of a periodic substructure in the symbol sequences: every other symbol is a "1" with high probability. In fact, at slightly lower parameter values where there are two bands, this oscillation does not die away.

If the measurement partition is changed, the set of symbol sequences change, and the entropy measured can also change. Fig. 4 shows how the entropy changes as the measurement partition is varied. The measurement partition is still a two element partition, $P(d) = \{[0, d], [d, 1]\}$, and the value of d is varied across the attractor. The fact that two values of d ($d = .5$, the critical point, and $d = .839$, an inverse image of the critical point) yield maximum values for the metric entropy is evidence that the resulting partitions are generating.

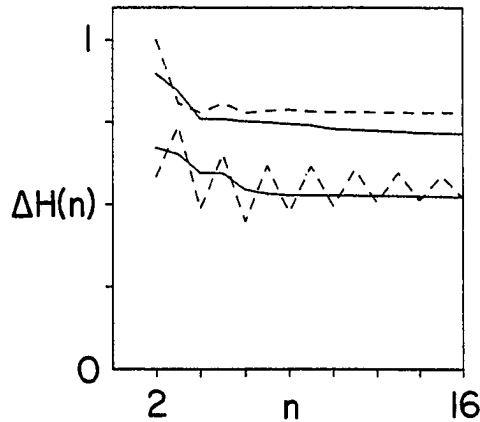


Fig. 3. Entropy convergence as a function of symbol length. Dashed lines are $\log N(n) - \log N(n-1)$, solid lines are $H(n) - H(n-1)$ for $r = 3.9$ (upper set) and $r = 3.7$ (lower set). 5×10^5 iterations were used

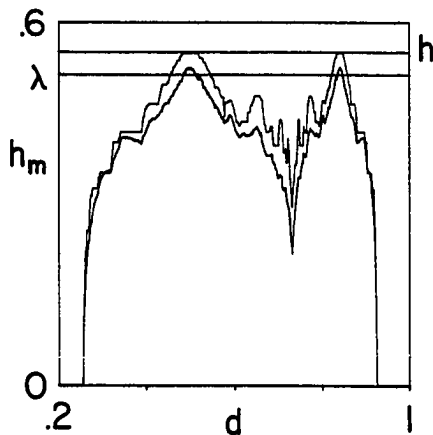


Fig. 4. Topological entropy (upper curve) and metric entropy (lower curve) of the shift induced by choosing different decision points d . The upper horizontal line is the topological entropy calculated to one part in 10^6 with the kneading determinant; see [10] for details. The lower horizontal line is the Lyapunov characteristic exponent calculated to within .1%. The parameter r is 3.7

We pause now to introduce Lyapunov characteristic exponents as another measure of chaos, and to discuss their relationship to the entropies described above. The Lyapunov characteristic exponents measure the average asymptotic divergence rate of nearby trajectories in different directions of a system's state space [11]. For our one-dimensional examples, $f: I \rightarrow I$, there is only one characteristic exponent λ . It can be easily calculated since the divergence of nearby trajectories is simply proportional to the derivative of f [4]:

$$\lambda = \lim_{N \rightarrow \infty} \frac{1}{N} \sum_{n=1}^N \log |f'(x_n)| = \int_0^1 \log |f'(x)| d\bar{u}.$$

The second expression assumes that an absolutely continuous invariant measure \bar{u} exists. This type of measure can be interpreted as a model for observable (asymptotic) behavior.

Our numerical experiments [1] indicate that the metric entropy is equal to the Lyapunov exponent for all chaotic parameter values of the logistic equation, thus indicating the existence of an absolutely continuous invariant measure. SHIMADA [12] obtained good agreement between the characteristic exponent and the metric entropy for the Lorenz attractor and its induced symbolic dynamics using only 9-cylinders. CURRY [13] has computed a metric entropy slightly lower than the positive characteristic exponent for Henon's two-dimensional diffeomorphism. These results are consistent with rigorous theory [14]. Though we find equality between the metric entropy and the Lyapunov characteristic exponent for one-dimensional maps, there are many interesting entropy convergence features that depend on the order of the map's maximum. Our numerical results indicate that any map that is strictly hyperbolic, i.e. one for which the absolute value of the first derivative is everywhere greater than one, displays rapid convergence of the metric entropy to the Lyapunov characteristic exponent. Maps that are not strictly hyperbolic have slower, and sometimes complex, entropy convergence properties (cf. [1]). We will now turn to a study of some of these convergence features; viz., those that are of importance to the experimental application of symbolic dynamics.

4. Symbolic Dynamics in the Presence of Fluctuations

In modeling a dynamical system immersed in a heat bath, i.e. one in contact with a fluctuations source, previous work [15] established that fluctuations act as a disordering field for chaotic dynamics. This perspective will guide the discussion here of the symbolic dynamics derived from the stochastic difference equation

$$x_{n+1} = f(x_n) + \tau_n,$$

where τ_n is a zero-mean random variable of standard deviation, or noise level, σ . We assume this random variable is delta-correlated, $\langle \tau_n \tau_m \rangle = \sigma^2 \delta_{nm}$. One general feature of adding noise to deterministic dynamics is that the resultant behavior and derived average quantities (observables), such as the entropies, depend very little on the type of noise distribution (as long as it is ergodic), and only on its standard deviation. The practical import of this is that results from different types of noise can be compared as long as the respective noise levels are used.

The general effects of fluctuations on the logistic equation and the period-doubling bifurcation have been discussed elsewhere [15,16]. Near the accumulation of the period-doubling bifurcation sequence, the effects of external noise produce a power law increase in the Lyapunov characteristic exponent, and can be described by a scaling theory and renormalization group approach [15,17].

There are various formal problems with the definition, as well as the calculation, of the entropies and Lyapunov characteristic exponents in the presence of noise. Some of the problems associated with entropy are: (i) The entropy for deterministic systems is defined as a supremum over all partitions, but as measurement partition elements become smaller than the noise level, the entropy diverges to infinity, rendering problematic the definition of a "true" entropy that is independent of partition. (ii) Even using a coarse (e.g. binary) partition, a fixed point with added noise will have nonzero entropy if a partition divider is placed on the fixed point. (iii) There is no longer any correspondence between symbol sequences and orbits, but rather between ensembles of orbits and distributions of symbol sequences. We have, then, no result analogous to KOLMOGOROV's theorem for generating partitions to ensure that the entropy we compute is the "true" entropy.

These problems are significant, but they do not prevent us from using the symbolic dynamics entropy algorithms to compute a value of the entropy with respect to a particular measurement partition. That is, we will take the approach of using information theory to quantify the observed chaos, leaving the formal interpretation for elsewhere [18].

The effect of noise on symbolic dynamics entropies was first discussed in [1]. We will summarize some of those results here. Adding external noise increases the rate of convergence of the entropies. As an example of this, at the merging of two bands into one in the logistic map, the topological entropy $h(\sigma_f)$ oscillates indefinitely, when calculated as the two-point slope $H(n) - H(n-1)$. When noise is added, the oscillation is "damped" and the topological entropy readily converges, albeit to a larger value than found with no noise added. As the metric entropy converges from above, the observer gains information about correlations between the observed symbols. When noise is added, these correlations decay, and so the metric entropy converges more rapidly to a higher value.

In the following we will concentrate on the metric entropy as it is of physical interest, being the information production rate (per iteration or per symbol) of a chaotic system.

Figure 5 shows the metric entropy $h_p = h(2^n, \sigma)$ as a function of length of n -cylinder and noise level σ , for the logistic map. We will also discuss results for the piecewise-linear tent map: $x_{n+1} = ax_n$, if $x_n < .5$; and $x_{n+1} = a(1-x_n)$, if $x_n \geq .5$. The parameter values of interest are where two bands merge into one: $r = 3.678\dots$ and $a = 1/\sqrt{2}$, respectively. The topological entropy in each case can be analytically calculated [10] to be $1/2$. We have also looked at several larger parameter values for these maps (for example, $r = 3.7$ and $a = 1.43$, respectively) that yield the same topological entropy ($h(f) \sim .52$). The latter condition assures that the maps have similar periodic orbit structure and so, in a sense, are comparable (or topologically conjugate, in mathematical parlance).

With all other variables fixed (e.g. noise level), we call a graph of entropy versus number of symbols an entropy convergence curve. Fig. 5, then, shows a family of 13 such entropy convergence curves at increasing noise levels for the logistic map at the parameter where two bands merge into one. As the noise level is increased, the metric entropy increases, especially for large number of symbols ($n \sim 24$). The noise appears to cause the entropy to level off, or to effectively converge, at successively shorter sequences of symbols, albeit to a larger value than the zero noise entropy. The convergence also exhibits certain periodic features: the entropy decreases more rapidly in going from an odd number of symbols to an even number, than visa versa. This is due to the periodic substructure of Σ_f . In the sequences of 1's and 0's obtained for the map

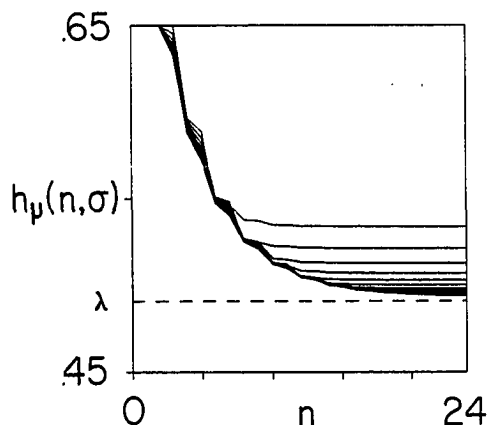


Fig. 5. Metric entropy convergence at different noise levels for the logistic map at band-merging ($r = 3.678\dots$). The noise levels are $\sigma = 0$ and $\sigma = 2^{-k}$, $k = -18, \dots, 7$. Each curve computed using 2×10^7 iterations. Uniformly distributed noise was used. Dashed curve is the Lyapunov exponent computed with 10^8 iterations and zero noise

at band merging, every other symbol is a "1".

5. Scaling of the Metric Entropy

We now introduce notions of scaling and show how these allow one to summarize the features observed in Fig. 5, as well as making precise the notion of convergence in the presence of noise. Scaling theory describes the singularities or "critical" properties of some state function, or "order parameter". For our purposes this function is properly called a "disorder parameter", and one can take it to be either the topological or metric entropies. In the following, we will present only the results for the metric entropy h_u .

We will consider the metric entropy disorder parameter as a function of two scaling variables: (i) $N = 2^n$, the total possible number of n -cylinders; and, (ii) σ , the noise level. Thus for fixed N and σ , $h_u(N, \sigma)$ is a number that describes the observed information production rate for the system: the average amount of information one gains in observing the next symbol, knowing the previous $n = \log(N)$ symbols. In the language of information theory N is the volume of the signal space or the total possible number of messages of length n . The data shown in Fig. 5 is a plot of metric entropy versus $n = \log(N)$. It is important to keep in mind that we are considering N as the scaling parameter, not n .

In scaling theory [19], the critical exponent w of a function $g(x)$ is defined

$$w = \lim_{x \rightarrow 0} \frac{\log(g(x))}{x}, \quad \text{or} \quad w = \lim_{x \rightarrow \infty} \frac{\log(g(x))}{x}, \quad (6)$$

where x is some normalized scaling variable. The form used depends on the type of "singular" behavior of $g(x)$. We have introduced the latter form in (6), although it is not typically considered a critical exponent. These expressions appear often in dynamical systems theory when one defines measures of chaos, such as the topological or metric entropies, the fractal dimension, the Lyapunov characteristic exponent, or the information dimension; and, also, in information theory as, for example, the channel capacity or the dimension rate.

This type of expression extracts the dominant power law behavior that $g(x)$ exhibits at its "singularity". The critical exponent quantifies that behavior. In other words, asymptotically (as $x \rightarrow 0$ or $x \rightarrow \infty$) the function behaves as

$$g(x) \approx x^w. \quad (7)$$

While (7) implies one of the forms in (6), the opposite is not true. And so, it is significant that the results described here typically satisfy (7) for all x and so one does not need to take the limits implied in (6). In the numerical work this saves a substantial amount of computation and, theoretically, the scaling results are more robust, in some sense, and easier to analyze.

This approach can be applied to see if there is scaling behavior in $h_u(N, \sigma)$. As a first step in this, we define a normalized metric entropy

$$\bar{h}_u(N, \sigma) = \frac{h_u(N, \sigma) - h_u(\infty, 0)}{h_u(\infty, 0)}.$$

This new quantity indicates the deviation of $h_u(N, \sigma)$ from the "true" entropy $h_u(\infty, 0)$ at finite number of symbols N and noise level σ . One might call it the excess entropy.

The features in Fig. 5 can be summarized by two power laws and corresponding critical exponents. The first describes the zero-noise convergence critical behavior,

$$\bar{h}_u(N,0) \approx N^{-\gamma};$$

and the second describes the effect of noise,

$$\bar{h}_u(\infty, \sigma) \approx \sigma^{-\beta}.$$

Table I summarizes the results for the critical exponents in four simple cases. The convergence critical exponent for the tent map at band-merging can also be analytically calculated to be exactly 1/2 [18]. The numerically obtained value in Table I is in excellent agreement with this. Details for other dynamical systems are reported in [18].

Figure 6 shows the log-log plot for the convergence critical exponent at zero noise of the logistic map at band merging. The periodic features of the convergence curves of Fig. 5 appear here as a pairwise grouping of points. The straight line is the least squares fit to the data points, and the good fit indicates that the convergence scaling hypothesis is correct. The slope of this line is the critical exponent γ . The same convergence plot for the tent map at band merging is virtually identical, also showing an extremely good least squares fit, but with different slope.

Figure 7 shows the scaling effect of increasing fluctuations, for the logistic map at band merging. Note that there is scaling over a wide range in noise levels. For the tent map at band merging the data again give a very good fit similar to that for the logistic map, but with a different critical exponent. It is illustrative to consider noise scaling for fixed n . Noise levels below some fixed $\sigma(n)$ do not affect the convergence of the entropy for less than n symbols. And so, there is some relationship between noise level and the number of symbols at which the entropy deviates from its zero noise convergence. We call this leveling off, as seen in Fig. 5, the convergence knee. This will be discussed shortly in greater detail as it will form the basis for the physical application of the scaling results and also because it points to a simple description of the effect of noise on the entropies.

Table I Critical exponents for noise scaling of the metric entropy

map	parameter	γ	β	ω
<u>Logistic</u>	band-merge	$.38 \pm .01$ (.59)	$.52 \pm .01$ (.95)	1.37
	$r = 3.7$	$.40 \pm .05$ (.51)	$.53 \pm .05$ (1.33)	1.3
<u>Tent</u>	band-merge	$.50 \pm .01$ (.82)	$1.01 \pm .01$ (16.7)	2.00
	$a = 1.43$	$.55 \pm .1$ (.76)	$1.06 \pm .08$ (34.8)	1.7

Note: (1) coefficient of proportionality in parentheses
 (2) errors are deviations from least squares fit to log-log plot of data

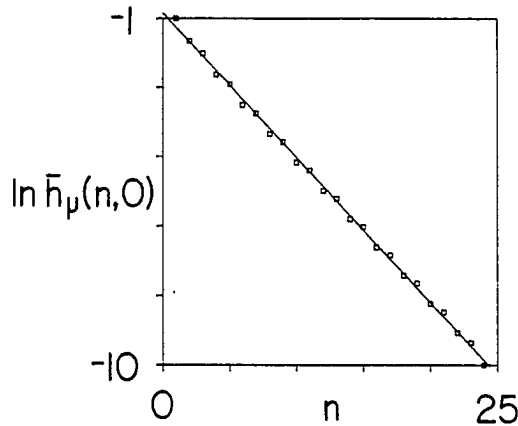


Fig. 6. Zero noise entropy convergence. Log-log display of data from Fig. 5

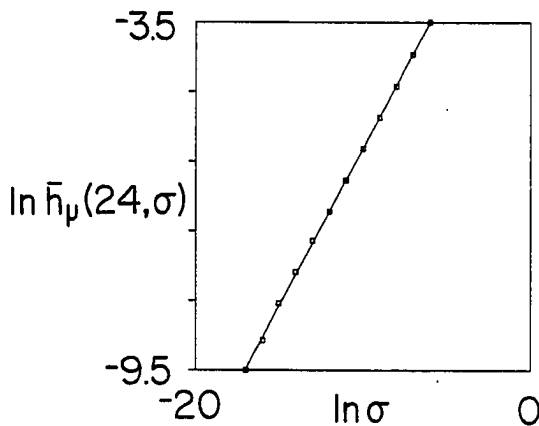


Fig. 7. Noise scaling of metric entropy. Log-log plot of data from Fig. 5 at n = 24

The property of scaling is a geometrical one that says, in effect, the change in one of the scaling variables is equivalent to some corresponding change in another variable. In the present case, our "scaling hypothesis" says the metric entropy $\bar{h}_u(N, \sigma)$ is a two-dimensional surface with the property that a scale change by (say) a factor of s in the coordinates N and σ does not change the surface's shape except by a constant multiplicative factor. Mathematically, this is equivalent to the requirement that $\bar{h}_u(N, \sigma)$ is a generalized homogeneous function $H(z)$, that takes the form

$$\bar{h}_u(N, \sigma) = \sigma^{-\beta} H(N\sigma^{-1/\beta}) . \tag{8}$$

The homogeneity property of $\bar{h}_u(N, \sigma)$ is equivalent to its having the form of a function of $z = N\sigma^{-1/\beta}$ times $\sigma^{-\beta}$. Homogeneity is the central property of scaling. Thus, if the noise effects (such as in Fig. 5) can be summarized by a single function of one variable

$H(z)$, then we have numerically verified that there is a scaling theory for the convergence of the symbolic dynamics metric entropy.

To see $H(z)$, Eqn. (8) says to rescale each of the convergence curves in Fig. 5 by various factors of the noise level. This is shown in Figure 8 for the logistic map at band merging. The plot contains the approximately 300 data points from Fig. 5. Since Fig. 8 shows that all the data points lie on a well-defined curve, the scaling theory is verified for the metric entropy.

If we define $\log N_c(\sigma)$ as the number of symbols at which \bar{h}_u has reached the knee of its convergence curve, then at twice the noise level (say) the entropy will level off at some lower number of symbols $\log N_c(2\sigma)$. This can also be summarized with another power law and a new critical exponent w :

$$N_c(\sigma) \approx \sigma^{-w}. \quad (9)$$

The knee also appears in Fig. 8 of the homogeneous function and we can use this to see that at the knee

$$\log(N_c \sigma^{\beta/\gamma}) = \text{constant}.$$

This can be rewritten as

$$N_c(\sigma) \approx \sigma^{-\beta/\gamma},$$

the power law in (9). This says then that there is a simple relationship between the critical exponents:

$$w = \beta/\gamma.$$

Table I lists the values of the knee critical exponent for our test cases.

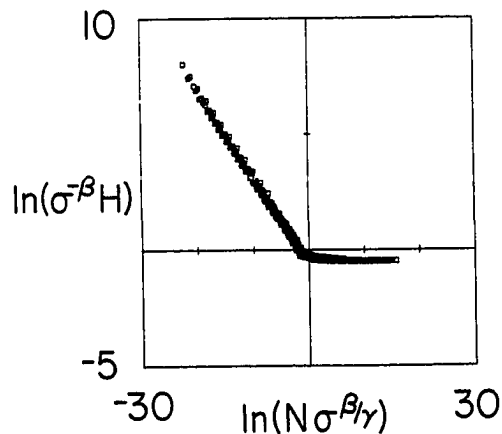


Fig. 8. Homogeneous function for noise and convergence scaling of the metric entropy. Log-log display of all data in Fig. 5

6. Experimental Symbolic Dynamics

The use of symbolic dynamics for the study of low-dimensional chaotic behavior in an experimental context begins with the reconstruction of a one-dimensional return map from the data as outlined in [5]. For simple chaotic dynamics, once the return map is constructed, the symbolic dynamics entropy algorithms can be applied as we have discussed above. Such a calculation has been carried through by R. Shaw on data from a chaotic dripping faucet [20].

The convergence and noise scaling of the metric entropy have not yet been measured for a physical system. They should, however, be measurable with current levels of experimental accuracy.

References

1. J.P. Crutchfield and N.H. Packard, *Int'l J. Theo. Phys.* 21, 433 (1982)
2. C. Shannon and C. Weaver, The Mathematical Theory of Communication, University of Illinois Press, Urbana, Illinois, (1949)
3. A.N. Kolmogorov, *Dokl. Akad. Nauk.* 119, 754 (1959)
4. R. Shaw, *Z. fur Naturforschung* 36a, 80 (1981)
5. N.H. Packard, J.P. Crutchfield, J.D. Farmer, and R. Shaw, *Phys. Rev. Let.* 45, 712 (1980); and H. Froehling, J.P. Crutchfield, J.D. Farmer, N.H. Packard, R. Shaw, *Physica* 3D, 605 (1981)
6. R.L. Adler, A.G. Konheim, and M.H. McAndrew, *Trans. Am. Math. Soc.* 114, 309 (1965)
7. B. Mandelbrot, Fractals: Form, Chance, and Dimension, W.H. Freeman, San Francisco, California (1977)
8. J.D. Farmer, in these proceedings
9. V.M. Alekseyev and M.V. Jakobson, *Physics Reports* (1981); and R. Shaw, in Order in Chaos, edited by H. Haken, Springer-Verlag, Berlin (1981)
10. P. Collet, J.P. Crutchfield, and J.-P. Eckmann, "Computing the Topological Entropy of Maps", submitted to *Physica* 3D (1981)
11. G. Benettin, L. Galgani, and J.-M. Strelcyn, *Phys. Rev. A* 14, 2338 (1976); and I. Shimada and T. Nagashima, *Prog. Theo. Phys.* 61, 1605 (1979)
12. I. Shimada, *Prog. Theo. Phys.* 62, 61 (1979)
13. J. Curry, "On Computing the Entropy of the Henon Attractor", IHES preprint.
14. R. Bowen and D. Ruelle, *Inv. Math.* 29, 181 (1975); D. Ruelle, *Boll. Soc. Brasil. Math.* 9, 331 (1978); and F. Ledrappier, *Ergod. Th. & Dynam. Sys.* 1, 77 (1981)
15. J.P. Crutchfield and B.A. Huberman, *Phys. Lett.* 77A, 407 (1980); and J.P. Crutchfield, J.D. Farmer, and B.A. Huberman, to appear *Physics Reports* (1982)
16. H. Haken and G. Mayer-Kress, *J. Stat. Phys.* 26, 149 (1981)
17. J.P. Crutchfield, M. Nauenberg, and J. Rudnick, *Phys. Rev. Let.* 46, 933 (1981); and B. Schraiman, G. Wayne, and P.C. Martin, *Phys. Rev. Let.* 46, 935 (1981)
18. N.H. Packard and J.P. Crutchfield, in the *Proceedings of the Los Alamos Conference on Nonlinear Dynamics*, 24-28 May (1982); and to appear in *Physica* 3D (1982)
19. H.E. Stanley, Introduction to Phase Transitions and Critical Phenomena, Oxford University Press, New York (1971)
20. R. Shaw *et al.*, in the *Proceedings of the Los Alamos Conference on Nonlinear Dynamics*, 24-28 May (1982); and to appear in *Physica* 3D (1982)

5.10. Symbolic Dynamics of Noisy Chaos

SYMBOLIC DYNAMICS OF NOISY CHAOS

J.P. CRUTCHFIELD and N.H. PACKARD

Physics Board of Studies, University of California, Santa Cruz, California, U.S.A.

One model of randomness observed in physical systems is that low-dimensional deterministic chaotic attractors underly the observations. A phenomenological theory of chaotic dynamics requires an accounting of the information flow from the observed system to the observer, the amount of information available in observations, and just how this information affects predictions of the system's future behavior. In an effort to develop such a description, we discuss the information theory of highly discretized observations of random behavior. Metric entropy and topological entropy are well-defined invariant measures of such an attractor's "level of chaos", and are computable using symbolic dynamics. Real physical systems that display low dimensional dynamics are, however, inevitably coupled to high-dimensional randomness, e.g. thermal noise. We investigate the effects of such fluctuations coupled to deterministic chaotic systems, in particular, the metric entropy's response to the fluctuations. We find that the entropy increases with a power law in the noise level, and that the convergence of the entropy and the effect of fluctuations can be cast as a scaling theory. We also argue that in addition to the metric entropy, there is a second scaling invariant quantity that characterizes a deterministic system with added fluctuations: I_0 , the maximum average information obtainable about the initial condition that produces a particular sequence of measurements (or symbols).

1. The role of fluctuations in dynamical systems modeling

The work of Lorenz [1] and Ruelle and Takens [2] have lead to the idea that randomness observed in physical systems may in some cases be modeled by low-dimensional chaotic attractors. A growing body of experimental evidence now supports this view [3]. This data also demonstrates that any purely deterministic model is incomplete, since the dynamics of physical systems is inevitably coupled to some source of fluctuations. We shall refer to these fluctuations as *External fluctuations**. An-

* We can give an unambiguous definition of this in terms of the ideas presented in this paper: External fluctuations may be regarded as a second dynamical system (coupled to the system of interest) with sufficiently high entropy h_μ so that all the information I from a measurement is lost after the typical time τ used for sampling the first system. In other words, $I/\tau \ll h_\mu$, where I/τ is the information acquisition rate. This allows for an operational definition of a non-deterministic source of random behavior as a deterministic system whose entropy is sufficiently large to preclude an observer's geometric reconstruction of the source's dynamics. All of our information quantities will be measured in bits and so, in particular, all logarithms will be taken to the base 2.

† We will assume fluctuations to be drawn from a stationary ensemble at each time.

other attribute that must be incorporated into an accurate model for observed randomness is fluctuations of the measurement instrument, these we will call *observational noise*. Observational noise differs markedly from heat bath fluctuations in that it does not affect the temporal evolution of the system being observed (assuming a classical measurement process); rather, it directly limits what may be inferred about the system under study. We will be concerned only with the effects of external fluctuations here; for further discussion of this classification of noise types see ref. 4.

Incorporation of any kind of fluctuation into a dynamical description implies that observables become average quantities, the average being taken over all possible fluctuations.† For the case of a chaotic deterministic dynamical system, we are led to the idea that observables are average quantities, where the average is taken with respect to the asymptotic probability distribution. When fluctuations are added to such a system, they produce a new asymptotic probability distribution. A formal expression of how this distribution arises will be presented below. In referring to a probability distribution $P(x)$ we will find it convenient to

also speak of the associated *measure* μ defined by

$$\mu(A) = \int_A P(x) dx,$$

where A is some set.

We will be concerned with the effect of fluctuations on measurements of randomness, in particular, their effect on the metric entropy. As we shall see from numerical computations, the metric entropy is relatively insensitive to observational noise, but is strongly dependent on external fluctuations coupled to the dynamics; and so we will concentrate mostly on this latter cause. The prototypical chaotic systems we shall use are iterated maps of the unit interval I onto itself: $x_{n+1} = f(x_n)$, where f is some nonlinear function. These will also be referred to as one-dimensional maps. We will model the effects of external fluctuations with a stochastic difference equation of the form

$$x_{n+1} = f(x_n) + \xi_n, \quad (1)$$

where ξ_n is a delta-correlated random variable. Numerical experiments [5] indicate that the response of the metric entropy to the added fluctuations ξ is insensitive to the details of their probability distribution. We will assume ξ to have zero mean, and to be evenly distributed over some finite interval, with a standard deviation, or *noise level*, σ .

For dynamical systems with added fluctuations there are not many rigorous results. Kifer [6] has proven that for hyperbolic attractors* the invariant measure converges weakly to the correct zero noise limit. Boyarsky [7] proved that for one-dimensional maps that have slope everywhere greater than one, there exists some noise level for which the invariant measure of the system with

* In the context of one-dimensional maps, this means that the absolute value of the slope of the map must be greater than one everywhere on the attractor.

fluctuations approximates the zero noise invariant measure with arbitrary accuracy (strong convergence), and that *all* initial conditions have time averages that correspond to averages with respect to the invariant measure.

We begin by reviewing entropy measurement techniques for deterministic systems. We will then investigate the effects of external noise on the symbolic dynamics, and discover that the amount of information $I(n)$ about the initial condition that produces a sequence of length n reaches a limit I_0 at some particular length n_c that is dependent on and scales with the noise level. Furthermore, the added noise produces entropy convergence features that also obey scaling laws. After describing the scaling features of the entropy, we will discuss numerical experiments in which we compute the scaling exponents for many different systems. We then describe an alternate entropy-like quantity similar in spirit to the Lyapunov characteristic exponent, conjecturing equality with the symbolic dynamics metric entropy. We conclude with an overview and a brief discussion of some experimental applications.

2. Symbolic dynamics and entropy for deterministic systems

We must first review the case of observing a deterministic dynamical system. We will consider time to be discrete, and the dynamical system to be a map f from a space of states M into itself, $f: M \rightarrow M$. We assume f has some ergodic invariant measure $\bar{\mu}$. If f has an attractor, we will restrict our attention to the attractor, and assume that almost all (with respect to Lebesgue measure m) initial conditions approach the attractor and have trajectories that are asymptotically described by the measure $\bar{\mu}$ on the attractor; i.e. that for almost all points the measure

$$\mu_N(x) = \frac{1}{N} \sum_{n=1}^N \delta_{f^n x}$$

converges weakly to $\bar{\mu}$. Oono and Osikawa [8] refer to this assumption as the "condition for observable chaos".

This may seem like an amazing assumption from a mathematical viewpoint, but it is proven rigorously for axiom-A systems, where $\bar{\mu}$ is the Bowen-Ruelle measure. For maps of the unit interval this assumption will hold for all maps that have an invariant measure that is absolutely continuous with respect to Lebesgue measure. Consideration of noise added to the dynamics also makes this assumption plausible for most physical contexts, as will be discussed in following section.

The behavior of a dynamical system $f: M \rightarrow M$ can have many symbolic representations, each obtained by using a *measurement partition*, $P = \{P_1, \dots, P_q\}$, to divide the state space M into a finite number of sets each of which is labeled with a symbol $s_i \in \{1, \dots, q\} \equiv S$. The time evolution (x_0, x_1, x_2, \dots) of the dynamical system $f: M \rightarrow M$ is then translated into a sequence of symbols labeling the partition elements visited by an orbit

$$s = \{s_0, s_1, s_2, \dots\}$$

and f itself is replaced by a *shift operator* σ which re-indexes a symbol sequence; that is,

$$\sigma(s) = s'$$

where for each symbol in the sequence s' ,

$$s'_i = (\sigma(s))_i = s_{i+1}.$$

Thus the shift operator σ merely moves the time origin of a symbol sequence one place to the right.

In the space of all possible symbol sequences

$$\Sigma = \{s = (s_0, s_1, \dots)\},$$

the *observed* or *admissible sequences* are those which satisfy

$$x_i = f^i(x_0) \in P_{s_i}.$$

The set of admissible sequences Σ_f along with the shift σ is called a *subshift*. (Σ_f, σ) is the symbolic dynamical system induced by f using the measurement partition P .

The symbol sequences of Σ_f are a coding for the orbits of $f: M \rightarrow M$. A finite sequence of symbols $(s_0^n, \dots, s_{n-1}^n)$ defines an *n-cylinder* $s^n \equiv \{s: s_i = s_i^n, i = 0, \dots, n-1\}$ which is a subset of Σ_f consisting of all sequences whose first n elements match with those of s_i^n . An *n-cylinder* s^n corresponds to a set of orbits that are "close" to one another in that their initial conditions and first $n-1$ iterates fall in the same respective partition elements. Since these orbits must follow each other for at least $n-1$ iterations, they must all have initial conditions that are close, belonging to some set $U \subset M$. We thus have a map Δ from *n-cylinders* to subsets of M :

$$\Delta(s^n) = \{x | f^i(x) \in P_{s_i}, \text{ for } i = 0, \dots, n-1\}.$$

To a different *n-cylinder* will correspond a different set of orbits whose initial conditions are contained in some other set $U' \subset M$. M will become partitioned into as many subsets as there are *n-cylinders*. As n is increased, this *n-cylinder partition* will become increasingly refined. The refinement caused by taking an increasing number of symbols is illustrated in fig. 1, where M is the unit interval

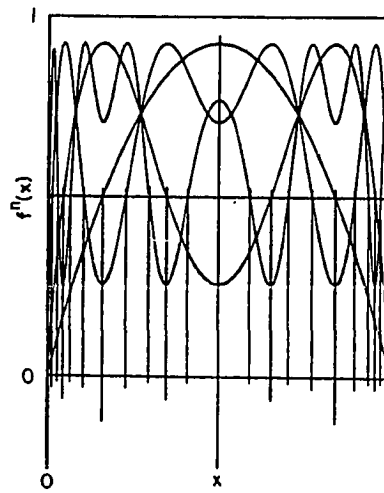


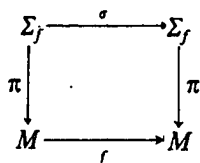
Fig. 1. Construction of the partition induced by taking n symbols (i.e. specifying an *n-cylinder*) with the measurement partition $\{[0, 0.5], (0.5, 1]\}$. The 1-cylinder, 2-cylinder, 3-cylinder, and 4-cylinder partitions are shown with successively shorter tic marks below the x -axis.

$[0, 1]$, and f is the quadratic logistic equation, $f(x) = rx(1 - x)$, with $r = 3.7$, and where we have used the measurement partition formed by cutting the interval in half at $d = 0.5$, the *critical point* of f where the slope vanishes. We will label the left subinterval "0" and the right "1". We see from the figure that the dividing points for the n -cylinder induced partition are simply the collection

$$\{d, f^{-1}(d), f^{-2}(d), \dots, f^{-(n-1)}(d) \dots\}$$

whenever the specified inverse images exist. If the map is not everywhere two onto one (i.e. $r < 4$), some of the inverse images will not exist, corresponding to the fact that some n -cylinders are non-admissible. Changing the measurement partition clearly generates a different set of admissible sequences, just as it generates different n -cylinder partitions.

The usefulness of symbolic dynamics as a representation for the orbits of f can be captured in the following commutative diagram:



with the projection operator

$$\pi(s_0, s_1, \dots) = \bigcap_{i=0}^{\infty} f^{-i}(P_{s_i}).$$

One can then study the simpler, albeit abstract, symbolic dynamical system in order to answer various questions about the original dynamical system. Within this construction, every point on

* An example of one such ambiguity is that there can be two symbol sequences that are nowhere the same, but label the same point on the interval: e.g. 100000... and 011111... both label the same point $x = 0.5$ in the limit of infinite length.

* Milnor and Thurston [9] show how to form a slightly more sophisticated "invariant coordinate" which is monotonic. Our entropy calculations do not require this feature, so we use the computationally simpler binary fraction.

the attractor will have at least one symbol sequence representation. There are a few ambiguities in the labeling of orbits by symbol sequences that prevent π from being invertible, but our discussion of the entropy will prove to be insensitive to the ambiguities*.

The space of one-sided symbol sequences can easily be metrized by mapping each symbol sequence to a power series

$$\phi(x) = \sum_{i=1}^{\infty} \frac{S(f^i x)}{q^i},$$

where $s(x)$ is the symbol labeling the measurement partition element containing x (the denominator is 2^i only if the partition has two elements). For the case of a binary partition, this map identifies every sequence with a binary fraction whose value lies in $[0, 1]$. We will conveniently confuse s^n with its binary fraction representation unless the distinction is necessary*.

A Cantor set structure in the symbol sequences of the chaotic logistic equation is revealed in fig. 2 by a sequence of probability distributions for n -cylinder binary fractions: with the increase in length of the n -cylinder the distributions show successively more, although narrower, peaks. Another demonstration of the Cantor set structure of

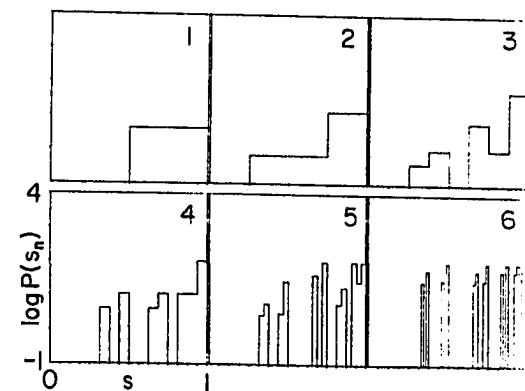


Fig. 2. The Cantor set structure of the subshift (Σ_f, σ) is shown in this sequence of probability distributions for n -cylinders: $n = 1, 2, 3, 4, 5$, and 6 . Each n -cylinder has been mapped onto the unit interval by using its binary fraction. In this example f is the quadratic logistic equation with $r = 3.7$.

Σ_f is the graph of the distribution of symbols s (truncated to a finite n -cylinder with $n = 12$ and mapped onto the unit interval using its binary fraction) versus position x , illustrated in fig. 3.

We will now embark on the task of characterizing the chaotic behavior in a dynamical system using topological and metric entropies, in that order. After giving their definitions, we will show how these quantities may be computed numerically using the symbol sequence representation of orbits. Our analysis follows Shannon [10].

Heuristically, the topological entropy of a dynamical system measures the asymptotic growth rate of the number of resolvable orbits (using a given measurement partition) whose initial conditions are all close. Equivalently, the topological entropy quantifies the average time-rate h of spreading a subset over nearby subsets. This process is most easily illustrated by considering a collection of subsets which form a "cover" of the state space M . The dynamic f spreads a single cover element over other elements after some time

t . The number of new cover elements $N(t)$ visited by points in the original cover element can be written,

$$N(t) \sim e^{ht},$$

where $h > 0$ for chaotic dynamical systems. With this geometric motivation, we will now consider a more formal definition of the topological entropy h [11].

For a compact topological space M , with an open cover U , let $N(U)$ be the number of sets in a subcover of minimal cardinality. Two covers U and Y may be "combined" to form a refinement W by

$$\begin{aligned} W &= U \vee Y \\ &= \{A \cap B \mid A \in U \text{ and } B \in Y\} \end{aligned}$$

Now if $f: M \rightarrow M$ is a continuous map, the *topological entropy* of f with respect to the cover U is defined as

$$h(f, U) = \lim_{n \rightarrow \infty} \log \frac{N(U^n)}{n},$$

where

$$U^n = U \vee f^{-1}U \vee \dots \vee f^{1-n}U.$$

The topological entropy $h(f)$ of the map itself is then the supremum of $h(f, U)$ over all open covers U .

The supremum is obtained only if the measurement partition is "good" in that there is an unambiguous correspondence between orbits of f and symbol sequences. Only with such a good partition is the topological entropy of Σ_f obtained using partition P exactly $h(f)$, the topological entropy of f . There is no general procedure for finding such a good partition, but we will give numerical evidence that such partitions are easily found for simple piecewise monotone maps of the unit interval. Given such a partition, however, we have a readily computable algorithm for $h(f)$:

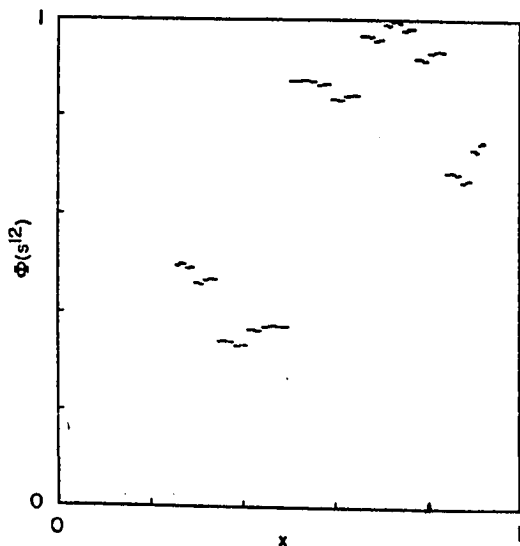


Fig. 3. 2000 iterations of the 'logistic equation' with $r = 3.7$, showing the Cantor set structure of the distribution of sequences in Σ_f . Graphed is $\Phi(s^{12})$ against position x , where s^{12} is the sequence obtained from the initial condition x . The density of points on the x -axis is the asymptotic distribution of f on the unit interval; the density of points on the y -axis is the Cantor distribution illustrated in the previous figure.

simply counting the number of n -cylinders. Note that in the space of symbol sequences Σ_f , each n -cylinder s^n is an open set, and the class of all n -cylinders is an open cover. Thus the topological entropy of the system (Σ_f, σ_f) is given by

$$\lim_{n \rightarrow \infty} \frac{\log N(n)}{n} \rightarrow h(\sigma_f),$$

where $N(n)$ is the number of admissible n -cylinders*. $N(n)$ is readily obtainable numerically, so this formula presents us with a computable algorithm for the topological entropy†.

In presenting the topological entropy before the metric entropy we have purposely reversed their historical order because there is a sense in which the metric entropy is a generalization of the topological entropy: the metric entropy also measures the asymptotic growth rate of the number of resolvable orbits (using a given measurement partition) having close initial conditions, but weights each orbit with its probability of occurrence.

The definition of metric entropy for the dynamical system (M, f) requires an invariant measure $\bar{\mu}$ and a sigma-algebra of measurable subsets of M : more structure than needed for the definition of topological entropy.

If $P = \{P_i\}$ is a finite measurable partition of M with p elements, we define the entropy of P as

$$H_{\bar{\mu}}(P) = \sum_{i=1}^p \bar{\mu}(P_i) \log(\bar{\mu}(P_i)).$$

* For the case of symbolic dynamics, this formula for the topological entropy was first introduced by Parry [12], but is essentially the same as the "channel capacity" introduced by Shannon [10].

† Crutchfield and Shaw [13] have developed other algorithms to compute the topological entropy of a map f based on representing the dynamics as a branching process with a deterministic transition matrix. For certain cases, these techniques allow one to analytically calculate the topological entropy and so to study, for example, the convergence of the topological entropy directly (c.f. ref. 14). These techniques are related to the kneading calculus of Milnor and Thurston [9].

* This theorem as well as the original definition of metric entropy are presented in Kolmogorov [15].

Given two partitions P and Q , their refinement is

$$P \vee Q = \{P_i \cap Q_j \mid P_i \in P \text{ and } Q_j \in Q\}.$$

The metric entropy of f with respect to the partition P is defined by

$$h_{\bar{\mu}}(f, P) = \lim_{n \rightarrow \infty} \frac{1}{n} H_{\bar{\mu}}(P^n),$$

where

$$P^n = P \vee f^{-1}P \vee \dots \vee f^{n-1}P.$$

Finally, the metric entropy of f itself is

$$h_{\bar{\mu}} = \sup_P h_{\bar{\mu}}(f, P),$$

where the supremum is taken over all partitions P .

As for the topological entropy, the supremum is obtained only for special partitions; Kolmogorov* proved that the desired requirement is that the partition be *generating*. This is the case if the smallest sigma-algebra containing $\Delta(s^n)$ for all $n > 0$ coincides with the sigma-algebra of measurable subsets in M . In simpler terms, a partition is generating if, as the length of all sequences becomes large, the sequences label individual points. Thus, only if P is a generating partition we have

$$h_{\bar{\mu}}(f) = h_{\bar{\mu}}(f, P).$$

Again, if we label the elements of the partition P with symbols, the entropy of $h_{\bar{\mu}}(\sigma_f)$ is exactly $h_{\bar{\mu}}(f, P)$, with

$$\mu(s^n) = \int_{\Delta(s^n)} d\bar{\mu} = \bar{\mu}(\Delta(s^n)).$$

Note that the entropy $h_{\bar{\mu}}$ of (Σ_f, σ) is equal to $h_{\bar{\mu}}(f)$ *only* if the measurement partition is generating. For arbitrary measurement partitions,

$$h_{\bar{\mu}}(\sigma_f) \leq h_{\bar{\mu}}(f).$$

Assuming a generating measurement partition, the identification between n -cylinders and elements of the refinement P^n allows us to estimate the measure of each element of P^n by accumulating a frequency histogram for the observed n -cylinders. (Note that P^n is exactly the n -cylinder partition illustrated in fig. 1 for $n = 4$.) We may then obtain an n -symbol estimate for the topological entropy from either

$$h(n) = \frac{\log N(n)}{n}$$

or

$$h(n) = \log N(n) - \log N(n - 1),$$

and estimates for the metric entropy from

$$h_\mu = \frac{H_\mu(n)}{n}$$

or

$$h_\mu(n) = H_\mu(n) - H_\mu(n - 1).$$

It is easily shown that the latter estimate for h_μ converges more quickly than the former [10], so all of our numerical computations of $h_\mu(n)$ will use this expression. Fig. 4 illustrates an example computation of $h(n)$ and $h_\mu(n)$ for the logistic equation, $f(x) = rx(1 - x)$ at a typical parameter value, $r = 3.7$.

In order to illustrate the dependence of the entropy on the measurement partition used, we have computed $h(13)$ and $h_\mu(13)$ for a range of binary (two-element) measurement partitions; the results are illustrated in fig. 5. We call the location $x = d$ at which we decide whether a point x on an orbit is either a "0" or a "1" the *decision point*. For two values of the decision point, $d = 0.5$ and $d = 0.839\dots$ (an inverse image of the critical point), $h_\mu(13)$ is maximized, giving evidence that these values of d yield a generating partition. Note that $h_\mu(13)$ is greater than the Lyapunov character-

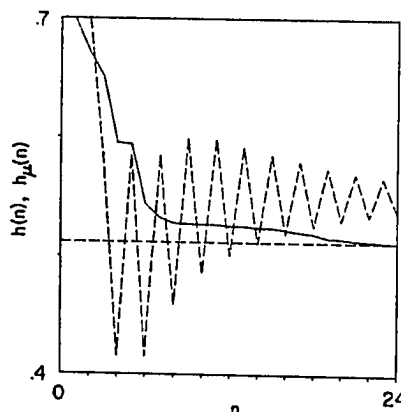


Fig. 4. Entropy convergence for the logistic equation $f(x) = rx(1 - x)$, with $r = 3.7$; the solid line represents $h_\mu(n)$ and the dotted line represents $h(n)$. 2×10^8 iterations were used.

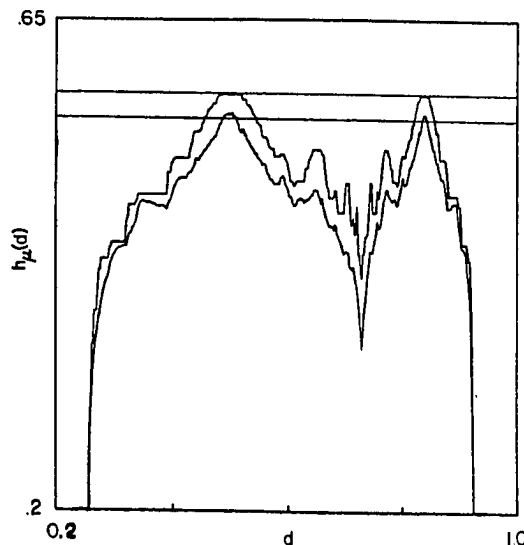


Fig. 5. $h(13)$ (upper curve) and $h_\mu(13)$ for the logistic equation with $r = 3.7$, using different measurement partitions obtained by varying the decision point d . $h(13)$ is actually an average of $h(6), \dots, h(13)$ to eliminate the oscillatory effects. The upper horizontal line is the topological entropy calculated to one part in 10^6 with the kneading determinant [9, 13]. The lower horizontal line is the Lyapunov characteristic exponent calculated to within 0.1%.

istic exponent (to be discussed in more detail shortly) because the metric entropy has not converged by thirteen symbols (cf. fig. 4).

From the above definition of the metric entropy,

it is easy to see that $h \geq h_\mu$, since $h(f, P^n)$ is maximized when each element of P^n is equally probable (i.e. $\mu(P_i^n)$ is the same for all i). In this case, the formula for the metric entropy reduces to that for the topological entropy. This is also evident from a theorem due to Goodwyn [16] and Dinaburg [17], which states that

$$h = \sup_{\mu} h_{\mu},$$

where the supremum is taken over all invariant measures μ .

One of the primary roles of entropy in dynamical systems theory is that it is an invariant [15], which is to say that any two dynamical systems (M, f, μ) and (M', f', μ') have the same metric entropy if they are related by an isomorphism that preserves measure. We will not use this fact at all in our entropy calculations for deterministic systems, but when noise is added to the dynamics, we will address the question of how the invariance of the entropy is affected.

We now introduce Lyapunov characteristic exponents as another measure of chaos, and discuss their relationship to the entropies described above. The Lyapunov characteristic exponents measure the average asymptotic divergence rate of nearby trajectories in different directions of a system's state space [18, 19]. For our one dimensional examples, $f: I \rightarrow I$, there is only one characteristic exponent λ . It can be easily calculated since the divergence of nearby trajectories is simply proportional to the derivative of f [19]:

$$\lambda = \lim_{N \rightarrow \infty} \frac{1}{N} \sum_{n=1}^N \log |f'(x_n)|.$$

* In the general case, the exponents are a function of initial condition, so the sum must be integrated over the attractor, but we will consider only the case of an ergodic attractor where the exponents are constant almost everywhere with respect to the asymptotic invariant measure.

* Curry's underestimate of the entropy is probably due to the fact that the partition he chose was not generating.

Or equivalently, if a continuous ergodic invariant measure $\bar{\mu}$ exists, then the characteristic exponent is given by

$$\lambda = \int_0^1 \log |f'(x)| d\bar{\mu}.$$

If M is an axiom-A attractor, there is a prescription for constructing a partition which is generating, and the equality of the metric entropy h_μ and the sum of the positive Lyapunov characteristic exponents can be proven [20]. In fact, whenever an absolutely continuous invariant measure exists, a theorem due to Piesin [21] shows that the metric entropy of a diffeomorphism is equal to the sum of the positive exponents*. Ruelle [22] proved that for any C^2 map that has an absolutely continuous invariant measure

$$h_\mu \leq \sum_i \lambda_i^+,$$

where the λ_i^+ are all the positive Lyapunov characteristic exponents, and he has conjectured that equality holds. For a wide class of maps of the unit interval, Ledrappier [23] has shown that an ergodic measure having positive metric entropy is absolutely continuous with respect to Lebesgue measure if and only if the metric entropy is equal to the Lyapunov exponent. Shimada [24] obtained good numerical agreement between the characteristic exponent and the metric entropy for the Lorenz attractor and its induced symbolic dynamics using only 9 symbols, and Curry [25] has computed a metric entropy slightly lower than the positive characteristic exponent for a two-dimensional diffeomorphism (Hénon's map)*. Our numerical results for several maps of the unit interval (including the logistic equation) indicate that the metric entropy is indeed equal to the Lyapunov exponent, supporting Ruelle's conjecture and indicating the existence of an absolutely continuous invariant measure whose probability distribution is well approximated by a frequency histogram.

3. Symbolic dynamics and entropy in the presence of noise

One of the reasons that there are so few results on the response of the metric entropy to added fluctuations is that there are problems with the definition of metric entropy (as well as its computation) in the presence of fluctuations. There are also problems with the definition and computation of Lyapunov characteristic exponents for systems with added fluctuations. Some of the problems associated with the metric entropy are:

(1) There is no clear definition of a generating partition for a deterministic system with added noise. Increasingly long sequences of measurements can no longer isolate the system into an arbitrarily fine partition element (where for fineness we mean to use Lebesgue measure on the unit interval).

(2) A related problem is that the entropy with respect to a particular partition diverges as the partition is made increasingly fine [26], rendering problematic the definition of a "true" entropy that is independent of partition.

(3) Even using a coarse (e.g. binary) partition, a fixed point with added noise will have nonzero entropy if a partition divider is placed on the fixed point*. (This entropy would then give an estimate of the external noise in the system.)

(4) The effect of adding noise will depend on what coordinate system the noise is added to. One

* This example is due to Doyne Farmer.

† The fact that the observed asymptotic probability distributions will depend on the coordinate system used suggests that if one has some a priori reason for believing the noise to have a particular distribution (e.g. Gaussian), one should, in principle, be able to adjust the coordinate system used to observe the system until the noise displays the correct distribution. An experimentalist's model would thus include the specification of a *physically preferred coordinate system* in which the noise was added. Most systems may be too complicated to give any clue about the "correct" noise distribution, however. For example, in fluid systems with some underlying low-dimensional chaotic attractor, even if we assume that the fluid is being driven by thermal noise, it is not a priori clear what form will be taken by the noise terms added to the equations of motion on the attractor, since the thermal noise will undoubtedly be filtered by many dynamical effects.

might hope that the response of the metric entropy to noise should be independent in the limit of small noise, but this point is not yet clear from the theory†.

In spite of these problems, we may take a well-defined operational approach to the measurement of metric entropy in the presence of noise: the algorithm embodied in the definitions and estimates yields an unambiguous value of the metric entropy with respect to a particular measurement partition. Any sequence of measurements on a physical system will produce a string of observed symbols; our operational approach will give a measure of the predictability of this string. The measurement partition we will use will be of the same form as that used for the deterministic one-dimensional maps, namely a binary partition of the form $\{[0, d), [d, 1]\}$ where $0 < d < 1$. Given this kind of binary partition, one may again ask if there is a value of d that maximizes the entropy, and we find empirically in fig. 6 that $d = 0.5$ gives a maximum value just as it does for the deterministic case illustrated in fig. 5. This is partial

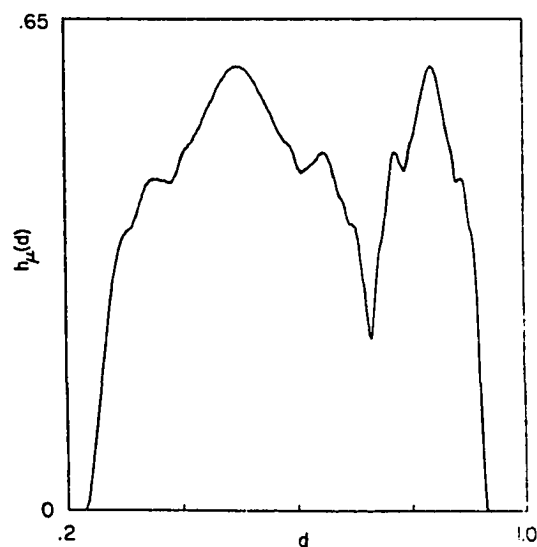


Fig. 6. Entropy h_μ with respect to a binary measurement partition $\{[0, d), [d, 1]\}$ as a function of the decision point d , for the logistic equation with $r = 3.7$ and added noise of width $\sigma = 2$. Compare fig. 5.

justification for our use of this particular measurement partition, but because we are considering only binary partitions, we have not escaped points (1) and (2) above. We must again stress that the metric entropy of a noisy process like eq. (1) depends on the measurement partition used, but we will take the liberty of referring to the "metric entropy" of such a system as that computed using the measurement partition $\{[0, 0.5), [0.5, 1]\}$ unless otherwise noted. Though the entropy h_μ diverges as the measurement partition becomes fine [26], we may still conjecture that for measurement partitions with coarser resolution than the noise level*, our computations give an invariant, well-defined value for h_μ †. To begin the discussion of our numerical computations of the entropy in the presence of noise we will first examine a few properties of the asymptotic probability distributions both of the noisy map on the interval and of the shift on the space of observed sequences Σ_f .

Before considering entropy computation, we will first remark on a few features of the invariant measure, which will in turn have certain implications for entropy measurements. In the deterministic case $f: M \rightarrow M$, the asymptotic invariant distribution function $\bar{P}(x)$ is the fixed point of the Frobenius-Perron operator L_f given by

$$(L_f P)(x) = \sum_{y=f^{-1}(x)} \frac{P(y)}{|f'(y)|}$$

This operator may be written as a Fredholm equation

$$(L_f P)(x) = \int \delta(f(y) - x) P(y) dy, \quad (2)$$

where the equivalence is established by integrating

* We mean here that the size of the smallest partition element must be smaller than the induced noise level. The induced noise level is obtained from the width of the distribution of the added noise by multiplying this width by the map's maximum slope.

† The well-defined value must still be obtained using a supremum over partitions of a given resolution similar to the supremum illustrated in fig. 6.

the right-hand side using a change of variables $y' = f(y)$.

If noise ξ (with a distribution $P_\sigma(\xi)$ having zero mean and width σ) is added to the deterministic map, forming the noisy map

$$x_{n+1} = f_\xi(x_n) = f(x_n) + \xi_n,$$

an additional average must take place with respect to the noise:

$$\begin{aligned} (L_{f_\xi} P)(x) &= \int \delta(f(y) + \xi - x) P_\sigma(\xi) P(y) dy \\ &= \int P_\sigma(f(y) - x) P(y) dy. \end{aligned} \quad (3)$$

Thus we see that the deterministic Frobenius-Perron operator is generalized to include the effects of fluctuations by simply replacing the delta function in eq. (2) by the noise distribution function. This formalism has been used by Schraiman, Wayne, and Martin [27], as well as Haken and Meyer-Kress [28], Takahashi [29], and Feigenbaum and Hasslacher [30]. The asymptotic probability distribution for the noisy map is in principle numerically computable using eq. (3). We have not used this expression to compute the distribution (our entropy computations are based on frequency histograms instead), but we may use eq. (3) to infer at least one qualitative property of the asymptotic distribution $\bar{P}(x)$ on the unit interval: Since the distribution must be invariant under the noisy Frobenius-Perron operator, which includes a convolution of the noise distribution, the asymptotic distribution $\bar{P}(x)$ will have no structure on length scales less than the noise level σ .

The primary difference between the symbolic dynamics of a purely deterministic system and that of a deterministic system with added noise is the nature of the identification between a particular symbol sequence and the set of initial conditions that might have produced that sequence. For the deterministic case there is a direct correspondence between symbol sequences and sub-intervals of the

unit interval, with the sub-intervals becoming increasingly small as the symbol sequences get longer (cf. the construction of the n -cylinder partition illustrated in fig. 1). When noise is added, instead of there being a sub-interval, every point of which produces a particular sequence, there is a set of points which have some probability of producing a particular sequence. We will label the probability distribution of finding the sequence s^n for an initial condition x as $P_{s^n}(x)$.

For the deterministic case, we have

$$P_{s^n}(x) = X_{\Delta(s^n)},$$

where $X_{[a,b]}$ is the characteristic function over the interval $[a, b]$:

$$X_{\Delta(s^n)}(x) = \begin{cases} 1, & \text{for } x \in \Delta(s^n), \\ 0, & \text{for } x \notin \Delta(s^n), \end{cases}$$

and where $\Delta(s^n)$ is the set of initial conditions that can produce s^n for the deterministic case. We may then use the Frobenius–Perron equation to find $P_{s^{n+1}}(x)$ from $P_{s^n}(x)$. First, for the deterministic case, this gives

$$X_{\Delta(s^{n+1})}(x) = \int_{y \in \Delta(s^n)} \delta(f(y) - x) \bar{P}(y) dy.$$

When noise is added, $P_{s^n}(x) = X_{\Delta(s^n)}$ becomes smeared because we must use the noisy Frobenius–Perron operator, which includes a con-

volution of the noise distribution P_σ :

$$P_{s^{n+1}}(x) = \int P_\sigma(f(y) - x) P_{s^n}(y) dy. \quad (4)$$

The smearing of the partition boundaries, or dividers, that takes place with each application of this operator decreases with successive applications*. The effective width of a partition element increases by $\sigma/|f'(y_i)|^n$, where the y_i are the appropriate inverse images of the deterministic divider. Another way of phrasing this observation is that averaging over fluctuations of width σ at each of n iterations is equivalent, for the purposes of constructing $P_{s^n}(x)$, to averaging over n sets of fluctuations of the initial condition each having a magnitude $\sigma \approx |f'(y_i)|^{-n}$. The convergence of the $P_{s^n}(x)$ to a distribution of a fixed width is illustrated for the logistic equation ($r = 3.7$) in fig. 7a. Note that $P_{s^n}(x)$ appears parabolic for large n in the semi-log plots of fig. 7, indicating that $P_{s^n}(x)$ is Gaussian, as might be expected from the repeated convolution of eq. (4).

We see, then, that the picture of bins (elements of an n -cylinder partition) being split into sub-bins (elements of an $(n+1)$ -cylinder partition) for the purely deterministic map (cf. fig. 1) is replaced by probability distributions splitting into daughter probability distributions for a deterministic map with added noise. Consider the situation when the width of the distribution $P_{s^n}(x)$ is large compared to the size of the deterministic bin (i.e. the length of $\Delta(s^n)$): Because $P_{s^n}(x)$ converges to a distribution of fixed width for large enough n , daughter distributions have nearly the same width (and in fact nearly coincide), as illustrated in fig. 8. Since the probability of s^n is given by

$$\mu(s^n) = \int P_{s^n}(x) \bar{P}(x) dx,$$

we see that for large enough n *

$$\mu(s^{n+1}) = \mu(s^n). \quad (5)$$

* Actually, the width decreases only when the slope evaluated at the appropriate inverse image of the deterministic divider is greater than one. It appears, however (as illustrated in the following figure) that even when there are occasional contributions of slopes less than one, as for the logistic equation, the fact that the “average asymptotic slope” is greater than one causes the width of the distributions $P_{s^n}(x)$ to approach a limit. If the “average asymptotic slope” (this quantity is really well defined only for purely deterministic systems) is less than one (i.e. when the attractor is a periodic orbit) $P_{s^n}(x)$ diverges to cover the entire interval, since in this case all initial conditions end up giving the same periodic symbol sequence.

* We are also using the fact that $\bar{P}(x)$ does not change much over the width of $P_{s^n}(x)$.

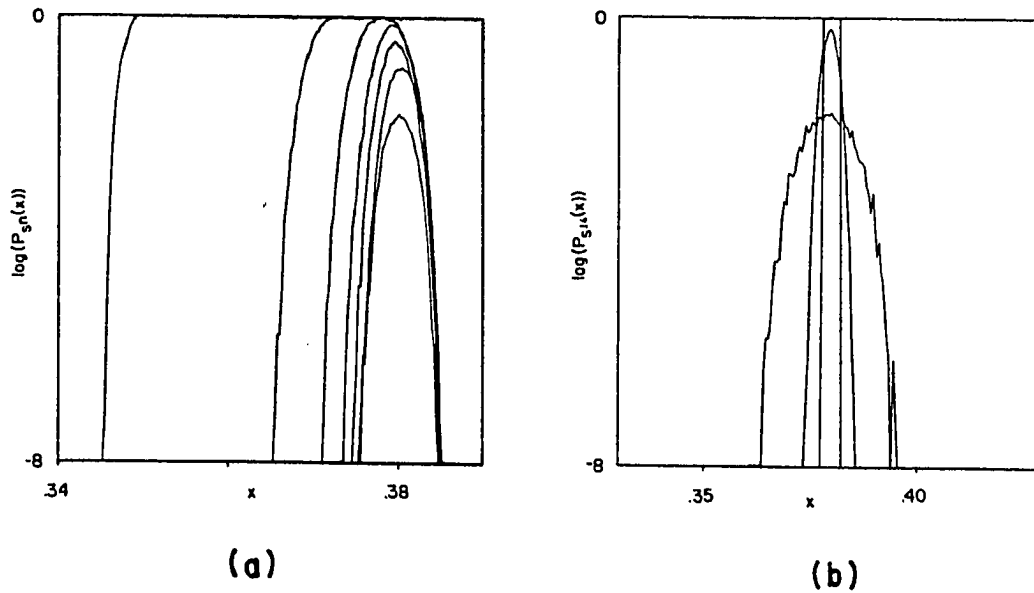


Fig. 3. (a) For a fixed noise level, shown is $P_{s^n}(x)$ for $n = 8, 9, 11, 13, 15, 16,$ and 18 (the values of n corresponding to splitting of this particular series of bins in the deterministic case). (b) Fixing $n = 14$, shown is $P_{s^n}(x)$ for the deterministic case and for two noise levels $\sigma = 2^{-10}$ and $\sigma = 2^{-7}$. The sequence used was $s^{14} = (01010111011111010)$ (the shorter sequences are truncations: $s^8 = (01010111)$, etc.).

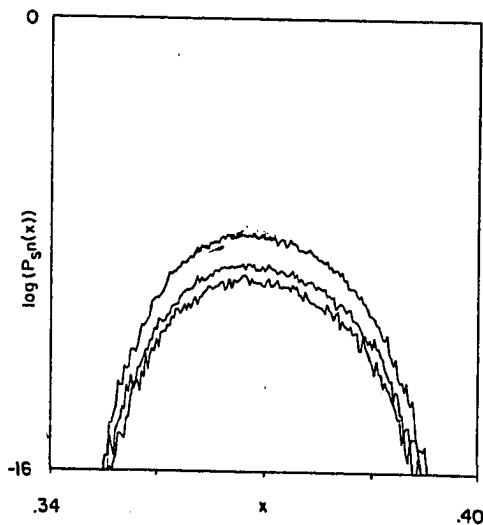


Fig. 8. Splitting of $P_{s^{17}}(x)$ into two daughter distributions $P_{s^{11}}$ and $P_{s^{10}}$. The top distribution is $P_{s^{17}}(x)$, the second distribution is $P_{s^{11}}$, and the third is $P_{s^{10}}$. s^{17} is the same as used in the previous figure.

This condition has some interesting implications that we will now discuss.

$P_{s^n}(x)$ is the distribution of initial conditions that produce the sequence s^n . We may then ask how much information about the initial condition is obtained by observing the sequence s^n , given the asymptotic distribution on the unit interval $\bar{P}(x)$. The appropriate informational measure turns out to be [31, 32]

$$I(s^n) = \int P_{s^n}(x) \log \frac{P_{s^n}(x)}{\bar{P}(x)} dx. \tag{6}$$

Then the average information obtained by specifying n symbols is

$$I(n) = \sum_{s^n} \mu(s^n) I(s^n). \tag{7}$$

For n large enough so that the width of $P_{s^n}(x)$ has reached its noisy asymptotic value we may use the conditions $\mu(s^{n+1}) \approx \mu(s^n)$ and $P_{s^{n+1}}(x) \approx P_{s^n}(x)$ to deduce that $I(n) \approx I(n+1)$, which means that for large enough n , observation of additional symbols

gives no additional information about the initial condition. Stated another way, in the presence of noise, the attainable information about the initial condition reaches some maximum value I_0 , which clearly depends on the noise level. The situation is illustrated schematically in fig. 9. For any given noise level, we may augment our conjecture that a well-defined metric entropy exists, and conjecture the existence of two well-defined invariant quantities that characterize a deterministic system with noise: h_μ and I_0^* .

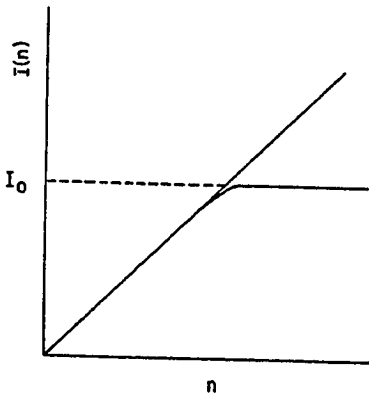


Fig. 9. Schematic illustration of the effect of noise on the attainable information, given by eq. (7), from a sequence of n measurements, or symbols.

We may also use the condition $\mu(s^n 0) \approx \mu(s^n 1)$ for n large enough to deduce entropy convergence properties. Convergence of the entropy for finite length n symbol sequences is exactly the condition that the symbolic dynamics be equivalent to an m -state Markov process, where m is the least integer that produces a distribution $P_{s^n}(x)$ satisfying

$$\text{Var } P_{s^n}(x) > \text{Var } X_{d(s^n)}(x).$$

* Of course we must still include the proviso that the measurement partition has coarser resolution than the noise level as long as we use our algorithm to compute h_μ . Rob Shaw (this volume) makes a similar conjecture for an entropy-like quantity computed using a measurement partition with resolution finer than the noise. We will discuss the relationship between these ideas in section 6.

The finite state Markov property insures that the entropy reaches its converged value for $n \geq m$; we will call this phenomenon the noise floor, and say that the convergence knee occurs at $n = m$. Fig. 10 shows that as the noise level is increased, the convergence knee occurs for smaller values of m . The following section shows how these effects may be described in terms of a scaling theory.

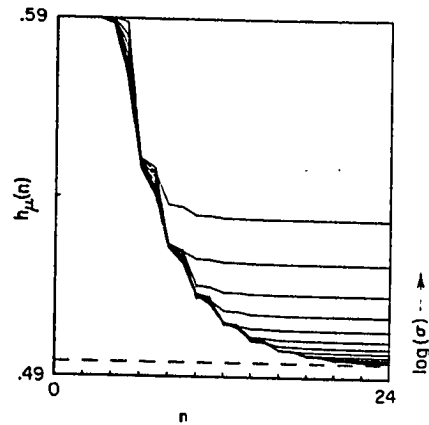


Fig. 10. Entropy convergence of the logistic equation at the parameter value where two bands join to one, $r = 3.67857 \dots$, for increasing noise levels $\sigma = 2^{-18}, \dots, 2^{-7}$. The Lyapunov characteristic exponent is shown by the dashed line.

4. Scaling Properties of Entropy Measurement

Considering the entropy as a function of both $N = 2^n$ and σ , we may define the normalized excess entropy as

$$\bar{h}_\mu(N, \sigma) = \frac{h_\mu(N, \sigma) - h_\mu(\infty, 0)}{h_\mu(\infty, 0)}.$$

We then find that the data illustrated in fig. 10 displays power law behavior in N :

$$\bar{h}_\mu(N, 0) \sim N^{-\gamma},$$

and power law behavior in σ :

$$\bar{h}_\mu(\infty, \sigma) \sim \sigma^\beta,$$

(where ∞ has been approximated by $N = 2^{24}$) [5]. The least squares fits used to estimate the convergence exponent γ and the noise exponent β are quite good (cf. table I). The scaling in N is visible in the zero noise curve of fig. 10, and the power law increase with noise is illustrated in fig. 11.

Our observation that the metric entropy increases with a power law in response to added fluctuations is reminiscent of some results concerning the response of the Lyapunov characteristic exponent to added fluctuations. It has been shown for maps with a quadratic maximum that at the asymptotic limit of a band merging cascade (i.e. at the onset of chaos) noise added to the dynamics cause a power law increase in the Lyapunov characteristic exponent [4, 27, 33]. The cause of this power law must, however, be fundamentally different from the cause of the power law reported here. Their derivation of power law behavior of the Lyapunov characteristic exponent at band merging cascades (as well as similar results near tangent bifurcations) relies on the change in the attractor's geometry (i.e. the structure of the attractor on the unit interval) as noise is added. Furthermore, only the nearness to crucial bifurcation parameter values allows the change in the attractor's geometry

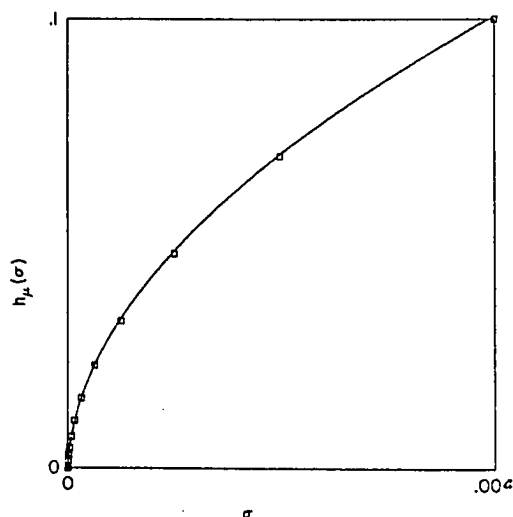


Fig. 11. Power law increase of $h_\mu(n = 24, \sigma)$ for the logistic map at $r = 3.67857\dots$ where two bands join to one.

to be systematically described using renormalization group techniques. The power law behavior we describe here appears to hold more generally, including parameter values away from bifurcation cascades, where the geometry of the attractor changes very little with added noise.

Table I
Numerical calculations of scaling exponents

System	γ	β	ω
Logistic $r = 3.9$	0.48 ± 0.2	$0.56 \pm 0.05 (1.0)$	0.86
logistic $r = 3.7$	0.4 ± 0.2	$0.53 \pm 0.05 (1.3)$	0.76
Logistic 2 \rightarrow 1 bands	0.38 ± 0.02	$0.52 \pm 0.01 (0.9)$	0.73
Logistic 4 \rightarrow 2 bands	—	$0.51 \pm 0.02 (1.5)$	—
Logistic r_c	—	$0.345 \pm 0.01 (1.0)$	—
Logistic 2 \rightarrow 1 bands (function space perturbation)	0.38 ± 0.02	$0.53 \pm 0.01 (1.0)$	0.72
Collet and Eckmann map (2 \rightarrow 1 band)	$0.41 \pm 0.1 (0.80)$	0.62 ± 0.1	0.66
Tent, $s = 1.43$	$0.55 \pm 0.1 (0.86)$	$1.01 \pm 0.01 (0.95)$	0.55
Tent, 2 \rightarrow 1 bands	$0.50 \pm 0.02 (0.82)$	$1.06 \pm 0.08 (35)$	0.47
Tent, 2 \rightarrow 1 bands (function space perturbation)	0.51 ± 0.1	1.05 ± 0.08	0.49
Cusp map	—	$1.04 \pm 0.05 (4.3)$	—
Random walk	—	$0.92 \pm 0.05 (0.05)$	—
Toral automorphism	—	$0.9 \pm 0.02 (0.5)$	—

Note: numbers in parentheses are constants of proportionality.

The two numerically observed power laws in N and σ lead us to posit the *scaling hypothesis* that $\bar{h}_\mu(N, \sigma)$ is a homogeneous function of N and σ , namely, that

$$\bar{h}_\mu(\lambda^\gamma N, \lambda^{-\beta} \sigma) = \lambda \bar{h}_\mu(N, \sigma),$$

where λ is an arbitrary change in scale. This sort of scaling hypothesis has been studied extensively in critical phenomena [34], and it is easily shown that the homogeneity of $\bar{h}_\mu(N, \sigma)$ in both variables implies that $\bar{h}_\mu(N, \sigma)$ may be written as a function of a single scaling variable multiplied by a power law. This reduction may be accomplished in two different ways:

$$\bar{h}_\mu(N, \sigma) = \sigma^\beta H(N\sigma^{\beta/\gamma}) \quad (8)$$

or

$$\bar{h}_\mu(N, \sigma) = N^{-\gamma} H'(\sigma N^{-\gamma/\beta}).$$

Since we are interested primarily in the response of $\bar{h}_\mu(N, \sigma)$ to noise, we will concentrate on the first scaling representation of $\bar{h}_\mu(N, \sigma)$.

The scaling hypothesis may be tested empirically (i.e. using data from a numerical simulation) by graphing $\sigma^{-\beta} \bar{h}_\mu(N, \sigma)$ as a function of the scaling variable $N\sigma^{\beta/\gamma}$, and observing whether or not the data lie on a well-defined function $H(N\sigma^{\beta/\gamma})$. The results of this procedure applied to the data shown in fig. 10 are displayed in fig. 12, where we see a convincing numerical verification of the scaling hypothesis. It is interesting to note that while in critical phenomena, scaling often occurs only asymptotically ("asymptotically" means $\sigma \rightarrow 0$ or $N \rightarrow \infty$ in this context) for this dynamical system we see scaling for *all* σ and N .

We see in fig. 12 that all of the convergence knees are mapped to a single knee of $H(N\sigma^{\beta/\gamma})$. This signals another scaling relation describing the convergence knee, since this implies that the set of (N, σ) for which a convergence knee occurs must satisfy

$$N\sigma^{-\gamma/\beta} = \text{constant}.$$

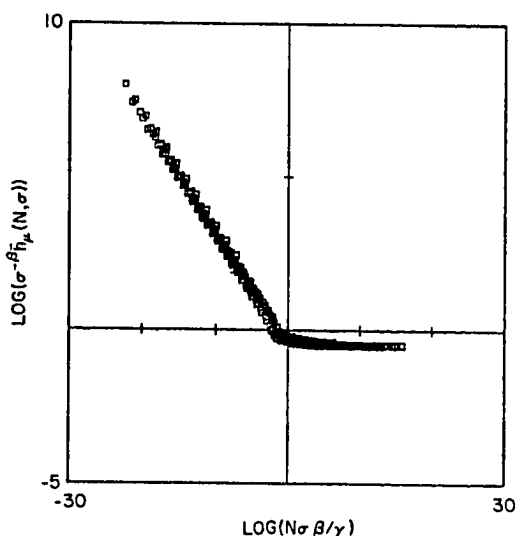


Fig. 12. All the data shown in fig. 10 are replotted here using the homogeneous function representation of eq. (8). The fact that all the data points lie on a well-defined function is verification of the scaling hypothesis.

Either N or σ may be regarded as dependent variables, $N_c(\sigma)$ or $\sigma_c(N)$, in this relation that defines the condition for the occurrence of a convergence knee. And at the convergence knee we may write either

$$N_c(\sigma) \sim \sigma^\omega \quad \text{or} \quad \sigma_c(N) \sim N^{1/\omega},$$

where we find the convergence knee exponent is given by

$$\omega = \gamma/\beta. \quad (9)$$

The same result may be obtained from an eigenvalue equation

$$\frac{\sigma_c(N)}{\sigma_c(2N)} \sim \frac{N_c(2\sigma)}{N_c(\sigma)} \sim \kappa,$$

where $\omega = \log \kappa$.

We have, then, two equivalent interpretations of the eigenvalue κ : First, it is the factor by which the convergence knee noise level σ_c must decrease if we are to observe convergence using symbol sequences

of length $n + 1 = \log(2N)$ rather than of length $n = \log(N)$. Second, if we decrease the noise level by a factor of 2, then κ gives the relative increase in the length of symbol sequence at which we will find convergence. κ will probably be easier to directly measure than the exponents and, at least, it provides a simple way to summarize the net effect of noise on entropy convergence. Values of ω derived from β and γ are tabulated in table I.

The type of relationship between different scaling exponents exemplified by eq. (9) is quite common in the study of critical phenomena. The scaling exponents may be viewed as parameters that describe a surface $\bar{h}_\mu(N, \sigma)$ over the (N, σ) plane. This surface is shown in fig. 13, which illustrates the geometrical significance of the scaling exponents γ , β , and ω .

5. Further numerical experiments

We will now discuss the results obtained from simulating several different systems. For each system we have computed the convergence and noise exponents; the results are tabulated in table I. We will first describe each of the systems studied, then discuss the numerical results.

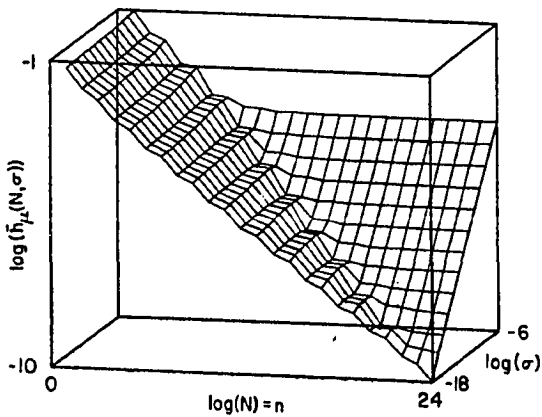


Fig. 13. All the data shown in fig. 10 are replotted as a three dimensional surface. The slope of the line along the front face is $-\gamma$, and the slope of the line along the right face is β . The intersection of these two surfaces defines a line of slope ω in the proper projection onto the scaling variable $N\sigma^7$.

We study four different one-dimensional maps of the unit interval:

- (i) the logistic equation, $f(x) = rx(1 - x)$ for five parameter values, $r = 3.9$, $r = 3.7$ (i.e. two "typical" chaotic parameter values), $r = 3.67857 \dots$ (where two bands merge into one), $r = 3.59257 \dots$ (where four bands merge into two), and $r = 3.5699456 \dots$ (the onset of chaos);
- (ii) the tent map:

$$f(x) = \begin{cases} sx & , \text{ for } 0 < x \leq 0.5, \\ s(1 - x), & \text{ for } 0.5 < x < 1, \end{cases}$$

with $s = 1.43$ (a "typical" chaotic parameter value with topological entropy approximately equal to that of the logistic equation at $r = 3.7$) and $s = \sqrt{2}$ (the parameter value where two bands join to one);

- (iii) Collet and Eckmann's map:

$$f(x) = \begin{cases} 2x, & \text{for } 0 < x < 0.5 - \delta, \\ 1 - \frac{(x - 0.5)^2}{\delta}, & \text{for } 0.5 - \delta \leq x \leq 0.5 + \delta \\ 2(1 - x), & \text{for } 0.5 + \delta < x < 1, \end{cases}$$

with $\delta = 1/6$ (the parameter value where two bands join to one); and

- (iv) the cusp map:

$$f(x) = a(1 - |2x - 1|^{1+\epsilon}),$$

with $\epsilon = -0.05$ and $a = 0.66445776 \dots$ (one of the parameter values where two bands join to one for this ϵ).

We include one two-dimensional system, the linear toral automorphism whose matrix is

$$T = \begin{bmatrix} 0 & 1 \\ 1 & 1 \end{bmatrix}.$$

There is a general procedure for constructing a Markov partition (that is generating) for such a map [35], and we use this as the measurement partition.

Another system we study has one of the simplest possible deterministic parts; a random walk on the circle (we have identified the ends of the unit interval to prevent escape of the orbit):

$$f_{\xi}(x) = x + \xi \pmod{1},$$

where the circle is coordinatized by the unit interval (with 0 and 1 identified, and the usual measurement partition $\{[0, 0.5), [0.5, 1)\}$ is used to produce the symbol sequences. The deterministic part of this map is simply the identity, $f(x) = x$, which has no attractor, and which clearly has zero entropy (the symbol sequence is periodic). As noise is added, however, every sequence becomes possible, though for small noise levels, long sequences of 0's and 1's will be most probable. As we have done for maps of the unit interval, we may, for this system, numerically accumulate probability histograms for n -cylinders and compute h_{μ} as before*. We find that $h_{\mu}(n)$ converges almost immediately to h_{μ} , i.e. $h_{\mu}(2) \approx h_{\mu}(\infty)$ †.

Before discussing the other numerical results contained in table I, we will consider a question concerning the nature of the fluctuations, and how they are coupled to the deterministic system. Eq. (1) represents a very specific model for external fluctuations, namely additive noise. There are, however, many alternatives to perturbing the deterministic function by simply adding noise; one example is multiplicative noise (for the logistic equation this is equivalent to adding noise to the parameter‡). A natural question then arises: which method of adding noise correctly models external fluctuations in a physical system?

* The probabilities of the n -cylinders (and hence h_{μ} itself) are analytically computable using techniques from the theory of random walks; this calculation will be presented in a future paper.

† This result is similar to the entropy convergence of the toral automorphism.

‡ Crutchfield, Farmer, and Huberman [4] have shown for the logistic equation that for any ensemble of additive fluctuations $\{\xi\}$ there is an equivalent ensemble $\{\xi'\}$ of parametric fluctuations (with a different distribution than that for ξ , in general) that will yield the same time averages over trajectories.

Perturbations of a physical system may best be thought of as a perturbation of the dynamics, and not simply a perturbation of the trajectory. A "correct" model for perturbations of a deterministic function $f \in F(M) = \{f: M \rightarrow M\}$ would choose a function at each time step from an ensemble of functions, with the ensemble centered about the deterministic zero noise limit f . Additive noise simply represents a choice from an ensemble that extends along a one-parameter family of functions $q \rightarrow f_q: M \rightarrow M: x \rightarrow f(x) + q$. We have modeled the more general case by expanding the function f in a Taylor series (for convenience we will now consider a map on the unit interval: $M = [0, 1]$), and perturb each coefficient separately:

$$f_{\xi}(x) = (a_0 + \xi_0) + (a_1 + \xi_1)x + (a_2 + \xi_2)x^2 \dots, \quad (10)$$

where each ξ_i is an independent random variable with zero mean, and where $\{a_i\}$ represent the Taylor coefficients of the deterministic function. For example, when we take the deterministic function to be the logistic map, $f(x) = rx(1-x)$, the deterministic coefficients are $\{a_0 = 0, a_1 = r, a_2 = -r, a_i = 0 \text{ for all } i > 2\}$.

The entries in table I labeled "function space perturbation" represent noise added as in eq. (10) up to sixth order. Comparing the noise exponents for these systems with the noise exponents obtained from simple additive fluctuations, we see agreement to within numerical error. This result gives some confidence that models using additive fluctuations may reflect behavior of physical systems with external fluctuations quite well.

We will now summarize a few interesting aspects of the results listed in table I. Some of the results may be coincidentally similar and lead to erroneous extrapolations. Conjectures based on these results must be verified with further numerical work as well as theoretical progress. The largest error in most of these computations is due to inaccuracy in the estimation of h_{μ} in the absence of noise; we have assumed the conjecture $h_{\mu} = \lambda$ (supported by our numerical evidence) and so

estimate h_μ by the Lyapunov characteristic exponent λ computed using 10^7 iterations (giving an accuracy of $\approx 0.1\%$).

The convergence exponents show no discernable features. For the logistic equation, the convergence exponent decreases from $\gamma = 0.48$ at $r = 3.9$ as the parameter is lowered; at r_c there is no power law convergence. In fact, it is easy to show that

$$h_\mu(n) \approx \frac{\log n}{n}.$$

The fact that all of the maps at 2→1 band joining parameter values do not agree in their convergence exponents reveals that the convergence exponent is not constant under topological conjugacy (for all such maps $h = 0.5$). There is no known general technique to compute the convergence exponents, but for special cases (e.g. tent maps at band joinings) γ can be computed exactly to be $\gamma = 0.5$ for 2→1 band merging [26]. This value agrees extremely well with the numerical value quoted in table I.

Both the random walk and the toral automorphism have $\beta \approx 0.9$ (we see no particular theoretical reason for such a close match). For the logistic map, β decreases from ≈ 0.56 at $r = 3.9$ to ≈ 0.34 at the onset of chaos*, $r_c = 3.5699456\dots$. For Collet and Eckmann's map at band joinings, we find $\beta \approx 0.6$, indicating that the noise exponent is neither a topological invariant nor universal for quadratic maps.

For all the tent maps simulated, we have $\beta \approx 1.0$, the same value of β as obtained for the cusp map. This leads us to the conjecture: everywhere expanding maps† have a noise exponent $\beta = 1$. There are other reasons for such a conjecture besides the numerical results listed in table I, for instance, the structure of the asymptotic probability distribution on the unit interval. Maps with a critical point

* This value for β agrees with the power law increase of the Lyapunov characteristic exponent at r_c for the logistic equation [4, 27, 33].

† A map $f: I \rightarrow I$ is everywhere expanding if $|f'| > 1$ for all points on the attractor.

(where the slope vanishes) have distributions with infinite singularities, expanding maps do not.

For maps with critical points, these singularities lead to a very non-uniform probability distribution of symbol sequences. In this case, the highly probable sequences are less affected by noise, and do not readily yield new observable sequences. Consequently, the entropy increases more slowly with noise level for maps with critical points. The first class of seven examples in table I with low noise exponents consists of maps with critical points; whereas the maps in the second class of six examples listed in the table have relatively high noise exponents, but no critical points.

6. Lyapunov characteristic exponents and other measures of chaos in the presence of fluctuations

In the context of deterministic systems, we have seen that for an attractor on the unit interval with one positive Lyapunov characteristic exponent λ and an absolutely continuous invariant measure μ [22],

$$h_\mu \leq \lambda,$$

and we have presented numerical evidence for equality. The purpose of this section is to see how this kind of result may be generalized to include systems with added fluctuations.

Just as the definition of metric entropy is problematic for systems with added fluctuations, so is the definition of Lyapunov characteristic exponents. For one-dimensional maps, the Lyapunov characteristic exponent can no longer be defined as the average slope of the map because the derivative of the noisy map is not defined. Two approaches to this problem have appeared in the literature. The first technique is to compute Lyapunov characteristic exponents numerically by using the deterministic slope of the map along a noisy trajectory [4, 33, 36]. These computations give quite good results at the asymptotic limit of band merging cascades, where the numerical re-

sults can be checked against theoretical predictions [27, 33]. This may seem surprising, but the numerical results are probably good for the same reason that the theoretical predictions can be made: at band merging cascades, the response of the Lyapunov characteristic exponent is dominated by the change in the geometrical structure of the attractor* when noise is added.

The second definition of Lyapunov characteristic exponents in the presence of noise is due to Schraiman, Wayne, and Martin [27]:

$$\lambda = \lim_{n \rightarrow \infty, \epsilon \rightarrow 0} \frac{\log \langle |f^n(x) - f^n(x + \epsilon)| \rangle}{\epsilon n}$$

where iteration of the noisy map is given by eq. (1), and where $\langle \dots \rangle$ denotes an average over the ensemble of noise fluctuations. The noise amplitude must be small enough, and the limits taken carefully for this definition to make sense. When thought of as a measure of the initial spreading rate of two noise distributions whose means are separated by ϵ , this expression for λ is close to a third formulation of Lyapunov characteristic exponents in the presence of noise which we will now discuss (equivalence may eventually be proven).

We have defined h_n in terms of symbolic dynamics (with a generating measurement partition), but there is another important alternate measure of a system's information generation in terms of the average initial spreading rate of narrow probability distributions*. This formulation has been discussed by Shaw [38]; Farmer, Crutchfield, Froehling, Packard, and Shaw [39]; and Farmer [32]. The spreading rate of sharp distributions is close in spirit to the definition of Lyapunov characteristic

* By "geometrical structure," we mean the band like structure of the attractor near r_c [37].

* Here we are identifying a narrow probability distribution with the ensemble of states the system may be in after a (precise but finite) measurement. The time evolution of a sharp distribution is obtained by application of the Frobenius-Perron operator as in eq. (2) (see eq. (3) for the case of added noise). The evolution of a sharp probability distribution is illustrated quite graphically in the movie "Mixing Properties of Strange Attractors," made by Doyno Farmer.

exponents (since the spreading of very sharp distributions is governed by the slope of the map) and the correspondence can be made exact for sufficiently simple maps (e.g. piecewise expanding maps). The main reason for discussing this spreading rate here is that it generalizes quite naturally to systems with added fluctuations, and such a measure may in fact be the most appropriate generalization of Lyapunov characteristic exponents for such systems. We will now define the spreading rate and discuss a few qualitative features for different examples, then outline some conjectures relating this picture to the symbolic dynamics quantities already discussed.

As we have noted previously, a one-dimensional map $f: I \rightarrow I$ has an associated Frobenius-Perron operator on the space of probability distributions on I given by

$$(L_f P)(x) = \int \delta(f(y) - x) P(y) dy.$$

If f has an asymptotic ergodic invariant measure $\bar{\mu}$, then its distribution function $\bar{P}(x)$ must be a fixed point of the operator L_f . Non-equilibrium distribution functions $P(x)$ approach $\bar{P}(x)$ under successive iterations of L_f . The essential idea is to formulate an informational measure of the rate that $P(x)$ approaches $\bar{P}(x)$.

To begin, the measure of the amount of information contained in $P(x)$ relative to $\bar{P}(x)$ is

$$\int P(x) \log \frac{P(x)}{\bar{P}(x)} dx.$$

Now consider how much information is obtained by making a measurement using a measurement partition $A = \{A_i\}$. If the system is found in the i th partition element, the amount of information obtained is

$$\begin{aligned} I_i &= \int X_{A_i}(x) \log \frac{x_{A_i}(x)}{\bar{P}(x)} dx \\ &= -\log \bar{\mu}(A_i). \end{aligned} \quad (11)$$

As time passes, if the system is chaotic, the information obtained by the measurement is lost because the distribution X_{A_i} spreads:

$$I_i(t) = \int L_j' X_{A_i}(x) \log \frac{L_j' X_{A_i}(x)}{P(x)} dx.$$

Note that for $t=0$, this equation reduces to eq. (11). We may now ask for the average information loss after a measurement, where the average is to be taken over all possible initial measurements*

$$\bar{I}(t) = \sum_i \bar{\mu}(A_i) I_i(t).$$

Farmer [32] has given an alternate (equivalent) expression for this quantity:

$$I(t) = \sum_{i,j} \bar{\mu}(f(A_i) \cap A_j) \log \frac{\bar{\mu}(f(A_i) \cap A_j)}{\bar{\mu}(f(A_i)) \bar{\mu}(A_j)}.$$

For a deterministic system we then have the situation illustrated in fig. 14a. A sharp distribution containing a significant amount of information $\bar{I}(0)$ gradually relaxes to the asymptotic distribution, at which point $\bar{I}(t) = 0$ for large enough t †. The slope of $\bar{I}(t)$ well before it goes to zero is then a measure of the loss rate of initial information, which we shall call k_μ . k_μ has been conjectured to be equal to h_μ (Shaw [38]; Farmer, Crutchfield, Froehling, Packard, Shaw [39]; Farmer [32]) for deterministic systems‡.

* Note that $I(t)$ must be distinguished from $I(n)$ defined in eq. (7); $I(n)$ is the rate that information (with respect to the previous $n-1$ symbols) is acquired with the observation of new symbols, and $I(t)$ is the average rate that information contained in an initial condition (using a particular measurement partition) is lost.

† This is actually a crude picture with details which may change for different systems; e.g.: (i) Phase coherent attractors have $I(t) > 0$ as $t \rightarrow \infty$ (cf. Farmer et al. [39]); (ii) Rob Shaw (this volume) has pointed out that for maps with a critical point the initial slope of $I(t)$ will be larger than H_μ , and then decrease to h_μ .

‡ Goldstein and Penrose [40] have introduced a similar information loss rate which, for certain systems, Goldstein [41] proved to be equal to the metric entropy.

For contrast, consider the case when the measurement partition is used simply to sample a white noise process. In this case, the probability of any measurement outcome is independent of all previous outcomes, so $\bar{I}(t)$ goes to zero after the first time step, as illustrated in fig. 14b.

When noise is added to a deterministic system, and a measurement partition finer than the noise level is used, we expect $\bar{I}(t)$ to behave something like fig. 14c. Much of the information obtained from an initial measurement using a measurement partition with a typical partition element size smaller than the noise level σ is immediately lost as the sharp probability distribution X_{A_i} spreads out on the first time step into a distribution of width $\approx \sigma$. $\bar{I}_0 \equiv \bar{I}(1)$ then represents the true amount of information that can be obtained from a measurement; using any finer measurement partition can give no more information about the future behavior of the system.

We are now in a position to phrase the conjectures relating this picture to the measurements of chaos using symbolic dynamics: (i) $k_\mu = h_\mu$ and (ii) $\bar{I}_0 = I_0$. The noise level must, of course be small enough so that there is some time interval for which $\bar{I}(t)$ displays a well defined constant slope. Numerical experiments are underway to check these conjectures.

7. Concluding comments

The effects of fluctuations added to chaotic deterministic dynamical systems reveal the concept of "infinitely precise points" as invalid in many contexts. A new mathematical foundation of classical mechanics is needed; one that uses primitives derived from noise processes. Ruelle [42] has made significant progress in this direction. Though the inclusion of fluctuations in a dynamical model adds many analytical complications to a subject already incompletely understood, there is hope, based on physical observations and numerical computations, that there may be several rewarding simplifications lurking in the theory. Assuming

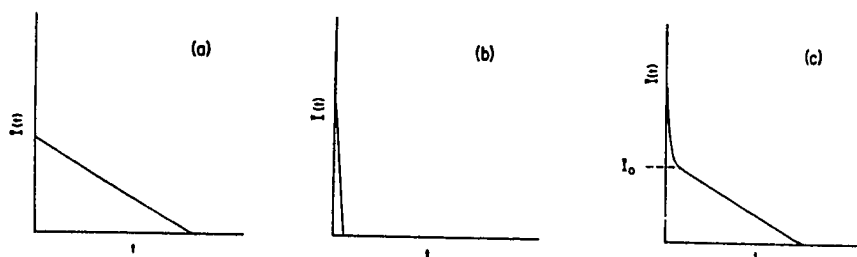


Fig. 14. (a) Schematic representation of $I(t)$ for a deterministic system. For certain systems (e.g. one dimensional maps with a critical point) the slope of $I(t)$ will be greater than k_μ at $t = 1$. (b) Schematic representation of $I(t)$ for measurements of a white noise process. (c) Schematic representation of $I(t)$ for a deterministic system with added noise, where a measurement partition finer than the noise level has been assumed.

such a theory may be formulated, most of the numerical results presented here should be consequences of the theory, so they will hopefully point the direction for some future theoretical developments. We will now review our results in this light.

For a chaotic deterministic system, successive measurements (using a "good" measurement partition) pinpoint the initial condition whose orbit produced the observations with arbitrary accuracy (i.e. an arbitrarily large amount of information about the initial condition may be obtained from an arbitrarily long sequence of measurements). When noise is added to the deterministic dynamics, we have observed that the initial condition may be specified only to within some uncertainty, even with an arbitrarily long sequence of measurements. This has led to the proposal that a chaotic system with added fluctuations is characterized by two invariant quantities: (i) I_0 : the maximum average information (about the initial condition) obtainable from a sequence of measurements; and (ii) h_μ : the average information generation rate (simply the metric entropy in the case of a deterministic system)*. These results should be compared with R. Shaw's results presented in this volume.

* We have also conjectured these two quantities to be equal to I_0 and k_μ , the maximum amount of information that can be stored in an initial condition, and the average loss rate of information after a measurement, respectively.

I_0 has not been computed numerically yet, but the information production rate h_μ (with respect to a given measurement partition) is easily computed using the same algorithms used to compute h_μ for deterministic systems. Upon pursuing the question of how h_μ depends on the fluctuations added to the deterministic dynamics, we find that h_μ increases with a power law in the noise level σ : $h_\mu \approx \sigma^\beta$. We have found that this power law increase seems to happen very generally (for all systems studied here). The exact value of the noise exponent β varies with the system under study, though our numerical experiments have led to the conjecture that a wide class of systems (those reducible to a one-dimensional map $f: I \rightarrow I$ with $|f'| > 1$) has a noise exponent $\beta = 1$. We have combined the power law response of h_μ with the power law convergence of the entropy as a function of the number of symbols observed, to form a homogeneous function description of entropy measurement. In this context, a scaling hypothesis has been verified numerically.

The power law increase in the metric entropy may be regarded as the discovery of a new phenomenon, an observable feature of the information production properties of any physical system that can successfully be modeled by a low dimensional chaotic dynamical system coupled to external fluctuations. There is a growing body of very good experimental evidence that supports such a model; convincing one-dimensional return maps have

been obtained for fluid systems and for chemical systems*.

The noise exponent should be measurable, given reasonable experimental accuracy, though we have no prediction for its value if the one-dimensional map that underlies the observed behavior has a critical point. So far, all the return maps constructed from experimental data appear to have a critical point (or several critical points). There are, however, many physical systems that should be describable by a one-dimensional return map whose slope (absolute value) is always greater than one. One example would be a Benard convection fluid system constrained to excite only those modes described by the Lorenz equations, which have a cusp-like one-dimensional return map. For these systems, we might expect a noise exponent of $\beta = 1$.

Fluctuations are now generally recognized as the source of much of the diverse complexity we see in the world around us (especially in the biosphere). It has been hypothesized (by R. Shaw [46], for example) that what we call "diverse complexity" is a result of intrinsic dynamical properties of some (complicated) dynamical system, in particular, of the system's information generating properties. The informational properties of most of the dynamical systems underlying and producing this complexity are, however, poorly understood. One example of how the current picture of information generation in chaotic dynamical systems must be generalized, is that unlike the chaotic systems studied here, the information generated by the dynamics of complicated evolving systems like the biosphere is stored in physical structures, which then serve as the base for even more complicated evolution. There are many other similar problems

* Cited here are "non-trivial" physical systems in which one might not naively expect to see low-dimensional chaos because of the many degrees of freedom that could potentially participate in the dynamics. Return maps have, of course, been successfully constructed for much simpler physical systems (e.g. electrical oscillator circuits) in which low-dimensional chaos is expected (cf Crutchfield [43]; Packard, Crutchfield, Farmer, Shaw [44]; Gollub, Romer, and Socolar [45]) because of the few degrees of freedom involved.

to be faced, but the results presented here will hopefully serve as a starting point for the study of the role fluctuations will play in the context of these more complicated systems.

Acknowledgements

The authors wish to thank Doyme Farmer, David Fried, John Gukenheimer, and Rob Shaw, for helpful discussions, and the Center for Non-linear Studies, Los Alamos National Laboratory, for the warm hospitality offered during the time this work was written up. This work was supported in part by NSF grant 443150-21299.

References

- [1] E.N. Lorenz, *J. Atmos. Sci.* 20 (1963) 130.
- [2] D. Ruelle and F. Takens, *Comm. Math. Phys.* 20 (1974) 167.
- [3] For example: J.L. Hudson and J.C. Manken, *J. Chem. Phys.* 74 (1981) 6171; J.C. Roux, A. Rossi, S. Bachelard and C. Vidal, *Phys. Lett.* 77A (1980) 391; R. Shaw (this volume); A. Libchaber (this volume); and H. Hauke and Y. Maeno (this volume).
- [4] J.P. Crutchfield and B.A. Huberman, *Phys. Lett.* 77A (1980) 407; J.P. Crutchfield, J.D. Farmer and B.A. Huberman, "Fluctuations and Simple Chaotic Dynamics", to appear *Physics Reports* (1982).
- [5] J.P. Crutchfield and N.H. Packard, *Int. J. Theo. Phys.* 19 (1982) 433; and J.P. Crutchfield and N.H. Packard, *Evolution of Ordered and Chaotic Patterns in Systems Treated by the Natural Sciences and Mathematics*, H. Haken, ed. (Springer, Berlin, 1982).
- [6] Ju. I. Kifer, *USSR Izvestija* 8 (1974) 1083.
- [7] M. Boyarsky, *Trans. Am. Math. Soc.* 257 (1980) 350.
- [8] Y. Oono and M. Osikawa, *Prog. Theo. Phys.* 64 (1980) 54.
- [9] J. Milnor and W. Thurston, "On Iterated Maps of the Interval, I and II", Princeton University preprint (1977).
- [10] C.E. Shannon and W.E. Weaver, *The Mathematical Theory of Communication*, (Univ. of Illinois Press, Urbana, Illinois, 1949).
- [11] R. L. Adler, A.G. Konheim and M.H. McAndrew, *Trans. Am. Math. Soc.* 114 (1965) 309.
- [12] W. Parry, *Trans. Am. Math. Soc.* 112 (1964) 55.
- [13] J.P. Crutchfield and R. Shaw (unpublished).
- [14] P. Collet, J.P. Crutchfield, J.-P. Eckmann, "On Computing the Topological Entropy of Maps", Université de Genève preprint (1981).
- [15] A.N. Kolmogorov, *Dokl. Akad. Nauk. SSSR* 119 (1958) 861; *Dokl. Akad. Nauk. SSSR* 124 (1959) 754.

- [16] L.W. Goodwyn, *Proc. Am. Math. Soc.* 23 (1969) 697.
- [17] E.I. Dinaburg, *Sov. Math. Dokl.* 11 (1970) 13.
- [18] G. Benettin, L. Galgani, A. Giorgilli and J.-M. Strelcyn, *Meccanica* (1980) 21, and *C.R. Acad. Sc. Paris* 286 (1978) 431. I. Shimada and T. Nagashima, *Prog. Theo. Phys.* 61 (1979) 1605.
- [19] R. Shaw, *Zeit. fur Naturfor.* 36a (1981) 80.
- [20] R. Bowen and D. Ruelle, *Inven. Math.* 29 (1975) 181.
- [21] Ya. B. Piesin, *Uspek. Math. Nauk.* 32 (1977) 55.
- [22] D. Ruelle, *Boll. Soc. Brasil. Math.* 9 (1978) 331; see also D. Ruelle, *Comm. Math. Phys.* 55 (1977) 47.
- [23] F. Ledrappier, *Ergod. Theo. Dyn. Sys.* 1 (1981) 77.
- [24] I. Shimada, *Prog. Theo. Phys.* 62 (1979) 61.
- [25] J.H. Curry, "On Computing the Entropy of the Henon Attractor", Institut des Hautes Etudes Scientifique, Bures-sur-Yvette, preprint (1981).
- [26] N.H. Packard, UCSC Ph.D. Dissertation (1982).
- [27] B. Schraiman, C.E. Wayne and P.C. Martin, *Phys. Rev. Lett.* 46 (1981) 935.
- [28] H. Haken and G. Mayer-Kress, *Z. Physik B* 43 (1981) 185; *Phys. Lett.* 84A (1981) 159.
- [29] Y. Takahashi, "Observable Chaos and Variational Principle for One-Dimensional Maps", Dept. Math., Coll. Gen. Educ., University of Tokyo, preprint (1981).
- [30] M. Feigenbaum and B. Hasslacher, "Irrational Decimations and Path Integrals for External Noise", Los Alamos Laboratory Preprint LA-UR-82-1461 (1982).
- [31] F. Schlogl, *Z. Physik* 243 (1971) 303.
- [32] J.D. Farmer, "Information Dimension and the Probabilistic Nature of Chaos", to appear *Zeit. fur Naturfor.* Sept. (1982); See also J.D. Farmer, UCSC Ph.D. Dissertation (1981).
- [33] J.P. Crutchfield, M. Nauenberg and J. Rudnick, *Phys. Rev. Lett.* 46 (1981) 933.
- [34] H.E. Stanley, *Introduction to Phase Transitions and Critical Phenomena* (Oxford Univ. Press, New York, 1971).
- [35] R.L. Adler and B. Weiss, *Mem. Am. Math. Soc.* 98 (1970) 1.
- [36] H. Haken and G. Mayer-Kress, *J. Stat. Phys.* 26 (1981) 149.
- [37] E.N. Lorenz, *New York Acad. Sci. Annals* 357 (1980) 282. J.P. Crutchfield, J.D. Farmer, N.H. Packard, R. Shaw, R.J. Donnelly and G. Jones, *Phys. Lett.* 76A (1980) 1.
- [38] R. Shaw, UCSC Ph.D. Dissertation (1980).
- [39] J.D. Farmer, J.P. Crutchfield, H. Froehling, N.H. Packard and R. Shaw, *New York Acad. Sci. Annals* 357 (1980) 453.
- [40] S. Goldstein and O. Penrose, *J. Stat. Phys.* 24 (1981) 325.
- [41] S. Goldstein, *Israel. J. Math.* 38 (1981) 241.
- [42] D. Ruelle, *Comm. Math. Phys.* 82 (1981) 137.
- [43] J.P. Crutchfield, UCSC Senior Thesis (1979).
- [44] N.H. Packard, J.P. Crutchfield, J.D. Farmer and R. Shaw, *Phys. Rev. Lett.* 45 (1980) 712.
- [45] J.P. Gollub, E.J. Romer and J.E. Socolar, *J. Stat. Phys.* 23 (1980) 321.
- [46] R. Shaw, cover letter for Louis Jacot Prize Competition, Paris (1977).

5.11. Computing the Topological Entropy of Maps

.

Computing the Topological Entropy of Maps

P. Collet¹, J. P. Crutchfield², and J.-P. Eckmann³

¹ Ecole Polytechnique, Laboratoire de Physique Théorique, F-91128 Palaiseau, France

² Physics Board of Studies, University of California, Santa Cruz, CA 95064, USA

³ Département de Physique Théorique, Université de Genève, CH-1211 Genève 4, Switzerland

Abstract. We give an algorithm for determining the topological entropy of a unimodal map of the interval given its kneading sequence. We also show that this algorithm converges exponentially in the number of letters of the kneading sequence.

It is by now well known that iterated maps of an interval, when viewed as dynamical systems, account for some of the irregular behaviour observed in physics. There are three commonly used indicators for the complexity of such systems: The metric entropy, the Liapunov exponent, and the topological entropy. Here we shall discuss an efficient method for calculating the weakest of these notions, namely the topological entropy.

A possible way of defining the topological entropy $h(f)$ of a function f is given by

$$h(f) = \lim_{n \rightarrow \infty} \frac{1}{n} \log_2 N(f^n), \quad (1)$$

where f^n denotes the n^{th} iterate of f , and $N(g)$ is the number of monotone pieces of the graph of the function g . Thus the topological entropy, if positive, measures the exponential growth rate of the number of laps of f^n as n increases. If f is continuous and has a single extremum, then $h(f)$ takes values in $[0, 1]$. If $h(f)$ is positive, then the map f has complex behaviour in the following sense:

1) f has infinitely many different types of aperiodic and periodic orbits. In particular, even if f has a stable periodic orbit, complicated transient behaviour will be observed.

2) Although the topological entropy gives essentially no information about attractors, it indicates, when positive, a sensitivity of the dynamical system to external noise [2, 4].

In this note, we prove that $h(f)$ can be computed efficiently from the orbit of the critical point of f , using the so-called kneading determinant of Milnor and Thurston [5].¹ Our theorem below shows that $h(f)$ can be computed with an error

¹ See also [1] for background material

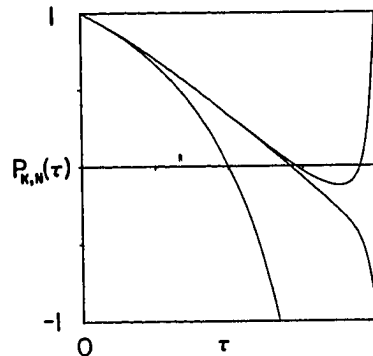


Fig. 1. Kneading determinant $P_{K,N}(\tau)$ vs. τ for the mapping $x_{n+1} = 1 - \mu x_n^2$: (left to right in the picture) $\mu = 2.0, 1.5436889\dots, 1.46610$. The first value corresponds to the maximum allowed height of the map, here $P_{K,N}(\tau)$ has a zero at $\tau = 1/2$ and the topological entropy $h(f) = \log_2(1/\tau) = 1.0$. The second is the parameter where two bands merge [2], $P_{K,N}(\tau)$ has a zero at $\tau = 1/\sqrt{2}$ and the topological entropy $h(f) = 1/2$. The last value is in a regime where there are two distinct bands comprising the attractor and so $h(f) < 1/2$. Each $P_{K,N}(\tau)$ calculated with $N = 40$

which exponentially decreases with the number of iterates of the extremum. Previous numerical calculations of $h(f)$ have suggested that it can be computed with several different, rapidly convergent algorithms [6]. Our theorem will be based on the estimate of the smallest positive root $\tau(f)$ of a certain polynomial (called the characteristic polynomial of f), for which it is known that $h(f) = -\log_2 \tau(f)$, (see e.g. [5]).

We present next the definition of characteristic polynomials for functions with one critical point, as given in [5]. In the sequel, assume f is a continuous map of $[-1, 1]$ to itself, satisfying $f(0) = 1$, with f strictly increasing on $x < 0$ and strictly decreasing on $x > 0$. The kneading sequence $\mathbf{K}(f) = K_1 K_2 K_3 \dots$ of f is the sequence of symbols K_i defined by

$$K_i = \begin{cases} R & \text{if } f^i(0) > 0, \\ C & \text{if } f^i(0) = 0, \\ L & \text{if } f^i(0) < 0. \end{cases}$$

We also define, for $i = 1, 2, \dots$

$$\varepsilon_i = \begin{cases} +1 & \text{if } K_i = L, \\ -1 & \text{if } K_i = R, \end{cases}$$

and, recursively

$$\varepsilon_k = \prod_{i=1}^{k-1} \varepsilon_i \quad \text{if } K_k = C.$$

Finally, given \mathbf{K} , the polynomials $P_{\mathbf{K},N}$ are defined by

$$P_{\mathbf{K},N}(\tau) = 1 + \sum_{n=1}^N \left(\prod_{j=1}^n \varepsilon_j \right) \tau^n.$$

Given f , the analytic function

$$P_{K(f)}(\tau) = \lim_{N \rightarrow \infty} P_{K(f), N}(\tau)$$

is called the *kneading determinant* [or (formal) *characteristic polynomial* of f].

Theorem 1 [5]. *The topological entropy of f equals $-\log \tau$, where τ is the smallest positive root of $P_{K(f)}$.*

We shall show below that the smallest positive root of $P_{K(f), N}$ rapidly approaches τ , providing thus an efficient means of computing τ . We shall see that the speed of convergence will depend (in a controllable manner) on $K(f)$. To state our result, we need the following definition. If A, B are two kneading sequences, we shall say that $A < B$ if there is an s such that $A_i = B_i$ for $i = 1, 2, \dots, s$ and if

- either $A_{s+1} < B_{s+1}$ and an even number of A_i 's, $i \leq s$ are equal to R ,
- or $A_{s+1} > B_{s+1}$ and an odd number of A_i 's, $i \leq s$ are equal to R .

This defines an ordering of kneading sequences, and one has

Lemma 2 [5]. *If $K(f) < K(g)$, then $h(f) \leq h(g)$.*

Our main result is the

Theorem 3. *If K is a kneading sequence and $K > RLR^\infty$, then $P_{K, N}$ has, for every $n \geq 18$ a smallest positive root $\tau_{K, n}$. This root is less than one, and $|\tau_K - \tau_{K, n}| < 18.6 \cdot 2^{-n/2}$.*

(Better bounds are sketched in the proof.)

Before indicating the algorithmic application of the theorem, we extend it to $K \leq RLR^\infty$. One defines [1], for any K

$$R * K = R\check{K}_1 R\check{K}_2 R\check{K}_3 \dots,$$

where

$$\check{K}_i = \begin{cases} L & \text{if } K_i = R, \\ C & \text{if } K_i = C, \\ R & \text{if } K_i = L. \end{cases}$$

(Under technical conditions, if $K(f) = R * A$, then $K(f(1)^{-1} f \cdot f(f(1) \cdot)) = A$ and f exchanges two subintervals of $[-1, 1]$.) Denote $R^{*m} = R * R * \dots * R$ (m times). We have now the

Corollary 4. *Let K be a kneading sequence and suppose $K > R^{*\infty}$.*

(i) *One can decide from the first 2^{m+1} symbols of K whether $K \geq R^{*m} * RL^\infty$, $m \geq 0$.*

(ii) *If K is in the interval $R^{*(m-1)} * RL^\infty \geq K > R^{*m} * RL^\infty$, then $|\tau_K - \tau_{K, n \cdot 2^{m-1}}| < 18.6 \cdot 2^{-n/2}$, provided $n \geq 18$.*

We now outline the algorithm for evaluating τ_K given $K = K(f)$. Set $K' = K$, $m = 0$, and perform the following steps.

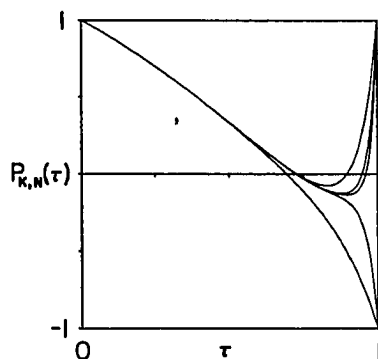


Fig. 2. Kneading determinant $P_{K,N}(\tau)$ vs. τ calculated with various numbers of terms at $\mu = 1.46610$. From left to right, for those $P(\tau)$ with $P(1) = 1$ in the figure, the number of terms are $N = 20, 40,$ and 50 ; for those with $P(1) = -1$, the number of terms are $N = 10$ and 30 , respectively

Step 1. Check if $K'_1 K'_2 K'_3 K'_4 \geq RLR$. If not proceed to Step 3.

Step 2. We must have $K' \geq RLR^\infty$, and hence $\tau_{K'} \leq 2^{-1/2}$. Apply Theorem 3 to K' , noting that

$$h(f) = -\frac{1}{2^m} \log_2 \tau_{K'}$$

(cf. proof of Corollary 4).

Step 3. Increase m by 1. We now know

$$h(f) \leq \frac{1}{2^m} \log 2$$

(cf. proof of Corollary 4). Replace K' by K'' which is defined by the equation $R * K'' = K'$. Proceed to Step 1.

The proof of Theorem 3 will be based on the implicit function theorem. The main ingredient for the proof is Lemma 5 below. Denote by J_1, \dots, J_8 the finite sequences given in Table 1. One can check [1] that every kneading sequence $K \geq RLR^\infty$ either starts out as $J_i \dots$ for some i or is equal to one of the "limiting sequences" of Table 1. In this latter case, the root τ_K of P_K is equal to a root of a polynomial of finite degree [5], and an approximate value for this root σ_j is given in the last column of Table 1. Denote by n_j the number of letters in J_j .

Lemma 5. If K is a kneading sequence, and $K = J_j B$ for some $j \in \{1, 2, \dots, 8\}$, then we have for all $n \geq n_j$:

$$\frac{d}{d\tau} P_{K,n} |_{\tau = 1/2, \sigma_j + 0.001} < -0.13.$$

The proof of Lemma 5 is a numerical verification of a finite number of cases, as we shall sketch now. Consider $K = J_j B$. Then, for $n \geq n_j$,

$$P_{K,n}(\tau) = P_{J_j, n_j}(\tau) + \sum_{i=n_j+1}^n \zeta_i \tau^i,$$

Table 1

	Limiting sequences	Values of τ_K for limiting sequence
$J_1 = RLR^8$	RLR^∞	$\sigma_0 = 1/\sqrt{2}$
$J_2 = RLR^6L$	$(RLR^8L)^\infty$	$\sigma_1 \sim 0.6938106281$
	$(RLR^6C)'$	
$J_3 = RLR^4L$	$(RLR^4C)'$	$\sigma_2 \sim 0.6823278038$
	$(RLR^2C)'$	
$J_4 = RLR^2L$	$(RLC)^\infty$	$\sigma_4 = 2/(\sqrt{5+1}) \sim 0.6180339887$
	$(RLLRLLR)^\infty$	
$J_5 = RLLRLLR$	$(RLLRLLR)^\infty$	$\sigma_5 = \sigma_4$
	$(RLLRC)^\infty$	
$J_6 = RLLRR$	$(RLLRC)^\infty$	$\sigma_6 \sim 0.580691832$
	$(RLLC)^\infty$	
$J_7 = RLLRLL$	$(RLLC)^\infty$	$\sigma_7 \sim 0.5436890127$
	RL^∞	
$J_8 = RLLL$	RL^∞	$\sigma_8 = 1/2.$

with $\zeta_i = \pm 1$. We bound the derivative of $P_{K,n}(\tau)$ by

$$-\partial_\tau P_{K,n}(\tau) > -\partial_\tau P_{J_j,n_j}(\tau) - \sum_{i=n_j+1}^n i|\tau|^{i-1}. \tag{2}$$

The first term on the right hand side of (2) is bounded explicitly, and the second analytically. Putting in the corresponding choices of J_j , and σ_j yields the result. (It seems that any subdivision which is coarser than the one in Table 1 does not lead to a strictly negative bound for the derivative.)

We need one more general result about kneading sequences for the proof of Theorem 3.

Lemma 6. [5]. (i) Let K be a kneading sequence. Then the smallest root τ_K in modulus of P_K is real, positive and less than or equal to 1.

(ii) If $K = J_j B$ with J_j from Table 1, then $\tau_K \in [\sigma_{j-1}, \sigma_j]$.

(This latter statement follows also from Lemma 2.)

Remark. At first sight one could think of applying the lemma directly to the $P_{K,n}$. The following example shows that this is not possible. Consider a kneading sequence $K = RLR^2L\dots$, and try to show that the root with smallest modulus of $P_{K,5}$, say $\tau_{K,5}$ is positive. One could be tempted to consider $K' = (RLR^2LC)^\infty$, and then $P_{K'}$ has a smallest root $\tau_{K'} = \tau_{K,5}$, as is easily seen. Although $P_{K'}$ has the same smallest positive root as $P_{K,5}$, we cannot apply Lemma 6 because K' is not a kneading sequence: No map f can have $K(f) = K'$.

Proof of Theorem 3. Suppose $K = J_j B$.

We use the notation $G_n(\tau) = P_{K,n}(\tau)$. By definition,

$$G_n(\tau) = P_K(\tau) + (P_{K,n}(\tau) - P_K(\tau)) = P_K(\tau) + \sum_{j=n+1}^{\infty} \zeta_j \tau^j, \tag{3}$$

with $\zeta_j = \pm 1$. Since $P_{\mathbf{K}}(\tau_{\mathbf{K}}) = 0$ and $\tau_{\mathbf{K}} < 2^{-1/2}$ by Lemma 6, we find

$$|G_n(\tau_{\mathbf{K}})| \leq \sum_{k=n+1}^{\infty} \tau_{\mathbf{K}}^k \leq 2^{-(n+1)/2} / (1 - 2^{-1/2}). \quad (4)$$

On the other hand, by Lemma 5

$$|G'_n(\tau)| > 0.13 \quad (5)$$

for all $\tau \in [-\frac{1}{2}, \sigma_j + 0.001]$. These two estimates imply that $G_n(\tau)$ has a unique zero in $[-\frac{1}{2}, \sigma_j + 0.001]$, provided we choose n so large that

$$|G_n(\tau_{\mathbf{K}})| < 0.0076 < 0.001/0.13,$$

($n \geq 18$ is sufficient). This proves Theorem 3 (i). We also find, combining (4) and (5)

$$|\tau_{\mathbf{K}} - \tau_{\mathbf{K},n}| < 2^{-n/2} 2^{-1/2} / ((1 - 2^{-1/2}) \cdot 0.13) < 18.6 \cdot 2^{-n/2}.$$

Proof of Corollary 4. The point (i) follows by inspection of the definition of R^* . Now point (ii) is an obvious consequence of the fact that if $\mathbf{K} = R^{*m} \mathbf{K}'$ with $\mathbf{K}' \geq RLR^\infty$, then only every 2^m -th digit of \mathbf{K} effectively contributes to \mathbf{K}' . But $h_{\text{top}}(\mathbf{K}) = \frac{1}{2^m} h_{\text{top}}(\mathbf{K}')$. The result follows, by reduction to the case $\mathbf{K}' \geq RLR^\infty$ using $P_{\mathbf{K}}(\tau) = P_{\mathbf{K}'}(\tau)Q(\tau)$, where all zeros of Q lie on the unit circle. Q.E.D.

Acknowledgement. Our collaboration took place in the stimulating environment of the Les Houches Summer-School. This work was supported by the Swiss National Science Foundation and National Science Foundation Grant 443150-21299.

References

1. Collet, P., Eckmann, J.-P.: Iterated maps on the interval as dynamical systems. Boston: Birkhäuser 1980
2. Crutchfield, J.P., Farmer, J.D., Huberman, B.A.: Fluctuations and simple chaotic dynamics. Physics Reports (to appear)
Crutchfield, J.P., Huberman, B.A.: Fluctuations and the onset of chaos. Phys. Lett. 77 A, 407 (1980)
3. Dieudonné, J.: Foundations of modern analysis. New York, London: Academic Press 1969
4. Mayer-Kress, G., Haken, M.: The influence of noise on the logistic equation. J. Stat. Phys. 26, 149 (1981)
5. Milnor, J., Thurston, W.: On iterated maps of the interval. I, II. Preprint Institute for Advanced Studies, Princeton University (1977)
6. Crutchfield, J.P., Shaw, R.: Unpublished

Communicated by O. E. Lanford

Received September 2, 1982

CHAPTER 6

Noisy Chaos

6.1. External Fluctuations

The physical basis of chaotic behavior lies in appreciating how external fluctuations affect it. This includes studies of how external noise enhances or destroys unpredictability for periodic or chaotic attractors and also how fluctuations alter bifurcation sequences of attractors.

Several bifurcation sequences leading to chaos display a high degree of scaling structure as a function of control parameter. The most widely studied of these is period-doubling bifurcation sequences. More recently the "phase-locking" or quasi-periodic bifurcation sequence has been shown to have scaling structure. In these cases, the effects of fluctuations can be described quite thoroughly using an extension of the deterministic scaling theory. The general analysis of these sequences and the effects of fluctuations upon them closely follows critical phenomena theory. The onset of chaos is considered a phase transition controlled by appropriate scaling variables (control parameters) and described by "disorder" parameters.

The three papers in this chapter summarize the original work on how fluctuations affect period-doubling sequences. The first letter introduces the notion of a "bifurcation gap" induced by added noise in the

sequence. This was observed in an experimental study of a nonlinear electronic oscillator and in numerical simulations of the logistic and other one-dimensional maps. The scaling behavior as a function of noise level is discussed briefly. The second paper details a complete scaling theory for the bifurcation gap. The final paper describes in detail, and in a review format, the work that went into the original, short letter. The reader looking for an introduction to period-doubling, one-dimensional maps, Lyapunov exponents, or the effects of fluctuations, should start with this review article.

6.2. Fluctuations and the Onset of Chaos

FLUCTUATIONS AND THE ONSET OF CHAOS

J.P. CRUTCHFIELD¹ and B.A. HUBERMAN*Xerox Palo Alto Research Center, Palo Alto, CA 94304, USA*

Received 3 April 1980

We consider the role of fluctuations on the onset and characteristics of chaotic behavior associated with period doubling subharmonic bifurcations. By studying the problem of forced dissipative motion of an anharmonic oscillator we show that the effect of noise is to produce a bifurcation gap in the set of available states. We discuss the possible experimental observation of this gap in many systems which display turbulent behavior.

It has been recently shown that the deterministic motion of a particle in a one-dimensional anharmonic potential, in the presence of damping and a periodic driving force, can become chaotic [1]. This behavior, which appears after an infinite sequence of subharmonic bifurcations as the driving frequency is lowered, is characterized by the existence of a strange attractor in phase space and broad band noise in the power spectral density. Furthermore, it was predicted that under suitable conditions such turbulent behavior may be found in strongly anharmonic solids [2]. Since condensed matter is characterized by many-body interactions, one may ask about the effects that random fluctuating forces have on both the nature of the chaotic regime and the sequence of states that lead to it. This problem is also of relevance to the behavior of stressed fluids, where it has been suggested that strange attractors play an essential role in the onset of the turbulent regime [3]. Although there are experimental results supporting this conjecture [4-6], other investigations have emphasized the possible role of thermodynamic fluctuations directly determining the chaotic behavior [7].

With these questions in mind, we study the role of fluctuations on the onset and characteristics of chaotic behavior associated with period doubling subharmonic bifurcations. We do so by solving the problem of

forced dissipative motion in an anharmonic potential with the aid of an analog computer and a white-noise generator. As we show, although the structure of the strange attractor is very stable even under the influence of large fluctuating forces, their effect on the set of available states is to produce a symmetric gap in the deterministic bifurcation sequence. The magnitude of this bifurcation gap is shown to increase with noise level. By keeping the driving frequency fixed we are also able to determine that increasing the random fluctuations induces further bifurcations, thereby lowering the threshold value for the onset of chaos. Finally, the universality of these results is tested by observing the effect of random errors on a one-dimensional map, and suggestions are made concerning the possible role of temperature in experiments that study the onset of turbulence.

Consider a particle of mass m , moving in a one-dimensional potential $V = a\eta^2/2 - b\eta^4/4$, with η the displacement from equilibrium and a and b positive constants. If the particle is acted upon by a periodic force of frequency ω_d and amplitude F , and a fluctuating force $f(t)$, with its coupling to all other degrees of freedom represented by a damping coefficient γ , its equation of motion in dimensionless units reads

$$\frac{d^2\psi}{dt^2} + \alpha \frac{d\psi}{dt} + \psi - 4\psi^3 = \Gamma \cos\left(\frac{\omega_d}{\omega_0}t\right) + f(t) \quad (1)$$

with $\psi = \eta/2\eta_0$, the particle displacement normalized to the distance between maxima in the potential (η_0

¹ Permanent address: Physics Department, University of California, Santa Cruz, CA 95064, USA.

$= (a/b)^{1/2}$, $\alpha = \gamma/(ma)^{1/2}$, $\Gamma = Fb^{1/2}/2a^{3/2}$, $\omega_0 = (a/m)^{1/2}$ and $f(t)$ a random fluctuating force such that

$$\langle f(t) \rangle = 0 \quad (2a)$$

and

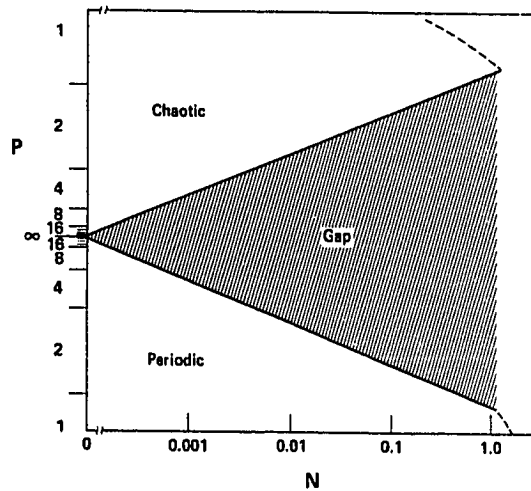
$$\langle f(0)f(t) \rangle = 2A\delta(t) \quad (2b)$$

with A a constant proportional to the noise temperature of the system.

The range of solutions of eq. (1), in the case where $f(t) = 0$ (the deterministic limit) has been investigated earlier [1]. For values of Γ and ω_d such that the particle can go over the potential maxima, as the driving frequency is lowered, a set of bifurcations takes place in which orbits in phase space acquire periods of 2^n times the driving period, T_d . At a threshold frequency ω_{th} , a chaotic regime sets in, characterized by a strange attractor with "periodic" bands. Within this chaotic regime, as the frequency is decreased even further, another set of bifurcations takes place whereby 2^m bands of the attractor successively merge in a mirror sequence of the 2^n periodic sequence that one finds for $\omega \rightarrow \omega_{th}^+$. The final chaotic state corresponds to a single band strange attractor, beyond which there occurs an irreversible jump into a periodic regime of lower amplitude.

In order to study the effects of random fluctuations on the solutions we have just described, we solved eq. (1) using an analog computer in conjunction with a white-noise generator having a constant power spectral density over a dynamical range two orders of magnitude larger than that of the computer. Time series and power spectral densities were then obtained for different values of Γ , A and ω_d . While we found that the folding structure of the strange attractor is very stable under the effect of random forces, the bifurcation sequence that is obtained in the presence of noise differs from the one encountered in the deterministic limit.

Our results can be best summarized in the phase diagram of fig. 1, where we plot the observed set of bifurcations (or limiting set) as a function of the noise level, N , normalized to the rms amplitude of the driving term, Γ . The vertical axis denotes the possible states of the system, labeled by their periodicity $P = 2^n$, which is defined as the observed period normalized to the driving period, T_d . As can be seen, with increasing noise level a symmetric bifurcation gap appears, deplet-



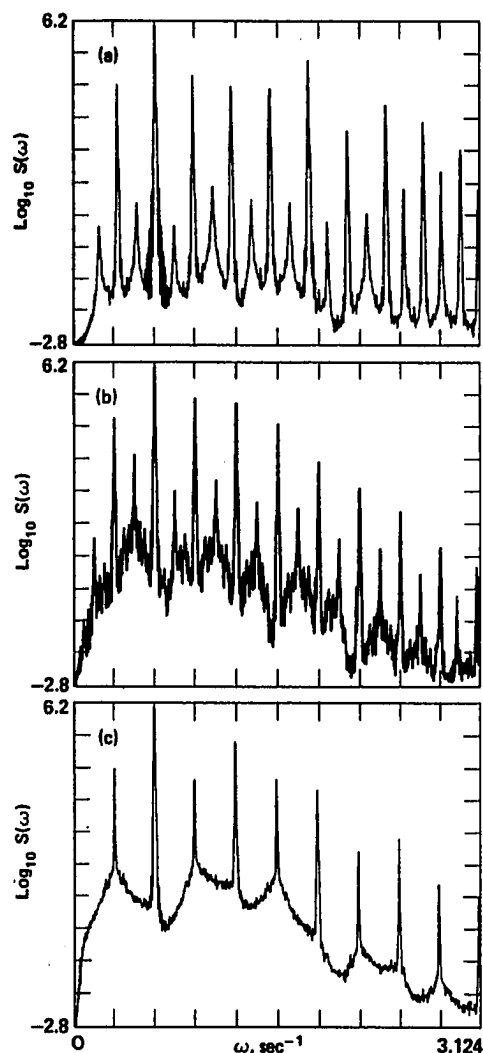


Fig. 2. Power spectral densities at increasing values of the effective noise temperature, for $\Gamma = 0.1175$, $\alpha = 0.4$, and $\omega_d = 0.6339 \omega_0$. Fig. 2(a): $N = 10^{-4}$. Fig. 2(b): $N = 0.005$. Fig. 2(c): $N = 0.357$.

chaotic state with $P = 2$ emerges. Physically, this sequence reflects the fact that a larger effective noise temperature (and hence a larger fluctuating force) makes the particle gain enough energy so as to sample increasing nonlinearities of the potential, with a resulting motion which in the absence of noise could only occur for longer driving periods ^{#2}.

^{#2} In the regime of subharmonic bifurcation the dependence of response amplitude on driving frequency is almost linear.

A different set of states appears if the noise level is kept fixed while changing the driving frequency. In this case the observed states of the system correspond to vertical transitions in the phase diagram of fig. 1, with the threshold value of the driving period, T_{th}^n , at which one can no longer observe periodicities $P \geq 2^n$, behaving like

$$T_{th}^n = T_{th}^\infty (1 - N_n^\gamma) \quad (3)$$

for $0 \leq N_n \leq 1$, with N_n the corresponding noise level, T_{th}^∞ the value of the driving period for which the deterministic equation undergoes a transition into the chaotic state, and γ a constant which we determined to be $\gamma \approx 1$ for $P \geq 2^{\pm 3}$.

In order to test the universality of the bifurcation gap we have just described, we have also studied the bifurcation structure of the one-dimensional map described by

$$x_{L+1} = \lambda x_L (1 - x_L) + n_L (0, \sigma^2) \quad (4)$$

where $0 \leq x_L \leq 1$, $0 \leq \lambda \leq 4$, and n_L is a gaussian random number of zero mean and standard deviation σ . For $n_L = 0$, eq. (4) displays a set of 2^n periodic states universal to all single hump maps [8-9], with a chaotic regime characterized by 2^m bands that merge pairwise with increasing λ [10]. For $n_L \neq 0$ and a given value of σ , the effect of random errors on the stability of the limiting set is to produce a bifurcation gap analogous to the one shown in fig. 1.

The above results are of relevance to experimental studies of turbulence in condensed matter, for they show that temperature plays an important role in the observed behavior of systems belonging to this same universality class. In particular, Belyaev et al. [11], Libchaber and Maurer [12] and Gollub et al. [13] have reported that under certain conditions the transition to turbulence is preceded and followed by different finite sets of 2^n subharmonic bifurcations. It would therefore be interesting to see if temperature changes or external sources of noise in the fluids can either reduce or increase the set of observed frequencies, thus providing for a test of these ideas. In the case of solids such as superionic conductors, the expo-

^{#3} Using the scaling relation $(T_{th} - T_n)/(T_{th} - T_{n+1}) = \delta$ [1] this implies that the threshold noise level scales like $N_n/N_{n+1} = \delta$, with $\delta = 4.669201609 \dots$.

nential dependence on temperature of their large diffusion coefficients might provide for an easily tunable system with which to study the existence of bifurcation gaps. Last, but not least, these studies can serve as useful calibrations on the relative noise temperature of digital and analog simulations.

In concluding we would like to emphasize the wide applicability of the effects that we have reported. Beyond the experimental studies of turbulence, there exist other systems which belong to the same universality class as the anharmonic oscillator and one-dimensional maps. These systems range from the ordinary differential equations studied by Lorenz [10], Robbins [14], and Rossler [15] to partial differential equations describing chemical instabilities [16]. Since period doubling subharmonic bifurcation is a universal feature of all these models, our results provide a quantitative measure of the effect of noise on their non-linear solutions.

The authors wish to thank D. Farmer, N. Packard, and R. Shaw for helpful discussions and the use of their simulation system.

References

- [1] B.A. Huberman and J.P. Crutchfield, *Phys. Rev. Lett.* **43** (1979) 1743.
- [2] See also, C. Herring and B.A. Huberman, *Appl. Phys. Lett.* **36** (1980) 976.
- [3] See, D. Ruelle, in *Lecture notes in physics*, eds. G. Dell'Antonio, S. Doplicher and G. Jona-Lasinio (Springer-Verlag, New York, 1978), Vol. 80, p. 341.
- [4] G. Ahlers, *Phys. Rev. Lett.* **33** (1975) 1185; G. Ahlers and R.P. Behringer, *Prog. Theor. Phys. (Japan) Suppl.* **64** (1978) 186.
- [5] J.P. Gollub and H.L. Swinney, *Phys. Rev. Lett.* **35** (1975) 927; P.R. Fenstermacher, H.L. Swinney, S.V. Benson and J.P. Gollub, in: *Bifurcation theory in scientific disciplines*, eds. D.G. Gorel and D.E. Rossler (New York Academy of Sciences, 1978).
- [6] A. Libchaber and J. Maurer, *J. Physique Lett.* **39** (1978) L-369.
- [7] G. Ahlers and R.W. Walden, preprint (1980).
- [8] T. Li and J. Yorke, in: *Dynamical systems, an International Symposium*, ed. L. Cesari (Academic Press, New York, 1972), Vol. 2, 203.
- [9] M. Feigenbaum, *J. Stat. Phys.* **19** (1978) 25.
- [10] E.N. Lorenz, preprint (1980).
- [11] Yu.N. Belyaev, A.A. Monakhov, S.A. Scherbakov and I.M. Yavorshaya, *JETP Lett.* **29** (1979) 295.
- [12] A. Libchaber and J. Maurer, preprint (1979).
- [13] J.P. Gollub, S.V. Benson and J. Steinman, preprint (1980).
- [14] K.A. Robbins, *SIAM J. Appl. Math.* **36** (1979) 451.
- [15] O.E. Rossler, *Phys. Lett.* **57A** (1976) 397; J.P. Crutchfield, D. Farmer, N. Packard, R. Shaw, G. Jones and R.J. Donnelly, to appear in *Phys. Lett.*
- [16] Y. Kuramoto, preprint (1980).

6.3. Scaling for External Noise at the Onset of Chaos

Scaling for External Noise at the Onset of Chaos

J. Crutchfield, M. Nauenberg, and J. Rudnick

Physics Department, University of California, Santa Cruz, California 95064

(Received 8 December 1980)

The effect of external noise on the transition to chaos for maps of the interval which exhibit period-doubling bifurcations are considered. It is shown that the Liapunov characteristic exponent satisfies scaling in the vicinity of the transition. The critical exponent for noise is calculated with the use of Feigenbaum's renormalization group approach, and the scaling function for the Liapunov characteristic exponent is obtained numerically by iterating a map with additive noise.

PACS numbers: 64.60.Fr, 02.90.+p, 47.25.Mr

The notion that the transition to turbulence in fluids has universality properties similar to those of critical phenomena has been suggested by Feigenbaum¹ on the basis of the scaling behavior of mathematical models near the onset of chaos.² A further impetus for an analogy between the transition to chaos and critical point phase transitions was given³ by the observation that as a control parameter r in these models increases past a critical value r_c into the chaotic regime the measure-theoretic entropy—the Liapunov characteristic exponent $\bar{\lambda}$ —has an envelope curve of the form $(r - r_c)^\tau$. The universal exponent τ is given by $\tau = \ln 2 / \ln \delta = 0.449\ 806\ 9\dots$, where δ is the maximum eigenvalue associated with perturbations about the invariant map¹ of the interval. The transition to chaos in these models is heralded by a cascade of period-doubling bifurcations,² which is also of interest to an understanding of the onset of turbulence in physical systems.⁴

Motivated by the interpretation of experiments in fluids⁵ and solids and by some recent numerical calculations,^{6,7} we have considered theoretically the effect of added external noise on the transition to chaos in maps of the interval. The main result to be reported here is that the noise amplitude behaves as a *scaling variable* and that the dependence of the Liapunov characteristic exponent $\bar{\lambda}$ on the noise amplitude σ and $\bar{\tau} = (r - r_c) / r_c$ is of the scaling form

$$\bar{\lambda}(r, \sigma) = \sigma^\theta L(\bar{\tau} / \sigma^\gamma) \quad (1)$$

with $L(y)$ a universal function, and θ and γ universal exponents. In the limit of vanishing noise $\sigma \rightarrow 0$ we have $\bar{\lambda} \propto \bar{\tau}^\tau$ which implies that as $y \rightarrow \infty$, $L(y) \propto y^\tau$, and leads to the exponent relation $\theta = \gamma\tau$.

The idea that the noise plays a role parallel to

that of the ordering field in a ferromagnetic transition was conjectured previously in Ref. 7. The noise exponent θ is a new critical exponent which we evaluate from an extension of Feigenbaum's scaling theory. Our result agrees with the recently observed value⁷ of θ to within the limits of accuracy of the measurement. We also report on the measured form of the scaling function $L(y)$.

We start out by specifying the form of the one-dimensional map with additive noise. It is defined by the stochastic recursion relation

$$x_{\kappa+1} = f(x_\kappa; r) + \xi_\kappa \sigma \quad (2)$$

with $f(x; r)$ a continuous function of x in a finite interval having a parabolic maximum, and r a parameter that controls the shape of the function.² A common example is the function $r x(1-x)$ with $0 \leq r \leq 4$, and $0 \leq x \leq 1$. The quantity ξ_κ is a random variable controlled by an even distribution of unit width, and σ is a variable that controls the width (or amplitude) of the noise. Note that when $\sigma = 0$ the map is perfectly deterministic.

We consider successive iterations of the stochastic map, Eq. (2) with r at the critical value r_c , following techniques introduced by Feigenbaum. Setting the origin of coordinates to the x for which the function $f(x; r)$ is a maximum and rescaling this maximum to 1, the 2^n th iterate of $f(x; r_c)$ converges to $(-\alpha)^n g(\alpha^n x)$, where $g(x)$ is a universal map satisfying the equation

$$g(g(x)) = -\alpha^{-1} g(\alpha x) \quad (3)$$

with $\alpha = -1/g(1)$. Adding a small amount of noise $\xi\sigma$, we assume that the corresponding 2^n th iterate of the map converges to $(-\alpha)^n [g(\alpha^n x) + \xi\sigma\kappa^n D(\alpha^n x)]$ with $D(x)$ a universal x -dependent noise amplitude function and κ a constant. When σ is small enough, we have

$$\begin{aligned} g(g(x) + \xi\sigma D(x)) + \xi'\sigma D(g(x) + \xi\sigma D(x)) &= g(g(x)) + \xi\sigma g'(g(x))D(x) + \xi'\sigma D(g(x)) + O(\sigma^2) \\ &= g(g(x)) + \xi^2\sigma^2 \{ [g'(g(x))D(x)]^2 + [D(g(x))]^2 \}^{1/2}. \end{aligned} \quad (4)$$

In going to the last line we used the fact that ξ and ξ' are independent random variables, and that ξ'' is also a random variable. This and our above assumption implies that $D(x)$ must satisfy the eigenvalue equation

$$KD(\alpha x) = \alpha \{ [g'(g(x))D(x)]^2 + [D(g(x))]^2 \}^{1/2}. \quad (5)$$

We have solved Eq. (5) for the eigenvalue κ and the corresponding eigenfunction $D(x)$ using the known results¹ for α and $g(x)$. Carrying out a calculation involving a polynomial interpolation for $D(x)$ we have found $\kappa = 6.619\,03\dots$

In the immediate vicinity above the transition to chaos the invariant probability distribution associated with the stochastic map will consist of 2^n bands, where n is an integer that grows in the case of the deterministic map by unit steps to infinity as the transition is approached.^{6,9} In the case of the stochastic map, n grows to a finite value—and then decreases by unit steps as one passes to the other side of the transition. This modification of the deterministic bifurcation sequence is called a bifurcation gap.⁶

We now extend to the present case the previous discussion in Ref. 2 of the scaling behavior of the Liapunov characteristic exponent $\bar{\lambda}$, given by

$$\bar{\lambda} = \lim_{N \rightarrow \infty} \frac{1}{N} \sum_{k=1}^N \ln |f'(x_k; \tau)|, \quad (6)$$

or alternatively

$$\bar{\lambda} = \int p(x) \ln |f'(x; \tau)| dx, \quad (7)$$

where $p(x)$ is the invariant probability distribution associated with the map. Applying the above-mentioned considerations we obtain¹⁰

$$\bar{\lambda} = 2^{-n} L(\delta^n \bar{\tau}, \kappa^n \sigma). \quad (8)$$

Now, we assume that there will be 2^n bands in the chaotic regime when $\kappa^n \sigma$ is of order unity so that $n = -\ln \sigma / \ln \kappa$. Substituting this result into Eq. (9) we obtain Eq. (1) for $\bar{\lambda}$ with the two exponents θ and γ given in terms of Feigenbaum's eigenvalue δ and the new eigenvalue κ by $\theta = \ln 2 / \ln \kappa = 0.366\,754\dots$ and $\gamma = \ln \delta / \ln \kappa = 0.815\,359\dots$. The appearance of a bifurcation gap implies that $L(y)$ vanish at some $y = y_0$, which in turn implies that the maximum number n of bifurcations is determined by the relation $\bar{\tau}_{n \text{ max}} = y_0 \sigma^\gamma$. This behavior has been observed numerically.⁶

Measurements of the behavior of $\bar{\lambda}$ as a function of σ at $\bar{\tau} = 0$ have already been made by numerically calculating $\bar{\lambda}$ according to Eq. (6) with varying amounts of noise.⁷ The measured value for θ is 0.37 ± 0.01 . This agrees with our theoretical value for θ to within the experimental error.

To verify the existence of the scaling function $L(y)$ of Eq. (1) we used our values of θ and γ to plot $\bar{\lambda} \sigma^{-\theta}$, with $\bar{\lambda}$ the result of numerical calculations of Eq. (6), as a function of $\bar{\tau} \sigma^{-\gamma}$. The results are shown in Figs. 1 and 2 for three different noise levels: $\sigma = 10^{-6}$, 10^{-8} , and 10^{-10} . The results for those three different noise levels all fall on a universal curve in the chaotic regime,

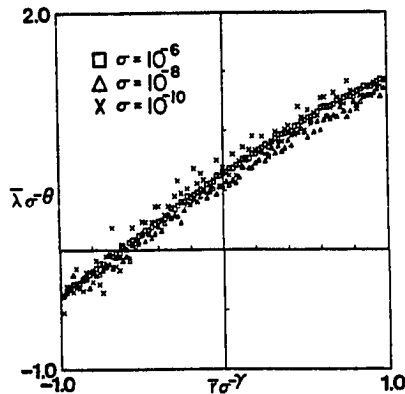


FIG. 1. Numerical determination of the scaling function $L(y)$, Eq. (1). The quantity $\bar{\lambda} \sigma^{-\theta}$ is plotted against 100 values of $y = \bar{\tau} \sigma^{-\gamma}$ at each of three noise levels: $\sigma = 10^{-6}$, 10^{-8} , and 10^{-10} . $\bar{\lambda}$ was calculated with use of Eq. (6), with $N = 10^6$ and with ξ_κ a uniformly distributed random number of standard deviation σ .

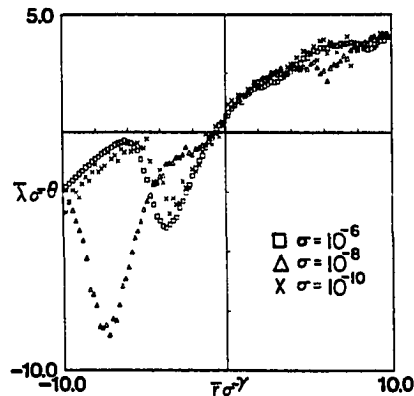


FIG. 2. $\bar{\lambda} \sigma^{-\theta}$ is plotted again, but over a wider range of $y = \bar{\tau} \sigma^{-\gamma}$ to illustrate the scaling regime. See text for discussion of various features. The details are the same as in Fig. 1, except that $\bar{\lambda}$ was calculated with $N = 10^5$ in Eq. (6).

and in its immediate vicinity, Fig. 1, and fit the asymptotic behavior $L(y) \sim y^\tau$ for large y . The results do *not* coincide in the periodic regime, Fig. 2, but they could have been made to agree if we had chosen noise amplitudes differing by factors of κ , instead of factors of 100. This more restricted scaling follows from considerations of the type enunciated above.

These results appear to us to be both exciting and highly provocative. A theoretical picture of the transition to turbulence is just beginning to emerge; the analogy to critical phenomena should lead to new and important insights into the nature and characteristics of this transition.

The authors have benefited from conversations with B. A. Huberman and wish to thank him for the use of computing facilities at Xerox Palo Alto Research Center. One of us (J.C.) would also like to acknowledge useful discussions with N. Packard and the receipt of a University of California Regents Fellowship. This work is supported by the National Science Foundation.

¹M. J. Feigenbaum, *J. Statist. Phys.* **19**, 25 (1978).

²For a recent monograph on this subject, see P. Collet and J. P. Eckmann, *Iterated Maps of the Interval as Dynamical Systems* (Birkhäuser, Boston, 1980).

³B. A. Huberman and J. Rudnick, *Phys. Rev. Lett.* **45**, 154 (1980). The exponent τ appears as t in this reference. We have replaced the latin by a greek letter for consistency with other critical exponents.

⁴A. Libchaber and J. Maurer, *J. Phys. (Paris)*, Colloq. **41**, C3-51 (1980); M. J. Feigenbaum, *Phys. Lett.* **74A**, 375 (1979); J. P. Gollub, S. V. Benson, and J. Steinman, *Ann. N.Y. Acad. Sci.* (to be published); B. A. Huberman and J. P. Crutchfield, *Phys. Rev. Lett.* **43**, 1743 (1979).

⁵G. Ahlers, private communication.

⁶J. P. Crutchfield and B. A. Huberman, *Phys. Lett.* **77A**, 407 (1980).

⁷J. P. Crutchfield, J. D. Farmer, and B. A. Huberman, to be published.

⁸J. P. Crutchfield, J. D. Farmer, N. Packard, R. Shaw, G. Jones, and R. J. Donnelly, *Phys. Lett.* **76A**, 1 (1980).

⁹E. N. Lorentz, *Ann. N.Y. Acad. Sci.* (to be published).

¹⁰The details of the derivation of the result (8), which involves a careful consideration of the structure of the bands, will be presented in a future paper.

6.4. Fluctuations and Simple Chaotic Dynamics

FLUCTUATIONS AND SIMPLE CHAOTIC DYNAMICS

J.P. CRUTCHFIELD and J.D. FARMER

Physics Board of Studies, University of California, Santa Cruz, California 95064, U.S.A.

and

B.A. HUBERMAN

Xerox Palo Alto Research Center, Palo Alto, California 94304, U.S.A.



NORTH-HOLLAND PUBLISHING COMPANY - AMSTERDAM

FLUCTUATIONS AND SIMPLE CHAOTIC DYNAMICS**J.P. CRUTCHFIELD and J.D. FARMER****Physics Board of Studies, University of California, Santa Cruz, California 95064, U.S.A.*

and

B.A. HUBERMAN*Xerox Palo Alto Research Center, Palo Alto, California 94304, U.S.A.*

Received July 1982

Contents:

1. Introduction	47	Appendix A. Fluctuations in a driven anharmonic oscillator	76
2. Dynamics in the absence of fluctuations	48	Appendix B. Characteristic exponents in period-doubling regimes	77
3. Dynamics in the presence of fluctuations	57	Appendix C. Equivalence of parametric and additive noise	80
4. Noise as a disordering field	68	References	81
5. Concluding remarks	74		

Abstract:

We describe the effects of fluctuations on the period-doubling bifurcation to chaos. We study the dynamics of maps of the interval in the absence of noise and numerically verify the scaling behavior of the Lyapunov characteristic exponent near the transition to chaos. As previously shown, fluctuations produce a gap in the period-doubling bifurcation sequence. We show that this implies a scaling behavior for the chaotic threshold and determine the associated critical exponent. By considering fluctuations as a disordering field on the deterministic dynamics, we obtain scaling relations between various critical exponents relating the effect of noise on the Lyapunov characteristic exponent. A rule is developed to explain the effects of additive noise at fixed parameter value from the deterministic dynamics at nearby parameter values.

* Present address: Center for Nonlinear Studies, MS B 258, Los Alamos Laboratories, Los Alamos, New Mexico 87545, U.S.A.

Single orders for this issue

PHYSICS REPORTS (Review Section of Physics Letters) 92, No. 2 (1982) 45-82.

Copies of this issue may be obtained at the price given below. All orders should be sent directly to the Publisher. Orders must be accompanied by check.

Single issue price Dfl. 20.00, postage included.

1. Introduction

Chaotic dynamical systems provide a significant new addition to the conventional dynamical repertoire of equilibrium and periodic oscillation. Central to their usefulness in describing observed random behavior is the issue of their stability and the observability of their bifurcation sequences in the presence of noise sources. In particular, given the fact that fluctuations are an important aspect of many-body systems, one would like to understand the role of fluctuations vis à vis the chaotic behavior generated by deterministic nonlinear dynamics.

Recently we have shown [1] that for a certain class of processes the effect of external fluctuations on the onset and properties of chaos can be described in fairly simple fashion. For systems displaying period-doubling bifurcations we found that the presence of noise leads to both a gap in the bifurcation sequence and a renormalization of the chaotic threshold. Furthermore, we noticed that for fixed parameter values the addition of noise to a nonlinear deterministic equation produces additional bifurcations,† which can be observed in measurable properties such as power spectra. These effects are of importance to current attempts at understanding turbulent behavior of fluids and solids in terms of chaotic, deterministic models.

In this paper we discuss in detail the effects of fluctuations on the cascade bifurcation to chaos. By the cascade bifurcation we shall mean not only the infinite sequence of subharmonic bifurcations, at each stage of which the period of a limit cycle is doubled, but also the symmetric bifurcation sequence above the chaotic threshold, in which n bands of a chaotic attractor merge pairwise to form an $n/2$ -band attractor. Ample illustration of the cascade bifurcation follows in the next section.

Previous work discussed the effect of external fluctuations on the cascade bifurcation found in a driven nonlinear oscillator [1]. That study was motivated in part by the fact that in condensed matter systems thermal fluctuations play an important role which had to be incorporated into the nonlinear equations leading to solid-state turbulence [2]. More generally, though, the cascade bifurcation sequence and its alteration in the presence of fluctuations is of interest in systems that range from fluid flows [3, 4] to noise phenomena in solid-state systems [5]. Moreover, this bifurcation sequence is found in numerical studies of a wide range of mathematical models, including nonlinear ordinary [6, 7] and partial [8] differential equations. In the experimental observation of bifurcation sequences in Bénard flow [3] and spherical Couette flow [4] one observes only a finite number (<4) of bifurcations in the cascade sequence, whereas the scaling theory developed by Feigenbaum [9] and Collet and Eckmann [10] for the period-doubling half of the cascade requires that the dynamics undergo an infinite number of bifurcations before the transition to chaos. Indeed, it is in just this limit of infinite bifurcation that the scaling theory becomes exact. As previously suggested [1], this discrepancy can be explained by the interaction of external fluctuations and the deterministic sequence of bifurcations.

From a study of the geometry of the attractors found in the driven anharmonic oscillator [1], we found that increased noise levels could induce a transition to chaotic behavior. Furthermore, rather than destabilizing or eradicating chaotic motions in the phase space, noise enhanced the chaotic behavior, while destroying periodic orbits. That is, the local instabilities responsible for the deterministic chaotic behavior actually increased the observability of chaos in the presence of fluctuations. Using Feigenbaum's scaling theory and the existence of the bifurcation gap, we derived a scaling relationship for the noise dependence of observable bifurcations in a cascade. These features were also found in a one-dimensional map typical of those for which the universal scaling theory was developed [1].

The present paper reports in more detail the results of our study of one-dimensional maps, that is, of

† We employ a broader definition of bifurcation than is typical: an observable, qualitative change in a system's behavior as a control parameter is slowly varied.

nonlinear transformations of the unit interval onto itself. The main results of our paper can be summarized as follows. In the absence of noise, we verify numerically the scaling predictions of Huberman and Rudnick for the behavior of the Lyapunov characteristic exponent λ and discuss several other features of λ found in the cascade bifurcation. The Lyapunov characteristic exponent can be thought of as a disorder parameter for chaos [11]. We show that the existence of a bifurcation gap implies a scaling behavior for the chaotic threshold and determine the associated exponent. By realizing that fluctuations act as a disordering field on the deterministic dynamics, we obtain a scaling relation between various critical exponents relating the effect of noise on λ , and develop the notion of a noise susceptibility. We also show that even in the periodic regime there is a non-trivial effect of external fluctuations on the period-doubling bifurcations. This is reflected in the fact that not only higher periods become obliterated by increasing noise, but the bifurcation points themselves become blurred. In particular, at the points of bifurcation, λ no longer vanishes as it does in the deterministic limit.

In section 2 we review the dynamics of maps of the interval in the absence of noise. We present a typical map which displays the cascade bifurcation and analyze it in detail. We summarize the scaling theory of bifurcations and discuss the Lyapunov characteristic exponent as a measure of the stability of the asymptotic behavior. Section 3 considers the effects of noise on the cascade bifurcation sequence and the onset of chaos. A rule is developed that allows the effect of noise at a fixed parameter value to be predicted from the knowledge of the purely deterministic dynamics at adjacent parameter values. In section 4 we discuss the role of noise as a disordering field and the scaling behavior of the noise critical exponents. Section 5 contains a summary of the scaling ideas and discusses the applicability of these ideas to physical systems. We then mention other questions related to the interaction of chaotic dynamics, external fluctuations, and observational noise. A set of appendices discusses details of the effect of fluctuations on a driven anharmonic oscillator, the scaling of the characteristic exponent within the period-doubling regime, and the noise equivalence rule of section 3.

2. Dynamics in the absence of fluctuations

Dynamical systems theory [12] describes the time evolution of a system as a trajectory, or an orbit, in a phase space of the system's possible states. Typically, the physically interesting behavior of a system is that which is observed after initial transients have died away. The set of states which an orbit eventually visits is called the system's attractor. The study of dynamical systems considers not only the structure of attractors but also the qualitative change, or bifurcation, from one type to another as some parameter is smoothly varied.

Since the first physically-motivated study of chaotic dynamics by Lorenz [13], one-dimensional (1D) maps have played a fundamental role in the field's development despite their apparent simplicity. The 1D map obtained from a system of ordinary differential equations captures the essential geometry underlying the chaotic dynamics. Although such a reduction of dimension (from three to one, in Lorenz's case) cannot be uniformly applied to all dynamical systems, for many problems the technique provides more than sufficient heuristic insight into the processes responsible for chaotic behavior. Specifically, by identifying all the points which asymptotically merge, that is, all the points on the same stable manifold, it is possible to summarize many of the properties of a simple chaotic attractor in three dimensions by a 1D map.

For dissipative systems with a chaotic attractor that appears locally two-dimensional, a cross section through the attractor intersects it in some curve. One can then consider the dynamics as a map from this cross section onto itself; this map is called the Poincaré map. By parametrizing points on the curve of

intersection (from 0 to 1) and collecting a set of successive points $\{x_1, x_2, x_3, \dots\}$ as an orbit passes through the section, the dynamics of the attractor can be summarized in a one-dimensional map of the form

$$x_{n+1} = f(x_n), \quad n = 1, 2, 3, \dots, \quad (2-1)$$

where x_n is the n th crossing of the orbit through the section and where f is a nonlinear function on the unit interval. In this sense, discrete time maps summarize the dynamics underlying chaotic behavior found in higher dimensional systems. From their simplicity, 1D maps have developed as prototypical models in the study of chaotic dynamics [14].

For dissipative dynamical systems, such as discrete mappings and ordinary and partial differential equations, that exhibit cascading bifurcations, the dynamics can be described in practice by a 1D map with a single smooth maximum. An example of such maps is provided by the logistic equation, which is defined by

$$x_{n+1} = rx_n(1 - x_n), \quad 0 < x_n < 1, \quad (2-2)$$

and where the bifurcation parameter r ($0 < r < 4$) determines the height of the quadratic function $f(x) = x(1 - x)$. As a graphic example of the complexity present in this class of maps, the bifurcation diagram of fig. 1 presents the change in the attractor of eq. (2-2) as a function of the bifurcation parameter r in the regime [3, 4].

At a fixed parameter value in the bifurcation diagram, a periodic orbit consists of a countable set of points, while a chaotic attractor fills out dense bands within the unit interval. Figure 2 shows the probability density for the two bands at $r = 3.59687$. The dominant bifurcation sequence seen in fig. 1 is the single 2^n cascade, through which the attractor first becomes chaotic and eventually fills the interval via the pairwise merging of bands. The period-doubling and band merging accumulates at a value

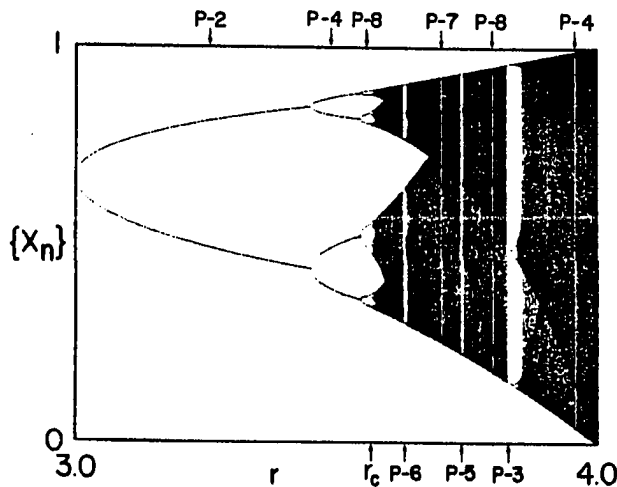


Fig. 1. The attractor versus bifurcation parameter r for the logistic map, eq. (2-2), $x_{n+1} = rx_n(1 - x_n)$. 700 iterations plotted after an initial 500 iterations for each increment in the bifurcation parameter. The parameter was incremented 1000 times in the interval [3, 4]. For the sake of clarity and resolution, only the bifurcation diagram for r in [3, 4] is shown. For r in [0, 1], $x_n = 0$ is the stable behavior; and for r in [1, 3], one has a stable fixed point described by $x = (r - 1)/r$.

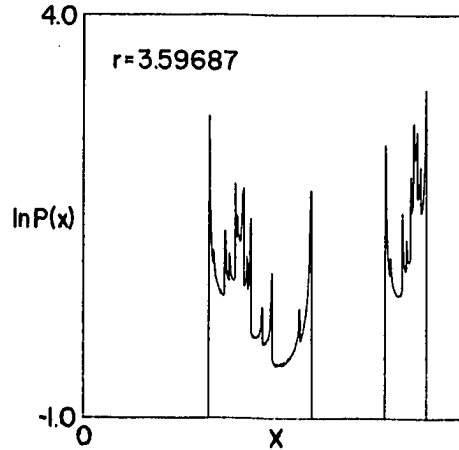


Fig. 2. Normalized probability density $P(x)$ of the two band attractor at $r = 3.59687$ shown on a logarithmic scale. $P(x)$ is a histogram of 10^7 iterations of eq. (2.2) partitioned into 1000 bins. The peaks in $P(x)$ are successive images of the maximum, or critical point, x_c . Note that each band is a mirror image of the other.

$r_c = 3.569945672 \dots$ after an infinite number of bifurcations. In the chaotic regime above r_c , one finds small windows of higher period cascades with periods $q \times 2^n$, with q an integer and where n denotes the degree of the period-doubling of a fundamental periodic orbit of period q . Within each such window, one also finds the associated reverse bifurcation [7] of $q \times 2^{n+1}$ bands merging into $q \times 2^n$ bands. In what follows we will call q the periodicity of the cascade; $q = 1$ for the primary cascade described above [15].

To describe in more detail the structure apparent in fig. 1 we now focus on the successive images of the map's maximum, called the map's critical point x_c , where the slope vanishes. One of the more striking features of the bifurcation diagram above r_c is the veil-like structure highlighted by dark lines which vary smoothly with the parameter. As the attractors in the chaotic regime consist of dense subsets of the interval rather than discrete points, one needs to consider the action of the map on a probability distribution. The dark lines in the diagram correspond, then, to successive images of the critical point and indicate regions of high probability density. These are seen in fig. 2 as spikes in the probability density. To describe their dependence on the bifurcation parameter r , it is useful to write

$$x_{n+1} = F(r, x_n), \quad (2-3)$$

with $F(r, x) = rx(1-x)$ in our example. Then the m th image of the critical point, $x_c = 0.5$, is a polynomial in r , $F^m(r, 0.5)$, where $F^m(r, x) = F(F^{m-1}(r, x))$. For example, above r_c , the first image of x_c defines the upper bound on $\{x_n\}$; it is the straight line

$$F(r, x_c) = r/4, \quad (2-4)$$

seen in fig. 1. Similarly, the second image defines the lower bound on $\{x_n\}$ which is given by

$$F^2(r, x_c) = \frac{r^2}{4} \left(1 - \frac{r}{4}\right). \quad (2-5)$$

Further iterates of the critical point must lie between these two. For example, the third iterate

$$F^3(r, x_c) = \frac{r^3}{4} \left(1 - \frac{r}{4}\right) \left(1 - \frac{r^2}{4} \left(1 - \frac{r}{4}\right)\right) \quad (2-6)$$

is a lower bound on the upper band in the two-band region. Similarly, the fourth iterate $F^4(r, x_c)$ is an upper bound on the lower band in the two band region. The pair of bands merges into one band at a parameter value r_{merge} determined by the intersection of $F^3(r, x_c)$ and $F^4(r, x_c)$, that is, where

$$F^3(r, x_c) = F^4(r, x_c) = F(r, F^3(r, x_c))$$

or (2-7)

$$1 = r(1 - F^3(r, x_c))$$

which gives $r_{\text{merge}} = 3.67857351 \dots$. It is now apparent that each of the dark lines in the chaotic region of the bifurcation diagram corresponds to one of the images of the critical point x_c .

The appearance of stable periodic orbits within the chaotic regime is signalled by the q th iterate of the critical point mapping onto itself; that is,

$$F^{m+q}(r, x_c) = F^m(r, x_c), \quad m = 1, 2, 3, \dots \quad (2-8)$$

As can be seen in the diagram, the labeled q -periodic regimes coincide with the crossing of the q th iterate of the critical point $F^q(r, x_c)$ through $x_c = 0.5$. In fact, the period q orbit becomes stable just before this point which is the point of superstability. The number of windows of a particular periodicity increases with q and each of these windows is generally of different width. Furthermore, the width of these windows decreases rapidly with increasing q [7].

In the chaotic regime, one can see the unstable remnants of the orbits of period 2^n which were stable below r_c . Indeed, once an orbit comes into existence at a given parameter value it does not vanish at higher parameter values, although its stability may change. These remnants are apparent as particularly low values in the probability density within the chaotic bands and emanate from the points at which the bands join. The white streaks corresponding to these unstable orbits are seen most readily when viewing fig. 1 from the side, looking parallel to the r -axis in the direction of decreasing r .

Despite the existence of such detailed structure, the bifurcation diagram exhibits a high degree of self-similarity. By self-similarity we mean the property of objects whose structure, as observed on one length scale, is repeated on successively smaller scales [16]. To describe this, we denote the value of r at a bifurcation by r_{m-n} , where, if $m < n$, a periodic orbit bifurcates from period m to period n and, if $m > n$, m bands merge into n bands. If we consider the bifurcation diagram for r in $[1, 4]$ as the first scale, where the attractor begins just above $r = 1$ as a period 1 orbit and ends at $r = 4.0$ as a single chaotic band, then this structure is repeated twice on a reduced scale within the parameter subinterval $[r_{1-2}, r_{2-1}] = [3, 3.67857 \dots]$, four times in the still smaller regime $[r_{2-4}, r_{4-2}] = [3.44944 \dots, 3.59257 \dots]$ and so on. In this manner, the period 6 regime can be thought of as two copies of the period 3 regime. Thus one need only describe in detail the periodic regimes in $[r_{2-1}, 4] = [3.67857 \dots, 4]$ in order to understand the periodic regimes in $[r_c, r_{2-1}] = [3.56995 \dots, 3.67857 \dots]$. Within this scheme, the period 7 window just below $r = 4.0$ gives rise to a period 14 counterpart just below r_{2-1} . Such self-similarity is also found within each window of higher periodicity.

Feigenbaum [9] has developed a scaling theory for the non-chaotic period-doubling side of the cascade bifurcation in 1D maps which exactly describes this self-similarity in the limit of highly

bifurcated attractors. This theory predicts that the parameters r_n at the bifurcation from a period 2^n to a period 2^{n+1} orbit scale according to

$$(r_c - r_n) \sim \delta^{-n} \quad (2-9)$$

where $\delta = 4.69920\dots$ depends only on the (quadratic) nature of the maximum of the map. It also predicts that the width of bifurcation "forks" in the periodic regime which straddle x_c decreases by a spatial rescaling constant $\alpha = 2.502907876\dots$. Lorenz [7], in turn, has shown that the bifurcation parameters for the band joinings in the chaotic regime also scale in this manner and that the width of the band containing x_c scales by α at band-merging bifurcations. Grossman and Thomae were apparently the first to measure the scaling factor δ for both the period-doubling and band-merging bifurcations [15]. Furthermore, the bifurcation parameters describing the cascades in all of the windows of higher periodicity exhibit this scaling behavior.

In the study of chaotic dynamics it is often useful to have some measure of the degree of randomness generated by the deterministic equations. Several quantities have been developed for this, but we shall only consider those related to orbital stability. Orbital stability for a given orbit depends on the behavior of its neighboring orbits. If points near an orbit converge toward it, then it is stable to small perturbations and is said to be locally stable. An orbit will be attracting, that is asymptotically stable, if on the average along the orbit it is locally stable. If neighboring points diverge away from an orbit, the corresponding behavior will be sensitive to small perturbations. In this case, the instability will amplify the perturbations and the orbit will be locally unstable, even if the orbit initially converged toward some attractor.

In the case of 1D maps, these stability criteria are measured directly by the slope of the map at points visited by an orbit. In particular, if the slope at a point is less than one, nearby points will be brought closer to it at the next iteration of the map. Similarly, if the slope at a point is greater than one, nearby points will be spread apart under iteration of the map. An asymptotically stable orbit, then, requires the geometric average of these slopes along the orbit to be less than one. When this average is greater than one the orbit is unstable and, consequently, initially small deviations from the orbit will increase under iteration of the map.

This sensitivity to small deviations has important consequences for the physical behavior associated with chaotic dynamical systems. For if these deviations are due to some initial uncertainty in specifying or measuring a state, then this uncertainty will grow (exponentially, at first) until one can no longer predict the state of the system within the attractor. The information about the initial state of the system is lost in a finite amount of time and so the system is effectively unpredictable [18, 19]. This sensitivity to small errors can be considered one of the defining features of chaos [20]. This in turn leads to a physical interpretation of the degree of randomness, given by the average local stability, as the rate at which information about states is lost [18, 19].

The measure of average local stability, the Lyapunov characteristic exponent λ , can be expressed in two different, but related, ways [21]. The first is the information-theoretic entropy, given in the case of 1D maps [19] by

$$\lambda(r) = \int_0^1 P(x) \ln|f'(r, x_n)| dx \quad (2-10)$$

where $P(x)$ is the asymptotic probability distribution of an orbit at a given parameter value, such as shown in fig. 2, and f' is the slope of the map. If one assumes ergodicity of the orbit within the attractor, there is an alternative form for computing $\lambda(r)$. It is given by

$$\lambda(r) = \lim_{N \rightarrow \infty} \frac{1}{N} \sum_{n=0}^{N-1} \ln |f'(r, x_n)|. \quad (2-11)$$

With this definition the measure of average local stability is such that if

- (i) $\lambda(r) < 0$, the orbit is stable and periodic;
- (ii) $\lambda(r) = 0$, the orbit is neutrally stable;

and (iii) $\lambda(r) > 0$, the orbit is locally unstable and chaotic.

Many of the features found in the bifurcation diagram of fig. 1 are reflected in the curve of the characteristic exponent as a function of r . This curve is shown in fig. 3 for the parameter regime of fig. 1. For $r < r_c$, $\lambda(r) \leq 0$, indicating the existence of periodic orbits only. In this regime, the period-doubling "pitchfork" bifurcations occur where λ vanishes. That is, an orbit must first pass through a neutrally stable attractor before it can take on a qualitatively different structure. Between these bifurcations, λ approaches $-\infty$ as the critical point x_c becomes a point on the periodic orbit. The orbit is said to be superstable. The logarithmic divergence of λ at this value of the parameter is easily inferred from eq. (2-10) or (2-11) because the slope at the critical point vanishes (see appendix B). The relaxation of initial transients onto the periodic orbit differs on either side of these superstable bifurcations. For r less than the bifurcation value $r_{\text{superstable}}$, the approach of an initial transient is (eventually) from only one side; while for $r > r_{\text{superstable}}$, a transient orbit alternates from one side of points on the periodic orbit to the other. For example, the period 1 orbit becomes superstable at $r = 2$. For $r < 2$, any initial condition will approach from the left of x_c , even though it may have started from the right half of the interval. For $r > 2$, initial transients alternate sides as they approach the periodic orbit. The period 2 orbit which becomes superstable at $r = 3.236068 \dots$ consists of two points. The transients in this case for $r < r_{\text{superstable}}$ eventually approach only from the lower side of each point, while for $r > r_{\text{superstable}}$ they approach the points of the attractor from each side. The change in stability associated with the superstable bifurcation is clear in the $\lambda(r)$ curve, despite the fact that it is not at all visible in the bifurcation diagram of fig. 1.

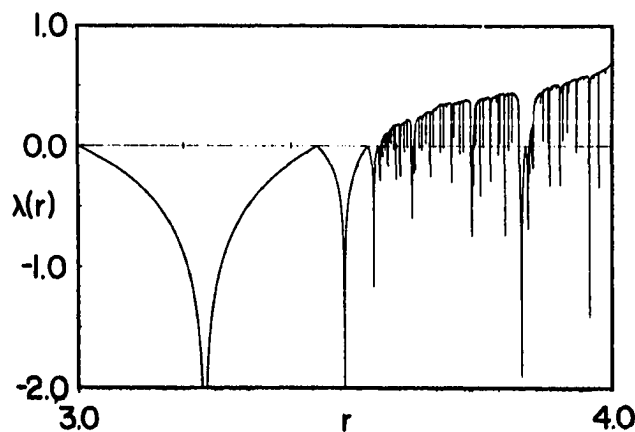


Fig. 3. Characteristic exponent versus bifurcation parameter for the logistic equation calculated using eq. (2-11) for 30 000 iterations at each of 7000 increments of r in $[3, 4]$.

Finally at $r = r_c$, $\lambda = 0$ and one sees a bifurcation to chaotic behavior indicated by positive λ for $r > r_c$. Huberman and Rudnick [22] have recently shown that the envelope of λ near r_c displays universal behavior reminiscent of an order parameter near the critical point of a phase transition. That is, one can write

$$\lambda(r) = \lambda_q (r - r_c)^\tau \quad (2-12)$$

with $\tau = \ln(2)/\ln(\delta) = 0.4498069 \dots$ and λ_q a constant. Cascades of higher periodicities in the chaotic regime are indicated by windows of negative λ in which λ goes through a period-doubling sequence of pitchfork and superstable bifurcations. Above the accumulation point in each window the envelope of positive λ scales as in eq. (2-12) except that the constant λ_q depends on the periodicity q and the width of the window. From numerical studies of the characteristic exponent using eq. (2-11), we have verified this scaling behavior for various periodicities. For example, for $q = 1, 3$ and 5 , $\tau = 0.45 \pm 0.01$, and $\lambda_1 = 0.84$, $\lambda_3 = 1.7$ and $\lambda_5 = 1.6$. Figure 4 shows $\lambda(r)$ and eq. (2-12) graphed with the values for $q = 1$ and 3 .

An estimate of λ_q can be based on the observation that at band joinings λ is inversely proportional to the number of bands. Specifically, at a bifurcation from $q \cdot 2^n$ to $q \cdot 2^{n-1}$ bands, the characteristic exponent is given by

$$\lambda(r) \sim \frac{\ln(2)}{q \cdot 2^n} \sim \frac{\ln(2)(r - r_c)^\tau}{q k^\tau}, \quad (2-13)$$

that is,

$$\lambda_q \sim \frac{\ln(2)}{q k^\tau}, \quad (2-14)$$

where the approximation is less than a few percent and k is the constant of proportionality of (2-9) which depends on the periodicity q [23].

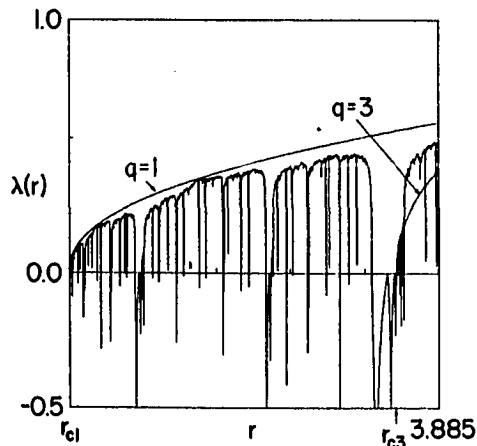


Fig. 4. Characteristic exponent curve $\lambda(r)$ from fig. 3 on an expanded scale from r_c to $r = 3.885$. The two smooth curves show the fit of eq. (2-12) to the envelope of the $q \cdot 2^n$ cascades. For $q = 1$ and $q = 3$, we find $\lambda_1 = 1.01$ and $\lambda_3 = 1.7$ in fitting eq. (2-12). The curve for the $q = 3$ chaotic regime has been extended beyond its range of validity to make it easier to see its fit to the envelope of positive characteristic exponent.

When one looks for the feature in $\lambda(r)$ corresponding to bands merging the self-similarity again becomes apparent in the $\lambda(r)$ curve of fig. 3. There is a peculiar upturn of $\lambda(r)$ toward $\ln(2)$ near $r = 4.0$ [24]. This upturn also displays a critical behavior given by [10]

$$\lambda(r) \sim 1 - b(4.0 - r)^{1/2} \quad (2-15)$$

where b is a constant. In this regime, there is a conspicuous absence of negative dips in $\lambda(r)$ indicating the existence of little observable periodic behavior. These features also occur for values of $r < 4.0$ at which bands merge. Several of the corresponding "steps" in $\lambda(r)$ can be seen in fig. 3. One of them is shown magnified in fig. 5 near the merging of two bands into one. Using eqs. (2-13) and (2-15), we obtain the following expression for $\lambda(r)$ near band joinings

$$\lambda(r) = \lambda_q(r - r_c)^q (1 - b_q(r_{\text{band}} - r)^{1/2}) \quad (2-16)$$

where b_q depends on the periodicity q . Thus, as one would expect, the entire $\lambda(r)$ curve exhibits the same type of self-similarity as the bifurcation diagram. $\lambda(r)$ in each of these self-similar subintervals is very near one-half of that in the preceding subinterval. Again, knowledge of the structure of the $\lambda(r)$ curve in $[r_{2-1}, 4.0]$ is sufficient to (qualitatively) determine the entire curve for $[r_c, 4.0]$.

Although $\lambda(r)$ is continuous in the chaotic regime, it does not converge to a limit curve with increasing resolution in r . It is a curve of infinite length that admits of no closed form representation. Some of the features associated with this property can be described by different types of self-similarity. Furthermore, these self-similar features can be described by a "fractal" dimension [16].

To emphasize the unusual nature of the $\lambda(r)$ curve, we shall mention three occurrences of self-similar structure. The first is the global self-similarity found in the bifurcation diagram. The features between r_{2-1} and $r = 4.0$ are repeated on smaller scales (reduced by a factor of δ) as one approaches r_c from above. This self-similarity has already been discussed above. Another property of the $\lambda(r)$ curve in the chaotic regime is that at every degree of resolution in r , there are windows of periodic behavior corresponding to the negative dips in $\lambda(r)$. The width of the windows rapidly decreases with increasing periodicity q . The number of windows observed at a given resolution in r appears, from our numerical

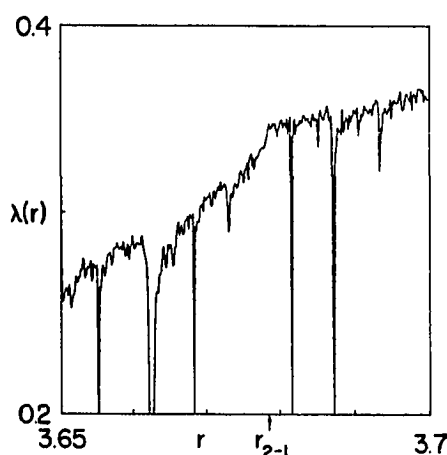


Fig. 5. $\lambda(r)$ near two bands merging into one at $r_{2-1} = 3.67857 \dots$. The kink in $\lambda(r)$ at r_{2-1} as seen in the figure is characteristic of bands merging. Note that $\lambda(r_{2-1}) \sim \ln(2)/2 \sim 0.35$. This picture is taken from the data of fig. 3.

work, to be roughly independent of the resolution at which $\lambda(r)$ is studied. This is the second self-similar feature of $\lambda(r)$: a local self-similarity. It depends on the parameter r and gives a measure of the density of periodic windows in the chaotic regime.

These two features, and the self-similar character they lend to $\lambda(r)$, can be summarized by the fractal dimension of the $\lambda(r)$ curve itself. We have measured the fractal dimension of $\lambda(r)$ for r in $[r_c, 4]$ using a standard algorithm discussed by Mandelbrot [16]. The fractal dimension of a curve describes how the curve's length increases when measured on smaller scales. To apply this to the curve of fig. 3, we measure the length of $\lambda(r)$ in units of $s \Delta r$, where s is some multiple of the increment Δr in parameter used in making fig. 3. The fractal dimension β is obtained then by varying the size of the measuring unit. The number N of measuring units of size $s \Delta r$ is given by

$$N = A s^{-\beta}, \quad (2-17)$$

where A is some constant dependent on Δr . The results of these length measurements are shown on a log-log plot in fig. 6. We have taken $s = 2^n$, $n = 0, 1, \dots, 11$, and found $\beta = 1.69$ and $A = 4.63 \times 10^5$ for r in $[r_c, 4]$. The fact that β is not 1, as would be the case for a simple smooth curve, indicates that as the measuring unit is decreased by 2 (say), more than twice as many units are required to cover $\lambda(r)$. Thus, as the resolution is increased more features in $\lambda(r)$ become apparent, so that in the limit the length, $l = N s \Delta r$, of $\lambda(r)$ is infinite.

The last self-similar feature we shall mention is the fractal dimension of the attractors themselves. Periodic orbits and chaotic attractors have trivial fractal dimensions 0 and 1, respectively. The former consist of a countable number of discrete points and the latter fill out dense bands in the interval. At the transitions to chaos, however, where $\lambda(r)$ vanishes, the attractors have a self-similar structure: the uncountable number of points on these orbits are distributed by factors of Feigenbaum's spatial scaling constant α . The fractal dimension of these attractors has recently been calculated to be $d_{\text{transition}} = 0.538 \dots$ [25].

These self-similar features are substantially modified in the presence of fluctuations. The fractal dimension of each, though, still gives a qualitative measure of the level at which fluctuations truncate the self-similar structure. We shall return to this point at the end of the following section.

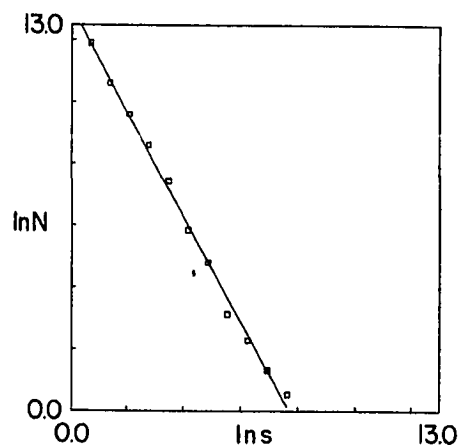


Fig. 6. Log-log plot of the length of the $\lambda(r)$ curve, for r in $[r_c, 4]$ versus the scale of measurement s . N is the number of measuring units of length $s \Delta r$ necessary to cover $\lambda(r)$, where Δr is the increment in r used to compute $\lambda(r)$ in fig. 3. According to eq. (2-17), the slope of the line is the fractal dimension β . For r in the chaotic regime $[r_c, 4]$ we have found the fractal dimension $\beta = 1.69$.

As a concluding remark, we should point out that self-similarity also leads to scaling predictions relating to the behavior of the power spectra associated with deterministic noise [26]. Once again, one can associate universal exponents with both the growth of deterministic noise as a function of the control parameter and the width of the bands past the bifurcation cascade.

This ends our review of the dynamics of 1D maps in the absence of fluctuations. In this section, we have emphasized the self-similarity of the dynamics as a function of the bifurcation parameter r . In the following sections we shall discuss how this self-similarity allows for a scaling description of the effect of fluctuations on the cascade bifurcation. In particular, we will study the effect of noise on the fractal attractor at r_c and will find that noise can be described by a scaling theory, such as found in the theory of critical phenomena. This noise scaling is also of interest in the study of the effect of noise on the fractal structure of chaotic attractors in higher dimension, even away from period doubling bifurcations.

3. Dynamics in the presence of fluctuations

The nature of the fluctuations introduced into a dynamical model depends on the coupling between the physical process to be described and the source of random perturbations. In describing a physical system specified by a set of differential equations, dynamical systems theory considers the action of a flow on a suitable phase space of states. From this perspective fluctuations can enter in two ways: first, as an "external" stochastic force that perturbs the phase space trajectory; and second, as a random perturbation of the parameters specifying the flow itself. We shall call the first additive noise and the second parametric noise. The analog of additive noise for 1D maps is of the following form,

$$x_{n+1} = f(r, x_n) + p_n \quad (3-1)$$

where p_n represents a random deviation from the deterministic orbit. For parametric noise, the fluctuations perturb the form of the nonlinear function or the parameters in the map. For example, if we write the deterministic equation as

$$x_{n+1} = r f(x_n) \quad (3-2)$$

with r as the bifurcation parameter, then parametric fluctuations would be of the form

$$x_{n+1} = (r + q_n) f(x_n) \quad (3-3)$$

or

$$x_{n+1} = r f(x_n) + q_n f(x_n) \quad (3-4)$$

with q_n representing the fluctuations in the parameter r . In the case of 1D maps, the two physically distinct types of fluctuation reduce to basically the same form, namely that of eq. (3-1), except that eq. (3-4) has different statistics for the "external" stochastic force: $q_n f(x_n)$ rather than just p_n . This will introduce higher-order correlations, but for small fluctuations the systems of eqs. (3-1) and (3-4) will exhibit the same behavior. In what follows we shall discuss the effect of changes in the level of fluctuations on the behavior of eq. (3-1) with $f(r, x) = rx(1-x)$. We shall take p_n as a Gaussian or

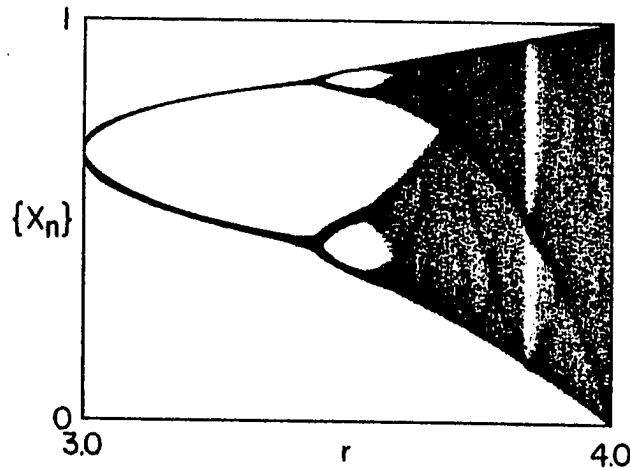


Fig. 7. Bifurcation diagram in the presence of zero-mean Gaussian fluctuations with standard deviation, or noise level, $\sigma = 10^{-3}$. Computational details are the same as in fig. 1, except that eq. (3-1) was used.

uniform random variable with standard deviation σ and zero mean. We have found that the results do not depend significantly on the choice of distribution. We will refer to σ as the noise level of the fluctuations.

A heuristic description of fluctuations, as imposing a minimum scale of deterministic resolution, leads one to properly anticipate the bifurcation diagram in the presence of noise. Figure 7 illustrates the effects of noise on the 1D map, with p_n a Gaussian random variable of standard deviation $\sigma = 10^{-3}$. As can be seen in comparing figures 1 and 7, the fluctuations truncate the detailed structure by smearing the sharp features of the probability distribution of the attractors seen in fig. 1. An example of this effect on two bands is shown in fig. 8 for $r = 3.7$ and $\sigma = 10^{-3}$. This should be compared to fig. 2. The periodic regime, where the orbits are slightly broadened, is easily distinguished from the chaotic regime, where the distribution of points within the bands appears more uniform than in fig. 1. When fluctuations of sufficient amplitude are added, periodic orbits broaden into bands similar to chaotic attractors. As one would expect, the reverse process of chaotic attractors turning into periodic orbits does not happen.

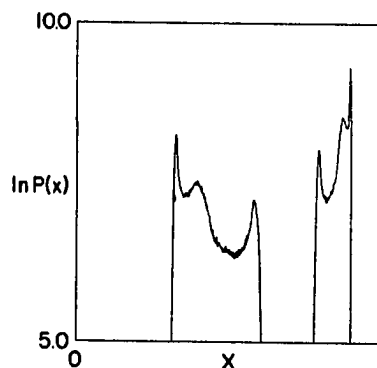


Fig. 8. Logarithmic plot of the (unnormalized) probability density $P(x)$ of the two band attractor at $r = 3.59687$ in the presence of $\sigma = 10^{-3}$ noise as in fig. 7. Compare this with fig. 2 in which there is no added noise. $P(x)$ is a histogram of 10^6 iterations of eq. (3-1) with p_n a uniformly distributed random variable of standard deviation $\sigma = 10^{-3}$. The points have been partitioned into 10^3 bins.

In other words, fluctuations generally increase the degree of randomness or chaos in the dynamics, while destroying the periodic windows encountered in the chaotic regime. This enhanced "observability" of the chaotic behavior in the presence of fluctuations originates in the local instabilities underlying the deterministic chaos. Thus fluctuations affect the local stability properties of the attractors, while leaving their global stability relatively unchanged.

Some of the structure observed in the deterministic limit ($\sigma = 0$) is still visible above r_c when noise is added. In particular, it is evident from fig. 7 that in the chaotic regime a period three orbit is still present, although, windows of higher periodicity are not. The cascades of higher periodicity become unobservable at noise levels whose intensities are proportional to the parameter width of the window. Also, as shown in figures 7 and 8, the images of the critical point still appear as regions of higher probability, but with fewer of the higher iterates encountered in the deterministic limit. Furthermore, for the noise level of fig. 7, a period of four is the highest that remains in the primary 2^n cascade, while all higher periods are washed out.

To summarize the effects of noise for a given cascade, we will define σ_p as the noise level that results in a maximum observable period p . This quantity determines a lower bound on those periods which have been washed out. The effect on the primary 2^n cascade is illustrated by a diagram, shown in fig. 9, displaying a gap in the observable periods which increases with noise level. This gap represents the set of attractors (both periodic orbits and chaotic bands) of periods greater than p which are inaccessible at a particular noise level σ_p . Figure 9 shows the qualitative dependence of the gap on the noise level, where the vertical axis denotes the period $p = 2^n$ of periodic orbits or the number of bands $p = 2^n$ of the chaotic attractor. The deterministic limit $\sigma = 0$ corresponds to the full cascade bifurcation. With increasing noise level, though, a symmetric gap in the bifurcation sequence appears, rendering unobservable successively more periodic and chaotic bifurcations. The gap in fig. 9 symbolizes a set of forbidden attractors whose periods cannot be observed at a given noise level. Both the largest

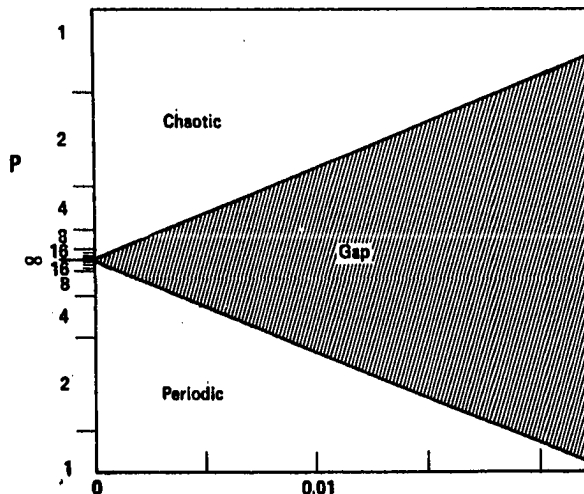


Fig. 9. The set of observable attractors for the cascade bifurcation as a function of (normalized) noise level. The vertical axis denotes the period p of an attractor given (i), in the case of a driven oscillator [1], by the ratio of the response period to the period of the driving force, or (ii), in general, by the period (number of bands) of the periodic (chaotic) attractor. The noise level σ along the horizontal axis corresponds to the standard deviation of thermal-like fluctuations in which the system is immersed. The shaded area represents the set, or "gap", of unobservable attractors obliterated by a given level of fluctuations.

observable period and maximum number of observable bands decrease with increasing noise level σ . As an example of the alteration of the cascade bifurcation with noise level, consider starting in fig. 9 from a period 4 orbit at $\sigma = 0$. As the noise level is increased from this point, the gap is finally reached at $\sigma \sim 5 \times 10^{-3}$ where the attractor appears almost like a 4 band chaotic attractor. The attractors observed at higher noise levels are those along the upper boundary of the gap, within the chaotic regime. That is, increasing noise levels strengthen the band-like character of the attractor, eventually inducing a transition to a chaotic attractor. This transition from a noisy periodic attractor to a chaotic one corresponds to a vertical jump across the gap. The attractor reaches another transition point at $\sigma \sim 10^{-2}$ where the fluctuations have become strong enough to broaden the four chaotic bands into two bands. A similar transition takes place, in principle, at $\sigma \sim 2 \times 10^{-2}$ where the 2 band attractor will broaden into one band. Similarly, at a fixed noise level in fig. 9, one encounters a transition to a chaotic attractor at parameter values which decrease with increasing noise level. Thus the existence of the gap also illustrates the fact that fluctuations can induce a transition to chaos at a lower threshold.

Since the exact values of σ and p for which a gap appears depends on the determination of when a given period becomes unobservable with increasing noise, we have calculated the Lyapunov characteristic exponent curve to provide a consistent measure of the onset of chaos as a function of noise level. When noise is added, the distinction between periodic orbits and chaotic attractors is no longer as straightforward as in the deterministic limit: all attractors eventually fill out intervals whose width depends on the noise level. Nevertheless, there is a qualitative difference between the stability properties of the two types of noisy attractors, a difference which is reflected in the behavior of the characteristic exponent. In calculating the characteristic exponent in the presence of noise, we used eq. (2-11) with f' the derivative of the deterministic map evaluated at points along an orbit $\{x_n\}$ taken from iterates of eq. (3-1).

Figure 10 shows our computation of $\lambda(r)$ at the same noise level as the bifurcation diagram of fig. 7. When this is compared to the deterministic case, fig. 3, several changes are immediately apparent. First, the small parameter windows of periodic behavior in the chaotic regime disappear. Second, the higher-order period-doubling bifurcations merge into a single smooth curve near r_c . Third, bifurcations between periodic orbits, where $\lambda = 0$ in the absence of noise, become more stable when fluctuations are added. Fourth, the first transition to positive λ occurs earlier in the bifurcation sequence. We will continue to associate this latter feature with the onset of chaotic behavior. And finally, the value of λ at parameter values that are chaotic in the deterministic limit is effected substantially less than for the case

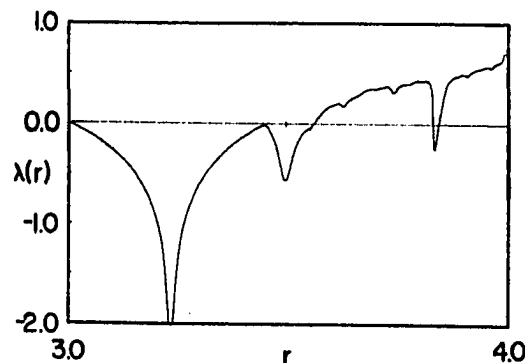


Fig. 10. Characteristic exponent versus bifurcation parameter r at the noise level of fig. 7: $\sigma = 10^{-3}$. Details of the calculation are the same as in fig. 3, except that eq. (2-11) was used with iterates of eq. (3-1).

of periodic behavior. In most chaotic regimes the addition of noise leaves λ unchanged over some range of noise level.

Figures 7 and 10 were constructed using additive noise at fixed parameter values. A study of these figures makes it clear that it is difficult to anticipate the effect of adding noise unless the behavior of the deterministic system is known at adjacent parameter values. Roughly speaking, adding fluctuations alters a deterministic orbit so that it wanders over points on the attractors at adjacent parameter values. This suggests a simple model for the action of noise on the deterministic behavior: the effect of fluctuations is to average the structure of deterministic attractors over some range of nearby parameters. That is to say, there is an equivalence between a perturbation of an orbit and a perturbation of the map itself, in the sense that at each iteration the effect of a perturbation of an orbit can also be obtained by a suitable change in parameter. With this equivalence, all of the features of the bifurcation diagram, fig. 7, and the $\lambda(r)$ curve, fig. 10, can be understood, as well as other consequences of adding noise.

To understand why this averaging of parameters is effective, consider an orbit $\{x_n\}$ of eq. (3-1), generated by some particular sequence of fluctuations $\{p_n\}$. If just the right sequence of fluctuations $\{q_n\}$ occurs, an identical trajectory will be produced by a parametric noise process of the form of eq. (3-3) or (3-4). This sequence $\{q_n\}$ can be found by equating the trajectories step by step, that is,

$$x_{n+1} = r f(x_n) + p_n = (r + q_n) f(x_n). \quad (3-5)$$

For the case $f(x) = x(1-x)$ we obtain the following equation for q_n

$$q_n = \frac{p_n}{x_n(1-x_n)}. \quad (3-6)$$

That is, at each iteration the effective parameter value is $r' = r + q_n$. For this particular iteration, the noisy system behaves just like a purely deterministic system at parameter value r' , except that the point x_n is not necessarily on the attractor for this parameter. Therefore, the attractor of the noisy system can be approximated by an appropriately weighted average of the deterministic attractors at nearby parameter values.

As may be seen from eq. (3-6), the statistical properties of $\{q_n\}$ are quite different from those of $\{p_n\}$. Since q_n depends on x_n , its statistics may be as complicated as those of x_n . For example, suppose the deterministic attractor is a period 2 orbit and the additive fluctuations p_n are small. Because the two points of the orbit have different values, eq. (3-6) says that the fluctuations q_n with odd n will on the average have a different magnitude than those with n even. Thus, in this case, if the additive fluctuations are ergodic, the parametric fluctuations are not. In addition, $\{q_n\}$ need not be Gaussian, even if $\{p_n\}$ is.

To calculate the statistical properties of $\{q_n\}$ exactly would require simulating the orbit $\{x_n\}$. Nevertheless, very crude estimates of a few moments of q_n , together with a knowledge of the deterministic bifurcations, provide a good understanding of the effect of additive noise. In what follows, we will estimate the first two moments of the equivalent parametric noise q_n . We will then discuss how this can be used to explain the observed effects of noise on figures 1 and 3.

We will now compute the average of q_n . Since the fluctuations p_n are statistically independent of x_n , we can write

$$\langle q_n \rangle = \langle p_n / (x_n(1 - x_n)) \rangle = \langle p_n \rangle \langle 1 / (x_n(1 - x_n)) \rangle = 0 \quad (3-7)$$

where $\langle \dots \rangle$ denotes time average and where we have assumed $\langle p_n \rangle = 0$. Thus the average of q_n is zero.

Estimating the second moment is more difficult. Squaring eq. (3-6) and again making use of the fact that p_n and x_n are uncorrelated, we obtain

$$\langle q_n^2 \rangle = \langle p_n^2 \rangle \langle 1 / (x_n(1 - x_n))^2 \rangle, \quad (3-8)$$

which, unfortunately, depends on an unknown moment of x_n . However, in many cases this moment can be estimated. For example, if the deterministic orbit approaches a fixed point, and the additive noise is small, the value of the fixed point can be used to obtain a good estimate of $\langle q_n^2 \rangle$. To do this for a limit cycle, the fluctuations about each point on the deterministic orbit must be considered separately, since in this case the fluctuations q_n are not ergodic.

A simpler, but less accurate, expression may be obtained by rewriting $x_n(1 - x_n)$ in terms of x_{n+1} ,

$$x_n(1 - x_n) = (x_{n+1} - p_n)/r. \quad (3-9)$$

Squaring, substituting this into eq. (3-8), and expanding the denominator, we obtain

$$\langle q_n^2 \rangle = \langle (rp_n/x_{n+1})^2 \rangle \langle 1 - 2p_n/x_{n+1} + 3(p_n/x_{n+1})^2 - \dots \rangle \quad (3-10)$$

with p_n and x_{n+1} correlated. If p_n is small, however, the dominant factor determining x_{n+1} is x_n , and p_n will be approximately uncorrelated with x_{n+1} . With this assumption, we find

$$\sigma_q \sim r\sigma_p \langle 1/x^2 \rangle^{1/2} \quad (3-11)$$

where σ_q and σ_p are the standard deviations of q_n and p_n , respectively. To estimate $\langle 1/x^2 \rangle$, we define $\Delta x^2 = x^2 - \langle x^2 \rangle$. If $\langle \Delta x^2 \rangle \ll \langle x^2 \rangle$, then $\langle 1/x^2 \rangle$ can be expanded to give

$$\sigma_q \sim \frac{r\sigma_p}{\langle x^2 \rangle^{1/2}} \left(1 - \frac{\langle \Delta x^2 \rangle}{\langle x^2 \rangle} \right)^{1/2}, \quad (3-12a)$$

which is a good approximation for periodic orbits. For chaotic attractors there is no reason to assume $\langle \Delta x^2 \rangle \ll \langle x^2 \rangle$ unless the probability density is sharply peaked or consists of bands. From numerical calculations, however, the moments in eqs. (3-8), (3-11) and (3-12a) all agree to within less than a percent for r in [3, 4].

In practice, then, very coarse approximations are effective. For example, if we take $r = 4.0$ where the chaotic attractor fills the entire interval, approximate $\langle x^2 \rangle^{1/2}$ by its median value of 0.5, and take $\Delta x^2 = 0$, we can obtain a crude approximation from eq. (3-12a) for the standard deviation of the equivalent parametric noise level σ_q for a given additive noise level σ_p . This estimate is given by

$$\sigma_q = 8\sigma_p. \quad (3-12b)$$

With this equivalence, it is possible to construct a good approximation to the noisy bifurcation diagram of fig. 7 from the deterministic bifurcation diagram of fig. 1. We have the following rule:

the behavior in the presence of noise can be determined by a weighted average over nearby deterministic dynamics with a distribution in r of standard deviation σ_r . For example, uniform averaging over a fixed range in r yields a good approximation to observed effects of fluctuations. To obtain the bifurcation diagram for fig. 7 from that of fig. 1, the averaging should use a window in r several standard deviations wide. Specifically, the standard deviation for parameter averaging in this case should be $\sigma_r = 8 \times 10^{-3}$. Appendix C discusses the use of this rule in more detail.

This rule provides a simple explanation of the bifurcation gap schematically shown in fig. 9. In the deterministic limit, for parameters close to r_c , it is possible to resolve a periodic orbit or a chaotic attractor of arbitrarily high period. If noise is added, however, the higher periods become unresolvable. According to the rule, this is due to the noise averaging over adjacent higher and lower period attractors. In particular, the transition to chaos lowers with increasing noise level as the behavior is averaged over a wider range of parameters so that periodic orbits at successively lower parameters are averaged with chaotic attractors.

Above r_c , the averaging over nearby parameters smears out all windows of periodic behavior, except the large period 3 window. As has been observed by Mayer-Kress and Haken [27], the effect of noise on the asymptotic probability density of this particular orbit is quite different than the effect of noise on (say) the period 4 orbit in the main period-doubling sequence. The probability density for the period 4 orbit consists of four delta functions in the deterministic limit. As fluctuations are added to the system, these delta functions broaden, with essentially zero density in between them. As more noise is added, this process continues until eventually the peaks merge pairwise so that the period of four is lost, leaving only two bands. The behavior of the period 3 orbit is quite different, as shown in the noise bifurcation diagram of fig. 11. As noise is added, in addition to some thickening of the three delta functions, a broad background suddenly fills in between the peaks. The sequence of probability distributions of fig. 12 illustrate the noise-induced bifurcations in more detail. With further increases in noise level, this background rises until the peaks are eventually washed out, as seen in fig. 12c. The changes in structure of $P(x)$ are also reflected in the characteristic exponent versus noise level curve of fig. 13. The rapid rise of λ for small noise corresponds to the broadening of the delta functions of the

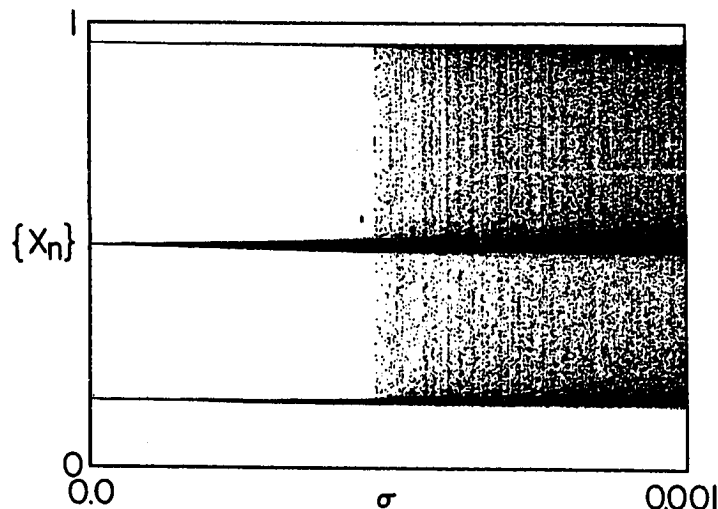


Fig. 11. Noise bifurcation diagram at superstable period 3 orbit: attractor versus noise level σ at fixed parameter $r_3 = 3.831874 \dots$. 500 iterates of eq. (3-1) are plotted after an initial 500 iterations at each of the 750 increments in σ .

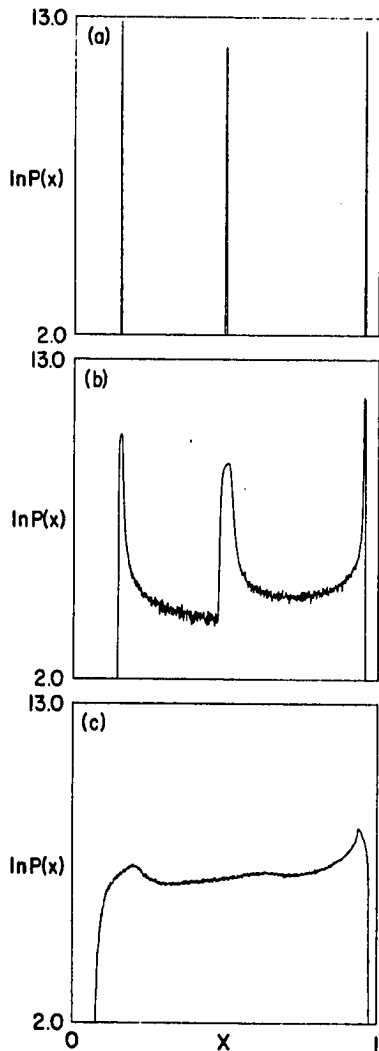


Fig. 12. Log plot of (unnormalized) probability density at the superstable period 3 orbit, $r_3 = 3.831874\dots$, for three different noise levels: (a) $\sigma = 10^{-4}$, (b) $\sigma = 10^{-3}$ and (c) $\sigma = 10^{-2}$. 10^6 iterates of eq. (3-1) were partitioned into 10^3 bins. (b) shows the probability density as seen in the bifurcation diagram of fig. 7. The noise induces a bifurcation from the period three orbit to a single band at a lower noise level than (say) in the 2nd cascade, as it is closer, in the sense of equivalent parametric noise, to the single large chaotic band at slightly lower parameter.

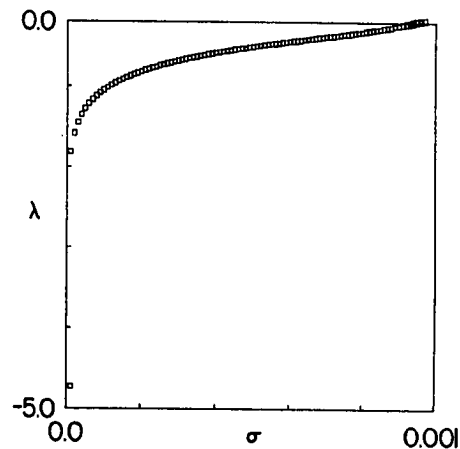


Fig. 13. Characteristic exponent λ at the superstable period 3 orbit as a function of noise level σ . At each noise level, λ was calculated with 10^6 iterations of eq. (3-1) using eq. (2-11). The rapid rise in λ for very small σ corresponds to the broadening of the delta functions of the periodic orbit, while the nearly linear increase in λ for moderate σ corresponds to the rise of the single band "floor" in $P(x)$ seen in the previous sequence of figures.

deterministic period 3 orbit, while for larger σ the nearly linear increase in λ reflects the rise of the background "floor" in $P(x)$ seen in figures 11 and 12.

To understand this effect in terms of equivalent parametric noise, notice that the period 3 orbit is close to a chaotic attractor that is a single band as wide as the period 3 orbit itself. At a sufficiently large noise level this chaotic attractor is averaged with the period 3 orbit, thereby creating the broad background in the probability density.

In contrast to the sensitivity of periodic behavior to added noise, we find that within various parameter regimes chaotic behavior is relatively insensitive to noise over a wide range of noise levels. As an example of this, consider the single band attractor at $r = 3.7$. Figure 14 contains probability distributions showing the attractor at $r = 3.7$ in the presence of noise at two different levels. Although increased noise obliterates the detailed delta-function structure in the distributions, the gross features, such as the width and average height of $P(x)$, are unchanged. As a quantitative measure of this insensitivity, fig. 15 shows the characteristic exponent as a function of noise at $r = 3.7$. Over a range in noise level similar to the previous figure, there is essentially no change in the characteristic exponent. This behavior is found for many chaotic regimes, although the corresponding range of noise levels depends on the particular band structure. As long as the noise affects only the delta-function structure, the characteristic exponent will change little, but once the noise starts to widen the chaotic bands the exponent will change noticeably.

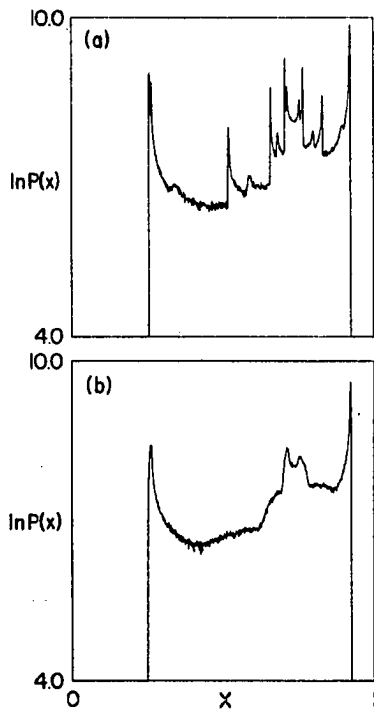


Fig. 14. Logarithmic plot of (unnormalized) probability density for the single band at $r = 3.7$ and two noise levels: (a) $\sigma = 10^{-4}$ and (b) $\sigma = 10^{-3}$. The noise obliterates the detailed structure of the delta functions, but otherwise does not change the width or height of $P(x)$.

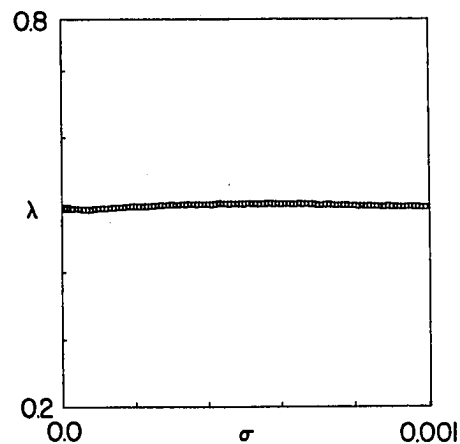


Fig. 15. Characteristic exponent λ for the single band at $r = 3.7$ as a function of noise level σ . At each noise level λ was calculated with 10^6 iterations of eq. (3-1) using eq. (2-11). As the figure shows, noise affects λ very little at chaotic parameter values over wide ranges of noise level. This depends on the degree to which noise changes the probability density (say) by widening it or by filling gaps. For the case of a single band, noise obliterates the peak structure, but this does not contribute significantly to the value of λ , and so λ is relatively independent of noise level.

We can extend the equivalent parametric noise rule to describe the noise-induced changes in $\lambda(r)$. Rather than averaging attractors at adjacent parameter values, we simply average the value of the characteristic exponent at nearby parameters. The deterministic $\lambda(r)$ curve of fig. 3 may be smoothed with a Gaussian distribution of standard deviation $\sigma_q \sim 8 \times 10^{-3}$ to obtain an approximation to the $\lambda(r)$ curve of fig. 10. The result of this is shown in fig. 16.

The fractal dimension of the $\lambda(r)$ curve, mentioned at the end of the previous section, provided a

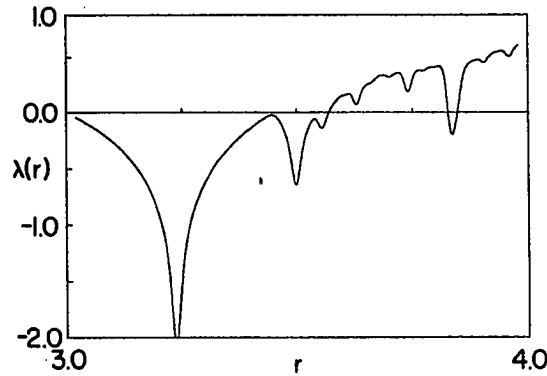


Fig. 16. Gaussian averaging of deterministic $\lambda(r)$ in fig. 3 over data points within two standard deviations. The equivalent parametric noise standard deviation σ_q was computed from eq. (3-12b); i.e., $\sigma_q = 8\sigma_p = 0.008$. The averaging of $\lambda(r)$ with equivalent parametric noise gives good qualitative agreement.

rough measure of the sensitivity of the self-similar dynamics to the addition of noise. In light of our discussion of the approximate equivalence between additive and parametric noise, we expect that at a given additive noise level σ_p periodic windows in the chaotic regime of size σ_q or smaller will be unobservable. Thus, in the sense that the fractal dimension of $\lambda(r)$ quantifies the repetition of bifurcation structure on successively smaller scales, it is also a measure of how this detail is washed out at a given noise level. As a first approximation, the noise level σ at which we can no longer observe a window of parameter width w is simply proportional to w . If we associate this noise width with the scale of resolution $\Delta r \cdot s$ used to derive eq. (2-17), then the length $l = N \Delta r \cdot s$ of the $\lambda(r)$ curve at a given noise level σ is

$$l \sim \sigma^{-(\beta-1)} = \sigma^{-0.69} \quad (3-13)$$

We see, then, that the fractal dimension does yield a qualitative measure of the effect of noise on the detailed structure found in $\lambda(r)$ in the chaotic regime. Before concluding this section, we should also mention a different type of chaotic behavior which is encountered whenever a tangent bifurcation occurs. This new phenomenon, which was originally studied in the context of the Lorenz model by Yorke and Yorke [28] and Pomeau and Manneville [29], is characterized by intermittency, or the appearance of noisy bursts in between laminar or periodic sequences. In what follows, we will consider it in the context of tangent bifurcations in systems exhibiting period doubling behavior [31–33].

Consider the third iterate of the map as given by

$$F^{(3)}(x) = F(F(F(x))) \quad (3-14)$$

with $F = Rx(x-1)$ and $R = R_c = 1 + \sqrt{8}$. For this value of R the map is just tangent to the line x at $x_c = (0.160, 0.514, 0.956)$. For $R > R_c$, $F^{(3)}(x)$ passes through the line x giving rise to six new fixed points of which three are stable. This phenomenon of tangent bifurcation is responsible for the way in which the periodic windows appear in the chaotic regime [14]. Now consider eq. (3-14) for R slightly smaller than R_c . A sequence of third iterates then would generate both a laminar phase (the iterates move slowly in a staircase fashion close to any of the x_c values) and a chaotic burst as the iterates move erratically under the map before being reinjected into any of the x_c values.

A number of predictions can be made on the basis of this picture. Expanding $F^{(3)}(x, R)$ about x_c and R_c one has

$$F^{(3)}(x, R) \cong x_c + (x - x_c) + a_c(x - x_c)^2 + b_c(R_c - R). \quad (3-15)$$

Setting $y_n = (x_n - x_c)/b_c$ the recursion relation for the three-fold iterate takes the form

$$y_{n+1} = y_n + ay_n^2 + \epsilon \quad (3-16)$$

with $\epsilon = R_c - R$. For the logistic map $a = 68.5$. Since the basic step size in the passage near x_c is small the recursion relation near x_c is well described by the differential equation

$$dy/dl = ay^2 + \epsilon. \quad (3-17)$$

Integrating this equation for $\epsilon > 0$ gives for the number of steps between y_{in} and y_{out} ,

$$l(y_{out}, y_{in}) = \frac{1}{\sqrt{a\epsilon}} [\tan^{-1}(y_{out}/\sqrt{\epsilon/a}) - \tan^{-1}(y_{in}/\sqrt{\epsilon/a})]. \quad (3-18)$$

To find the average length of a laminar region, y_{in} is averaged over the probability $P_{in}(y_{in})$ of entering some acceptance region $(-G, G)$ and y_{out} is set equal to G . So long as $G \gg \sqrt{\epsilon/a}$, it is given by

$$\langle l \rangle = \frac{1}{\sqrt{a\epsilon}} \tan^{-1}(G/\sqrt{\epsilon/a}), \quad (3-19)$$

a result obtained if the probability distribution $P_{in}(y_{in})$ is taken to be uniform over $(-G, G)$.

In order to look for this intermittent route to chaos in the presence of external noise, one has to study

$$x_{n+1} = Rx_n(1 - x_n) + \bar{\sigma}\xi_n. \quad (3-20)$$

Here ξ_n is a Gaussian random variable with $\langle \xi_n \xi_{n'} \rangle = \delta_{nn'}$. Proceeding as before, the 3-fold iterate can be represented near the contact point by the Langevin equation

$$dy/dl = ay^2 + \epsilon + \sigma\xi. \quad (3-21)$$

Here $\xi(l)$ is a Gaussian white noise source such that

$$\langle \xi(l) \xi(l') \rangle = \delta(l - l') \quad (3-22)$$

and σ is proportional to $\bar{\sigma}$. Introducing the corresponding Fokker-Planck equation, one can solve for the average path length in the presence of noise [31]. Here we consider the scaling limit valid for small ϵ . In this limit it can be shown that the average path length in the presence of noise satisfies the scaling relation

$$\langle l \rangle = \frac{1}{\sqrt{\epsilon}} f(\sigma^2/\epsilon^{3/2}). \quad (3-23)$$

As $\sigma^2/\epsilon^{3/2}$ vanishes, f goes to a constant and we recover the previous result, eq. (3-19). For $\sigma^2/\epsilon^{3/2} \gg 1$, $f(x) \sim x^{-1/3}$ so that in the limit of large noise

$$\langle l \rangle \sim 1/\sigma^{2/3} \quad (3-24)$$

and a chaotic burst as the iterates were erratically under the map before being reinjected into any of the x_c values.

In this section we have described several important effects that additive noise has on the dynamics of the quadratic 1D map. We have also indicated that these can be understood in terms of averaging the dynamics over nearby parameters with an equivalent parametric noise and that the fractal dimension of $\lambda(r)$ gives a qualitative measure of the sensitivity of the bifurcation features to noise. In the next section we shall consider a more quantitative description of the scaling behavior of noise near the accumulation points of period-doubling bifurcations.

4. Noise as a disordering field

Several features of the $\lambda(r)$ curve shown in fig. 10 allow the definition of a criterion for the lowering of the chaotic threshold. First, as any amount of noise obliterates at some scale the detailed self-similarity near r_c , the first positive transition of λ near r_c becomes easier to detect. The transition to chaos (fig. 10) is not only lower than in the deterministic limit (fig. 3), but the slope of the envelope of $\lambda(r)$ at the zero-crossing is no longer infinite. Second, the points of neutral stability ($\lambda \sim 0$) corresponding to the period-doubling bifurcations below r_c , are made more stable by the addition of fluctuations. In fig. 10, for example, the $\lambda(r)$ curve is smoothed and made more negative, indicating greater stability at the points of bifurcation. These two features taken together make the first positive transition of λ unambiguous. Hence, we can define the onset of chaos, $r^+(\sigma)$, as the value of the parameter r at noise level σ for which $\lambda(r)$ first becomes positive. For convenience we will use the normalized parameter $\bar{r} = (r - r_c)/r_c$. From an extensive study of $\lambda(r)$ versus noise level σ , in conjunction with the corresponding bifurcation diagrams, we can summarize the effect of fluctuations on the cascade bifurcation in fig. 17, which avoids certain ambiguities associated with fig. 9. Thus we can now follow differing bifurcation paths to the same point in the diagram of fig. 17 unambiguously and without the need for a special transition rule as is the case for fig. 9.

One feature that becomes apparent in the diagram of fig. 17 is the scaling behavior of the onset of chaos $r^+(\sigma)$ as a function of noise level σ . If we denote by $r^+(\sigma)$ the value of r for which the characteristic exponent becomes positive at fixed noise level, we can write

$$r^+(\sigma) = k_q \sigma^\gamma \quad (4-1)$$

where γ is a critical exponent summarizing the power law behavior of the onset of chaos as a function of noise level and k_q is a constant of proportionality depending on the periodicity of the cascade. Using eq. (2-11), we have determined the exponent γ and constant k_q from numerical experiments to be

$$\gamma = 0.82 \pm 0.01 \quad (4-2)$$

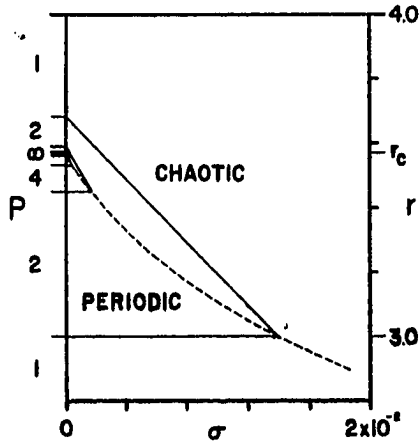


Fig. 17. A rendition of the bifurcation "gap" which does not have any of the associated ambiguities of fig. 9. Period p and bifurcation values of the parameter versus logarithm of the noise level σ . The dashed line represents $r^+(\sigma)$ (defined in text) versus σ and indicates that higher noise levels induce an earlier transition to chaos. For numerical details of $r^+(\sigma)$ refer to the following figure. Above the dashed line the attractors are chaotic, below periodic.

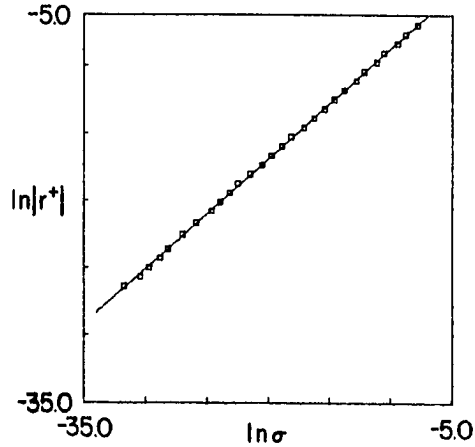


Fig. 18. Lowering of the chaotic threshold r^+ with increasing noise level σ for the 2^n cascade on a log-log scale. The absolute value of r^+ is used as $r^+ < 0$. The 10 orders of magnitude in r^+ correspond to orbits of periods from 2^4 to 2^{16} , in the deterministic limit. The noise level ranges over 12 orders of magnitude. Each data point comes from a binary search at fixed r of a λ vs. σ curve for the zero-crossing of λ . During the search each λ was calculated with $N = 10^6$ or 10^7 (small σ) in eq. (2-11).

for both $q = 1$ and 3 , and

$$k_1 = 0.60 \pm 0.01, \quad k_3 = 0.40 \pm 0.01. \tag{4-3}$$

Figure 18 shows a log-log plot of r^+ versus σ over 12 orders of magnitude in σ . The range in r corresponds, in the deterministic limit, to orbits from period 2^4 to period 2^{16} .

If we recall the definition of σ_p as the noise level at which one can observe an orbit of at most period p and if we define $r^+(\sigma_p) = r_p^+$, then eq. (2-9) written in terms of the normalized parameter gives

$$\bar{r}_p / \bar{r}_{2p} = \delta \tag{4-4}$$

and, also,

$$r_p^+ / r_{2p}^+ = \delta. \tag{4-5}$$

Using eq. (4-1), we then obtain [1]

$$\sigma_p / \sigma_{2p} = \delta^{1/\gamma}. \tag{4-6}$$

Thus for a cascade where one can observe at most a period of p at a given noise level σ_p , one must reduce the noise level by a factor of $\delta^{1/\gamma} \sim 6.6$ in order to resolve a period of $2p$.

The behavior of λ near r_c in the absence and presence of noise as shown in figures 9 and 17, leads to the notion of external fluctuations acting as a disordering field on the deterministic dynamics. As we pointed out in section 2, in the deterministic limit λ behaves as a disorder parameter for chaos, with a power law given by eq. (2-12). As the strength of the external noise is increased, λ acquires a finite value

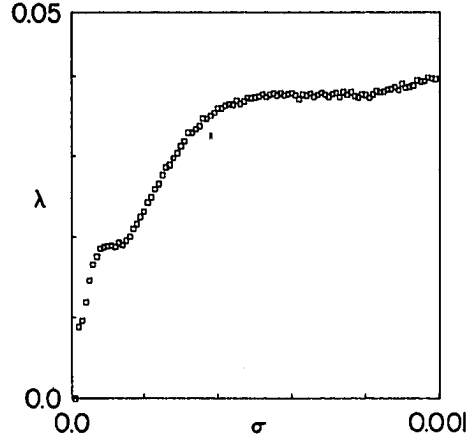


Fig. 19. Characteristic exponent λ versus noise level σ at r_c for the 2^n cascade. λ was calculated with $N = 10^6$ in eq. (2-11) for 100 values of σ . The steps correspond to the noise-induced merging of bands. The overall power law behavior, though, can be summarized by the critical exponent θ of eq. (4-7).

at r_c , while the zero crossing is renormalized according to eq. (4-1). Furthermore, since the presence of a bifurcation gap implies the smearing of bands in the chaotic regime, λ will no longer possess an infinite slope at the threshold in the presence of a disordering field.

These considerations lead us naturally to expect that at r_c , the Lyapunov characteristic exponent λ will scale with noise according to

$$\lambda(r, s) = A\sigma^\theta \quad (4-7)$$

where θ is a universal exponent which plays a role similar to the isothermal exponent in critical phenomena [34]. Figure 19 shows the dependence of the characteristic exponent at $r = r_c$ on the noise level σ . In addition to an overall power law behavior, several "steps" are apparent in the curve of $\lambda(\sigma)$. The steps are separated by factors of $\delta^{1/\gamma} \sim 6.6$ in the noise level and correspond to the noise-induced merging of bands. The sequence of probability distributions of fig. 20 illustrates the rescaling of the dynamics by changes in the noise level of factors of $\delta^{1/\gamma}$. As the noise increases by $\delta^{1/\gamma}$ from (a) to (b) and again from (b) to (c), the structure of the band probability distribution is seen to be the same, except for a spatial rescaling. Figure 19 also shows that λ increases relatively linearly with noise level until bands merge, at which point λ levels off with increasing noise level because the probability density changes little. This is verified by the noise bifurcation diagram of fig. 21 which shows 16 bands merging into 8 and 8 bands merging into 4 at noise levels corresponding to the steps in $\lambda(\sigma)$ of fig. 19.

In order to determine the validity of eq. (4-7) we have measured the change of λ at $r = r_c$ with increasing noise level over 9 orders of magnitude in σ . As can be seen in fig. 22, a log-log plot of the data reveals a straight line from which we can extract the values

$$\theta = 0.37 \pm 0.01, \quad A_1 = 0.58 \pm 0.01 \quad (4-8a)$$

for the period 1 cascade and

$$\theta = 0.37 \pm 0.01, \quad A_3 = 1.13 \pm 0.01 \quad (4-8b)$$

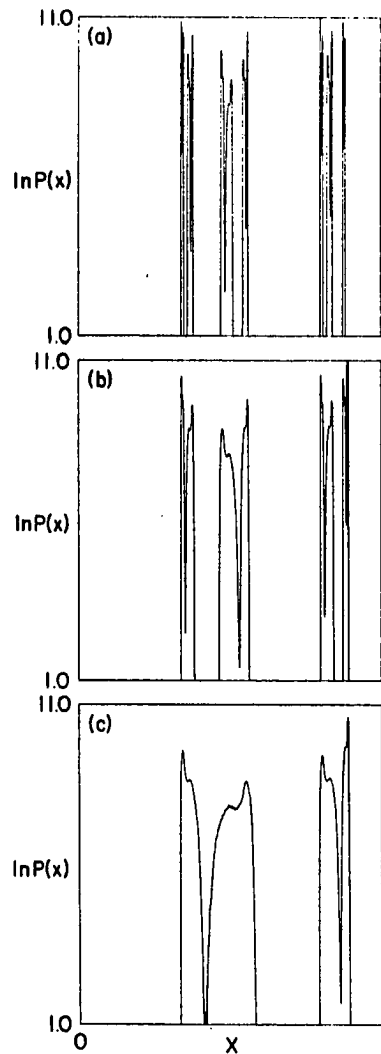


Fig. 20. Logarithmic plot of (unnormalized) probability density at the accumulation point $r_c = 3.569945\dots$ of the 2^n cascade for three different noise levels separated by factors of $\delta^{1/\nu} \sim 6.6$: (a) $\sigma = 2.3 \times 10^{-5}$, (b) $\sigma = 1.5 \times 10^{-4}$, and (c) $\sigma = 10^{-3}$. The last corresponds to the noise level of fig. 7 in which 4 bands are apparent. The sequence illustrates the band-merging bifurcations at r_c induced by increasing noise levels. Again, 10^6 iterations of eq. (3-1) were partitioned into 10^3 bins. The difference in noise levels is chosen to illustrate the noise scaling structure of $P(x)$.

for the period 3 cascade. The deviations from a straight line, seen as groupings of 2 and 3 data points in fig. 22, are due to the noise-induced bands mergings found in fig. 19.

These results together with the Huberman–Rudnick scaling of the characteristic exponent, eq. (2-12), and recent scaling theories [35, 36], suggest the existence of a homogeneous scaling function $F[\bar{r}, \sigma]$ such that

$$\lambda(\bar{r}, \sigma) = -\frac{d}{d\sigma} F[\bar{r}, \sigma] \quad (4-9)$$

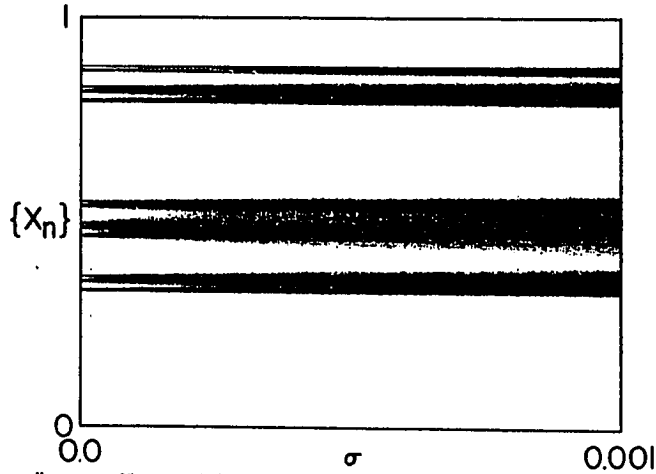


Fig. 21. Noise bifurcation diagram at 2^n accumulation point: attractor $\{x_n\}$ versus noise level σ at $r_c = 3.56995 \dots$. 500 iterates of eq. (3-1) are plotted after an initial 500 iterations at each of the 10^3 increments in σ .

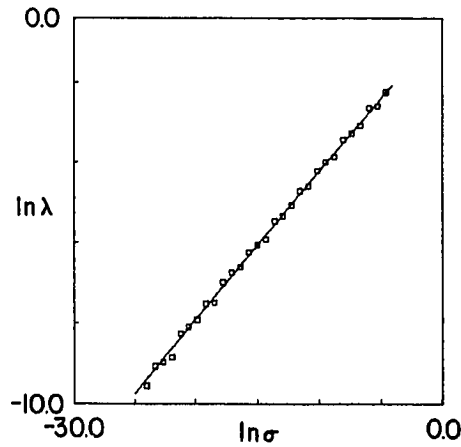


Fig. 22. Log-log plot of λ versus noise level σ showing the data used to obtain $\theta = 0.37$ and $A_1 = 0.58$ for eq. (4-7). The groupings of 2 and 3 data points reflect the noise-induced band mergings. λ was calculated with $N = 10^6$ in eq. (2-11) at 30 values of σ which ranged over 9 orders of magnitude.

and satisfying a scaling behavior, i.e.

$$F[L^{a_r} \bar{r}, L^{a_\sigma} \sigma] = L F[\bar{r}, \sigma], \quad (4-10)$$

where a_r and a_σ are scaling parameters.

In particular, when $\sigma = 0$, eqs. (4-9) and (4-10) imply

$$\lambda(\bar{r}, 0) = (-\bar{r})^{(1-a_\sigma)/a_r} \lambda(-1, 0) \quad (4-11)$$

which together with eq. (2-12) gives

$$\tau = (1 - a_\sigma)/a_r. \quad (4-12)$$

Similarly, we can express the exponent θ in terms of the scaling parameters a_r and a_σ . Setting $r = 0$ in eqs. (4-9) and (4-10) and letting $\sigma \rightarrow 0$, we obtain

$$\lambda(0, \sigma) = \sigma^{(1-a_\sigma)/a_\sigma} \lambda(0, 1) \quad (4-13)$$

which, together with eq. (4-7) gives

$$\theta = (1 - a_\sigma)/a_\sigma. \quad (4-14)$$

In order to obtain an explicit relation between τ and θ , we can introduce a noise susceptibility $X(\bar{r}, \sigma)$ defined as

$$X(\bar{r}, \sigma) = d\lambda/d\sigma. \quad (4-15)$$

The magnitude of the noise susceptibility X gives a measure of the sensitivity of the dynamics to the addition of noise. For example, at the transitions to chaos and at points of superstability, X diverges, although nearby it is finite and positive. Actually, near the transition to chaos, the behavior of X is complicated somewhat by the accumulation of self-similar structure. The addition of a small amount of noise, however, truncates this structure so that the nature of the divergence at the transition can be studied in practice. Near r_c , then, X should also obey a scaling law

$$X(\bar{r}, 0) = c\bar{r}^{-\omega}. \quad (4-16)$$

Taking derivatives of eqs. (4-9) and (4-10) we obtain

$$\omega = (2a_\sigma - 1)/a_r \quad (4-17)$$

which together with eqs. (4-12) and (4-14) lead to the relation

$$\omega = \tau(\theta^{-1} - 1). \quad (4-18)$$

Using the known values for τ and θ , eq. (4-18) yields a prediction for the noise susceptibility critical exponent of $\omega = 0.77$. In the previous section we noted that the addition of noise lowered the characteristic exponent at the period-doubling bifurcations. Thus X is negative near period-doubling bifurcations and apparently diverges at this point of bifurcation too. We also pointed out that for a single chaotic band the characteristic exponent is affected very little over a wide range of noise level. In such cases, the noise susceptibility will be very small, if not zero.

The results of this section show that the existence of a homogeneous scaling function F with universal properties leads to scaling relations very similar to those encountered in critical phenomena. In particular, one is able to accurately predict the value of the exponents that relate the effect of external fluctuations on the chaotic behavior of deterministic systems exhibiting period-doubling cascade bifurcations. Recent work [35, 36] points to a renormalization group description of the scaling behavior revealed by the above numerical investigations. In fact, these approaches yield critical exponents in excellent agreement with those reported above.

5. Concluding remarks

Using the simplest dynamical system which undergoes cascade bifurcations we studied in a quantitative manner the fluctuation effects reported earlier in a system of nonlinear ordinary differential equations [1]. In particular, we have described the fluctuation-induced gap in the cascade bifurcation sequence and the scaling behavior of both the threshold noise and the disordering field. Our investigations provide strong evidence for the consideration of the Lyapunov characteristic exponent as a disorder parameter for chaos. We have also derived the scaling behavior of the effects of fluctuations using results from the universal scaling theory for the period-doubling bifurcation. Thus these results should be relevant to other dynamical systems, including weakly turbulent fluid flows, which undergo cascade bifurcation.

The existence of deterministic models that show chaotic or unpredictable behavior puts in a new light questions on the physical origins of noise processes. With this in mind, we would like to consider the larger context in which this paper should be placed. For models of classical physical systems we can distinguish three types of fluctuation. The first, observational noise, is due to the finite resolution of physical measurements, that is, instrumentation error. Problems associated with observational noise are often considered the province of the mathematical theory of communication, which describes the effect of random errors on a signal representing some physical quantity [37]. When a physical system is in contact with a "heat" bath in which a large number of particles (or degrees of freedom) are excited, a second type of fluctuation, external noise, appears. This second type of noise adds a stochastic force to the dynamical equations and the resulting non-deterministic problem is solved with statistical assumptions and techniques [38]. The Langevin equation describing Brownian motion exemplifies this class of stochastic model. Finally, chaotic dynamical systems exhibit stochasticity or random behavior, although they are completely deterministic. This deterministic randomness is the third type of fluctuation, which we shall call intrinsic noise. It is of interest, for example, to the study of nonlinear differential equations whose phase space descriptions require at least three dimensions.

In current attempts to relate deterministic chaotic models to turbulent physical systems, one of the outstanding problems is the interaction between each of these types of fluctuation. On one hand, noise appears as an everpresent but undesirable artifact which, more often than not, complicates experimentalists' interpretation of their data. On the other hand, from the theoretical point of view, the introduction of fluctuations in a problem implies a simplification of a model. Such an ansatz represents an explicit lower bound on the level of description below which the detailed dynamics are not to be considered. The results we have presented here and previously [1] suggest a role for fluctuations intermediate between the extremes of experimental complexity and theoretical simplicity. We have shown that a broad class of transitions to chaotic behavior can be characterized by its alteration in the presence of thermal-like noise. In principle, this should aid in distinguishing the type of model appropriate to describe observed, random behavior.

Aside from the particular behavior discussed here for the cascade bifurcation, we wish to emphasize the importance of considering fluctuations in modeling turbulent physical systems. From an understanding of the changes induced by fluctuations in the geometry of the phase space flow, one may be able to elucidate the relationship between simple chaotic dynamics and turbulent physical systems, such as turbulent fluid flow [39] and noisy solid state systems [1, 5]. Currently, simple chaotic models serve only as metaphors for turbulent behavior in continuous (infinite dimensional) physical systems. Although one finds electronic and mechanical systems corresponding to chaotic models [40] and recent application of phase space reconstruction techniques to stirred chemical reactions [41], there

is as yet no direct experimental evidence that chaotic dynamics describes observed random behavior in continuum systems, such as turbulent fluid flow. At present, the comparison of bifurcation sequences of power spectra between experiment and model systems and the reconstruction of phase space pictures provide the only methods of validation of the conjecture. Hopefully, an understanding of the relationship between the three types of fluctuation (observational, external and intrinsic) in model systems will lead to experimental tests which will determine the relevance of chaotic dynamics to noisy physical processes.

We should mention another approach to distinguishing between types of intrinsic noise that is of interest in distinguishing between intrinsic and thermal noise. It considers, first of all, the reconstruction of phase space dynamics from a single experimental variable and then determines the number of independent variables underlying the reconstructed dynamics, that is the intrinsic dimensionality of a phase space description [42, 43]. According to this approach, different types of intrinsic noise require different numbers of phase space dimensions. Thermal noise, considered as a deterministic process, would be characterized by a relatively large number of phase space dimensions. It is still an open question whether practical algorithms can be devised to distinguish between thermal and intrinsic noise when the dimension of the underlying physical process is inherently large. At the present time, there appear to be substantial computational difficulties for the experimental determination of the intrinsic dimension of physical processes even when the dimension is as low as 5 (say), not to mention the problems of visualizing a chaotic attractor of that dimension with the reconstruction techniques currently proposed. The utility of these techniques will probably be limited in answering questions about the interaction of thermal noise and chaotic dynamics. Nonetheless, the conceptual framework that these techniques provide allows one to understand the transition from low dimensional chaotic dynamics to high dimensional, deterministic, thermal-like noise processes.

From a different perspective, Ruelle [44] and Shaw [19] estimate that the time necessary for a thermal fluctuation to affect the macroscopic motion of fully-developed turbulence in a fluid is relatively short, being on the order of seconds for air. Ruelle concludes, however, that in this regime, because thermal fluctuations must compete with many other perturbations of similar energy which are also amplified by the flow, changes in the level of thermal fluctuations would probably not be experimentally observable. In the weakly turbulent regime though, the changes in the level of thermal fluctuations could be quite noticeable, as suggested by our results on the cascade bifurcation to chaos. Fluctuations are of interest from a mathematical point of view, thermal fluctuations may also play an important role in selecting the relevant stationary measure on the chaotic attractor describing turbulence. In principle, there are many such measures, but, as Kifer [45] has shown for Axiom-A systems, only one is stable under small stochastic perturbations.

The picture of microscopic fluctuations determining macroscopic behavior is one that is generally associated with locally unstable or chaotic dynamics. Shaw [19] develops this notion by considering chaotic dynamical systems as sources of information; this information originates in the microscales beyond experimental resolution. He discusses the unpredictability of chaotic systems in terms of finite measurement resolution, or observational noise, to use the above terminology. As an example, he estimates how long it takes a chaotic system to become unpredictable. If the state of a system can be determined to within some finite resolution σ (measured relative to the total number of resolvable states) and if one knows a priori the information loss rate λ_0 (such as the maximum Lyapunov characteristic exponent), then the system is effectively unpredictable a time $t = \ln(\sigma)/\lambda_0$ after a measurement. As a first approximation to an observation theory of chaos, this argument raises an interesting question for experimentalists: Without knowing the rate of information loss, how can the

rate itself be measured experimentally in the presence of observational noise? Or, indeed, in the presence of the other types of noise mentioned above? [46].

As an explicit example of the relationship between thermal-like fluctuations and intrinsic noise, we have studied a model exhibiting chaotic behavior, eq. (3-1), which included a stochastic force. This "thermal fluctuation" term was in practice a deterministic pseudo-random number generator implemented on a digital computer. Its iterative algorithm was operated on a different time scale than the 1D map in order to let the correlations die out, and so give the desired statistics. This time scale is determined by the degree of randomness of the algorithm which can be measured with a characteristic exponent, that is, a measure of the divergence of nearby states. The introduction of pseudo-random noise imposed a scale of resolution below which we did not consider the dynamics. This "thermal" noise was characterized by suitable statistical quantities, such as the mean and standard deviation, although it was a deterministic process. From the opposite perspective, this suggests that in pursuing the understanding of a noisy physical process to finer degrees of resolution, the "noise source" may appear as a deterministic nonlinear system with chaotic dynamics. This certainly was the case for our numerical experiments.

Acknowledgements

The authors have benefited from discussions with John Guckenheimer, Michael Nauenberg, Norman Packard, Joe Rudnick and Rob Shaw. They also wish to thank Ralph Abraham and Joe Rudnick for their support of the authors' computational work at UCSC and to acknowledge the help provided by the late Joe Maleson with the computers at Xerox PARC. Rob Shaw has generously provided fig. 2 from his unpublished work. This work was supported in part by the National Science Foundation Grant No. 443150-21299. JDF gratefully acknowledges the support of the Fannie and John Hertz Foundation. JPC was supported by a University of California Regents Fellowship.

Appendix A. Fluctuations in a driven anharmonic oscillator

Although characteristic exponents provide an unambiguous criterion for the early transition to chaos induced by increasing noise levels, for systems more complex than 1D maps, their calculation becomes quite time consuming. In the case of the driven anharmonic oscillator initially studied [1] one can observe this effect in the variation of Poincaré sections with noise level more readily, in fact, than in changes in the 1D map attractors with noise level. Generally, chaotic behavior appears with a particular degree of mapping, or folding, of orbits onto each other. Calculation of characteristic exponents gives the best determination of when this folding occurs in 1D maps. For driven oscillators, and other chaotic systems whose attractors appear sheet-like (of topological dimension two), on the other hand, this point is reached when the first folding appears in the attractor's geometry, as revealed in a sequence of Poincaré sections. From the underlying geometry of the attractor one can then infer the transition to chaos.

We include here two sets of Poincaré sections (figures A1 and A2), taken at different noise levels for the oscillator of ref. [1], to illustrate in another context the qualitative effects of fluctuations discussed in this paper. The anharmonic oscillator studied there is given by

$$\ddot{x} + g\dot{x} + ax - bx^3 = F \cos(\omega t). \quad (\text{A-1})$$

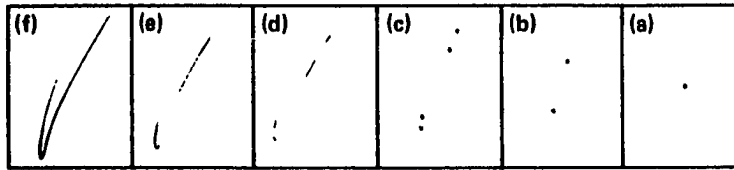


Fig. A1. A set of phase-zero Poincaré sections at different driving frequencies along the horizontal axis for the anharmonic oscillator studied in ref. [1] for a (normalized) noise level $\sigma = 10^{-3}$. The set (a)–(f) shows a cascade bifurcation as the driving frequency is lowered (toward the left in the figure). At this noise level only a maximum period of four can be observed. The folding geometry is apparent for the band attractors in (d)–(f).

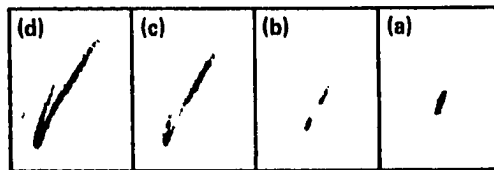


Fig. A2. The set of Poincaré sections (a)–(d) are similar to the first set in figure A1, except they are taken at a noise level $\sigma = 10^{-2}$. Only a maximum period of two is present for this noise level. Notice also that the fluctuations spread more in the direction along the unstable manifold (bands) than along the stable manifold (transverse to the bands).

Figures 9 and 17 summarize the observable periods at a given noise level and periodicity, as is seen in figures A1 and A2. An important feature revealed by the Poincaré sections is that the fluctuations spread out the orbits more along the “soft” directions within the attractor (the unstable manifold) than in the transverse directions (stable manifold), along which orbits contract very rapidly onto the attractor. The explanation for the induced transition to chaos with increasing noise level, then, is that the fluctuations fill out the folds of the attractor, causing the orbits to describe a geometry which is effectively chaotic. The existence of such folding geometry cannot be easily inferred from the bifurcation diagrams of the 1D map.

Appendix B. Characteristic exponents in period-doubling regimes

The characteristic exponent in periodic regimes, as seen in fig. 3, has a distinctive shape between period-doubling bifurcations. Although the dependence of the characteristic exponent λ on the parameter r cannot be analytically calculated in general, it can be straightforwardly determined from eq. (2-10) for a few simple cases. The nature of the divergence at superstable orbits can also be elucidated using eq. (2-10). Furthermore, once we have these results, a scaling of $\lambda(r)$ in the periodic regime, analogous to the scaling above r_c of eq. (2-12), follows easily.

A period p orbit consists of the set of stable fixed points $\{x_i\}$, $i = 1, \dots, p$, of the p th iterate of the map. These are given by the equation

$$x_i = f^p(r, x_i). \quad (\text{B-1})$$

Eq. (B-1) implicitly determines the dependence of the fixed points x_i on r . Thus, the bifurcation of periodic orbits reduces to the study of the real roots x_i of the polynomial in r , $x_i - f^p(r, x_i)$. Only p of these roots correspond to the points of the stable orbit; the others correspond to unstable orbits. For period 1 orbits of the logistic equation, we have the roots $x = 0$ and

$$x_1 = (r-1)/r. \quad (\text{B-2})$$

The root x_1 describes the stable period 1 orbit for r in $[1, 3]$. For period 2, there are four roots of the polynomial

$$x - f^2(r, x) = x - r^2x(1-x)(1-rx(1-x)). \quad (\text{B-3})$$

The period 1 root and $x = 0$ are also roots of this polynomial, but they correspond to unstable orbits. The remaining two roots describe the stable period 2 orbit for r in $[3, r_{2-4}]$; they are

$$x_{\pm} = \frac{1+r \pm (r^2-2r-3)^{1/2}}{2r}. \quad (\text{B-4})$$

Generally, a period p orbit is determined by the roots of a polynomial of order 2^p . For a period 2^n orbit, the roots corresponding to the unstable orbits of periods 2^{n-1} , 2^{n-2} , ..., and 1, can be factored out of the polynomial $x - f^{2^n}(r, x)$, in principle. This would leave a 2^n -order polynomial whose roots are the points of the stable 2^n orbit.

From the equations for the dependence of the periodic orbits on r , the dependence of the characteristic exponent can be obtained from eq. (2-10). For a period p orbit $\{x_i\}$, the probability density $P(x)$ is a set of p delta functions, $\delta(x - x_i)$. In this case, eq. (2-10) becomes

$$\lambda(r) = \sum_{i=1}^p \ln|f'(r, x_i)|. \quad (\text{B-5})$$

For the logistic equation we have studied, the slope is given by

$$f'(r, x_i) = r(1-2x_i). \quad (\text{B-6})$$

For the period 1 orbit, then, the characteristic exponent is

$$\lambda(r) = \ln|2-r|, \quad (\text{B-7})$$

for r in $[1, 3]$. The argument of the logarithm indicates that the bifurcations, where $\lambda \rightarrow 0$, from $x = 0$ to the period 1 occurs at $r = 1$ and from period 1 to period 2 occurs at $r = 3$. It also shows that the superstable orbit, where $\lambda \rightarrow -\infty$, is found at $r = 2$. Similarly for the period 2 orbit, we find

$$\lambda(r) = \ln|r^2-2r-4|, \quad (\text{B-8})$$

for r in $[3, r_{2-4}]$. The argument of the logarithm yields $r_{2-4} = 1 + \sqrt{6}$ and for the superstable period 2 orbit $r = 1 + \sqrt{5}$.

The characteristic exponent diverges at superstable orbits $\{x_i\}$ as one of the x_i approach the critical point $x_c = 0.5$, where the slope vanishes. To show this in general, we must first determine how the particular x_i in question, denoted by x^* , approaches x_c as the parameter approaches the superstable value r_s . x^* is given by one branch of roots of the polynomial $x - f^p(r, x)$. This gives x^* implicitly as a function of r ; that is, if $g(r)$ is the single branch containing x_c , then we write

$$x^*(r) = g(r) \quad (\text{B-9})$$

where $x_c = g(r_s)$. As can be seen from the bifurcation diagram of fig. 1, $g(r)$ is a smooth curve near r_s . If we define $dr = r - r_s$, then

$$dx^*(r) = \frac{d}{dr} g(r) dr. \quad (\text{B-10})$$

Close to r_s , the slope of $g(r)$ is very nearly a constant $k = (d/dr)g(r_s)$, which gives

$$dx^* \sim k dr. \quad (\text{B-11})$$

Next, we must determine how the slope changes near r_s . If we define $dx = x^* - x_c$ and dr as above, simple expansion gives

$$f'(r, x^*) = f'(r_s, x_c + dx) \sim f'(r_s, x_c) + f''(r_s, x_c) dx + O(dx^2). \quad (\text{B-12})$$

By definition the first, third and higher, terms vanish. Furthermore, $f''(r, x) = -2r$ so that we have

$$f'(r, x^*) = -2r_s dx \quad (\text{B-13})$$

near r_s . From eqs. (B-11) and (B-13), the slope's dependence on r near r_s is then given by

$$f'(r, x^*) \sim -2r_s k dr. \quad (\text{B-14})$$

The divergence of $\lambda(r)$ is dominated by the term in eq. (B-5) whose slope is vanishing, and so we can ignore the contributions from the other $(p-1)$ points along the orbit. Thus, we see from eq. (B-5) that the divergence of $\lambda(r)$ is logarithmic near r_s and given by

$$\lambda(r) \sim \ln|2r_s k dr| \sim \ln|r_s - r|. \quad (\text{B-15})$$

We now turn to the scaling properties of the superstable dips. As r approaches r_c the width w_n of the n th dip in $\lambda(r)$ decreases exponentially at a rate given by

$$w_n = r_{n+1} - r_n \sim \delta^{-n}. \quad (\text{B-16})$$

Furthermore, as the period doubles for each successive dip, the magnitude of $\lambda(r)$ decreases by a factor of two from its value on the previous dip. Within a single dip then, we can write

$$\lambda_n(r) = \frac{\lambda_0}{2^n} \ln \left| \frac{2(r_s - r)}{w_n} \right|, \quad (\text{B-17})$$

where λ_0 is a constant and r_s is the value of the parameter r at the superstable orbit. The depth of the superstable dips, as seen in fig. 3, decreases as r approaches r_c , although in principle, $\lambda(r)$ is infinite at the superstable orbits. This effect is due to the resolution in r at which fig. 3 was made, but also reveals

a scaling behavior of the superstable dips. This behavior can be accounted for by calculating the average of $\lambda(r)$ between period-doubling bifurcations. This average is given by

$$\lambda_n = \frac{1}{w_n} \int_{r_n}^{r_{n+1}} \frac{\lambda_0}{2^n} \ln \left| \frac{2(r_s - r)}{w_n} \right| dr. \quad (\text{B-18})$$

Since the dips are nearly symmetric, the lower limit can be changed from r_n to r_s . Performing the integration we find

$$\lambda_n = -\lambda_0/2^n. \quad (\text{B-19})$$

Solving eq. (2-9) for n in terms of r , we find

$$\lambda(r) = -\lambda'_0(r - r_c)^\tau \quad (\text{B-20})$$

where $\tau = \ln(2)/\ln(\delta) = 0.4498\dots$, and λ'_0 is a constant. Thus, we see that the average value of $\lambda(r)$ scales in a manner analogous to the envelope of positive characteristic exponent above r_c , as shown in ref. [22].

Admittedly these are simple considerations. A more detailed analysis along these lines, as developed by Daido [47], shows that the argument of the logarithm in eq. (B-17) approaches a universal polynomial. Eqs. (B-7) and (B-8) are the first approximations to the universal expression for the Lyapunov exponent in the period doubling regime.

Appendix C. Equivalence of parametric and additive noise

The equivalent parametric noise rule, introduced in section 3, allows one to construct a good approximation to the noisy bifurcation diagram of fig. 7 from the deterministic bifurcation diagram of fig. 1. Simply stated, the noisy bifurcation diagram is obtained by the convolution of the deterministic bifurcation diagram with a Gaussian probability distribution in r whose standard deviation is given by eq. (3-12b). A good approximation of this process can be constructed in the following manner: In a piece of paper cut a slit that is parallel to the x axis of fig. 1. The width of the slit in the r direction should be equal to several standard deviations of the equivalent parametric fluctuations. To estimate the noisy attractor at any particular value, place the slit over fig. 1 so that its midline lies at the parameter value of interest. Now project all the points of the neighboring attractors that are visible within the slit onto the midline. If the width of the slit is appropriately chosen, the resulting distribution of points will give the attractor in the presence of noise.

As a first estimate of the proper slit width, we assume that the slit width is constant in x and use eq. (3-12b). If the slit width is set at $3\sigma_q$, then 99.9% of the equivalent parametric fluctuations will have magnitudes that lie within the slit. For the example of fig. 7 the magnitude of the additive fluctuations is $\sigma_p = 10^{-3}$ and the estimated slit width is $3\sigma_q = 24\sigma_p = 0.024$. That is, the slit width to be used with fig. 1 to obtain fig. 7 should be 2.4% of the horizontal axis.

Let us now construct an approximation of fig. 7 using such a slit and fig. 1. Notice that the slopes of the bifurcation curves in fig. 1 are large near the period-doubling bifurcation to period 4. Consequently, the noisy bifurcation curves of fig. 7 are broadened near this point by the projection onto the midline of

the slit. Similarly, the bifurcation to the period 8 orbit is so close to the period 16 that the values of x visible within the slit never separate. The period 8 orbit, and all higher period orbits, never become visible in the noisy bifurcation diagram of fig. 7. The other noise effects discussed in section 3 can be explained in an analogous manner.

This approximation neglects the x -dependence of the equivalent parametric fluctuations. Notice, for example, that the width of the upper fork of the period 2 bifurcation curve is much thinner than that of the lower fork. One of the reasons for this is apparent from the slit construction: the upper bifurcation curve has a smaller slope. Another reason is that the equivalent fluctuations are not ergodic. Eq. (3-6) predicts that the q_n fluctuations are larger when $x_n \sim 0.8$, i.e. the upper fork, than they are when $x_n \sim 0.5$, i.e. the lower fork. At first glance this may appear to have an effect counter to that which we are trying to explain. However, the influence of the larger fluctuations on the upper fork is only felt on the succeeding iteration, that is, by the lower fork. Both of these effects combine to make the upper branch for fig. 7 considerably narrower than the lower.

In order to take this second effect into account automatically, rather than using a slit of fixed width, the width can be varied as a function of x . To do this it is necessary to consider the amplitude of the parametric fluctuations as a function of the value of x on the next iteration, when they are most strongly felt. From eq. (3-5) we see that

$$p_n = q_n f(x_n) \quad (\text{C-1})$$

and that

$$f(x_n) = (x_{n+1} - p_n)/r. \quad (\text{C-2})$$

Assuming $p_n \ll 1$ and eliminating $f(x_n)$ from eqs. (C-1) and (C-2), we find

$$q_n \sim rp_n/x_{n+1}. \quad (\text{C-3})$$

The fluctuation q_n is felt on the $(n+1)$ st iteration; that is, q_n affects x_{n+1} . Thus, at any given value of x the slit width $w(x)$ is given by

$$w(x) = 3\sigma_q(x) = 3r\sigma_p/x, \quad (\text{C-4})$$

if one takes three standard deviations.

References

- [1] J.P. Crutchfield and B.A. Huberman, *Phys. Lett.* 74A (1980) 407.
- [2] B.A. Huberman and J.P. Crutchfield, *Phys. Rev. Lett.* 43 (1979) 1743.
- [3] A. Libchaber and J. Maurer, *J. de Physique* 41 (1979) 51;
J.P. Gollub, S.V. Benson and J. Steinman, A Subharmonic Route to Turbulent Convection, in: *Annals of the New York Academy of Sciences* 357 (1980) 22.
- [4] Yu.N. Belyaev, A.A. Monakhov, S.A. Scherbakov and I.M. Yavorshaya, *JETP Lett.* 29 (1979) 295.
- [5] B.A. Huberman, J.P. Crutchfield and N.H. Packard, *App. Phys. Lett.* 37 (1980) 750.
- [6] J. Crutchfield, D. Farmer, N. Packard, R. Shaw, G. Jones and R. Donnelly, *Phys. Lett.* 76A (1980) 1.
- [7] E.N. Lorenz, *Annals of the New York Academy of Sciences* 357 (1980) 282;
and J. Crutchfield, D. Farmer, R. Shaw, G. Jones and R. Donnelly, *Phys. Lett.* 76A (1980) 1.
- [8] Y. Kuramoto found the cascade bifurcation in a set of nonlinear partial differential equations: *Diffusion-Induced Chemical Turbulence*, Physics Department, Kyoto University, Japan, preprint (1979).
- [9] M. Feigenbaum, *J. Stat. Phys.* 19 (1978) 25; 21 (1979) 669.
See also C. Tresser and P. Coulet, *CR. Acad. Sci.* 287A (1978) 577.
- [10] P. Collet and J.-P. Eckmann, *Iterated Maps of the Interval as Dynamical Systems*, Birkhauser (1980), and references therein.
- [11] Y. Oono and M. Osikawa, *Prog. Theo. Phys.* 64 (1980) 54.

- [12] For a pictorial introduction to dynamical systems theory see R.H. Abraham and C.D. Shaw, *Dynamics: The Geometry of Behavior* (Aerial Publications, Santa Cruz, California, 1982).
For a mathematical introduction to dynamical systems theory see D.R.J. Chillingworth, *Differential Topology with a View to Applications* (Pitman, 1976),
or J. Guckenheimer, J. Moser and S.E. Newhouse, *Dynamical Systems* (Birkhauser, 1980).
- [13] E.N. Lorenz, *J. Atmos. Sci.* 20 (1963) 130.
- [14] R. May, *Nature* 261 (1976) 459.
- [15] Numerical investigations of the features discussed here were also reported by S. Grossmann and S. Thomae, *Z. Naturforschung* 32A (1977) 1353.
- [16] B. Mandelbrot, *Fractals: Form, Chance, and Dimension* (W.H. Freeman, San Francisco, California, 1977).
- [17] J. Milnor and W. Thurston, *Institute for Advanced Study, Princeton University*, preprint (1977).
- [18] A.N. Kolmogorov, *Dokl. Akad. Nauk. SSSR* 119 (1958) 861.
- [19] R. Shaw, *Z. Naturforschung* 36a (1981) 80.
- [20] J. Guckenheimer, *Commun. Math. Phys.* 70 (1979) 133.
- [21] For the general theory of Lyapunov characteristic exponents see V.I. Oseledec, *Trans. Moscow Math. Soc.* 19 (1968) 197;
Ja.B. Pesin, *Russ. Math. Surv.* 32 (1977) 55.
- [22] B.A. Huberman and J. Rudnick, *Phys. Rev. Lett.* 45 (1980) 154.
- [23] J.P. Crutchfield and R. Shaw, unpublished;
T. Geisel, J. Nierwetberg and J. Keller, *Phys. Lett.* 86A (1981) 75.
- [24] At $r = 4.0$ the map becomes fully two-onto-one, taking the entire interval onto itself with one fold. λ can be calculated directly at this point from eq. (2-10) to find $\lambda(4.0) = \ln(2)$; in other words, one bit of information is lost per iteration.
- [25] P. Grassberger, *Physics Dept., University of Wupertal, Germany*, preprint WU-B-80-33 (1980).
- [26] B.A. Huberman and A. Zisook, *Phys. Rev. Lett.* 46 (1981) 626;
J.D. Farmer, *Phys. Rev. Lett.* 42 (1981) 179;
S. Grassmann, *J. Stat. Phys.* 26 (1981) 485.
- [27] G. Mayer-Kress and H. Haken, *J. Stat. Phys.* 26 (1981) 149.
- [28] J. Yorke and E. Yorke, *J. Stat. Phys.* 21 (1979) 263.
- [29] P. Manneville and Y. Pomeau, *Phys. Lett.* 75A (1979) 1.
- [30] P. Manneville and Y. Pomeau, *Commun. Math. Phys.* 79 (1980) 189.
- [31] J.P. Eckmann, L. Thomas and P. Wittmer, *J. Phys. A* 14 (1982) 3153.
- [32] J.E. Hirsch, B.A. Huberman and D.J. Scalapino, *Phys. Rev. A* 25 (1982) 519.
- [33] H. Haken and G. Mayer-Kress, *Z. Phys. B* 43 (1981) 185.
- [34] S.-K. Ma, *Modern Theory of Critical Phenomena* (Benjamin, Massachusetts, 1976).
- [35] B. Shraiman, C.E. Wayne and P.C. Martin, *Phys. Rev. Lett.* 46 (1981) 935.
- [36] J.P. Crutchfield, M. Nauenberg and J. Rudnick, *Phys. Rev. Lett.* 46 (1981) 933.
- [37] C.E. Shannon and W. Weaver, *The Mathematical Theory of Communication* (University of Illinois Press, 1962).
- [38] S. Chandrasekhar, *Rev. Mod. Phys.* 15 (1943) 1.
- [39] D. Ruelle and F. Takens, *Comm. Math. Phys.* 50 (1976) 69.
- [40] See, for example, Y. Ueda, C. Hayashi and N. Akamatsu, *Elect. Comm. Jap.* 56-A (1973) 27;
P.J. Holmes, *Phil. Trans. Roy. Soc. Lond.* 292 (1979) 419;
F.C. Moon, *Experimental Models for Strange Attractor Vibrations in Elastic Systems*, in: *New Approaches to Nonlinear Problems in Dynamics*, ed. P.J. Holmes (S.I.A.M., Philadelphia, 1980).
- [41] J.C. Roux, A. Rossi, S. Bachelart and C. Vidal, *Phys. Lett.* 77A (1980) 391.
- [42] N.H. Packard, J.P. Crutchfield, D. Farmer and R. Shaw, *Phys. Rev. Lett.* 45 (1980) 712;
H. Froehling, J.P. Crutchfield, J.D. Farmer, N.H. Packard and R. Shaw, *On Determining the Dimension of Chaotic Flows*, *Physica* 3D (1981) 605.
- [43] F. Takens, *Detecting Strange Attractors in Turbulence*, to appear in the *Proceedings of the Warwick Symposium* (1980).
- [44] D. Ruelle, *Phys. Lett.* 72A (1979) 81.
- [45] Ju.I. Kifer, *USSR Izvestija* 8 (1974) 1083.
- [46] The following references represent one approach to these questions:
J.P. Crutchfield and N.H. Packard, *Int'l J. Theo. Phys.* 21 (1982) 433; also in: *Evolution of Ordered and Chaotic Patterns in Systems Treated by the Natural Sciences and Mathematics*, ed. H. Haken (Springer-Verlag, Berlin, 1982); and to appear in the *Proceedings of the Order in Chaos Conference*, Los Alamos, New Mexico (1982).
- [47] H. Daido, *Phys. Lett.* 83A (1981) 246.

CHAPTER 7

Solid State Turbulence

7.1. Some Historical Remarks

Hydrodynamic turbulence is often credited as the physical phenomenon that instigated the study of (dissipative) chaotic dynamics. The work of Lorenz in the '60's and a decade later of Ruelle and Takens on low-dimensional dynamics in hydrodynamic flows lend credence to this historical view. Upon closer examination of dynamical systems work immediately preceding Lorenz, one finds that both Hayashi and Ulam observed chaotic behavior in electronic simulations on analog and digital computers. The first experiential observation of chaos, though, predates this by thirty years.

In the 10 September 1927 issue of Nature Balthasar van der Pol, a Dutch radio engineer, reported on frequency locking and subharmonic generation in driven nonlinear "relaxation" oscillators. As many have now come to realize, the occurrence of a rich subharmonic structure, or "frequency demultiplication" as van der Pol called it, often presages the appearance of chaos. This is just what van der Pol discovered between the frequency locking regimes. In his words,

"Often an irregular noise is heard in the telephone receiver before the frequency jumps to the next lower value."

As a radio engineer he was most interested in the frequency demultiplica-

tion phenomenon as a practical device for electronic signal processing. Unfortunately, he was not interested in the nature of the noise, which he largely ignored. He continues,

"However, this [noise] is a subsidiary phenomenon, the main effect being the regular frequency demultiplication."

These early examples of experimental chaos in analog electronic devices fall under the rubric of "solid state turbulence". The application of solid state turbulence now ranges from the use of nonlinear oscillators modeling ideal anharmonic crystals to the interaction of densely-packed nonlinear semiconductor devices in state-of-the art integrated circuits.

Just as van der Pol found, while nonlinearity is often necessary to perform signal processing, such as demodulation and amplification, it also leads to noise production. As long as noise or chaos is undesirable, there will be inherent compromises in building nonlinear solid state systems. Understanding the cause of solid state turbulence allows one to make the trade off intelligently. One wonders if and when chaos will be realized to play a positive role in solid state dynamics.

The first paper in solid state turbulence makes the simple remark that chaotic behavior is important to the dynamics of nonlinear solid state systems. The second paper addresses the specific problem of how experimentally observed noise arises in superconducting Josephson junction devices. The underlying dynamics of these devices is just that of a driven, damped pendulum. As such, this dynamics is a superset of that

7.3

exhibited in the first paper on simple anharmonic oscillators.

There are two interesting aspects of the pendulum dynamics. The first is the simultaneous occurrence of slow time scale diffusive motion and fast time scale chaotic oscillations. As far as I am aware this was the first report of deterministic diffusion in a dissipative physical system. The picture one gleans from simulations of this system is of a localized chaotic attractor diffusing randomly along an infinite lattice. The second aspect is the intermittent jumping between different attractor basins giving rise to burst-like behavior and power-law divergence in the power spectrum. These two behavior types occur in a very limited parameter regime of the first paper's anharmonic oscillator.

7.2. Chaotic States of Anharmonic Systems in Periodic Fields

Chaotic States of Anharmonic Systems in Periodic Fields

B. A. Huberman

Xerox Palo Alto Research Center, Palo Alto, California 94304

and

J. P. Crutchfield

Physics Department, University of California, Santa Cruz, California 95064

(Received 17 September 1979)

It is shown that the nonlinear dynamics of anharmonically interacting particles in the presence of periodic fields leads to a set of cascading bifurcations into a chaotic state. This state is characterized by the existence of a strange attractor in phase space and associated broadband noise in the spectral density. It is suggested that solid-state turbulence is likely to be found in weakly pinned charge-density-wave systems and superionic conductors.

The problem of anharmonicity in condensed matter is an old and important one. Relevant to thermal expansion, heat conductivity, impurity modes, lattice dynamics,¹ and nonlinear optics,² to name a few topics, it led to the development of perturbation techniques that have been quite successful in explaining the experimental results. There exist a number of systems, however, for which small-amplitude results are not entirely appropriate. As exemplified by displacive phase transitions and superionic conductors, the dynamics of soft-mode behavior and ion transport is characterized by large atomic displacements which require nonperturbative theories. In the absence of damping processes, singular results have been obtained, indicating the existence of

kinks or solitons.³ These nonlinear solutions also appear as relevant degrees of freedom in field theory.^{4,5}

In this paper we study the nonlinear dynamics of particles in anharmonic potentials in the presence of an external periodic field. As we will show, there exists a range of parameter values for which the solutions of the corresponding deterministic equation display a set of cascading bifurcations into a chaotic state, characterized by a strange attractor in phase space, and associated broadband noise in the spectral density. These features are reminiscent of the transition to turbulence encountered in stressed fluids,^{5,6} some dissipative dynamical systems,⁷ and simple mathematical models.⁸ By constructing the re-

turn maps associated with the Poincaré sections of our problem we are able to determine that the transition to the chaotic regime belongs to the same universality class as the recursion relations recently studied by Feigenbaum.⁹ We also determine the phase diagram in the amplitude-frequency plane and establish the existence of hysteresis effects. Finally, we suggest that solid-state turbulence is likely to be found in weakly pinned charge-density-wave (CDW) systems and superionic conductors.

Consider a particle of mass m and charge Q moving in a one-dimensional potential given by

$$V(\eta) = \frac{1}{2}a\eta^2 - \frac{1}{4}b\eta^4, \quad (1)$$

where η denotes the particle displacement from equilibrium, and the constants a and b are positive. Furthermore, we assume that the particle is subjected to a periodic external electric field of frequency ω .¹⁰ If the coupling to all the other degrees of freedom of the solid is characterized by a phenomenological damping coefficient γ , the deterministic equation of motion for the charge reads

$$m d^2\eta/dt^2 + \gamma d\eta/dt + m\omega_0^2\eta - b\eta^3 - QE \cos(\omega t) = 0 \quad (2)$$

with $\omega_0^2 = a/m$ and $\gamma > 0$. In the limit of small fields and displacements, the solutions of Eq. (2) can be obtained via perturbation theory.¹¹ Within that scheme the effect of anharmonicity is to produce a renormalization of the damping coefficient and to cause mixing between the frequencies ω and ω_0 . The phase portraits acquire some complexity but can, nevertheless, be analyzed in terms of simple limit cycles and fixed points. But as the amplitude of the electric field becomes large the consequent large- η behavior becomes increasingly difficult to treat perturbatively and the limit cycles encountered in the small-field limit become unstable. As we show below, in the large-amplitude regime one encounters a rich variety of behavior, which includes aperiodic solutions with very sensitive dependence on initial conditions.

In order to study Eq. (2), it is convenient to rewrite it in dimensionless form. Using the saddle-point solution, η_0 , of the potential $V(\eta)$ as a natural length scale, and the inverse natural frequency ω_0^{-1} to set the basic time scale, we

can rewrite Eq. (2) as

$$d^2\psi/d\tau^2 + \alpha d\psi/d\tau + \psi - 4\psi^3 = \Gamma \cos[(\omega/\omega_0)\tau] \quad (3)$$

with $\psi = \eta/2\eta_0$, $\tau = t\omega_0$, $\alpha = \gamma/m\omega_0$, $\Gamma = \eta_0 QE/8V_0$, and where

$$V_0 = a^2/4b \quad (4a)$$

and

$$\eta_0 = (a/b)^{1/2}. \quad (4b)$$

Equation (3) was solved by using a Systron-Donner analog computer to obtain the phase portraits and time series for the spectral densities as a function of Γ and ω for fixed α . For values of Γ large enough so as to make the particle visit the anharmonic component of the potential ($|\psi| \sim \frac{1}{2}$), the bifurcation scheme that results differs markedly from that which one obtains using perturbation theory. In Fig. 1 we show the schematic phase diagram for fixed values of Γ and α as a function of the external field frequency, normalized to ω_0 . Starting at point A, as the frequency decreases the solutions correspond to limit cycles of period 1 with increasing amplitude. Be-

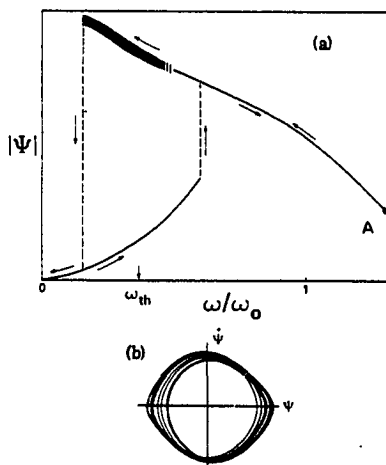


FIG. 1. (a) Schematic phase diagram for the anharmonic oscillator of Eq. (3). The thin solid lines denote periodic solutions, whereas the thick solid one corresponds to the chaotic state. The short vertical lines denote the set of cascading bifurcations. For the actual parameter values used ($\alpha = 0.4$, $\Gamma = 0.115$) we found $\omega_{th} \approx 0.5567\omega_0$. (b) Phase portrait of the strange attractor for $\omega = 0.552\omega_0$.

low $\omega/\omega_0=1$, a set of cascading bifurcations at frequencies ω_n starts taking place until a chaotic state, characterized by the appearance of a strange attractor in phase space [Fig. 1(b)], is reached at ω_{th} .¹² A more vivid picture of this transition can be obtained by looking at the power spectral density $S(\omega)$, which is depicted in Fig. 2. Each part of Fig. 2 is the average of ten spectral densities, obtained using the fast Fourier transform to process 4096-point time series which were initially shaped by a cosine bell window.

For values of $\omega > \omega_{th}$ [Fig. 2(a)] sharp peaks appear, which correspond to periodic states characterized by limit cycles of period $2^n T$, where T is the driving period. Beyond the chaotic threshold the power spectrum acquires the shape shown in Fig. 2(b). As can be seen, large-amplitude broadband noise appears, together with some well-defined frequencies. For lower values of ω [Fig. 2(c)] the system appears even more chaotic, and the strange attractor acquires a two-fold band shape. If the frequency is lowered even further a sudden transition to an ordered state of period 1 takes place, a point below which perturbation theory becomes applicable. On reversing the sequence we have just described, the periodic behavior persists up to frequencies $\omega > \omega_{th}$, with a discontinuous jump into an ordered state with same period but larger amplitude. For our parameter values the hysteresis loop has $\Delta\omega = 0.143\omega_0$.

A sequence of Poincaré sections of the strange attractor, which we show in Fig. 2(d) at multiples of $\frac{1}{4}\pi$ in the driving phase, offers some insight into the nature of the chaotic state. As can be seen, it exhibits the typical folding process discussed by Shaw,¹³ which signals the irreversible mixing and exponential divergence of trajectories. In fact, inspection of the sequence of sections reveals two complete folding processes per cycle of the driving force. For slightly larger driving frequency an asymmetric strange attractor, exhibiting a single folding process, was found.

In order to study in more detail the set of cascading bifurcations that precede the onset of the turbulent regime we constructed the return maps⁸ associated with the Poincaré sections as $\omega - \omega_{th}^+$ and for $\omega < \omega_{th}$. In this fashion we circumvented the errors associated with determining the exact frequencies at which new bifurcations set in. Although the details will be presented elsewhere, we observed that the return maps showed a single-hump feature with a parabolic maximum,

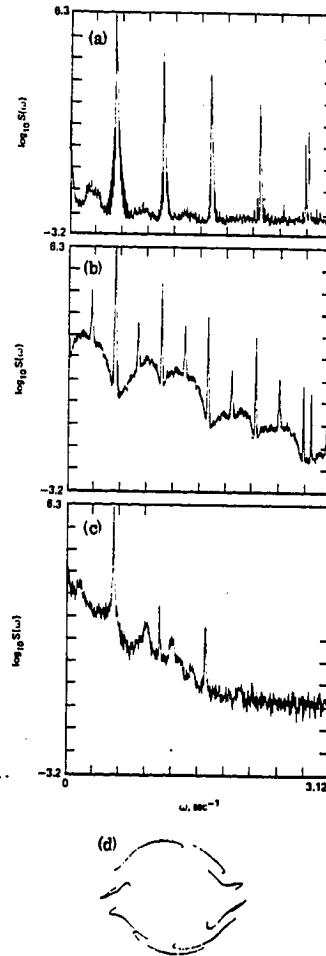


FIG. 2. (a)-(c) Fourier transform of the velocity autocorrelation function for several values of the field frequency with $\alpha = 0.4$ and $\Gamma = 0.115$, $\omega_0 = 1 \text{ sec}^{-1}$. (a) Driving frequency = 0.5623 sec^{-1} . (b) Driving frequency = 0.5558 sec^{-1} . (c) Driving frequency = 0.5529 sec^{-1} . (d) Poincaré sections of the strange attractor for $\omega = 0.5529\omega_0$ at multiples of $\frac{1}{4}\pi$ in the driving phase.

characteristic of the general class of recursion relations studied by Feigenbaum.⁹ We are therefore able to ascertain that for large n the bifurcation sequence will display the same universal behavior, i.e.,

$$(T_{th} - T_n)/(T_{th} - T_{n+1}) = \delta, \quad (5)$$

where $\delta = 4.669\,201\,609\dots$ and T_n is the value of the driving-force period at which the period- $2^n T_n$ limit cycle bifurcates to one of period $2^{n+1}T_{n+1}$.

The phenomena which we have just described could be found in solids whose anharmonic degrees of freedom can couple to a periodic field. Two likely candidates are weakly pinned charge-density waves (CDW) in anisotropic solids,¹⁴ and superionic conductors.¹⁵ In CDW systems, such as $K_2Pt(CN)_4Br_{0.3} \cdot 3H_2O$, tetrathiafulvalene-tetracyanoquinodimethane, and $NbSe_3$, it has been determined that charged impurities or commensurability act so as to prevent the CDW from freely sliding along the background lattice.¹⁶⁻¹⁸ In that situation the enhanced electron density executes low-frequency (microwave to low infrared)^{19,20} oscillations about the pinning center, and can be depinned by applying an external electric field of small magnitude (typically 10^{-2} V for $NbSe_3$). It should therefore be possible to drive the CDW in $NbSe_3$ into the turbulent regime by applying a microwave or infrared field of small magnitude in the temperature regime $59\text{ K} < T < 144\text{ K}$ (the region where only one CDW is present²¹). In fact, a recent experiment of Fleming and Grimes²² reports conduction noise in $NbSe_3$ at temperatures below 59 K , where the second instability sets in. Although this observation was made in the presence of a static electric field, it is possible that the coexistence of two CDW's might have produced a time-varying field of the type we have discussed.²³

In superionic conductors, the ionic carriers oscillate around their potential minima with typically low optical-phonon frequencies²⁴ and hop over potential barriers with heights of order 0.1 to 0.2 eV. In particular, a class of superionic conductors displays large conduction anisotropies, a fact which renders the problem one-dimensional from our point of view. With $Li_2Ti_3O_8$, as an example,²⁵ it would require an infrared laser of moderate power to generate the phase diagram we have studied. The observation of the turbulent state could then be made by monitoring the absorption spectra.

In conclusion, we have shown that chaotic behavior is expected to occur in strongly anharmonic systems in the presence of periodic fields. Since the suggestions which we have made for the experimental search are by no means exhaustive, it is likely that such a phenomenon will be found in many other anharmonic condensed-matter systems.²⁶

We have profited from conversations with

G. Ahlers, S. Doniach, R. Fleming, and C. Her-ring. We wish to thank D. Farmer, H. Froehling, N. Packard, and R. Shaw, of the University of California, Santa Cruz, Dynamical Systems Group, for the use of their simulation system and for their helpful suggestions.

¹M. Born and K. Huang, *Dynamical Theory of Crystal Lattices* (Oxford University Press, Oxford, 1954).

²N. Bloembergen, *Nonlinear Optics* (Benjamin, New York, 1965).

³J. A. Krumhansl and J. R. Schrieffer, *Phys. Rev. B* **11**, 3535 (1975). A recent review of the subject can be found in *Solitons and Condensed Matter Physics*, edited by A. R. Bishop and T. Schneider (Springer Verlag, New York, 1978).

⁴R. F. Dashen, B. Hasslacher, and A. Neveu, *Phys. Rev. D* **10**, 4114 (1974).

⁵See G. Ahlers and R. P. Behringer, *Prog. Theor. Phys. Suppl.* **64**, 186 (1978); H. L. Swinney and J. P. Gollub, *Phys. Today* **31**, No. 8, 41 (1978).

⁶D. Ruelle, in *Lecture Notes in Physics*, edited by G. Dell'Antonio, S. Doplicher, and G. Jona-Lasinio (Springer-Verlag, New York, 1978), Vol. 80, p. 341.

⁷I. Shimada and T. Nagashima, *Prog. Theor. Phys.* **59**, 1033 (1978); R. Shaw, unpublished.

⁸T. Li and J. Yorke, in *Dynamical Systems, an International Symposium*, edited by L. Cesari (Academic, New York, 1978), Vol. 2; R. May, *Nature* **261**, 459 (1976).

⁹M. Feigenbaum, *J. Stat. Phys.* **19**, 25 (1978), and to be published.

¹⁰Although for the sake of concreteness we restrict ourselves to the case of charged particle in an electric field, these considerations also apply to other periodic fields such as strains or magnetic forces.

¹¹N. N. Bogoliubov and Y. A. Mitropolsky, *Asymptotic Methods in the Theory on Non-Linear Oscillations* (Gordon and Breach, New York, 1961).

¹²From rigorous mathematical considerations, A. D. Morosov, *Differ. Uravn.* **12**, 241 (1976) [*Differ. Equa.* **12**, 164 (1976)] has indicated the possibility of strange attractor solutions of Eq. (2) by proving the existence of homoclinic intersections of the stable and unstable manifolds.

¹³R. Shaw, to be published.

¹⁴F. J. Di Salvo and T. M. Rice, *Phys. Today* **32**, No. 4, 32 (1979).

¹⁵J. B. Boyce and B. A. Huberman, *Phys. Rep.* **51**, 189 (1979).

¹⁶K. Maki, *Phys. Rev. Lett.* **39**, 46 (1977).

¹⁷P. A. Lee and T. M. Rice, *Phys. Rev. B* **19**, 3970 (1979).

¹⁸J. Bardeen, *Phys. Rev. Lett.* **42**, 1498 (1979).

¹⁹P. Bruesch, S. Strassler, and H. R. Zeller, *Phys. Rev. B* **12**, 219 (1975).

²⁰J. E. Eldridge, *Solid State Commun.* **19**, 607 (1976).

²¹P. Monceau, N. P. Ong, A. M. Portis, A. Meers-

chaut, and J. Rouxel, *Phys. Rev. Lett.* **37**, 37 602 (1976); R. M. Fleming, D. E. Moncton, and D. B. McWhan, *Phys. Rev. B* **18**, 5560 (1978).

²²R. M. Fleming and C. C. Grimes, *Phys. Rev. Lett.* **42**, 1423 (1979).

²³It has recently been shown by J. C. Gill (to be published) that in a small temperature range below $T = 59^\circ\text{K}$ there exist different thresholds for depinning the two charge-density waves which at a lower temperature become locked together.

²⁴M. J. Delaney and S. Ushioda, in *Physics of Superionic Conductors*, edited by M. B. Salamon (Springer-Verlag, New York, 1979).

²⁵B. A. Huberman and J. B. Boyce, *Solid State Commun.* **25**, 759 (1978).

²⁶In a separate paper we report the results for $a > 0$, $b < 0$ in Eq. (1) which also show strange-attractor behavior, and $a < 0$, $b < 0$. Results for this latter case have also been obtained by P. J. Holmes, *Appl. Math. Mod.* **1**, 362 (1977), and J. P. Crutchfield, unpublished.

7.3. Noise Phenomena in Josephson Junctions

Noise phenomena in Josephson junctions

B. A. Huberman

Xerox Palo Alto Research Center, Palo Alto, California 94304

J. P. Crutchfield and N. H. Packard

Physics Department, University of California, Santa Cruz, California 95064

(Received 30 June 1980; accepted for publication 13 August 1980)

We suggest that the reported noise-rise phenomenon observed in Josephson oscillators can be understood in terms of the full nonlinear and deterministic junction dynamics. We show that the drive damped pendulum equation describing the junction behavior exhibits chaotic solutions associated with the appearance of strange attractors in phase space. These results are relevant to the general problem of turbulent behavior of anharmonic systems.

PACS numbers: 74.50. + r

Several experiments on Josephson junction oscillators have revealed a striking noise-rise phenomena which cannot be accounted for in terms of thermal fluctuations. Chiao and co-workers¹ have reported that when superconducting junctions are used as unbiased parametric amplifiers (SUPARAMPS), an increase in the amplitude of the oscillatory driving signal can lead to broad-band voltage fluctuations with equivalent noise temperatures of 5×10^4 K. This behavior, which has been observed in many other experiments,^{2,3} defies explanations based on either amplification of thermal noise⁴ or stability analysis of the equations governing the phase oscillations.⁵

In this letter, we suggest that this broad-band noise-rise phenomenon can be understood in terms of the existence of chaotic solutions to the full nonlinear junction dynamics. This turbulent behavior, which gives rise to broad-band power spectra, is associated with the appearance of a strange attractor⁶ in phase space. Besides providing an explanation for the observed voltage fluctuations in some Josephson devices, our theory points to these junctions as attractive experimental tools for the study of solid-state turbulence and nonlinear dynamics. Also, since the equations that we study appear in a number of different systems, our results are relevant to problems that range from soliton dynamics⁷ to solid-state turbulence.^{8,9}

Consider a Josephson oscillator in the presence of microwave radiation and described by a current-driven shunted-junction model.¹⁰ If C is the junction capacitance, R the normal-state resistance, and V the potential difference across the junction, the superconducting phase φ is determined by the following equations:

$$C \frac{dV}{dt} + \frac{V}{R} + I_c \sin\varphi = I_J \cos\omega_d t, \quad (1)$$

$$\frac{d\varphi}{dt} = \frac{2e}{\hbar} V, \quad (2)$$

where I_c is the critical supercurrent and I_J the amplitude of the microwave field at the driving frequency ω_d . Replacing the potential in Eq. (1) by its expression in terms of the phase [Eq. (2)], we obtain the nonlinear differential equation for φ

$$\frac{d^2\varphi}{dt^2} + \frac{1}{\tau} \frac{d\varphi}{dt} + \omega_0^2 \sin\varphi = \frac{2e}{\hbar C} I_J \cos\omega_d t, \quad (3)$$

where $\tau \equiv (RC)$ is the damping time and $\omega_0 = (2eI_c/\hbar C)^{1/2}$ the plasma frequency of the junction. This description of the driven damped motion of a particle in a spatially periodic potential forms the basis of extensive work on a number of devices utilizing either point junctions or microbridges.^{2,10-13} It also appears as a generalization of the anharmonicity problem in solid-state systems driven by periodic fields.^{8,9}

For small enough values of the amplitude of the phase oscillations, it is possible to study the stability of Eq. (3) against fluctuations by converting it into a Mathieu-type equation.¹² As the value of φ increases, however, the first two terms of a Taylor-series expansion for the $\sin\varphi$ term lead to a cascade of bifurcations into a chaotic regime which cannot be obtained via perturbation theory.⁸

In order to study the full nonlinear solutions of Eq. (3) we express it in terms of dimensionless variables. Introducing a new time scale $t' = t/\alpha$ and writing $\Gamma \equiv (2e^2\alpha/\hbar C)I_J$ and $\Omega_0 \equiv \alpha\omega_0$, we obtain

$$\frac{d^2\varphi}{dt'^2} + \frac{\alpha}{\tau} \frac{d\varphi}{dt'} + \Omega_0^2 \sin\varphi = \Gamma \cos\omega_d t'. \quad (4)$$

This equation was solved by using a hybrid digital-analog computer system. Starting with typical junctions parameters such as $R = 4 \Omega$, $C = 5$ pF, $I_c = 100 \mu\text{A}$, and choosing $\alpha = 10^{-11}$, we find $\alpha/\tau = 0.5$ and $\Omega_0^2 = 6.4$.

Although a detailed description of the possible solutions to Eq. (4) will be published elsewhere, our main result can be summarized in the bifurcation diagram of Fig. 1, where we show the types of behaviors to be expected for different values of the driving amplitude and frequency. As can be seen, for frequencies that are either much smaller or much larger than ω_0 one encounters periodic solutions which can, in some cases, become fairly complicated (i.e., subharmonic and harmonic content, hysteresis loops, etc.). A noteworthy periodic regime, which occurs at fairly high values of Γ , is the one in which φ undergoes successive 2π rotations in phase with the driving frequency, corresponding to the periodic motion of the particle from one potential well to another (region A). This kind of behavior represents the running periodic solutions described by Levi *et al.*¹²

In region B, the phase amplitude is confined to one potential well, i.e., $0 < \varphi < 2\pi$. In this regime the solutions exhib-

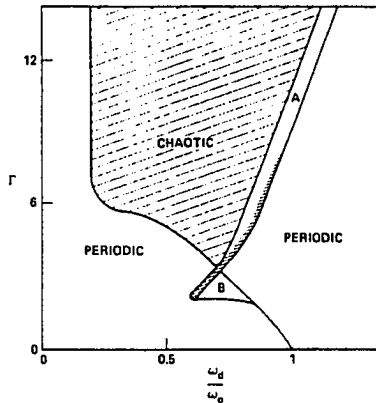


FIG. 1. Bifurcation diagram for Eq. (4) with $\alpha/\tau = 0.5$, $\Omega_0^2 = 6.4$, and $\alpha = 10^{-11}$, obtained by varying ω_d at constant Γ . The chaotic regime contains small regions of periodic solutions. Region A: periodic running solutions. Region B: amplitude hysteresis and cascading bifurcations of Ref. 8. Narrow shaded region: full extent of period-doubling chaos.

it the amplitude hysteresis and the set of period-doubling cascading bifurcations into a chaotic state which was found for the anharmonic potential.⁸ Beyond this regime, φ is no longer bounded and a complicated turbulent behavior ensues, characterized by strange attractors in phase space¹⁴ whose Poincaré sections¹⁵ display an infinite lattice structure with the spatial periodicity of the potential (Fig. 2). The structure of these strange attractors can be understood in terms of two distinct time scales which the motion exhibits: The shorter time scale corresponds to fast oscillations between a small number of wells; the longer time scale is associated with a slower diffusion throughout the lattice. This turbulent behavior is best characterized by the power spectral density shown in Fig. 3, which was obtained for the parameter values $\Gamma = 3.8$, $\omega_d/\omega_0 = 0.64$. $S(\omega)$ denotes the Fourier transform of the autocorrelation function for the time derivative of the phase which, by Eq. (2), is proportional to the voltage fluctuations across the junction. This broad-band spectrum, generated by the deterministic Eq. (4), is quite similar to some of those observed in Josephson oscillators



FIG. 2. Poincaré section of the strange attractor at parameter values $\Gamma = 3.8$ and $\omega_d/\omega_0 = 0.64$. Points comprising the section are taken at positive-going zero crossings of the driving force (zero phase). The section represents a six-well segment of the strange attractor lattice. The vertical and horizontal coordinates denote $\dot{\varphi}$ and φ , respectively.

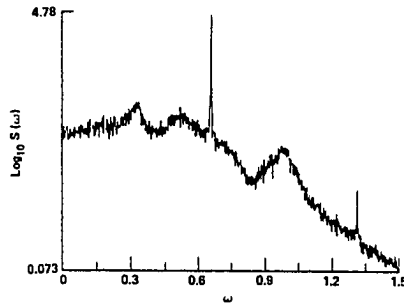


FIG. 3. Power spectrum of the strange attractor for same parameter values of Fig. 2. $S(\omega)$ is the Fourier transform of the voltage autocorrelation function, computed from 12 averages of a 4096-point fast Fourier transform. The frequency has been normalized to ω_0 .

operated as parametric amplifiers.¹⁻³ We should also add that even though the sharp peak observed at the driving frequency appears narrow, it broadens at larger driving amplitudes.

Our results suggest an explanation for the noise-rise phenomenon based on the intrinsic nonlinearity of the junction dynamics. Whether this theory accurately describes the observed behavior depends on the extent to which the driven damped pendulum models the actual junction dynamics. If that were the case, the phase diagram of Fig. 1 could also provide some guidelines for operating superconducting parametric amplifiers in noise-free regions. Moreover, if broad-band noise in Josephson oscillators is due to the presence of strange attractors in phase space, they could become likely candidates for the study of solid-state turbulence and nonlinear dynamics, a subject which is just beginning to be studied experimentally.

Finally, we should point out that these results are of relevance to the wide variety of problems that can be modeled by the driven damped pendulum of Eq. (4). In particular, they show that the range of parameter values for which chaotic solutions can occur is much larger than that found for the single-well anharmonic problem.⁸ This is of importance to experiments dealing with turbulent properties of solids.

We wish to thank T. Claeson for his encouragement and many instructive remarks. We have also benefited from conversations with R. Y. Chiao, D. Farmer, P. L. Richards, R. Shaw, and L. Wennerberg. Part of this work has been supported by NSF Grant No. 41350-21299.

¹R. Y. Chiao, M. J. Feldman, D. W. Peterson, B. A. Tucker, and M. T. Levinsen, in *Future Trends in Superconductive Electronics*, AIP Conf. Proc. 44 (AIP, New York, 1978).

²Y. Taur and P. L. Richards, *J. Appl. Phys.* 48, 1321 (1977).

³T. Claeson (private communication).

⁴M. J. Feldman, *J. Appl. Phys.* 48, 1301 (1977).

⁵D. W. Peterson, Ph.D. thesis, University of California, Berkeley, 1978 (unpublished).

⁸That is, a region of phase space characterized by the fact that (i) all trajectories in its neighborhood must enter it and (ii) almost all trajectories diverge within the attractor. For a more rigorous definition, see D. Ruelle and F. Takens, *Commun. Math. Phys.* **20**, 167 (1971).

⁹See, for example, *Solitons and Condensed Matter Physics*, edited by A. R. Bishop and T. Schneider (Springer, New York, 1978).

¹⁰B. A. Huberman and J. P. Crutchfield, *Phys. Rev. Lett.* **43**, 1743 (1979).

¹¹C. Herring and B. A. Huberman, *Appl. Phys. Lett.* **36**, 976 (1980).

¹²W. C. Stewart, *Appl. Phys. Lett.* **12**, 277 (1968); E. E. McCumber, *J. Appl. Phys.* **39**, 3113 (1968). A recent review appears in N. F. Pedersen, M. R. Samuelsen, and K. Sævermark, *J. Appl. Phys.* **44**, 5120 (1973). This model assumes no frequency dependence for the quasiparticle and pair current amplitudes, so it cannot be expected to describe the junction in detail. We have also neglected the phase dependence of the quasiparticle resistance,

an approximation which has been shown not to change the qualitative predictions of the theory.

¹³See, for example, V. N. Belykh, N. F. Pedersen, and O. H. Soerensen, *Phys. Rev. B* **16**, 4853–4860 (1977); **16**, 4860 (1977).

¹⁴M. Levi, F. C. Hoppensteadt, and W. L. Miranker, *Q. Appl. Math.* **36**, 177 (1978).

¹⁵N. F. Pedersen, O. H. Soerensen, B. Ducholm, and J. Mygind, *J. Low Temp. Phys.* **38**, 1 (1980).

¹⁶This result is supported by the qualitative investigations of Ref. 11, which show the existence of transversal homoclinic intersections of the stable and unstable manifolds.

¹⁷See, for example, H. W. Hirsch and S. Smale, *Differential Equations, Dynamical Systems and Linear Algebra* (Academic, New York, 1974).

CHAPTER 8

Hydrodynamic Chaos

8.1. Experimental Observation of Chaos

The physical relevance of chaotic dynamics is decided by its application to experiments. The previous chapters discussed the successful analysis of chaotic dynamics in nonlinear electronic circuits. Needless to say, these are physical devices subject to thermal fluctuations, errors in construction, and measurement uncertainties. On this basis alone, one may conclude that the study of chaotic dynamics has proved its usefulness by providing insight to some portion of the physical world. This is not a sufficiently convincing verification of chaotic dynamics, however, because to a very good approximation one knows what the relevant degrees of freedom are in these systems. The real test of dynamical systems lies in the analysis of experiments for which the relevant degrees of freedom are not known a priori.

This chapter presents the analysis of two hydrodynamic flow experiments with a tremendous number of intrinsic degrees of freedom. As will be seen, in the regimes studied, the flows exhibit very low-dimensional periodic and chaotic behavior that can be successfully characterized using dynamical systems concepts.

The analysis of chaotic signals is a fairly standard procedure. The first step consists of a rough classification of behavior as a function

of control parameters using power spectra. Bifurcations can be identified by changes in the power spectra. The changes can be quite varied: the appearance or disappearance of periodic components (peaks) or broad band noise, the increase or decrease in the DC component, the appearance of subharmonic or incommensurate frequencies, or alterations in the shape of the broad band noise.

Once an interesting control parameter regime is selected the actual dynamical systems analysis of the signal begins with the reconstruction of a state space. This step is absolutely essential for further analysis. A number of reconstruction methods have been employed depending on the nature of the experiment. For example, the coordinates of the reconstructed space have been taken as

- (1) successive delays in the signal;
- (2) the signal's derivatives;
- (3) signals from spatially separated points; and
- (4) various system observables.

If the chaotic behavior is of sufficiently low dimension, it is possible to make a picture revealing the attractor's structure. To reduce the attractor's dimensionality, cross sections or Poincare sections can be made. This renders the dynamics discrete in time. Occasionally, a further reduction by coordinatizing data on the section can be employed. These attractor visualization techniques typically cannot be applied to attractors with more than four dimensions.

8.3

As I have emphasized the most important physical property of a chaotic physical system is its degree of unpredictability. It can be measured directly from data using the techniques developed up to this point. Fortunately, this measurement is independent of the reconstruction of low-dimensional attractors. Another important quantity is the attractor's dimension. This is the average number of numbers needed to uniquely specify the system's state. It too can be directly measured from chaotic signals.

The following sections illustrate these procedures and the determination of the entropy and dimension of the attractors. The next section discusses my analysis of chaotic data from Rob Shaw's "dripping faucet" experiment. These results were presented by him at the Order in Chaos conference held 24 - 28 May 1982 at the Los Alamos National Laboratory. The third section then analyzes Harry Swinney's and Anka Brandstater's data from wavy-vortex Couette flow. It includes a joint paper summarizing a rather wide-ranging analysis of this data that is submitted to Physical Review Letters.

8.2. The Dripping Faucet

The dripping faucet experiment studies the dynamics of "water falling from an orifice," as Rob Shaw describes it. Otto Rossler was the first to appreciate the possibility of low-dimensional chaotic behavior in this system, especially its relaxation oscillator dynamics.

The following data was taken from apparatus set up by Rob Shaw, Peter Scott, and Phil Martien. The experimental apparatus consists of a

suspended reservoir that feeds water through a microcomputer-controlled flow valve. The water then falls from a round orifice into a drain. The orifice measures a few millimeters in diameter. The water drops interrupt a laser light beam incident on a photo detector, producing a voltage pulse in the detector's output. The time between these pulses, and hence the drops, is measured by the microcomputer in increments of 16 microseconds. Typical drop rates vary from 2 to 20 per second. The

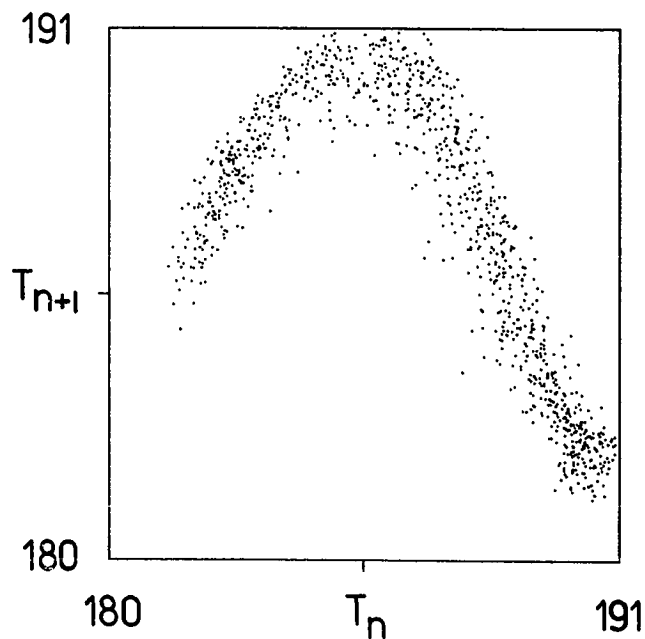


Figure 8.1.

An example from the period-doubling sequence: a noisy one-band chaotic attractor. An inter-drop time return map. The axes are labeled in milliseconds.

chosen observable is thus the inter-drop time interval. The first experimental studies of this system by Shaw used the amplified output of a microphone upon which the drop directly fell. In 1978, Shaw and I made an introductory video tape that featured a chaotic dripping faucet and Shaw's analog computer simulations of a model for the drop behavior.

8.2.1. Attractors from the Data

For modest flow rates Shaw found several simple periodic and chaotic attractors, amidst much interesting complex dynamical behavior. One example was a noisy period-doubling bifurcation sequence to chaos. To motivate the next section's entropy calculations, this section includes some reconstructed pictures of the simplest attractors. The data sets used typically consisted of several thousand drop intervals. In the period-doubling sequence the dynamics can be represented as a one-dimensional map as in figure 8.1. At neighboring flow rates, complex appearing attractors were also found. In these cases a multi-dimensional reconstructed state space was required to unambiguously represent the dynamics. Figures 8.2 and 8.3 show two examples of stereoscopic plots of three-dimensional reconstruction. The first is the above one-band attractor, for reference, and the second is a more complicated and apparently higher-dimensional attractor. Note for comparison's sake, that the one-band attractor still appears one-dimensional in the three-dimensional space. The dimension of the second attractor is not clear from its picture.

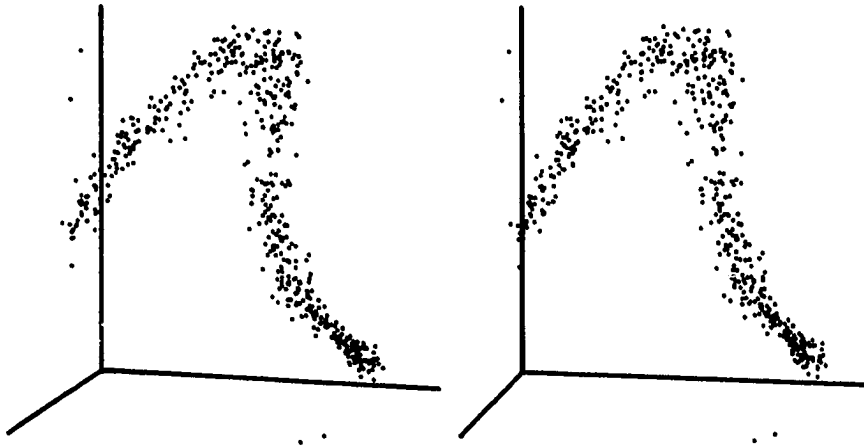


Figure 8.2.

Stereoscopic three-dimensional reconstruction of the one-band attractor.
The axes are (T_n, T_{n+1}, T_{n+2}) .

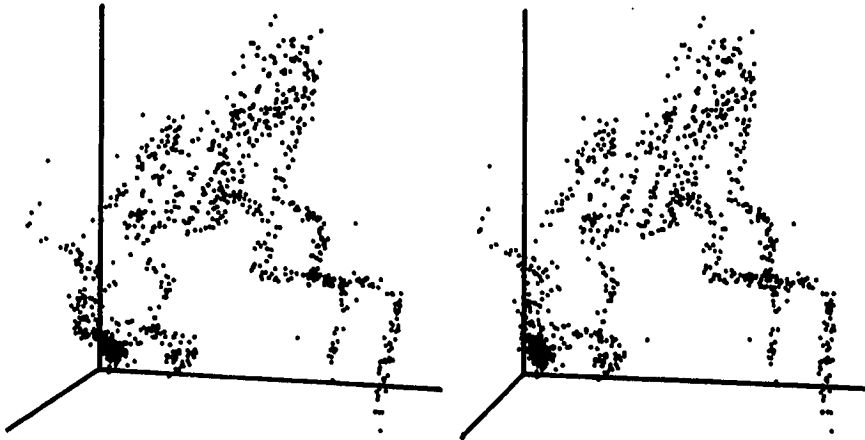


Figure 8.3.

A more chaotic attractor at a nearby flow rate. The axes are (T_n, T_{n+1}, T_{n+2}) .

8.2.2. The Drip's Unpredictability

The entropies can be used to quantify the chaos found in the drip experiment. Using binary-symbol techniques an effective generating partition for the one-band attractor can be found as in figure 8.4. The metric entropy for the one-band attractor is .60 bits per drop for a decision point at 11668 (16 microsecond) time units. The information production rate is the product of the metric entropy per drop and the average drop interval. The latter is 187.7 milliseconds. Hence, at the

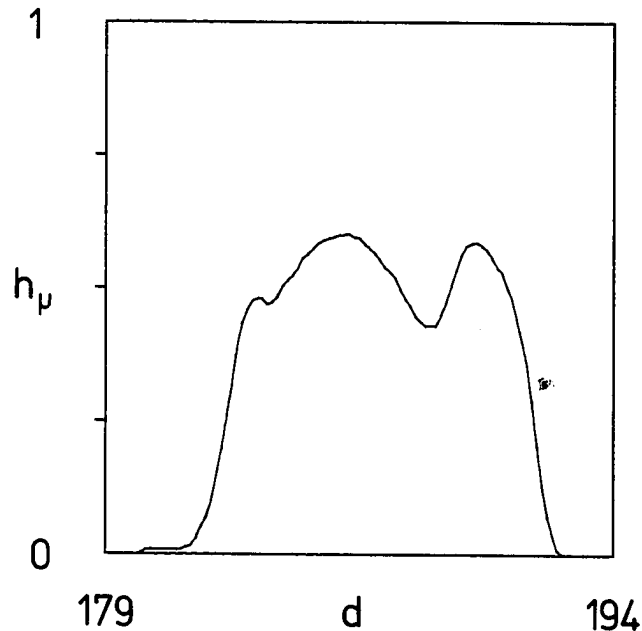


Figure 8.4.

Metric entropy versus decision point d for the one-band attractor. The abscissa is labeled in milliseconds and the ordinate in bits per drop. At the "generating" decision point $d = 186.7$ milliseconds, the metric entropy is .60 bits per drop.

end of its period-doubling sequence in the noisy one-band regime, the dripping faucet has an information production rate of 3.2 bits per second.

To estimate the effect of extrinsic noise, figure 8.5 shows the entropy convergence. It graphs the entropies as a function of the number of binary measurements using the effective generating partition found above. The noise causes the metric entropy to converge for

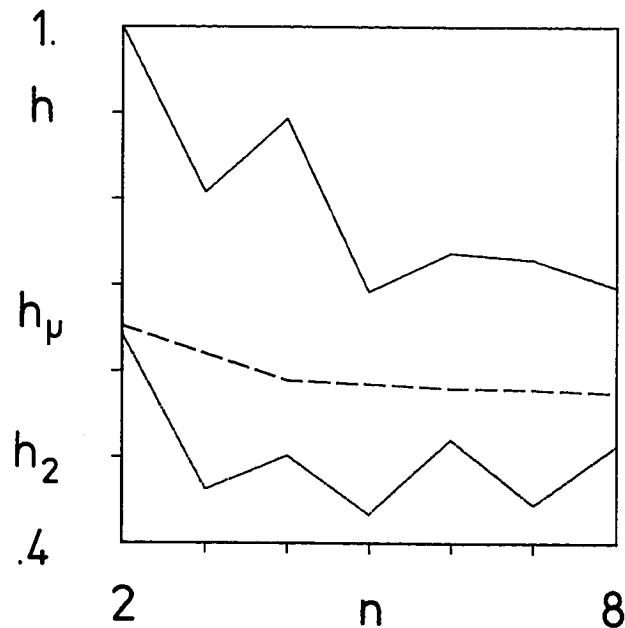


Figure 8.5.

Entropy convergence for the one-band attractor using a generating partition. Topological, metric, and correlation entropies versus measurement sequence length.

measurement sequences approximately $n_c = 4$ in length. n_c is called the noise convergence knee.

These results can be used to make some specific physical statements about the drops' chaotic behavior in the one-band regime. First, a crude estimate of the noise level can be deduced from the entropy at the generating partition and the noise convergence knee n_c . For sequences of length n_c the refined partition elements are roughly of size $\epsilon_c \sim$

$2^{-h_u n}$. This follows from the fact that the effect of noise, and consequent smearing of the partition elements, does not come into play until n_c . For sequences of this length and longer the associated elements are limited to about the same size ϵ_c by the noise. Longer measurement sequences yield no more information about the system's state, and additional symbols are independent of the preceding sequence. However, below n_c the average partition element sizes for length n sequences are reduced by a factor of 2^{-L} from their average size for length $(n-1)$ sequences, where L is the Lyapunov characteristic exponent. As the Lyapunov exponent is believed to be equal to the metric entropy, we can take this factor to be 2^{-h_u} .^{*} Thus, for length n sequences the average bin size is $2^{-h_u n}$ relative to the attractor's size. For the one-band attractor, substituting in the measured values of h_u and n_c , the noise level is roughly $\epsilon_c \sim 20\%$. This is what one expects from the attractor's fuzziness as seen in its reconstructed pictures.

The second quantitative description of the drops' behavior is the calculation of the amount of information I_0 contained in a noisy state. Using the approximation introduced in chapter 5, the Gaussian-shaped partition element distributions can be taken to be of uniform width ϵ_c . The noisy one-band attractor's probability distribution is also nearly uniform. Consequently using arguments from chapter 5, the noisy state information is $I_0 \sim -\ln(\epsilon_c)$. Thus, for the one-band attractor, the

^{*}This factor also follows directly from the structure of the state transition matrix, without the need to appeal to the intuitive, but questionably defined, Lyapunov exponent for a noisy system.

noise limits an observable state to contain only 2.3 bits of information.

The third quantitative result is the explicit calculation of the drops' unpredictability. There are two possible estimates of the unpredictability based on whether the underlying dynamics is "phase coherent" or "phase incoherent". A phase coherent chaotic attractor has a well-defined periodic component that is predictable along with an unpredictable component. Phase incoherent attractors do not have a periodic component and so they do not require accounting for this predictable component in estimating the unpredictability.

The attractors in period-doubling sequences are phase coherent. Hence, the noisy one-band attractor can be assumed to come from a Poincare section of a phase coherent attractor. As seen from the range of drop intervals, the chaotic component is a moderately small fraction of the average drop interval. The attractor's width of 12.6 milliseconds is small compared to the average drop interval of 187.7 milliseconds. The initial unpredictability is dominated by the rapid error growth due to this small chaotic component. This initial unpredictability can be estimated as follows.

Although the timing accuracy of the measurement system is quite high (16 microseconds), the extrinsic noise limits the experimental resolution to ~20% of the attractor's range. The effective timing accuracy is thus $\langle t_{\sigma} \rangle \sim \epsilon_c \sim 20\%$. In informational terms this noise-limited measurement resolution is $I_0 = \ln_2 \langle t_{\sigma} \rangle \sim \ln(20\%) \text{ bits} \sim 2.3$

bits. After a time $t_p \sim \frac{I_o}{h_u} t_d \sim .7$ seconds or 4 drops later the system is no longer predictable within the attractor. All information about its location on the attractor is lost. The chaotic component has produced an uncertainty of $\epsilon_{\sigma-} \sim 7\%$ that is set by the size of the band relative to the duration of the periodic component. Beyond this time, the errors grow as in a random walk, i.e. $\sim \epsilon_{\sigma-} t^{1/2}$. The chaotic component determines the characteristic time to be t_p . Error growth due to the periodic component is thus given by $\epsilon_{\sigma-} (\frac{t}{t_p})^{1/2}$. All information is lost when this error is unity. Hence, the drop is completely unpredictable after a time $t^* \sim 150$ seconds or 800 drops.

Shaw's drip experiment is an ideal system with which to study physical chaos for several reasons. At low flow rates, the observable is discrete drop intervals and this reduces the dimension of the reconstructed state space from that required for a continuous time series. Furthermore, the system is remarkably stable in comparison with the traditionally studied hydrodynamic flows, such as the Couette system described in the next section. This stability leads to long data records and so provides very good statistics for the measurement of its unpredictability. More systematic analysis of its behavior at higher flow rates will allow for the detailed study of how a hydrodynamic system becomes successively more turbulent. To date the drip experiment is certainly the best "model chaotic system", as Shaw describes it, for the experimental study of chaos.

8.3. Wavy-Vortex Couette Flow

Couette flow is a classical hydrodynamic experiment on the fluid flow between two coaxial differentially-rotating cylinders. Typically, the cylinders are vertical and only the inner cylinder rotates, at a controlled speed. The frequency of this rotation is the main control parameter. It is often quoted as the Reynolds number which roughly measures the ratio of the torque-induced stress to the viscous dissipation. The inter-cylinder radius and height of the cylinders are also possible control parameters.

For low rotation speeds (low Reynolds numbers) the fluid moves in a laminar shear flow with a constant velocity gradient. At the critical Reynolds number R_c , doughnut-shaped, vertically-stacked "Taylor vortices" appear. Their diameter is close to the inter-cylinder radius. At higher Reynolds numbers the vortices become azimuthally modulated. This appears as waves that travel around the cylinder. This is called wavy-vortex flow. Another, perhaps independent, azimuthal modulation appears at yet higher speeds. Near this regime the fluid becomes weakly turbulent. The question then is whether this turbulent behavior is associated with low-dimensional chaotic dynamics. To address this problem, the next section illustrates selected data sets from this regime. It also briefly discusses entropy computations of the reconstructed dynamics as a function of Reynolds number to show that the system becomes increasingly more unpredictable. The third section is a joint paper on the dynamical systems analysis of wavy-vortex flow. The data presented here were taken by Anka Brandstater in Harry Swinney's

laboratory using laser Doppler velocimetry to measure a single component of the flow velocity field at a point.

8.3.1. Attractors and Their Unpredictability

This brief section presents power spectra and stereoscopic reconstructions for three data sets from those analyzed in the paper. The Reynolds numbers are quoted relative to the critical Reynolds number R_c .

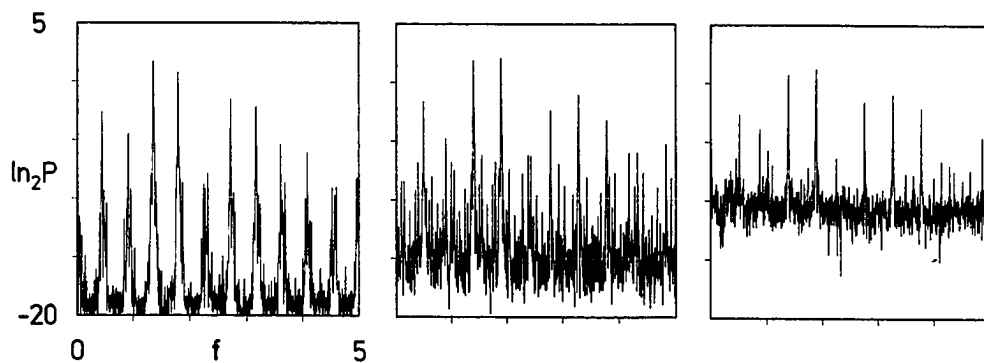


Figure 8.6.

Power spectra of wavy-vortex Couette flow at successively higher Reynolds numbers (a) $R = 10.2$ (b) $R = 12.92$ and (c) $R = 15.2$.

Figure 8.6 shows three power spectra from data sets taken at Reynolds numbers 10.2, 12.92, and 15.2. The first example comes from a predictable quasi-periodic flow. The large peaks in the spectrum reflect this periodicity. In the second spectrum a broad band noise floor appears along with the original peaks. The third spectrum, at yet higher Reynolds number, shows a slightly different peak structure and more broad band noise.

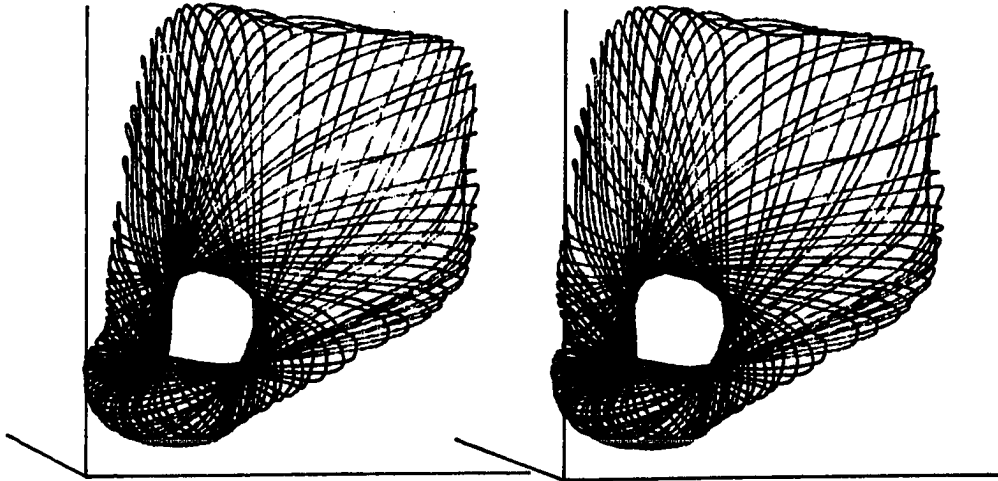


Figure 8.7.

Stereoscopic reconstruction of the attractor at $R = 10.2$. A simple torus attractor.

The stereoscopic reconstructions of these same three data sets also exhibit increasing complexity in the attractor. (See figures 8.7, 8.8, and 8.9.) The delayed-signal reconstruction method was used with a delay time of 100 (~6 millisecond) sample times. The coordinates are (T_n, T_{n+1}, T_{n+2}) . The first figure shows a predictable torus attractor that is usually associated with the existence of two dominant and incommensurate frequencies as was seen in the first spectrum. The torus can be seen to cross through itself in this three dimensional

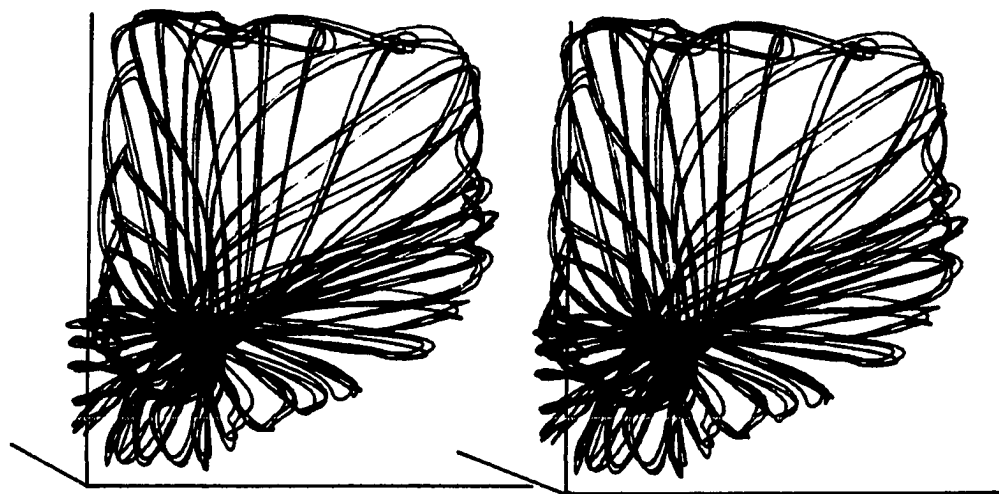


Figure 8.8.

Stereoscopic reconstruction of the attractor at $R = 12.92$.

projection. Presumably in a higher dimensional reconstructed state space this degeneracy disappears. The following two figures illustrate more complex attractors. They are still of relatively low dimension, although the actual dimension is not clear from the figures.

That these attractors are chaotic also cannot be deduced directly from the pictures. To check whether they are indeed chaotic, the metric entropies were computed from Poincare maps of the above attractors. The entropy estimates employed two and three element partitions. In each

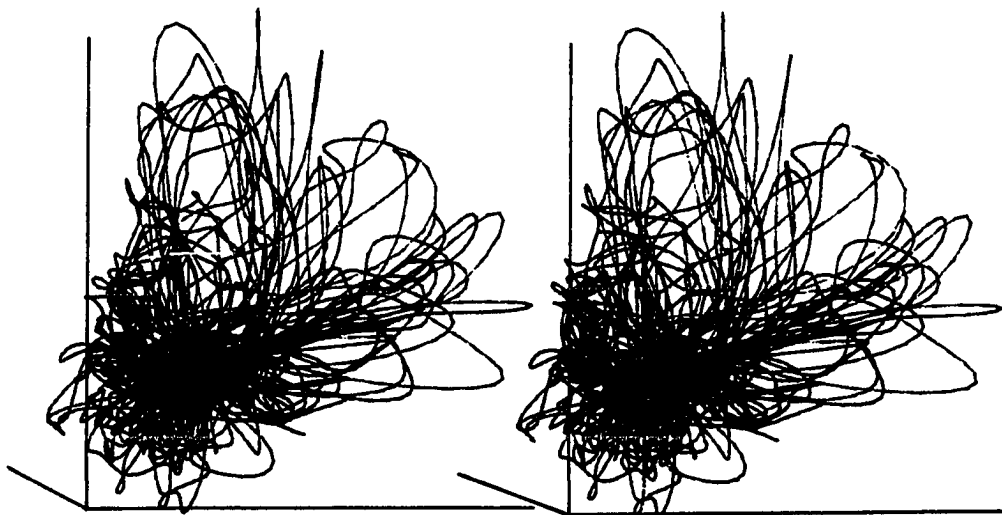


Figure 8.9.

Stereoscopic reconstruction of the attractor at $R = 15.2$.

case, the partition dividers were systematically varied to give all possible partitions and the maximum entropy was taken to be the metric entropy. There was insufficient data (~300 points) in the sections to warrant finer partitions. As it turned out, the binary and trinary entropies agreed to within 20%, with no apparent systematic deviation between the two quantities for each data set. When possible the Poincare maps were reduced to circle maps. The entropies were also computed for these one-dimensional maps. These entropies agreed well (<15% deviation) with those from the Poincare sections. The errors in the entropies are fairly large due to the small data sets available. Unfortunately, the error decreases slowly with increasing data set size. The detailed entropy calculations are presented in the next section's paper.

8.3.2. Chaos in Couette Flow

Submitted to Phys. Rev. Lett., July 20, 1983

Low-Dimensional Chaos in a System
with Avogadro's Number of Degrees of Freedom

A. Brandstätter, J. Swift, Harry L. Swinney and A. Wolf

Department of Physics, University of Texas, Austin, Texas 78712

and

J. Doyne Farmer and Erica Jen

Center for Nonlinear Studies, Los Alamos National Laboratory, Los Alamos, NM 87545

and

J. P. Crutchfield

Department of Physics, University of California, Santa Cruz, CA 95060

PACS numbers 03.40.Gc, 05.70.Ln, 47.25.-c

We present evidence for low-dimensional strange attractors in Couette-Taylor flow data. Computations of the largest Lyapunov exponent and metric entropy show that the system displays sensitive dependence on initial conditions. Computations of the fractal dimension show that although the phase space is very high dimensional, motion is restricted to an attractor of dimension less than five for Reynolds numbers up to 30% above the onset of chaos. All of these quantities generally increase with Reynolds number.

Lorenz¹ and Ruelle and Takens² have suggested that fluid turbulence corresponds to strange (chaotic) attractors, that is, nonperiodic motion generated by finite-dimensional deterministic dynamics. This contrasts with Landau's suggestion that turbulence corresponds to multiperiodic motion with many incommensurate frequencies. An experiment by Gollub and Swinney³ showed that the Landau hypothesis fails, but until now the strange attractor hypothesis has eluded verification. Using improved techniques for experimental data acquisition and analysis, we present positive evidence in this paper that the transition to turbulence in Couette-Taylor flow is initiated by low-dimensional strange attractors.

In a deterministic system chaos is reflected by exponentially fast separation (on the average) of nearby points in phase space. This sensitive dependence on initial conditions is reflected by a positive Lyapunov exponent⁴ λ_1 and positive metric entropy⁵ h_μ . The fractal dimension⁶ D of an attractor, if small and nonintegral, confirms that the dynamics admits a low-dimensional deterministic mathematical description characterized by a strange attractor.

In this paper we use recently developed techniques for computing λ_1 , h_μ , and D from experimental data in order to make the strongest possible test of the strange attractor hypothesis. Difficulties arise in applying the formal definitions of λ_1 , h_μ , and D to experimental data, because the required limiting processes break down at small scales due to instrumental noise; nevertheless, it is still possible to approximate λ_1 , h_μ , and D for experimental systems since the geometrical form of a strange attractor persists in the presence of small amounts of noise.

We now describe the experiment and the phase portraits and Poincaré sections constructed from the data, and then we present calculations of λ_1 , h_μ , and D .

Measurements were made on a concentric cylinder system with radius ratio 0.875, outer radius 5.946 cm, and a fluid height-to-gap ratio 20; rigid end boundaries were provided by rings attached to the stationary outer cylinder.⁷ The modulated wavy vortex flow state studied had 16 Taylor vortices and 4 azimuthal waves in each traveling wave train.⁷ Measurements were made for Reynolds numbers R in the range $10R_c$ to $15R_c$, where R is proportional to the angular velocity of the inner cylinder and R_c is the critical Reynolds number for the onset of Taylor vortex flow. Laser Doppler velocimetry was used to measure the radial component of the velocity at a point in the fluid, usually chosen to be at the middle of the gap between the cylinders at a height about one-sixth of an axial wavelength away from a vortex outflow boundary. (The exact position is not important since λ_1 , h_μ , and D were found to be independent of position at fixed R .) Velocity values $V(t_k)$ at times $t_k = k\Delta t$ ($k=1, \dots, 32768$; typically $\Delta t = 6$ ms) were determined using a 256-channel pulse correlator to obtain the temporal autocorrelation function of the scattered light intensity. The resulting velocity values are far more accurate than those obtainable by the usual analog velocimetry methods.

Our methods of analysis require multidimensional phase space portraits which we construct from measurements of the single dynamical observable, $V(t_k)$. Phase portraits of dimension m can be constructed from the vectors $\{V(t_k), V(t_k+\tau), \dots, V(t_k+(m-1)\tau)\}$ where the delay time τ is essentially arbitrary.⁸ We will refer to m as the embedding dimension.

Figure 1(a) shows phase portraits at $R/R_c=10.2$, where the velocity power spectrum contains only sharp peaks at two fundamental frequencies and their combinations, and at $R/R_c=12.0$ and 15.2 , where the spectrum contains broadband noise in addition to the sharp spectral components. Figure 1(b) shows two-dimensional Poincaré sections given by the intersection of orbits in

three-dimensional portraits with planes. The closed loop corresponding to the surface of a torus is well-defined at $R/R_c=10.2$; the small amount of scatter presumably arises from instrumental noise. The surface of a torus is still clear, although fuzzier at $R/R_c=12.0$.⁹ However, at $R/R_c=15.2$ a torus is no longer apparent -- phase portraits and Poincaré sections no longer yield useful information. Therefore, we turn to more quantitative methods of data analysis, i.e., computation of a Lyapunov exponent, the metric entropy, and the fractal dimension.

The largest Lyapunov exponent of a dynamical system provides both qualitative and quantitative information about the average behavior of nearby orbits in an attractor. If the largest exponent is negative, the attractor is a fixed point; if zero, the attractor is a limit cycle or torus; and if positive the attractor is strange. In a strange attractor nearby points diverge at an exponential rate dominated by the largest Lyapunov exponent.

Previous calculations of the largest Lyapunov exponent from experimental data have involved the construction of an underlying one-dimensional map. This approach has been found not to be numerically robust¹⁰ and, moreover, our attractors are not well described by such maps at higher Reynolds numbers. Exploiting the definition of the Lyapunov exponents, we have developed a new algorithm for estimating the non-negative exponents of an attractor from measurements of a single observable.¹⁰

To find the largest Lyapunov exponent we continuously monitor the long term evolution of the separation between a pair of initially adjacent data points in a phase portrait of suitably high dimension. When this separation is no longer small, the second point of the pair is replaced by a new "nearest neighbor" chosen so that the separation is again small, subject to the constraint that the orientation of the separation vector is most nearly preserved. Using files of

~300 orbits (~100 points/orbit) in five-dimensional reconstructions of the attractors, we found that the Lyapunov exponent generally increased with Reynolds number from small values, presumably zero, through the transition, as shown in Fig. 2.

Although our method works quite well on a variety of model systems with known Lyapunov exponents¹⁰ we find that in the presence of instrumental noise there are numerical problems that cause the magnitude of the computed exponent to depend on the embedding dimension m . Our interest here, however, is in the sign of the exponent and its functional dependence upon the Reynolds number rather than its precise magnitude, and these are independent of m . We can therefore state unambiguously that there is sensitive dependence on initial conditions that generally increases with R .

The metric entropy provides another way of quantifying the unpredictability of dynamical motion. For a long sequence of measurements made at successive times the metric entropy h_μ is the average amount of new information gained with each measurement. For regular motion (fixed points, limit cycles, tori, etc.) $h_\mu = 0$; for a strange attractor, $0 < h_\mu < \infty$; and for a classical random process, $h_\mu = \infty$. The metric entropy is believed to be equal to the sum of the positive Lyapunov exponents.⁵

To compute the metric entropy,⁵ the phase space is partitioned into discrete cells that represent possible outcomes of measurements made with finite precision. As a trajectory traverses the phase space, it moves through different cells, generating a sequence of measurement outcomes. The probability of occurrence of each sequence of finite length can then be approximated by the relative number of times that it occurs, i.e., $p(S_m) = N(S_m)/N_t$, where $N(S_m)$ is the number of times a particular sequence S_m occurs and N_t is the total number of occurrences of all possible sequences of length m . The information contained

in sequences of length m is $I_m = - \sum_{S_m} p(S_m) \log_2 p(S_m)$ and the metric entropy is the average amount of new information: $h_\mu = \lim_{m \rightarrow \infty} \lim_{N \rightarrow \infty} (I_{m+1} - I_m)$.⁵

We compute the metric entropy only at lower Reynolds numbers, where it is possible to construct a one-dimensional circle map from the data. This allows us to choose the cells in an optimal manner so that only two are required to get an accurate value of the entropy⁵, and the procedure outlined above can be carried out for fairly large values of m . For large Reynolds numbers, however, this method fails, since the attractor is too large in dimension to be accurately represented by a one-dimensional map. The results of our measurements of metric entropy as a function of Reynolds number are shown in Fig. 2.

The dimension of an attractor provides a way of quantifying the number of independent degrees of freedom present in dynamical motion. We use three methods^{11,12} for computing the dimension of the attractors obtained from our data. To understand the basic idea behind these methods, consider a solid object of unknown dimension D sitting in Euclidean space of dimension m . The mass contained inside a small ball of radius ϵ is proportional to ϵ^D and thus the dimension of the object can be determined by the scaling of mass with radius. In the context of a dynamical system the ball exists in an m -dimensional phase space and D is the dimension of the attractor. Mass is replaced by natural measure, i.e., the relative frequency with which a trajectory passes through the ball. The natural measure can be estimated by simply counting the number of data points N inside the ball. Our first method of estimating dimension is to compute the average of $\log N$ for many balls of radius ϵ , and to measure the slope of $\log N$ vs. $\log \epsilon$ for increasing embedding dimension. Following ref. 6, we call the resulting quantity the average pointwise dimension. The second method is similar, except that N is made the

independent variable: the distance ϵ from a given point to its N th nearest neighbor is computed, and then ϵ is averaged over many points, for increasing embedding dimension. These two methods in principle produce the same number, which we call here the fractal dimension (the dimension of the natural measure in ref. 6). Our third method, due to Grassberger and Procaccia, is to compute a lower bound on the fractal dimension as described in reference 12.

Determination of dimension by method two is illustrated in Fig. 3(a). Plots of $\log N$ vs. $\log \epsilon$ are approximately straight lines with slopes that initially increase as the embedding dimension increases. The fact that the slope approaches an asymptotic value in each case [e.g., see inset of Fig. 3(a)] is strong evidence that the nonperiodic motion of the fluid takes place on a finite (in fact low) dimensional strange attractor. Figure 3(b) shows the growth of fractal dimension with Reynolds number.

In summary, we would like to emphasize not the precise values of the largest Lyapunov exponent, the metric entropy, and the fractal dimension, but that above the onset of chaos (marked by the appearance of broadband spectral noise) λ_1 and h_μ become positive and D remains small. The growth of λ_1 and h_μ with Reynolds number indicates an increase in the unpredictability of the flow and the growth of D with Reynolds number indicates an increase in the number of active degrees of freedom in the fluid with increased stress. Although the fluid could potentially have a very large number of degrees of freedom,¹³ our studies indicate that there are only a few independent degrees of freedom, certainly less than five, even at a Reynolds number 30% above the onset of chaos.

While this paper was in preparation we learned of related studies of dimension by P. Berge, and M. Dubois, and by J. Guckenheimer, G. Buzyna, and

8.27

-8-

R. Pfeffer. Our experiments were conducted at the University of Texas with the support of National Science Foundation Grant MEA82-06889.

References

1. E. N. Lorenz, *J. Atmos. Sci.* 20, 130 (1963).
2. D. Ruelle and F. Takens, *Commun. Math. Phys.* 20, 167 (1971).
3. J. P. Gollub and H. L. Swinney, *Phys. Rev. Lett.* 35, 927 (1975);
P. R. Fenstermacher, H. L. Swinney, and J. P. Gollub, *J. Fluid Mech.* 94,
103 (1979).
4. R. Shaw, *Z. Naturforsch.* 36a, 80 (1981).
5. J. P. Crutchfield and N. H. Packard, *Physica* 7D (1983).
6. J. D. Farmer, E. Ott, and J. Yorke, *Physica* 7D (1983).
7. R. S. Shaw, C. D. Andereck, L. A. Reith, and H. L. Swinney,
Phys. Rev. Lett. 48, 1172 (1982).
8. N. H. Packard, J. P. Crutchfield, J. D. Farmer, and R. S. Shaw,
Phys. Rev. Lett. 45, 712 (1980); F. Takens, in *Lecture Notes in Math.* 898,
ed. by D. A. Rand and L.-S. Young (Springer, Berlin, 1981), p. 366.
9. High quality Poincaré sections of a torus below and above the onset of
turbulent convection have been obtained by M. Dubois, P. Bergé,
and V. Croquette, *J. Phys. Lett. (Paris)* 43, L295 (1982).
10. A. Wolf and J. Swift, in Statistical Physics and Chaos in Fusion Plasmas,
ed. by W. Horton and L. Reichl (Wiley Interscience, New York, 1983), and to
be published.
11. J. D. Farmer and F. Jen, "A guide to computing dimension and entropy of
chaotic systems," to be published.
12. P. Grassberger and I. Procaccia, *Phys. Rev. Lett.* 50, 346 (1983).
13. Viscous dissipation limits the number of degrees of freedom possible to
a number much smaller than Avogadro's number. At $R/R_c = 15.2$ we compute
the Kolmogorov microscale length to be 0.014 mm; the number of microscale
volumes in our system is then 6×10^6 .

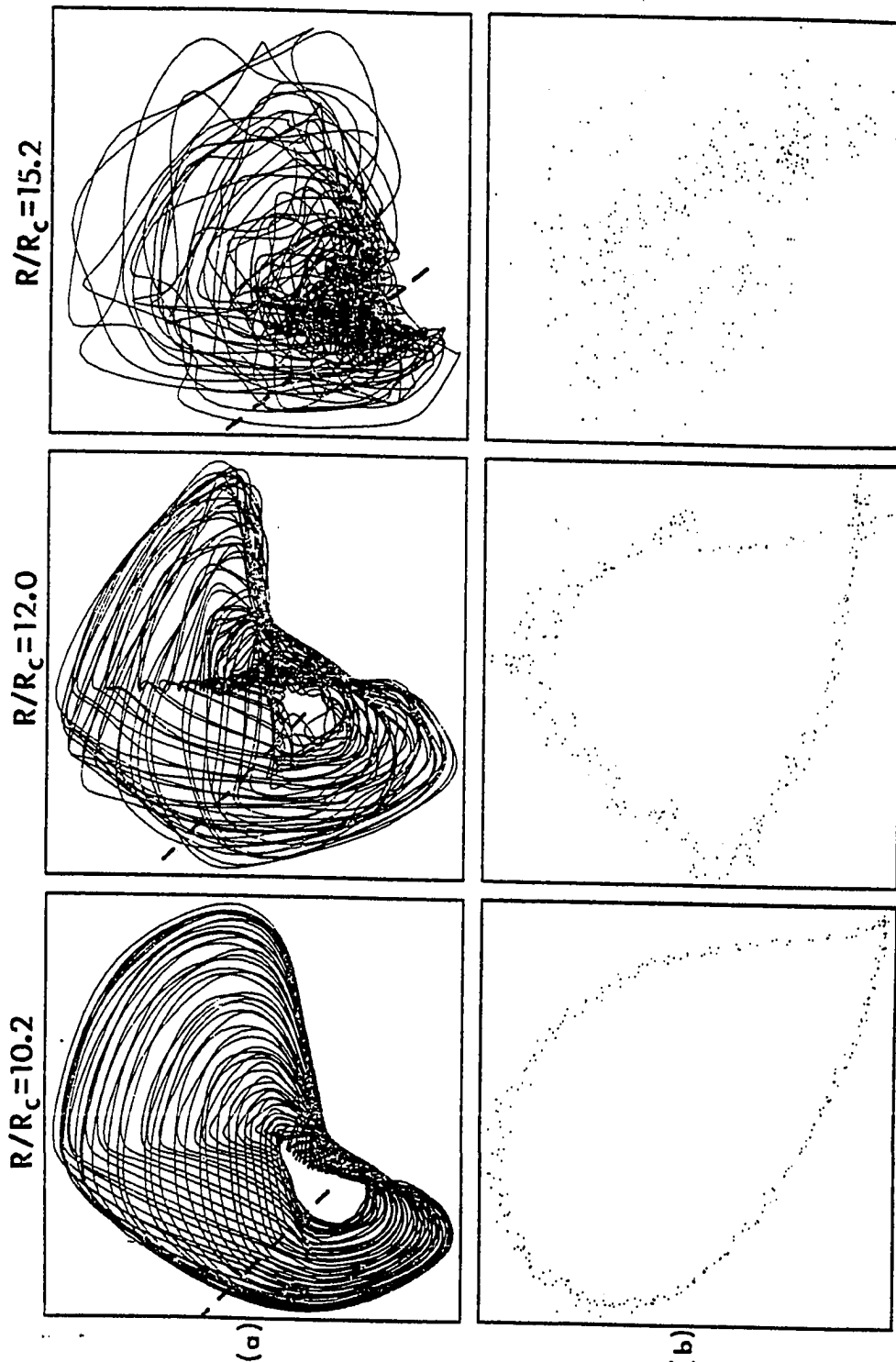


Figure 1(a). Two-dimensional phase portraits ($T=130$ ms). (b) Poincaré sections given by the intersection of orbits in a three-dimensional phase portrait [with the third axis normal to the paper given by $v(t_k+2T)$] with a plane normal to the paper passing through the dashed line in (a).

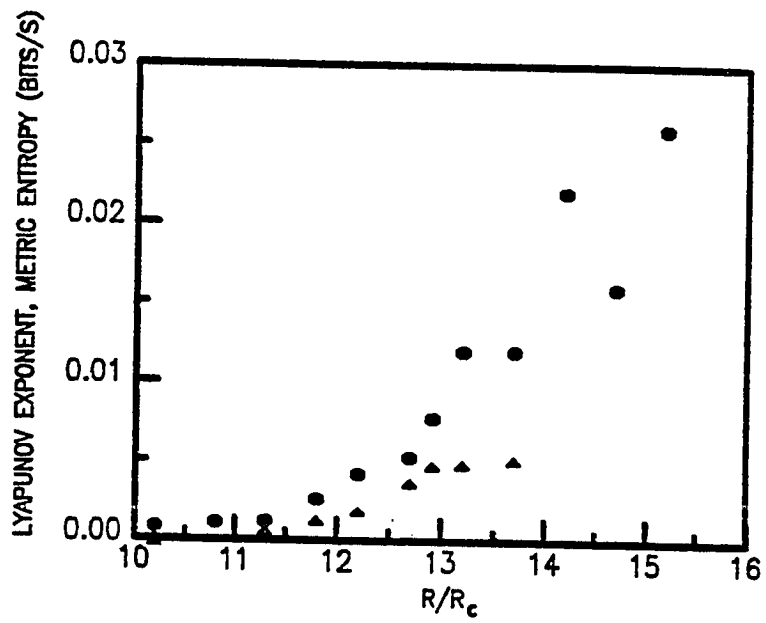


Figure 2. The largest Lyapunov exponent λ_1 (the points \bullet) obtained from five-dimensional phase portraits and the metric entropy h_μ (the points \blacktriangle) as a function of Reynolds number.

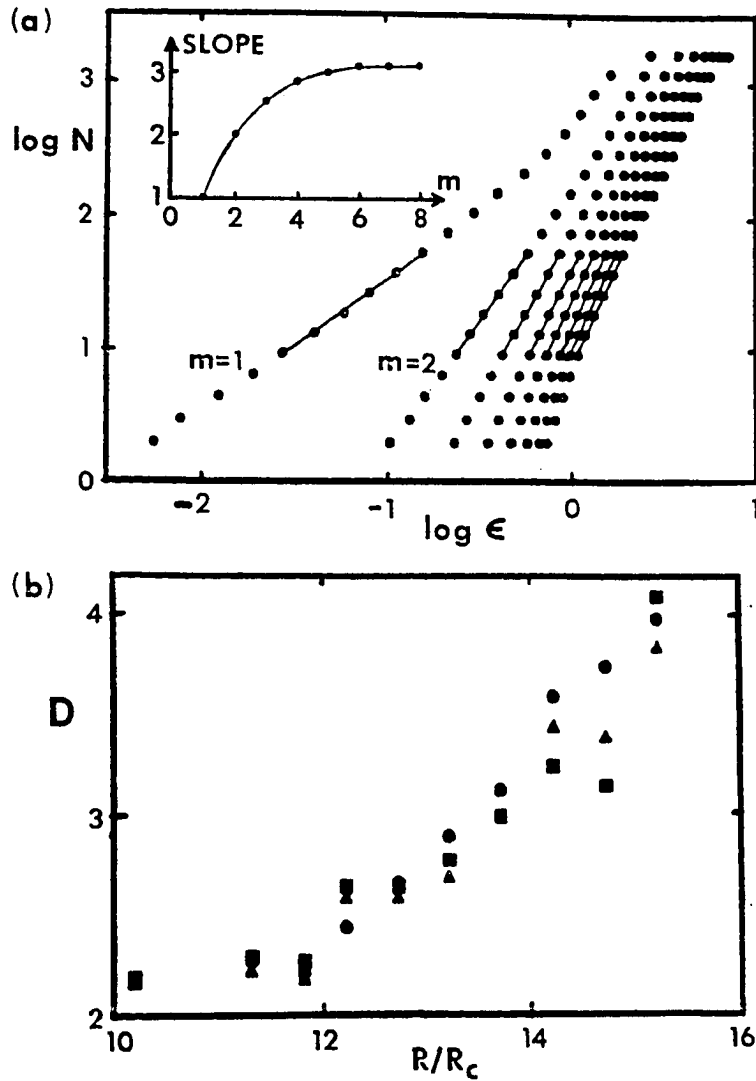


Figure 3.(a) Curves used to deduce the fractal dimension by method 2 from data (2048 points spanning about 300 orbits) at $R/R_c = 13.7$ for different embedding dimensions m . The asymptotic slope for large m (see inset) is an estimate of the dimension. There are systematic errors for large and small ϵ ; therefore, as shown in the figure, only the middle portion of the curve is used for the fit. (b) The Reynolds number dependence of the fractal dimension computed using methods 1(\bullet), 2(\blacksquare), and 3(\blacktriangle), as described in the text.

CHAPTER 9

Complexity in Spatially Extended Systems

9.1. Spatially-Extended Systems

So far the application of dynamical systems has been explicitly to finite dimensional chaotic dynamics. With the driven oscillators and discrete mappings the dimension of the dynamics' domain was known a priori. In the hydrodynamic experiments, it was observed that a signal from a single observable was sufficient to characterize the entire systems' dynamics in a low-dimensional reconstructed state space. However, this is not always the case for these experiments. When the stress in, or energy flow through, the hydrodynamic systems increases their behavior becomes spatially as well as temporally, complex. In these regimes, the system's state no longer can be uniquely characterized by a time series from a single point, rather several spatially-separated time series becomes necessary.

The appearance of spatial complexity with changes in control parameters is a common physical phenomenon, and certainly not restricted to hydrodynamic flows. In this chapter a simple electronic system is presented that exhibits a striking range of spatial and temporal complexity. This system is called video feedback. Before embarking on its description, I would like to discuss how spatial complexity may be modeled abstractly and quantified. This is particularly appropriate in light of the dynamical systems and entropy concepts developed up to this

point.

A spatially extended system consists of two components. First, the local dynamics governs the evolution of the system's variables at a point. Second, there is spatial coupling of the variables at a point with those of neighboring points. Figure 9.1 illustrates this for a one-spatial-dimension system. Information flows into and out of each

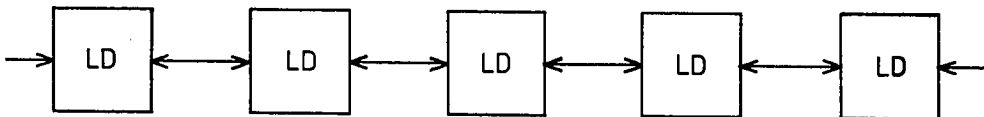


Figure 9.1.

"Flow-box" picture of a spatially extended dynamical system: A one-spatial-dimension system is illustrated. LD is the local dynamics. The arrows represent the coupling and direction of information flow.

spatial point.*

As an example of this type of system, a discrete time and space lattice dynamical system was studied [13]. The logistic equation was chosen as the local dynamics. The coupling was a symmetric nearest-neighbor interaction: a finite difference approximation of the Laplacian. Both fixed and periodic boundary conditions were considered. The parameters of interest here are the height of each map and the strength of the coupling. As one expects, for very low coupling the entire lattice displayed the well-known period-doubling route to chaos. If the initial conditions of neighboring maps laid in different basins of attraction of the zero-coupling attractors, "dislocations" or spatial jumps arose in the time evolution. Increased coupling strength induced a bifurcation gap in the period-doubling sequence. This gap had the same scaling structure as the noise induced gap for a single logistic map, as described previously. Additionally, within the gap time-dependent, stationary spatial waves occur. Associated with this is a two-dimensional torus in the reconstructed state space. Power spectral analysis revealed that the torus is associated with two incommensurate frequencies. Beyond the torus chaos appears. The scaling theory analysis is underway.

Aside from highly discretized cellular automata, such nonlinear lattice dynamical systems appear to be the simplest theoretical examples

* Coupling dynamical systems together in this manner led to a mechanism for intermittency that used unidirectional coupling and information flow [19].

available for the study of spatial complexity. The preliminary conclusions from the above study is that in some regimes their behavior is described using established techniques for low-dimensional dynamics. For the logistic lattice described the behavior should have the same applicability and range of "universality" as that ascribed to the logistic map itself. These simple lattice systems also lend themselves to the development and study of measures of spatial complexity.

The entropies, dimensions, and characteristic exponents already introduced can be generalized to apply to spatially extended systems. The density of each of these quantities is defined as that derived from the signal at a single point. Thus at every point in a spatially-extended system, the desired quantity is measured for the dynamics in a reconstructed state space.

Ruelle [20] has established that this procedure is well-defined. He has shown that the sum of the positive characteristic exponents at a point is finite in such systems. Ruelle has previously shown that the metric entropy is bounded above by the sum of positive exponents, given appropriate assumptions. And so, the metric entropy density and the higher order Renyi entropies, too, are finite. It is a plausible conjecture that the dimensions and the topological entropy are also finite. Intermittency may cause large deviations of the fractal dimension density from the information dimension density and of the topological entropy density from the metric entropy density.

As a first step in understanding spatially complex systems, the following presents in some detail experiments with a two-dimensional spatially extended system: video feedback. One video feedback's main benefits is that it provides a readily available experimental system to study complex spatial and temporal dynamics. The natural time scale is quite fast in comparison with hydrodynamic flows, and so video feedback allows for a reasonable data acquisition rate in experiments. This is quite important for computing the above densities. The following sections outline the use and modeling of video feedback systems. They include a discussion of video physics and propose two models for video feedback dynamics based on a discrete-time iterated functional equation and on a reaction-diffusion partial differential equation. Color photographs illustrate results from actual video experiments. Digital computer simulations of the models reproduce the basic spatio-temporal dynamics found in the experiments.*

9.2. In the Beginning there was Feedback

Video technology moves visual information from here to there, from camera to TV monitor. What happens, though, if a video camera looks at its monitor? The information no longer goes from here to there, but rather round and round the camera-monitor loop. That is video feedback. From this dynamical flow of information some truly startling and

*This chapter will appear as "Space-Time Dynamics in Video Feedback", in the Proceedings of the Interdisciplinary Workshop on Cellular Automata, held 7 - 11 March, Los Alamos National Laboratory, Los Alamos, New Mexico, a special issue of Physica D (1983).

beautiful images emerge.

In a very real sense, a video feedback system is a space-time simulator. My intention here is to discuss just what is simulated and I will be implicitly arguing that video feedback is a space-time analog computer. To study the dynamics of this simulator is also to begin to understand a number of other problems in dynamical systems theory [1], iterative image processing [2], cellular automata, and biological morphogenesis, for example. Its ready availability, relative low cost, and fast space-time simulation, make video feedback an almost ideal test bed upon which to develop and extend our appreciation of spatial complexity and dynamical behavior.

Simulation machines have played an very important role in our current understanding of dynamical behavior.[3] For example, electronic analog computers in their heyday were used extensively to simulate complex behavior that could not be readily calculated by hand. They consist of function modules (integrators, adders, and multipliers) patched together to form electronic feedback networks. An analog computer is set up so that the voltages in different portions of its circuitry evolve analogously to real physical variables. With them one can study the response and dynamics of a system without actually building or, perhaps, destroying it. Electronic analog computers were the essential simulation machines, but they only allow for the simultaneous computation of a relatively few system variables. In contrast, video feedback processes entire images, and does so rapidly. This would require an analog computer of extremely large size. Video

systems, however, are not as easily broken down into simple function modules. But it is clear they do simulate some sort of rich dynamical behavior. It now seems appropriate that video feedback take its proper place in the larger endeavor of understanding complex spatial and temporal dynamics.

Cellular automata are the simplest models available for this type of complexity. Their study, however, requires rapid simulation and the ability to alter their governing rules. Video feedback does, in fact, simulate some two-dimensional automata and rapidly, too. With a few additions to the basic system, it can easily simulate other rules. Thus video feedback has the potential to be a very fast and flexible two-dimensional automata simulator. The dynamics of cellular automata are governed by local rules, but video feedback also allows for the simulation of nonlocal automata. At the end, I will come back to these possibilities and describe how simulations of cellular automata, and their generalization to nonlinear lattice dynamical systems, can be implemented with video feedback.

This is largely an experimental report on the dynamics of a physical system, if you like, or a simulation machine, called video feedback. My intention is to make the reader aware of the fascinating behavior exhibited by this system. In order to present the results, however, section 2 includes the necessary background on the physics of video systems and a very straightforward description of how to start experimenting. An important theme here is that the dynamics can be described to a certain extent using dynamical systems theory. Section 3

develops those ideas and proposes both discrete and continuous models of video feedback dynamics. The experimental results, then, take the form in section 4 of an overview of a particular video feedback system's behavior and several snapshots from a video tape illustrate a little bit of the dynamical complexity.*

9.3. Video Hardware

In all feedback systems, video or other, some portion of the output signal is used as input. In the simplest video system feedback is accomplished optically by pointing the camera at the monitor, as shown in figure 9.2. The camera converts the optical image on the monitor into an electronic signal that is then converted by the monitor into an image on its screen. This image is then electronically converted and again displayed on the monitor, and so on ad infinitum. The information thus flows in a single direction around the feedback loop. Figure 9.2 indicates the information flow with arrows moving in a counter-clockwise loop. This information is successively encoded electronically, then optically, as it circulates.

Each portion of the loop transforms the signal according to its characteristics. The camera, for example, breaks the continuous-time optical signal into a discrete set of rasters thirty times a second. (See figure 9.3) Within each raster it spatially dissects the incoming picture into a number of horizontal scan lines. It then superimposes

* At this point the gentle reader may wish to peek at the photographs of section 4.

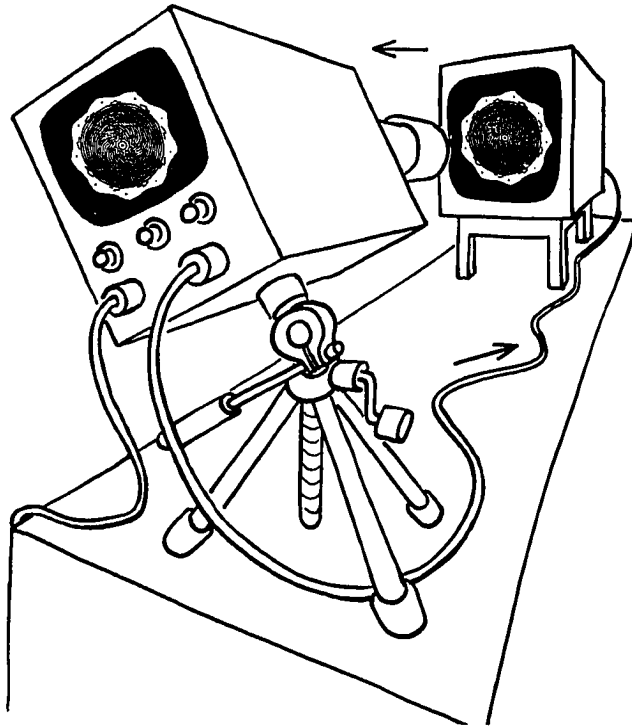


Figure 9.2.

Simple Video Feedback. Arrows indicate the direction of information flow through the electronic and optical pathways.

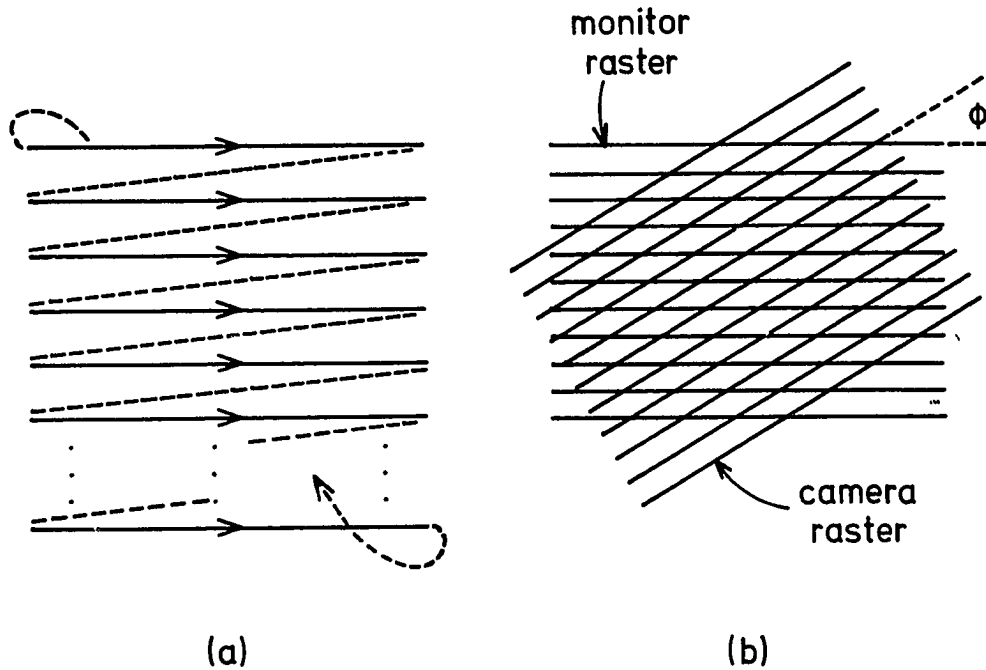


Figure 9.3.

Video raster with arrows indicating the direction of scanning. Solid lines correspond to when the electron beam is on; the dashed lines when the beam is off during the retrace time. (b) Since the raster defines the horizontal, in a feedback system the relative orientation as shown of the camera and monitor is an important control parameter.

synchronizing pulses to the electronic signal representing the intensity variation along each scan line. This composite signal drives the monitor's electron beam to trace out in synchrony the raster on its phosphor screen and so the image is reconstructed. The lens controls the amount of light, degree of spatial magnification, and focus, of the image presented to the camera.

Although there are many possible variations, in simple video feedback systems there are only a few easily manipulated controls. (See Table I.)

The optical controls provide gross spatial transformations of the image seen by the camera. Zoom, available on most modern color cameras, conveniently allows for spatial magnification or demagnification. The same effect can be produced using a camera without a zoom lens by moving it closer to or further from the monitor. Focus controls image sharpness by moving the focal plane in front or behind the camera tube's image target. The total amount of light admitted to the camera is set by

TABLE I. Typical Control Parameters in Color Video Feedback

Name	Function
Optical	
zoom	spatial magnification
focus	image clarity
f/stop	attenuates incident light level
rotation	relative angle of monitor and camera rasters
translation	relative position of monitor and camera raster centers
Electronic	
Camera	
light level	adjust sensitivity of camera pickup tube
luminance inversion	inverts intensity signal for each color
Monitor	
brightness	varies overall intensity signal
contrast	amplifies dynamic range of intensity
color	attenuates color signals to black and white
hue	relative signal strength of colors

the f/stop or iris control. When pointing the camera at the monitor the relative position, or translation, of the raster centers and the relative angle, or rotation, (figure 9.3(b)) are important controls.

Electronic transformation of the signal occurs in both the camera and the monitor. The sensitivity of the camera's tube is adjusted by a light level control. Some cameras also provide for luminance inversion that inverts the intensity of the color signals. When switched on, this allows one, for example, to view a color negative print with the camera as it would appear in a positive print. The image intensity can be adjusted again on the monitor with the brightness. The contrast controls the dynamic range of the AC portion of the intensity signal. On color monitors the amount of color in the image is set by the color control and the relative proportion of the primary colors (red-green-blue) is governed by the hue.

While the effect of each individual adjustment can be simply explained, taken together they present a formidable number of control variables that can interact nontrivially. These problems will be considered in greater detail in the ensuing discussion of TV theory and possible mathematical models of feedback dynamics. This section now ends with a "cookbook" procedure for setting up a feedback system.

Although the detailed and quantitative dynamics will vary with the specific equipment used, my experience indicates that almost all servicable cameras and monitors will give some interesting behavior. This may require some patience as there are a number of controls to be

properly set. But once "tuned up" a system will exhibit complex and striking imagery in a reasonably wide control range. For the movie[4] and pictures described later the camera used was a Sony Trinitron HVC-2200 and a Sony Trinitron TV/Monitor KV-1913.*

A typical start-up procedure might be as follows:

- (1) Connect equipment as shown in figure 9.2;
- (2) Place camera five to six feet from monitor. The distance will depend on the monitor screen size and is not that important if the camera has a zoom lens;
- (3) Point camera at some object other than the monitor. Adjust camera and monitor controls to give a good image on the monitor. Vary these controls to get a feeling for their effect on the image;
- (4) Now turn the camera to face the monitor;
- (5) Again adjust the camera controls, especially the zoom and focus, noting their effect. A warning is necessary at this point: it is not a good idea to let the camera see any steady very bright image for more than 10 to 20 seconds.** Bright, dynamic moving images are generally OK;

*The cost for this space-time simulator is a little over \$1000, approximately a cheap home computer.

**Some new cameras incorporate "burn proof" camera tubes. They are much less susceptible than earlier cameras to the image "burn" that can permanently damage the tubes. Caution should still be exercised. Excessively bright images will shorten tube life.

- (6) Adjust camera on its tripod so that it can be tilted about its optical axis;
- (7) Point the camera again at the monitor, focus on the monitor front, and zoom in enough so that the "first" image of the monitor front fills 90% of the screen;
- (8) Slowly tilt the camera trying to maintain the camera pointing at the screen's center. On almost all tripods this will take some fiddling and readjustment. Try zooming in at various rotation angles between 20 and 60 degrees.

Another important element in this is the room light level. Some behavior is quite sensitive to, or will not appear at all if, there is any external source of light. Although, a flashlight, candle, or a quick flip of the light switch, can be good light sources to get the system oscillating again if the screen goes dark.

With this short description and a modicum of patience the experimenter has a good chance of finding a wealth of complex and fascinating spatial and temporal dynamics.

9.4. Toward a Qualitative Dynamics

In the beginning, I argued that a video feedback system is a space-time simulator. But a simulator of what exactly? This section attempts to answer this question as concretely as possible at this time. A very useful tool in this is the mathematical theory of dynamical systems. It provides a consistent language for describing complex

temporal behavior. Video feedback dynamics, though, is interesting not only for the time-dependent behavior but also for its complex spatial patterns. In the following section I will come back to the question of whether current dynamical systems theory is adequate for the rich spatio-temporal behavior found in video feedback.

This section introduces the qualitative language of dynamical systems[5], and then develops a set of discrete-time models for video feedback based on the physics of video systems. At the section's end I propose a continuum model akin to the reaction-diffusion equations used to model chemical dynamics and biological morphogenesis.

Dynamic, time-dependent behavior is best described in a state space. A particular configuration, or state, of a system corresponds to a point in this space. The system's temporal evolution then becomes the motion of an orbit or trajectory through a sequence of points in the state space. The dynamic is the collection of rules that specify the evolution from each point to the next in time. In many cases these rules can be simply summarized as transformations of the state space to itself by iterated mappings or by ordinary differential equations.

As will be seen shortly, video feedback is a dissipative dynamical system. This means that on the average "volumes" in the state space contract, or in physical terms, that energy flows through the system and is lost to microscopic degrees of freedom. This property limits the range of possible behavior. Starting from many different initial states, after a long time the system's evolution will occupy a relatively small

region of the state space, this is the system's attractor.^{*} An attractor is globally stable in the sense that the system will return if perturbed off the attractor. Different initial conditions, even states very near each other, can end up on different attractors. The set of points, though, that go to a given attractor are in its basin of attraction. The picture for a particular dynamical system is that its state space is partitioned into one or many basins of attraction, perhaps intimately intertwined, each with its own attractor.

Very roughly there are three flavors of attractor. The simplest is the fixed point attractor. It is the analog to the physicist's notion of equilibrium: starting at various initial states a system asymptotically approaches the same single state. The next attractor in a hierarchy of complexity is the limit cycle or stable oscillation. In the state space this is a sequence of states that is visited periodically.

The behavior described by a fixed point or a limit cycle is predictable: knowledge of the system's state determines its future. The last type^{**} of attractor, that is in fact a very broad and rich class, gives rise to unpredictable behavior. These are the chaotic attractors. While globally stable, they contain local instabilities that amplify noise, for example. They also have extremely complex orbit structure

^{*} Unbounded or divergent behavior can be interpreted as an attractor at infinity.

^{**} For simplicity's sake, I have not included the predictable torus attractor. It is essentially the composition of periodic limit cycle attractors.

composed of unstable periodic orbits and aperiodic orbits.

An important branch of dynamical systems theory concerns how one attractor changes to another, or disappears altogether, with the variation of some control parameter. The motivation for this line of inquiry is clearly to model experimentalists' control over their apparatus. A bifurcation occurs when an attractor changes qualitatively with the smooth variation of control parameter. Changing controls corresponds to moving along a sequence of different dynamical systems. In the space of all dynamical systems, the sequences appear as arcs punctuated by particular control settings at which bifurcations occur. It is now known that these punctuations can be quite complex: continuous arcs themselves or even Cantor sets or fractals. The physical interpretation of these possibilities is very complex sequences of bifurcations. Thus dynamical systems theory leads us to expect not only unpredictable behavior at fixed parameters, but complex changes between those chaotic attractors.

With modifications much of this qualitative picture can be carried over to the dynamics of video feedback. It is especially useful for describing the context in which the complex behavior arises. In the following I also will point out possible inadequacies of the naive application of dynamical systems.

A single state of a video feedback system corresponds to an entire image, on the monitor's screen, say. The state is specified not by a small set of numbers, but rather a function $I(\bar{x})$: the intensity at

points \bar{x} on the screen. The dynamics of video feedback transforms one image into another each raster time. The domain of the intensity function $I(\bar{x})$ is the bounded plane, whereas the domain of the dynamics is the space of functions or, simply, the space of images.

This picture can be conveniently summarized by introducing some notation. The monitor screen is the bounded plane $\bar{R}^2 = [-1,1] \times [-1,1]$ where the coordinates of a point \bar{x} take values in the range $[-1,1]$. With this convention the center of the screen is $(0,0)$. For the incoherent light of video feedback, there is no phase information and so intensity is all that is significant. The appropriate mathematical description of an image's intensity distribution is the space of positive-valued functions. We will denote the space of all possible images by \underline{F} . The video feedback dynamic then is a transformation T that takes elements I in \underline{F} to other elements: $T: \underline{F} \rightarrow \underline{F} : I \mapsto I'$.

The task of modeling video feedback is now to write down the explicit form of T using our knowledge of video system physics. To simplify matters, I will first develop models for monochrome (black & white) video feedback. With color systems the modeling is complicated by the existence of three color signals and the particular camera technology. Once the monochrome model is outlined, however, it is not difficult to make the step to color.

The construction of the monochrome model requires more detailed discussion of the electronic and optical transformations in the feedback loop. Figure 9.4 presents the schematic upon which this model is based.

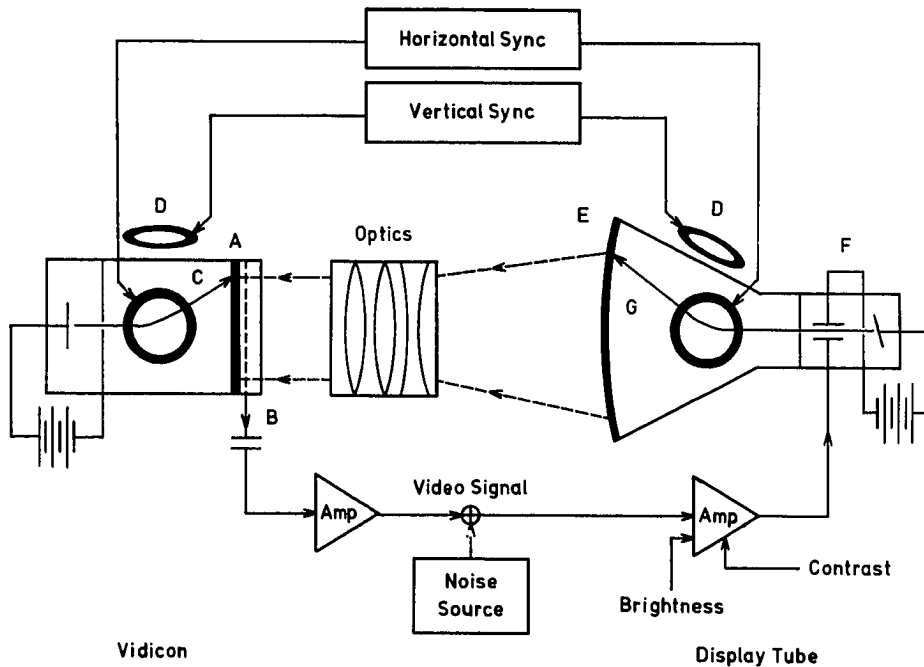


Figure 9.4.

Idealized Monochrome Video Feedback. A: photoconductive image target; B: pickup for video signal; C: camera electron beam; D: scanning coils for electron beams; E: phosphor screen; F: beam intensity modulator; G: monitor electron beam.

With the physics of these transformations as discussed in the appendix, a relatively complete model can be constructed.

The appendix reviews the operation of the common vidicon camera tube, how it (i) stores and integrates images and (ii) introduces a diffusive coupling between picture elements. These attributes impose upper temporal and spatial frequency cutoffs, respectively. The focus turns out to be an easily manipulated control of the spatial diffusion

rate. The monitor's phosphor screen also stores an image but for a time negligible compared to that of the vidicon. The appendix indicates various deviations from the ideal video feedback system of figure 9.4.

With the physics and electronics of video systems in mind, the details of the transformation T can be elucidated for the monochrome model. The first and perhaps most significant assumption, is that T be taken as a discrete-time transformation of a spatially continuous function, the image I_n ,

$$I_{n+1} = T(I_n) .$$

Employing a "bias intensity", the intensity at a point $I_n(\bar{x})$ can be scaled to take values in the range $[-1,1]$; -1 being black and 1 white. For comparison at the end of this section, I consider how a continuous time and space model can be applied to video feedback using reaction-diffusion equations.

The new image I_{n+1} consists of two parts: the first, the "old image" stored in the photoconductor, and the second, the "incoming image" from the monitor screen. This, and the process of successive feedback of images, can be expressed as an iterated functional equation. The first model of the dynamic T is the following

$$I_{n+1}(\bar{x}) = LI_n(\bar{x}) + sfI_n(bR\bar{x}) , \quad (9.1)$$

where \bar{x} is a point in \bar{R}^2 . The first term represents the old image whose

intensity at the point \bar{x} has decayed by a factor of L each time step. Thus L is the intensity dissipation of the storage elements, including the monitor phosphor, but dominated by the photoconductor. The second term represents the incoming image that is possibly rotated by an angle ϕ and spatially magnified by a factor b . R is then a simple rotation

$$R = \begin{vmatrix} \cos(\phi) & \sin(\phi) \\ -\sin(\phi) & \cos(\phi) \end{vmatrix}$$

due to the relative raster orientations; b corresponds to the zoom control. If $\bar{x}' = bR\bar{x}$ lies outside of \bar{R}^2 then $I_n(\bar{x}') = 0$. The parameter $f \in [0,1]$ corresponds to the f /stop. For a system with luminance inversion black regions become white and vice versa. To take this into account the parameter s is set to -1 , rather than its normal value of unity.

Spatial diffusion due to the photoconductor, but largely controlled by focus, contributes to the intensity at a point. It produces a spatial coupling to neighboring pixels that can be represented continuously by the following convolution integral

$$\langle I_n(\bar{x}) \rangle = \int_{\bar{R}^2} d\bar{y} I_n(\bar{y}) \exp\left(\frac{-|\bar{y}-\bar{x}|^2}{2(\sigma_f^2 + \sigma_v^2)}\right), \quad (9.2)$$

assuming a Gaussian shape for the diffusion profile. The denominator in the exponential controls the width of the smoothing with σ_f representing the focus control and σ_v the intrinsic smoothing in the vidicon.

A more complete model including the major features of video feedback systems is the following

$$I_{n+1}(\bar{x}) = LI_n(\bar{x}) + L\langle I_n(\bar{x}) \rangle_x + sfI_n(bR\bar{x}) \quad (9.3)$$

with the parameter L' setting the magnitude of the intensity signal contributed (or leaked) to that at \bar{x} during one raster time.

Furthermore, the first term in Eq. 9.3 can be modified to include the temporal storage and integration of images and their successive decay. This can be effected by a weighted sum of past images,

$$\langle I_n(\bar{x}) \rangle_{\uparrow} = \sum_{i=0}^n I_{n-i}(\bar{x})L^i$$

where the decay parameter L is the same as above. This gives equations corresponding to the video feedback system as laid out in figure 9.4,

$$I_{n+1}(\bar{x}) = L\langle I_n(\bar{x}) \rangle_{\uparrow} + L'\langle I_n(\bar{x}) \rangle_x + sfI_n(bR\bar{x}) . \quad (9.4)$$

For a color system the scalar intensity becomes a vector of red, green, and blue intensities, $\bar{I}(\bar{x}) = (\bar{R}(\bar{x}), \bar{G}(\bar{x}), \bar{B}(\bar{x}))$. There are also couplings between the colors caused by a number of interactions and imperfections, such as

- (1) incorrect convergence of the monitor electron beams on the screen phosphor color dots;

- (2) non-ideal color filters and differential diffusion rates for the photo electrons in the vidicon;
- (3) aberration in the optical system;
- (4) electronic cross-talk between the color signals in pickup, amplification, and reconstruction, of the image.

A model for color feedback can be developed as an extension of Eq. 9.4 based on the evolution of a vector intensity \bar{I}

$$\bar{I}_{n+1}(\bar{x}) = \bar{L}\langle\bar{I}_n(\bar{x})\rangle_t + \bar{L}'\langle\bar{I}_n(\bar{x})\rangle_x + sf\bar{I}_n(bR\bar{x}) \quad (9.5)$$

where \bar{L} and \bar{L}' are matrices. Their diagonal elements control the color intensity decay, while their off-diagonal elements the coupling of the color signals. In a first order approximation, this model summarizes the various couplings only linearly although it is clear that nonlinear couplings could be added.

Along the same lines a continuous-time model can be developed that for many purposes is easier to study. This also allows for the comparison of video dynamics to other work on spatial complexity in biological and chemical systems. The type of model proposed here is generally called a reaction-diffusion partial differential equation. A.M. Turing introduced this kind of system in 1952 as a model for biological morphogenesis.[6] The general form of these equations is

$$\frac{d\bar{I}}{dt} = \bar{F}(\bar{I}) + D \nabla^2 \bar{I} \quad (9.6)$$

for the evolution of the "field" $\bar{I} = (I_1, I_2, \dots, I_k)$ of concentration variables. The function $\bar{F} = (F_1, F_2, \dots, F_k)$ represents the local "reaction" dynamics of these variables without diffusion. D is a matrix describing the spatial coupling and diffusion rate of the concentration variables. For linear \bar{F} Turing showed that this system gives rise to spatial patterns that can oscillate temporally. He also considered the addition of a noise term and its effect on the selection of spatial patterns.

These equations naturally take into account spatial diffusion with the Laplacian operator on the RHS of Eq. 9.6. Furthermore, the continuous time derivative and the local reaction dynamics can be used to implement a temporal low pass filter. Thus, reaction-diffusion models can be constructed that satisfy the basic criteria already laid down for video feedback. Video feedback differs from Turing's reaction-diffusion models because of a nonlocal spatial coupling resulting from the spatial rotation and magnification. In direct analogy with the previous arguments, the proposed reaction-diffusion equation for color video feedback dynamics is

$$\frac{d\bar{I}(\bar{x})}{dt} = L\bar{I}(\bar{x}) + s\bar{I}(bR\bar{x}) + \sigma - \nabla^2\bar{I}(\bar{x}) \quad (9.7)$$

where the parameters s , f , b , L , and R , are as before, and σ is a matrix summarizing the spatial diffusion rate. The first term on the RHS of Eq. 9.7 is the "old image", the next term is the nonlocal "incoming image", and the last is the diffusion coupling. For spatial

structure and temporal behavior well below the spatial and temporal frequency cutoffs discussed above, this model should be valid.[2] As will be seen in the next section, video feedback dynamics has very similar phenomenology to that of chemical and biological systems described by this type of model. The reaction-diffusion model provides a conceptual simplicity as well as simpler notation. In fact, video feedback could be used to experimentally study this widely used class of models for spatio-temporal complexity.

The previous iterated functional equation model Eq. 9.4 can be derived from Eq. 9.7 upon discretization. Eq. 9.7 is the differential form of Eq. 9.4, an iterated integro-functional equation. A digital computer simulation of this continuum model naturally involves spatial and temporal discretization. Thus, as far as verifying the models by simulation, it is a moot point as to which is better, the iterated functional equation or reaction-diffusion model.

Having constructed these models, the burning question is whether their dynamics describe that actually found in real video feedback systems. For the very simplest behavior there is hope that the equations can be solved analytically. In general, though, simulating the models in a more controlled environment on a digital computer, for example, seems to be the only recourse.[7] After describing the dynamics typically observed in a real video feedback system in the next section, I will come back to the results of just such a digital simulation.

9.5. Video Software

The models and discussion of video physics in the last section may have given an impression of simplicity and straightforwardness in understanding video feedback dynamics. The intent in this section is to balance this with a little bit of the richness found in an actual color video system. An overview of the observed dynamics will be presented initially from a dynamical systems viewpoint. I will also address the appropriateness of this framework for some of the more complex dynamics. Then a brief description of a movie on video feedback follows. Stills from the movie illustrate some of the curious features of video feedback dynamics. And finally, these "experimental" results will be compared to those from preliminary digital computer simulations.

Video feedback dynamics can be roughly categorized as in Table II. For the simplest temporal behavior, descriptive terms from dynamical systems seem appropriate as in the first four behavior types. At first, let's ignore any possible spatial structure in the images. When a stable time-independent image is observed, it corresponds to a fixed point in the image space \bar{F} . Much of the behavior seen for wide ranges of control parameters falls into this category. Thus on the large scale video systems are very stable, as they should be in order to operate properly in a wide range of environments. For extreme parameter settings, such as small rotation, low contrast, large demagnification, and so on, equilibrium images are typically observed. For example, when the zoom is much less than unity then one observes an infinite regression of successively smaller images of the monitor within the monitor within

Table II. Video Feedback Dynamics

Observed	Attractor in Image Space
equilibrium image	fixed point
temporally repeating images	limit cycle
temporally aperiodic images	chaotic attractor
random relaxation oscillation	limit cycle with noise-modulated stability
spatially decorrelated dynamics (e.g. dislocations)	quasi-attractor with local temporal dynamics: fixed point limit cycle chaotic attractor
spatially complex image	spatial attractor: fixed point limit cycle chaotic attractor
spatially and temporally aperiodic	nontrivial combination of the above

.... The image is similar to that seen when two mirrors face each other. With a bit of rotation the infinitely regressing image takes on an overall "logarithmic spiral" shape that winds into the origin.

When the parameters are set to moderate values, one of the first non-trivial dynamics to appear is a simple oscillation. This would be a limit cycle in image space: a sequence of dissimilar images that after some time repeats. Because entire images repeat, individual points on the screen exhibit periodic behavior. Consequently, the values of intensity at a point cycle repetitively.*

At parameter values nearby often lie temporally aperiodic image sequences. Chaotic attractors in image space are most likely a good

description of this behavior type in the simplest cases.* When non-repeating images are reached from limit cycles with the change of a parameter, the bifurcation occurs in one of (at least) three ways:

- (1) Simple lengthening of the limit cycle period, until it is sufficiently long to be effectively aperiodic: for example, going from a limit cycle of 10 seconds to one of hours. New images are introduced, but are not sufficiently similar to be considered as close "recurrences";
- (2) The introduction of subharmonics at frequencies lower than that of the original limit cycle: these subharmonics are small modulations of the image's geometric structure. The overall image sequence remains the same, but differs in the modulated detail;
- (3) Suddenly at some critical parameter value, the limit cycle disappears and aperiodicity set in.

A very telling indication that complex behavior lies at nearby parameter settings comes from slightly perturbing the system. This can be done most conveniently by waving a finger between the monitor and camera. Once perturbed, the nearby complexity reveals itself by long and convoluted transients as the system settles down to its original simple fixed point or limit cycle. The closer in parameters to aperiodic behavior, the longer the transients. The simple dynamics discussed so

* In this case, given a time series of intensity values at a point, it is possible to "reconstruct" a state space picture of the attractor.[8]

far are globally stable in just this sense of returning to the same image(s) when perturbed. Of course, one can perturb the system too much, knocking it into another basin of attraction and so losing the original behavior. It is a common experience, in fact, that hand-waving perturbations will leave the screen dark, with the system requiring a "positive" stimulus of light from some source to get back to its initial attractor.

At large zoom, or spatial magnification, the system noise is readily (and exponentially) amplified. This regime is dominated by bursts of light and color. Depending on the controls, the bursts can come at regular intervals or at random times. Also, the particular features of the bursts, such as color, intensity, or even the pattern, can be the same or apparently randomly selected. This behavior is quite reminiscent of a limit cycle with (noise) modulated stability.[9]

The dynamics discussed so far is simple in the sense that its temporal features are the dominant aspect. No reference was made to spatial structure as the temporal dynamics was readily distinguished from it. A more precise way to make this distinction is in terms of whether the behavior at a suitably chosen point captures the dynamics.[8] Using intensity data from this point, if a simple attractor can be reconstructed, then the behavior is of a simple type that can be decomposed into temporal and spatial components. The last entries in Table II are an attempt to indicate that there is much more than this simple decomposable dynamics. Indeed, the spatial structure and its interaction with the temporal dynamics are what makes video feedback

different from other systems with complex dynamics, like chaotic nonlinear oscillators. But this difference presents various (intriguing) difficulties, especially because a dynamical system description does not exist for spatial complexity.[10] Nonetheless, a qualitative description is possible and, hopefully, will lead to the proper theoretical understanding of spatial dynamics.

Much of the following description, and the categorization used in Table II, is based on observed similarities in spatial structure. While it may be very difficult to unambiguously state what a complex image is, we as human beings can easily discern between two images and can even say some are "closer" than others in structure. I am not currently aware, however, of any mathematical definition of "closeness" for spatial structure that is of help with the dynamics observed in video feedback. Such a concept would be of immense value in sorting out complex dynamics not only in video feedback but in many other branches of science.

To denote images that are observed to be similar, but different in spatial detail, I introduce the phrase "quasi-attractor" for the associated object in state space. These state space objects appear to be globally stable to small perturbations and it is in this sense that they are attractors. Once perturbed, the video system returns to similar images, although in spatial detail they may be slightly altered from the original.

A good example of quasi-attractors is the class of images displaying dislocations. This terminology is borrowed from fluid dynamics, where dislocations refer to the broken structure of convective rolls in an otherwise simple array. Dislocations are regions of broken symmetry where the flow field has a singularity. The formation of this singularity typically requires a small, but significant, energy expenditure.* In video feedback, dislocations appear as inter-mingled light and dark stripes. The overall pattern can be composed of regular parallel arrays of alternating light and dark stripes with no dislocations, and convoluted, maze-like regions where stripes break up into shorter segments with many dislocations. The boundaries between segment ends form the dislocations. They can move regularly or wander erratically. Dislocations form in pairs when a stripe breaks in two. They also annihilate by coalescing two stripes. Dislocations make for very complex, detailed patterns whose temporal evolution is difficult to describe in terms of dynamical systems because of their irregular creation and annihilation. Nonetheless, when perturbed very similar images reappear. A quasi-attractor would be associated with global features, such as the relative areas of regular stripe arrays and dislocation regions, the time-averaged number of dislocations, or the pattern's gross symmetry.

* Both Couette flow [11] and Benard convection[12] exhibit this phenomenon. In nematic liquid crystal flow these are called disclinations. Similar structures appear in spin systems, such as magnetic bubble devices, and in the formation of crystals. Turing's discussion [6] of "dappled patterns" in a two-dimensional morphogen system is also relevant here.

Dislocations fall into the behavior class of spatially decorrelated dynamics. Moving away from one point on the screen, the spatial correlations decay rapidly enough so that eventually there is no phase relationship between the behavior of different regions. The governing dynamics in any one area is similar to that of other areas. The local behavior, however, can take on the character of a fixed point, limit cycle, or chaotic attractor. Thus while globally stable, the entire image cannot be described by a single attractor in the conventional sense of dynamical systems theory. This behavior type has been studied quantitatively in simple nonlinear lattice models.[13] Spatially decorrelated dynamics apparently is the cause of heart fibrillation that results in sudden cardiac death.[14]

The existence of spatial attractors that describe an image is another useful notion in classifying video dynamics. Intensity values as a function of a "pseudo-time" can be obtained by following along a simple parametrized curve on the screen. These values then can be used to reconstruct a "state space" picture [8] that captures some features of an image's structure. These features naturally depend on the type of curve selected. For example, data from a circle of fixed radius elucidates the rotational symmetry in an image. Similarly, data from along a radial line allows one to study radial wave propagation caused by magnification. The reconstruction of spatial attractors has been carried out for the above-mentioned lattice models.[13]

The rough classification is not yet complete. There are also image sequences that appear to be combinations of spatially-decorrelated

dynamics and complex spatial attractors. The latter entries in Table II indicate these possibilities.

The interaction of spatial and temporal dynamics makes it very difficult to describe the more complex behavior in any concise manner. To alleviate this problem a short video tape was prepared to illustrate the types of behavior in Table II.[4] The movie is particularly effective in giving a sense of the temporal evolution, stability, and richness of video feedback dynamics. An appreciation of the spatial complexity can be gleaned in a few stills from the movie. (See photos 1 - 5.) This will compensate hopefully those readers who do not have access to a video feedback system or who have not seen the movie.

The examples have a few common features. Regarding parameter settings, they were all made at rotations of approximately 40 degrees and with spatial magnifications slightly less than unity, unless otherwise noted. The discreteness caused by the finite resolution is apparent in each photo. Note that the spatial structures are typically many pixels in extent, so that the discreteness does not play a dominant role.

Photo 1 presents a typical nontrivial equilibrium image, or fixed point. It has an approximate nine-fold symmetry that comes from the rotation angle: $360/40 = 9$. The intensity at each point as a function of angle is periodic, with periods not greater than nine. The overall spatial symmetry as a function of rotation ϕ exhibits a "symmetry locking" highly reminiscent of that found in temporal frequency locking

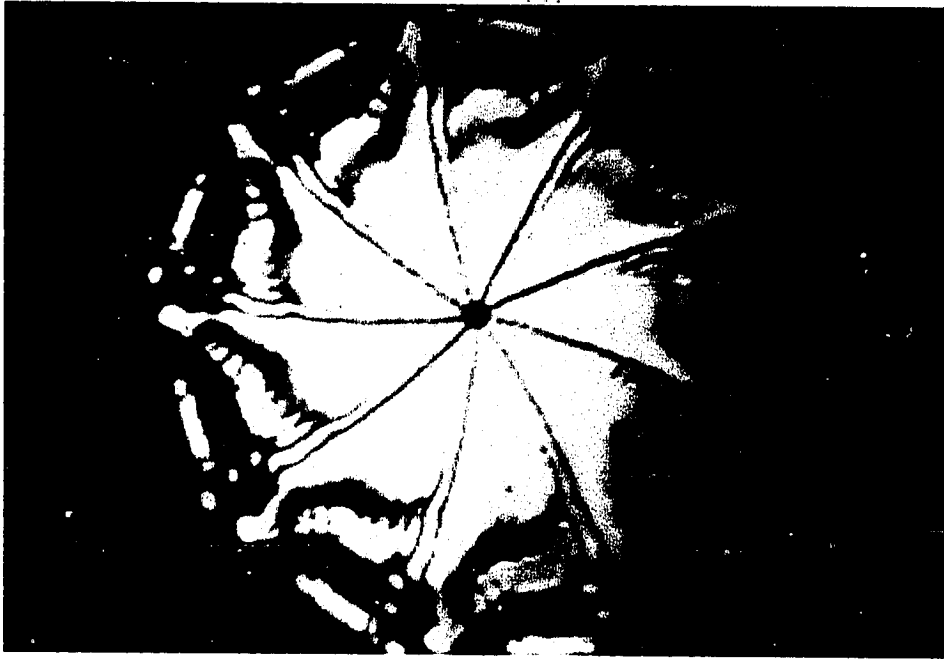


Photo 9.1.

Equilibrium Image

in nonlinear oscillators.[3] One noteworthy similarity is that the parameter window for which a given symmetry dominates decreases in width with increased order of the symmetry. For example, spatially symmetric images of period 31 occur for a much smaller rotation range those with period 9 symmetry.

One image out of a long limit cycle is shown in Photo 2. The limit cycle period was approximately 7 seconds. Initially, a green disk nucleates at the center of a homogeneous light blue disk. The green disk

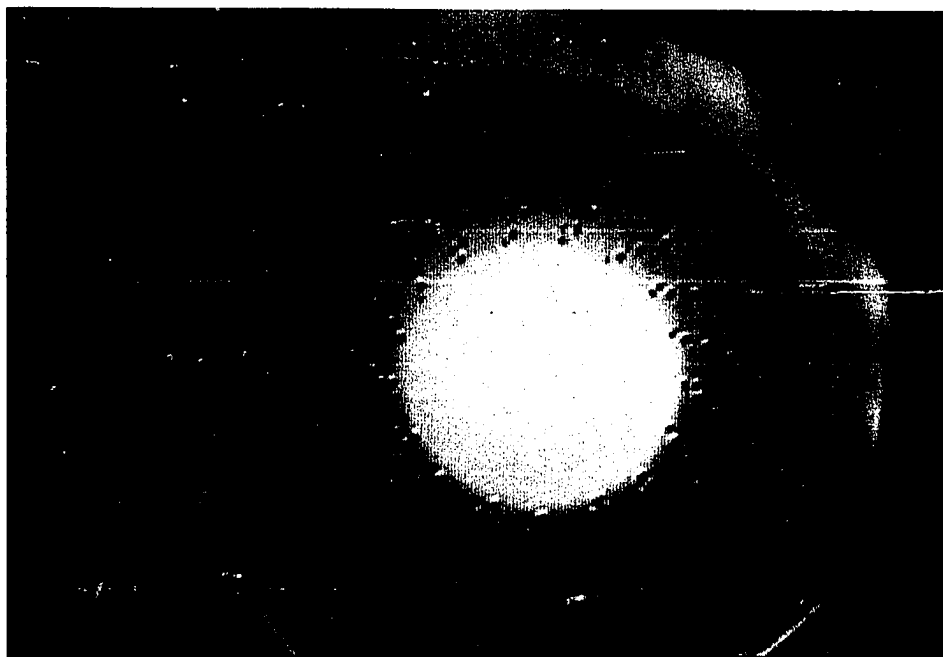


Photo 9.2.

Snapshot of a limit cycle.

grows to fill 80% of the illuminated area leaving a blue annulus. A red disk then nucleates inside the green disk, along with an outside ring of nine dots. The oscillation consists largely of the radially outward moving red disk, that intercepts the inward propagating dots. The still is taken at the moment of collision. The disk expands engulfing the dots and the green annulus, then itself is over taken by the inside boundary of the blue annulus that moves inward. The outer boundary of the red disk then recedes before the blue annulus. The screen then eventually becomes entirely light blue, at which moment the center nucleates a

growing green disk, and the cycle repeats. This limit cycle was stabilized by a very small marking near the screen's center.*

Photo 3 shows a still from a sequence of images with slowly moving dislocations. Toward the outside there is a "laminar" region of stripes. Moving inward from this, the first ring of nine dislocations is encountered. These were seen to move smoothly counter-clockwise. The

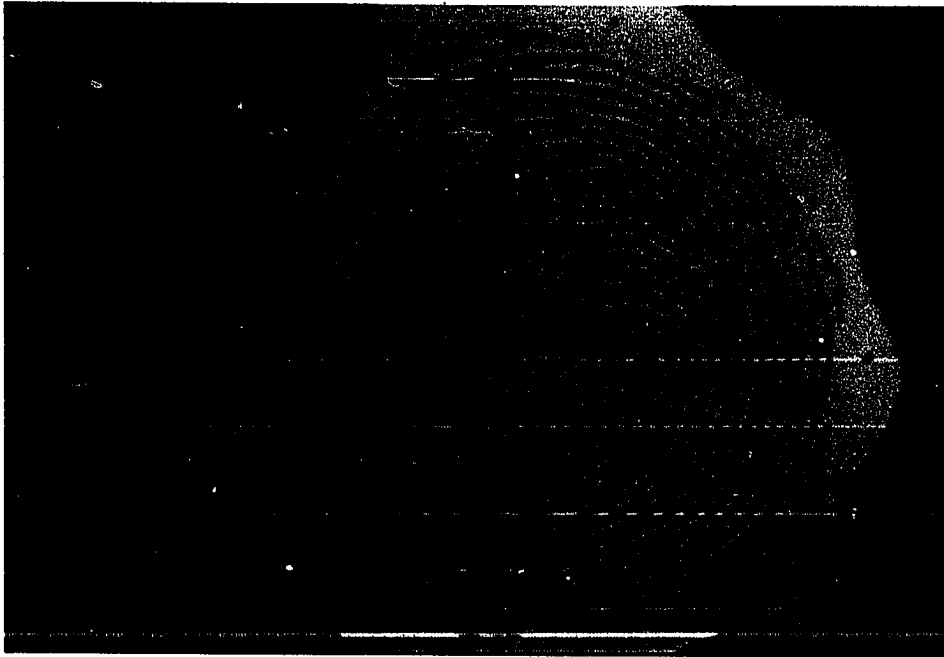


Photo 9.3.

Dislocations.

* One evening this cycle was allowed to oscillate for two hours with no apparent deviation from periodicity before the power was turned off.

center, however, periodically ejected thin white annuli that propagated out radially, only slowly acquiring clockwise rotation. The interface between the inner and outer regions caused the intervening maze-like dislocation pattern. The entire image shows a high degree of nine-fold symmetry although in the dislocation region it is quite complex.

Spiral patterns are quite abundant, as one expects from a transformation with rotation and magnification. Photo 4 illustrates a logarithmic spiral that dynamically circulates counterclockwise outward.



Photo 9.4.

Logarithmic spiral.

Temporally, the behavior is periodic with color and structure flowing outward from the center. The rotation here is $\phi = -30$ degrees. The logarithmic spiral can be easily described as a parametrized curve with angle ϕ and scaling b controls as follows

$$(x,y) = (b\cos(\phi\log t), b\sin(\phi\log t)) .$$

with $t \in [0,1]$. The structure and periodic coloring occur often in organisms, such as budding ferns and conch shells.

With relativey high zoom, or large spatial magnification greater than unity, noise in intensity and spatial structure is exponentially amplified. A common manifestation of this is periodic or random bursts. Photo 5 shows a snapshot of a developed burst that had spiralled clockwise out of the center in about one second. After a burst the screen goes dark with faint flickering, until another fluctuation occurs of sufficient magnitude to be amplified into a spiralling burst. The video system's finite resolution can be seen as a graininess on a scale larger than the intrinsic discreteness.

Luminance inversion stabilizes images by amplifying contrast. Black regions map into white and colors map to their opposite. This sharpens boundaries between dark, light, and colored areas in an image. Section VI of reference [2] discusses this stabilizing effect in more detail. Photo 6 shows an example of the "pinwheels" that dominate the images



Photo 9.5.

Relaxation oscillation at high zoom.

found with luminance inversion.* The rotation for this photo was $\phi = -90$ degrees. By adjusting the rotation, focus, and/or hue, controls the pinwheels are seen to move either clockwise or counter-clockwise. Winfree discusses similar "rotating waves" of electrical impulses that cause the heart's coordinated beating. Photo 6 should be compared to the figure on page 145 of reference [14].

* Bob Lansdon introduced me to these pinwheel images. See also reference [2].

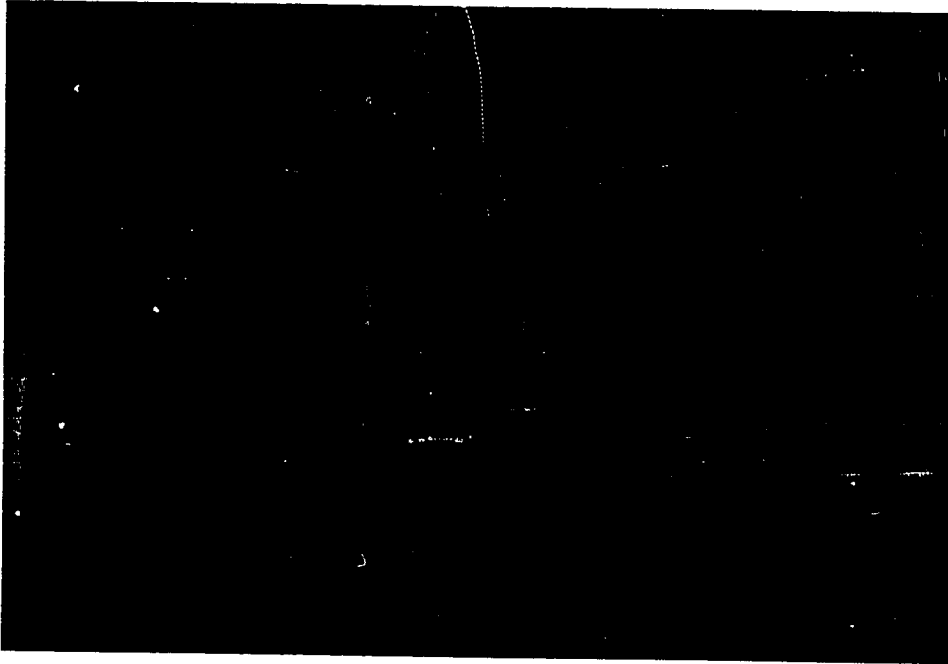


Photo 9.6.

Pinwheels.

Photo 7, also made with luminance inversion, is a snapshot of outward spiralling "color waves". These are very reminiscent of the ion concentration waves found in the Belousov-Zhabotinsky chemical reaction.[15] The rotation parameter here is roughly $\phi = -40$ degrees. As in the above pinwheels, every point in the image has a well-defined temporal phase, except for the center where there is a phase singularity.

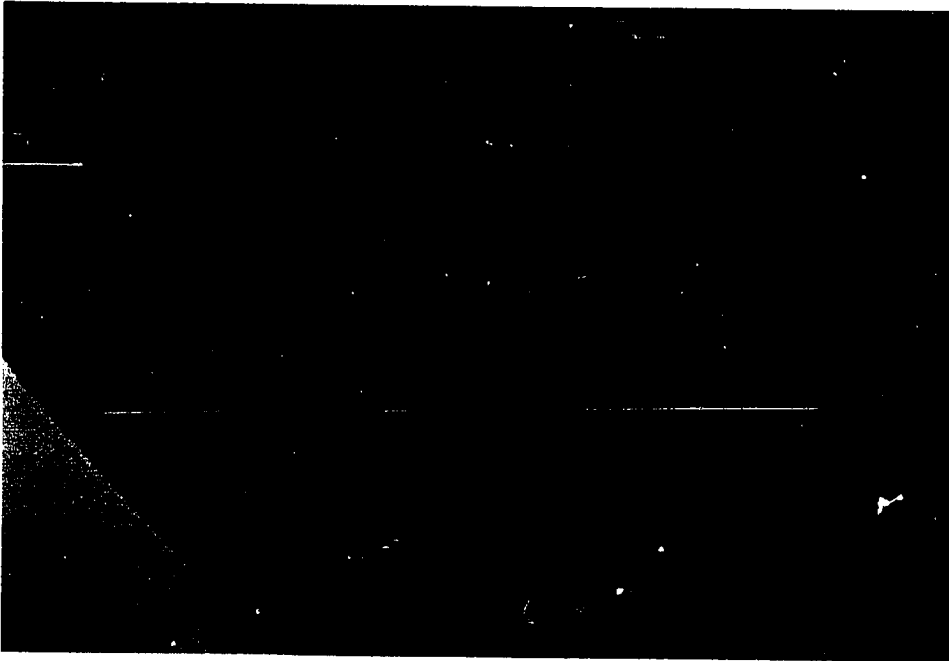


Photo 9.7.

Spiral waves.

A digital simulation based on Eqs. 4 and 7 captures some of the gross features of video feedback. To this extent the proposed models are correct. It is still an open question as to whether they reproduce the detailed spatio-temporal dynamics. Such comparison is a difficult proposition even in modeling temporal chaos alone. Digital simulations are many orders of magnitude slower than the space-time analog simulations of video feedback. And for this reason it is difficult, given model equations, to verify in detail and at numerous parameter settings their validity. To date digital simulations [16] have

reproduced the following features typical of video feedback:

- (1) equilibrium images with spatial symmetry analogous to Turing's waves [6];
- (2) fixed point images stable under perturbation;
- (3) meta-stability of fixed point images: sufficiently large perturbations destroy the image;
- (4) logarithmic spirals;
- (5) logarithmic divergence when the rasters are not centered.

At this preliminary stage of digital simulation it is not possible to discuss much in detail. In fact, it may be a long time until extensive digital simulations are carried out on the proposed models. The construction of, or use of pre-existing, special purpose digital image processors to simulate video feedback may be more feasible than using conventional digital computers. The next and final section comes back to address these questions of future prospects for understanding video feedback.

9.6. Variations on a Light Theme

Video feedback is a fast and inexpensive way to perform a certain class of space-time simulations. It also provides an experimental system with very rich dynamics that should be describable in some regimes by dynamical systems theory, while in other regimes it poses interesting questions about extending our current descriptive language to spatial

complexity.

One goal in studying video feedback is to see whether it could be used as a simulator for dynamics in other fields. Turing's original proposal of reaction-diffusion equations for biological morphogenesis comes to mind, as well as the image processing [17] and hallucinogenic dynamics [18] of the visual cortex. Naturally, the first task in this is to understand video feedback itself as completely as possible. Toward this immediate end, I have proposed models based on video physics and presented an overview of the possible behavior in a particular color video system. The next steps in this program are to make a more quantitative study of the attractors and bifurcations with calibrated video components. Data from these experiments would be analyzed using techniques from dynamical systems to (i) reconstruct state space pictures of the simpler attractors, and (ii) quantify the unpredictability of the simple aperiodic behavior.

A second approach to understanding video feedback dynamics is to study other configurations of video components. The possibilities include:

- (1) masking portions of the screen to study the effect of boundary conditions;
- (2) optical processing with filters, lenses, mirrors, and the like;
- (3) using magnets to modulate the monitor electron beam scanning;

- (4) connecting two camera-monitor pairs serially, thus giving twice as many controls;
- (5) nonlinear electronic processing of the video signal;
- (6) inserting a digital computer into the feedback loop via a video frame buffer.

The possible modifications are endless. But, hopefully, they will help point to further understanding and lead to applications in other fields.

Variations (5) and (6) may lead to the most fruitful applications of video feedback. For example, they allow one to alter the governing rules in simulations of two-dimensional local and nonlocal automata. In this process an image is stored each raster time. Each pixel and its neighbors are operated on by some (nonlinear) function. For rapid ("real-time") simulation this function is stored in a "look-up" table. The pixel value and those of its neighbors form the input to the table. The table's result then becomes the pixel's new value that is stored and displayed. This is a very general configuration. With video feedback one has simple control over the nonlocality of the rules using rotation and spatial magnification, and over the number of neighboring pixels using the focus.

A monochrome system, employing an intensity threshold to give crisp black and white images, could be used to simulate binary cellular automata. This restriction on the intensity range falls far short of the possible pixel information in video systems. Indeed, as discussed in the

appendix, color systems are capable of transmitting roughly 20 bits of information per pixel. This including a random "noise floor" for small signals. Generalizing cellular automata, from a few states per site to many, leads to lattice dynamical systems [13]. This corresponds in the video system to removing the above thresholding. Thus this video configuration will be especially useful in the experimental study of lattice dynamical systems and in the verification of analytic and numerical results, such as spatial period-doubling, found in some nonlinear lattices [13].

A number of video image processors are available, both analog and digital. Many have been constructed solely according to their aesthetic value by video artists. Certainly, among this group there is a tremendous amount of qualitative understanding of video dynamics. At the other extreme of the technical spectrum, many of the emerging supercomputers have adopted architectures very similar to that of video feedback systems. These machines would be most useful in detailed quantitative simulations. And, in turn, video feedback might provide an inexpensive avenue for initial study of simulations planned for these large machines.

Physics has begun only recently to address complex dynamical behavior. Looking back over its intellectual history, the very great progress in understanding the natural world, with the simple notions of equilibrium and utter randomness, is astounding. For the world about us is replete with complexity arising from its intimate interconnectedness. This takes two forms. The first is the recycling of

information from one moment to the next, a temporal inter-connectedness. This is feedback. The second is the coupling at a given time between different physical variables. In globally stable systems, this often gives rise to nonlinearities. This inter-connectedness lends structure to the chaos of microscopic physical reality that completely transcends descriptions based on our traditional appreciation of dynamical behavior.

From a slightly abstract viewpoint, closer to my personal predilections, video feedback provides a creative stimulus of behavior that apparently goes beyond the current conceptual framework of dynamical systems. Video feedback poses significant questions, and perhaps will facilitate their answer. I believe that an appreciation of video feedback is an intermediary step, prerequisite for our comprehending the complex dynamics of life.

9.7. Acknowledgements

I am particularly indebted to Ralph Abraham for introducing me to video feedback a number years ago. Special thanks are due to Doyme Farmer and the Center for Nonlinear Studies, Los Alamos National Laboratory, for the support and encouragement of this project. Larry Cuba generously loaned his video equipment for Photos 6 and 7. Elaine Ruhe was especially helpful in the preparation of the video tape and stills. I would also like to thank the Automata Workshop participants who played with the video feedback demonstration and discussed their ideas with me. Particular thanks go to Bob Lansdon, Alice Roos, Otto

Rössler, and Art Winfree, for useful discussions on video feedback.

Appendix. Video Physics

There are many types of camera pickup tubes, but for concreteness I will concentrate on the common vidicon tube and describe how it converts an image to an electronic signal. The vidicon relies on the photoconductive properties of certain semiconductors (such as selenium). When light is incident on these materials their electrical resistance is reduced. Photoconductors can have quite large quantum efficiencies, approaching 100%, with virtually all the incident photon energy being converted to mobilizing electrons in the material. Once energized these electrons diffuse in an ambient electric field.

The vidicon takes advantage of these mobile electrons in the following way. (Refer to figure 9.4.) An image is focused on a thin photoconducting layer (A) approximately one square inch in size. Spatial variation in an image's light intensity sets up a spatial distribution of mobile electrons. Under the influence of a small bias field these diffuse toward and are collected at the transparent video signal pickup conductor (B). During operation the photoconductor/pickup sandwich acts as a leaky capacitor with spatially varying leakage: the more incident light, the larger the local leakage current. The electron beam (C) from the vidicon's cathode scans the back side of the photoconductor depositing electrons, restoring the charge that has leaked away, and hence, bringing it to a potential commensurate with the cathode. The coils (D) supply the scanning field that moves the electron beam over

the photoconductor. They are driven synchronously with the horizontal and vertical raster timing circuits (top of diagram). The output video signal corresponds to the amount of charge locally deposited by the beam at a given position during its scan. This charge causes a change in the leakage current and this change is picked up capacitively and then amplified.

The important features of this conversion process, aside from the raster scanning geometry already described, are

- (1) the diffusion of electrons as they traverse the photoconductor, and
- (2) the local storage and integration of charge associated with the light incident during each raster time.

The diffusion process directly limits the attainable spatial resolution. This places an upper bound on the number of horizontal lines and the number of pixels (distinct picture elements) within each line. The effect on spatial patterns is that there can be no structure smaller than this diffusion limit. Another interpretation of this is that, over the period of several rasters, there is a diffusive coupling between elements of an image.

The high spatial frequency cutoff can be easily estimated. The electron beam forms a dot on the photoconductor's backside approximately 1 to 2 mils in diameter. Diffusion then spreads this out to roughly twice this size by the time these electrons have traversed the layer, yielding an effective 3 to 4 mils minimum resolution. For a vidicon with

a one inch square photoconducting target, this results in a limit of 250 to 300 pixels horizontally and the same number of lines vertically. These are in fact nominal specifications for consumer quality cameras. Additionally, although the raster geometry breaks the image into horizontal lines, the resolution within each line is very close to that given by the number of scan lines. It will be a reasonable approximation, therefore, to assume that the spatial diffusion is isotropic.

In a similar manner the charge storage and integration during each raster time places an upper limit on the temporal frequency response of the system. In fact, this storage time τ_s can be quite a bit longer than the raster time τ_r of $\frac{1}{30}$ second. A rough approximation to this would be $\tau_s \sim 10\tau_r \sim \frac{1}{3}$ second. Thus the system's frequency response should always be slower than 3 Hz. And this is what is observed experimentally. Even the simplest (linear) model for video feedback must contain spatial and temporal low pass filters corresponding to the above limitations.

The optical system that forms the image on the photoconductor has spatial and temporal bandwidths many orders of magnitude greater than the vidicon itself. Hence these intrinsic optical limitations can be neglected. The optical system controls, however, are quite significant. The focus, for example, can affect an easily manipulated spatial diffusion by moving the image focal plane before or behind the photoconductor. In addition, by adjusting it to one side of exact focus the image can be inverted. Very small changes in the zoom, or spatial magnification, can have quite large qualitative effects because the

image information repetively circulates in the feedback loop. A spatial magnification greater than unity increases exponentially with the number of passes through the loop. Similarly, adjusting the admitted light with the f/stop can cause the light in an image to dissipate completely when set below some intrinsic threshold.

The image intensity can again be adjusted with the brightness control on the monitor, perhaps to compensate for the camera's f/stop setting. The brightness adjusts the DC intensity level of the video signal, while the contrast amplifies its dynamic range, or the AC portion of the video signal. High contrast will amplify any noise or spurious signal into an observable flickering of the image. A monochrome monitor's screen (E) is coated with a uniform layer of phosphor that emits light when struck by the electron beam (G). Using the monitor's driving coils (D), the raster synchronizing circuits move the beam to the appropriate position on the screen for the incoming video signal. This signal modulates the beam's intensity (F). The screen's spatial resolution is effectively continuous with a lower bound significantly less than that imposed by the vidicon resolution and by the finite number of scan lines. Additionally, the phosphor stores each raster for a short time to reduce flickering. Thus there is another image storage element in the feedback loop. The phosphor's persistence is typically a single raster time and so it can be neglected compared to the vidicon's storage time.

There are a number of sources of error, or deviations from the idealized video feedback system. Here I will briefly mention a few that

could be taken, more or less easily, into account in the modeling, but for simplicities sake will not be included. The first omission that I have made in describing the functioning of video systems, is that the bulk of them transmit two interlaced half-rasters, or fields, every sixtieth of a second. A complete raster is still formed every thirtieth of a second, but the successive images appear to flicker less than without interlaced fields. Since the time scale of this is much less than the image storage and integration time of the vidicon it can be neglected.

A second and important error source is the intrinsic noise of the intensity signal. A number of physical processes contribute to this noise. The discreteness of the quantum processes and the electron charge produce resistive noise in the photoconductor. The electronic amplifiers for the signal also introduce noise. The net effect though is a signal to noise ratio of about 40 db. This translates into about 10 mV white noise superimposed on the 1 V standard video signal, or into about 1% fluctuation in the intensity of pixels on the monitor's screen.

The photoconductor's monotonic, but nonlinear, current output i_o as a function of light intensity I_i adds a third error. For vidicons $i_o \sim I_i^g$ with $g \in [.6, .9]$. Furthermore, this response function saturates above some intensity threshold I_{sat} . Vidicon photoconductors also exhibit a nonuniform sensitivity of about 1% over the target region.

When the camera is very close to the monitor, there is significant geometric distortion due to the screen's curvature. Geometric distortion

also arises from other errors in the system, such as the adjustment of the horizontal and vertical raster scanning circuitry. These distortions can be reduced to within a few percent over the image area. Finally, within the monitor there are saturating nonlinearities in its response to large intensity signals and high brightness or high contrast settings. This list is by no means exhaustive, but at least it does give a sense of the types of errors and their relative importance.

References

1. R. Abraham, "Simulation of Cascades by Video Feedback", Lect. Notes in Math. 525 (1976) 10.
2. G. Ferraro and G. Häusler, "TV Optical Feedback Systems", Opt. Eng. 19 (1980) 442; see references in section 5 of S.A. Collins and K.C. Wasmundt, "Optical Feedback and Bistability: a review", Opt. Eng. 19 (1980) 478.
3. B. van der Pol, "Frequency Demultiplication", Nature 120 (1927) 363; C. Hayashi, Forced Oscillations in Nonlinear Systems, Nippon Printing and Publishing Co., Osaka, Japan, 1953.
4. J.P. Crutchfield, "Dynamics in the Space of Images", 1983, Entropy Productions, P.O. Box 8045, Santa Cruz, California 95060; 12 min. video tape: U-matic, VHS, and Beta formats.
5. See for example R. Abraham and C.D. Shaw, Dynamics - The Geometry of Behavior, Vols. I and II, Aerial Press (1982), P.O. Box 1360, Santa Cruz, California 95061; D.R.J. Chillingsworth, Differential Topology with a View to Applications, Pitman, London, 1976; or P. Collet and J.-P. Eckmann, Iterated Maps of the Interval as Dynamical Systems, Birkhauser (1980).
6. A.M. Turing, "A Chemical Basis for Biological Morphogenesis", Phil. Trans. Roy. Soc. (London), Ser. B, 237, (1952) 37.
7. J.P. Crutchfield, in preparation.
8. N.H. Packard, J.P. Crutchfield, J.D. Farmer, and R.S. Shaw, "Geometry from a Time Series", Phys. Rev. Lett. 45, (1980) 712; see also H. Froehling, J.P. Crutchfield, J.D. Farmer, N.H. Packard, and R.S. Shaw, "On Determining the Dimension of Chaotic Flows", Physica 3D (1981) 605.
9. See section 9 of Ref. [Turing] and J.D. Farmer, "Sensitive Dependence to Noise without Sensitive Dependence to Initial Conditions", LANL Preprint.

10. For one approach to quantifying spatial complexity see J.P. Crutchfield, Noisy Chaos, Ph.D. dissertation, University of California, Santa Cruz (1983).
11. R.J. Donnelly, K. Park, R.S. Shaw, and R.W. Walden, "Early Non-periodic Transition in Couette Flow", *Phys. Rev. Lett.* 44 (1980) 987.
12. K.E. Heikes and F.H. Busse, "Weakly Nonlinear Turbulence in a Rotating Convection Layer", *New York Acad. Sci.* 357 (1980) 28.
13. J.P. Crutchfield, "Spatial Complexity in Lattice Dynamical Systems: The Logistic and Circle Lattices", in preparation.
14. A.T. Winfree, "Sudden Cardiac Death: A Problem in Topology", *Sci. Amer.* 248 (5) (1983) 144.
15. See for example A.T. Winfree, "Singular Filaments Organize Chemical Waves in Three Dimensions: Parts 1, 2, and 3", preprint, Department of Biological Sciences, Purdue University.
16. J.P. Crutchfield, in preparation.
17. J. Herault, G. Bouvier, and A. Chehikan, "A New Algorithm for Image Processing based on the Properties of Neural Nets", *J. Phys. Lett.* 41 (1980) L-75.
18. J.D. Cowan, "Spontaneous Symmetry Breaking in Large Scale Nervous Activity", *Int'l J. Quant. Chem.* 22 (1982) 1059.
19. J.P. Crutchfield, Prediction and Stability in Classical Mechanics, University of California, Santa Cruz, 1979.
20. D. Ruelle, "Large Volume Limit of the Distribution of Characteristic Exponents in Turbulence", Institut des Hautes Etudes Scientifiques, Bures-sur-Yvette, France, preprint, 1982.

APPENDIX A

Algorithms for Dynamical Systems

1. Introduction

This appendix presents a few of the programs used in the foregoing work. The intention of providing these is to allow the interested reader to see the algorithmic implementation of dynamical systems concepts. While the included programs are not written in their full generality (e.g. arbitrary dimension) they provide the experimentalist with the basic ideas that will lead to appropriate algorithms.

The programs are written in the C language and were developed and run on several VAX11/780 UNIX systems. C programs from experienced programmers can be quite terse and the advanced logical structures obscure. The C language constructs employed in these programs, however, are very straightforward so that transcription into other languages should be easy once the algorithm is understood. The algorithms are implemented efficiently, but no "tweaking" for speed was included as this tends to obscure the code.

Although these programs have been used extensively by myself and checked numerous times they are probably not error free. The following sections contain program listings with comments and short introductory remarks. The programs are lightly commented. For language reference see The C Programming Language by Brian Kernighan and Dennis Ritchie

(Prentice-Hall, 1978).

The programs are structured in the following order: introductory comments, preprocessor (#) commands, variable and function definitions, preliminary set up of variables (including I/O), main algorithm, and finally subroutines. The curly brackets denote different levels of loop nesting or "logical depth".

2. Binary Entropy (topological and metric)

This is the basic algorithm for computing the topological, metric, and correlation entropies. It is set up for binary symbols from a two element partition of the cusp-to-hump map family. A loop is included to compute these entropies at different decision points and so to search for an effective generating partition. Furthermore, the added noise may be varied. As the metric entropy is the growth rate of information with increasing symbol sequence length, the algorithms would seem to require accumulation of probability histograms for each length of symbol sequence. This is circumvented by accumulating a single histogram for the longest length sequence and then grouping bins of this histogram to get the probabilities for shorter lengths. This provides a space and time savings. The entropies are estimated by the "two-point slope" at the program's end.

```

/* entvsdnois.c: calculates the entropies versus decision point in */
/*                order to find an effective generating partition */
/*                at a given noise level.                          */
/*                The topological, metric, and correlation          */

```

A.3

```

/*          entropies are computed.          */
/*          Entropy is calculated as H(n) - H(n-1).      */

#include <stdio.h>

#define NumofSym 16          /* maximum length of sequences */
#define two2NumSym 65536    /* maximum number of 16-sequences */

main(argc,argv)
int argc;
char *argv[];
{
    double metent,topent,height,epsilon,pow();
    double a,x,r,temp,noise,etobin,decision,dmax,dmin,dinc;
    double metric[NumofSym],topo[NumofSym],correl[NumofSym];
    double sqrt(),log(),fabs(),atof();
    register int i,j,symbol;
    int iterations,k,l,num=0,pair;
    int dnum,rand(),atoi(),psym[two2NumSym];
    int mask = two2NumSym - 1;
    FILE *fp,*fopen();

    etobin = 1./log(2.);
    srand(214794745);

    if(argc != 5)
    {
        printf("usage: entvsdnois decsnmin decsnmax numofdecnpts noise
");
        exit();
    }

    dmin = atof(argv[1]);
    dmax = atof(argv[2]);
    dnum = atoi(argv[3]);
    noise = sqrt(3.0)*atof(argv[4]);

    printf("%f %f %d %f ",dmin,dmax,dnum,atof(argv[4]));
    dinc = (dmax-dmin)/(float)dnum;
    height = 3.8/4.;
    epsilon = 1. - .1;
    x = 1./3.1;
    iterations = 100000;

    for(decision=dmin;decision<dmax;decision+=dinc)
    {
        for(i=0;i<two2NumSym;i++) psym[i] = 0;
        for(i=0;i<300;i++) /* transient iterations */
        {
            if(x < .5)
                temp = 1. - 2.*x;

```

```

else
    temp = 2.*x - 1.;
x = height*(1.-pow(temp,epsilon));
symbol <<= 1; /* initial symbol sequence set up */
if(x > decision) ++symbol; /* right <=> 1, left <=> 0 */
symbol &= mask;
}
for(i=0;i<iterations;i++) /* histogram accumulation */
{
if(x < .5) /* The Hump */
    temp = 1. - 2.*x; /* to */
else /* Cusp */
    temp = 2.*x - 1.; /* map */
x = height*(1.-pow(temp,epsilon)) /* family */
    + noise*(rand(1)/1073741827.5-1.); /* with noise */
symbol <<= 1;
if(x > decision) ++symbol;
symbol &= mask; /* unused bits are masked off */
++psym[symbol]; /* to form index to histogram */
}

pair = 2; /* compute entropies by grouping bins */
for(i=0;i<2;i++)
{
metric[i] = 0.;
topo[i] = 0.;
correl[i] = 0.;
for(k=0;k<two2NumSym;k+=pair)
{
temp = 0.;
for(l=0;l<pair;l++) temp += (float)psym[k+l];
if(temp != 0.)
{
++topo[i];
temp = temp/((float)iterations);
metric[i] -= temp*log(temp);
correl[i] += temp*temp;
}
}
topo[i] = etobin*log(topo[i]);
metric[i] = etobin*metric[i];
correl[i] = -etobin*log(correl[i]);
pair = pair/2;
}
printf("%f %f ",
topo[1]-topo[0],metric[1]-metric[0],correl[1]-correl[0]);
}
}

```

3. Lyapunov Characteristic Exponents

```

/* 3dlce.c: Computes the spectrum of Lyapunov Characteristic      */
/*           for three-dimensional flows. For speed the flow is    */
/*           defined in the preprocessor #define statements       */
/*           In this example we have Rossler's equations.        */
/*           The method is due to Shimada and Nagashima which uses */
/*           the tangent space flow to evolve the tangent vectors. */
/*           This differs from my Senior Thesis technique that uses */
/*           only the base space equations to flow the fiducial    */
/*           basis along. The Shimada-Nagashima technique is      */
/*           slightly more efficient. See I. Shimada and T.      */
/*           Nagashima, "A Numerical Approach to Ergodic Problem  */
/*           of Dissipative Dynamical Systems", Prog. Theo. Phys. */
/*           vol. 61 (1979) 1605.                                  */
/*           */

#define xdot(X,Y,Z) (-(Y)-(Z))
#define ydot(X,Y,Z) ((X)+a*(Y))
#define zdot(X,Y,Z) (b+(X)*(Z)-c*(Z))
#define dxdot(dX,dY,dZ) (-(dY)-(dZ))
#define dydot(dX,dY,dZ) ((dX)+a*(dY))
#define dzdot(dX,dY,dZ) ((dX)*z+(x-c)*(dZ))

double x,y,z,a,b,c,timestep;

main(argc,argv)
int argc;
char *argv[];
{
    double normalize(),dot(),log(),atof();
    double dx[3],dy[3],dz[3],time,lengthdx,lengthdy,lengthdz;
    double dotxy,dotxz,dotyz,exponent1=0.,exponent2=0.,exponent3=0.;
    register i,j,tsperpb;
    int numpb,atoi();

    x      = atof(argv[1]);
    y      = atof(argv[2]);
    z      = atof(argv[3]);
    numpb  = atoi(argv[4]);
    a      = atof(argv[5]);
    b      = atof(argv[6]);
    c      = atof(argv[7]);
    timestep = atof(argv[8]);
    tsperpb = atoi(argv[9]);

    dx[0] = 1.; dx[1] = 0.; dx[2] = 0.;
    dy[0] = 0.; dy[1] = 1.; dy[2] = 0.;

```

```

dz[0] = 0.; dz[1] = 0.; dz[2] = 1.;

for(i=0;i<numpb;i++)
{
    for(j=0;j<tsperpb;j++)
    {
        tangflow();
        cotangflow(dx);
        cotangflow(dy);
        cotangflow(dz);
    }
    lengthdx = normalize(dx);
    dotxy = dot(dx,dy);
    vectorsub(dy,dotxy,dx);
    lengthdy = normalize(dy);
    dotxz = dot(dx,dz);
    dotyz = dot(dy,dz);
    vectorsub(dz,dotxz,dx);
    vectorsub(dz,dotyz,dy);
    lengthdz = normalize(dz);
    exponent1 += log(lengthdx);
    exponent2 += log(lengthdy);
    exponent3 += log(lengthdz);
}
time = numpb*tsperpb*timestep;
printf("%f,%f,%f,%f ",
        time,exponent1/time,exponent2/time,exponent3/time);
}

double normalize(vctr)
double vctr[];
{
    double length,sqrt();
    length = sqrt(vctr[0]*vctr[0]+vctr[1]*vctr[1]+vctr[2]*vctr[2]);
    vctr[0] /= length;
    vctr[1] /= length;
    vctr[2] /= length;
    return(length);
}

double dot(v1,v2)
double v1[],v2[];
{ return(v1[0]*v2[0]+v1[1]*v2[1]+v1[2]*v2[2]); }

vectorsub(v1,scale,v2)
double scale,v1[],v2[];
{
    v1[0] -= scale*v2[0];
    v1[1] -= scale*v2[1];
    v1[2] -= scale*v2[2];
}

```

```

tangflow()
{
  double x1,x2,x3,x4,y1,y2,y3,y4,z1,z2,z3,z4;
  x1 = xdot(x,y,z);
  y1 = ydot(x,y,z);
  z1 = zdot(x,y,z);
  x2 = xdot(x+timestep*x1/2.,y+timestep*y1/2.,z+timestep*z1/2.);
  y2 = ydot(x+timestep*x1/2.,y+timestep*y1/2.,z+timestep*z1/2.);
  z2 = zdot(x+timestep*x1/2.,y+timestep*y1/2.,z+timestep*z1/2.);
  x3 = xdot(x+timestep*x2/2.,y+timestep*y2/2.,z+timestep*z2/2.);
  y3 = ydot(x+timestep*x2/2.,y+timestep*y2/2.,z+timestep*z2/2.);
  z3 = zdot(x+timestep*x2/2.,y+timestep*y2/2.,z+timestep*z2/2.);
  x4 = xdot(x+timestep*x3,y+timestep*y3,z+timestep*z3);
  y4 = ydot(x+timestep*x3,y+timestep*y3,z+timestep*z3);
  z4 = zdot(x+timestep*x3,y+timestep*y3,z+timestep*z3);
  x += (x1+2.*x2+2.*x3+x4)*timestep/6.;
  y += (y1+2.*y2+2.*y3+y4)*timestep/6.;
  z += (z1+2.*z2+2.*z3+z4)*timestep/6.;
}

cotangflow(oneform)
double oneform[];
{
  double d1,d2,d3,x1,x2,x3,x4,y1,y2,y3,y4,z1,z2,z3,z4;

  d1 = oneform[0];
  d2 = oneform[1];
  d3 = oneform[2];

  x1 = dxdot(d1,d2,d3);
  y1 = dydot(d1,d2,d3);
  z1 = dzdot(d1,d2,d3);
  x2 = dxdot(d1+timestep*x1/2.,d2+timestep*y1/2.,d3+timestep*z1/2.);
  y2 = dydot(d1+timestep*x1/2.,d2+timestep*y1/2.,d3+timestep*z1/2.);
  z2 = dzdot(d1+timestep*x1/2.,d2+timestep*y1/2.,d3+timestep*z1/2.);
  x3 = dxdot(d1+timestep*x2/2.,d2+timestep*y2/2.,d3+timestep*z2/2.);
  y3 = dydot(d1+timestep*x2/2.,d2+timestep*y2/2.,d3+timestep*z2/2.);
  z3 = dzdot(d1+timestep*x2/2.,d2+timestep*y2/2.,d3+timestep*z2/2.);
  x4 = dxdot(d1+timestep*x3,d2+timestep*y3,d3+timestep*z3);
  y4 = dydot(d1+timestep*x3,d2+timestep*y3,d3+timestep*z3);
  z4 = dzdot(d1+timestep*x3,d2+timestep*y3,d3+timestep*z3);
  oneform[0] += (x1+2.*x2+2.*x3+x4)*timestep/6.;
  oneform[1] += (y1+2.*y2+2.*y3+y4)*timestep/6.;
  oneform[2] += (z1+2.*z2+2.*z3+z4)*timestep/6.;
}

```

4. Kneading Calculus

These two programs provide very accurate and very fast methods for computing the topological entropy of one-dimensional maps with two monotone pieces: "two-lap maps". The first finds the lowest root of Milnor's and Thurston's "kneading determinant". The negative logarithm of this root is the topological entropy. The kneading determinant is a formal power series with successive terms that follow the left (-1) and right (+1) behavior of iterates of the map's maximum. Left and right are defined relative to which side of the maximum the iterate falls. The root is found by a binary search.

The second program determines the topological entropy of two-lap maps using Rob Shaw's "mother-daughter" algorithm. This method computes the entropy as the growth rate of the number of monotone pieces (laps) of the map's n-th iterate. The algorithm identifies the generation of new laps by noting which laps are "folded" upon iteration by the map's maximum.

```

/* knddetbif.c: Employs Milnor and Thurston's Kneading Determinant */
/*              to compute a map's topological entropy as the lowest */
/*              real root of the characteristic polynomial from the */
/*              map's kneading sequence.                               */
/*              See P. Collet, J.P. Crutchfield, and J.-P. Eckmann, */
/*              "On Computing the Topological Entropy of Maps", Comm.*/
/*              Math. Phys. vol. 88 (1983) 257.                       */

#include <stdio.h>
#define iterations 100

main(argc,argv)
int argc;

```

```

char *argv[];
{
double x,incr,minr,maxr,r,t,decision=0.5,KneadDet,error,tlow,thigh;
double log(),pow(),atof();
register int i,j;
int num,sign[iterations];
char label[100];

minr = atof(argv[1]);
maxr = atof(argv[2]);
num = atoi(argv[3]);

error = .0001;
incr = (maxr - minr)/num;
for(r=minr;r<=maxr;r+=incr)
{
x = decision;
sign[0] = 1.0;
for(i=1;i<iterations;i++)
{
x = r*x*(1.-x);
if(x > decision)
sign[i] = -sign[i-1];
else if(x == decision)
sign[i] = 1;
else
sign[i] = sign[i-1];
}
tlow = 0.0;
thigh = 1.0;
while((thigh - tlow) > error)
{
t = (thigh + tlow)/2.;
KneadDet = 1.0;
for(i=1;i<iterations;i++)
{
KneadDet += sign[i]*pow(t,(float)i);
}
if(KneadDet >= 0.)
tlow = t;
else
thigh = t;
}
printf("%1.10f,%1.10f ",r,1./log(2.)*log(1./t));
}
}

```

```

/* telap.c: Employs R. Shaw's Mother-Daughter algorithm to compute */
/*          a map's topological entropy by counting the growth rate */
/*          of the number of laps with iteration.                    */

#include <stdio.h>
#define iterations 100

main(argc,argv)
int argc;
char *argv[];
{
    double sxy,sx,sy,sxx,denom,topent;
    double r,oneside,otherside,etobin,log(),fabs(),atof();
    double topo[iterations],laps;
    double current[iterations],previous[iterations];
    int itemp,fitnum,branch[iterations];
    int atoi();
    register int i,numtype,onesidenum;

    r          = atof(argv[1]);
    etobin     = 1./log(2.);
    oneseide   = 0.5;
    oneseide   = r*oneside*(1.-oneside);
    otherside  = r*oneside*(1.-oneside);
    onesidenum = 1;
    previous[1] = 1.;

    for(numtype=2;numtype<iterations;numtype++)
    {
        if((oneside-0.5)*(otherside-0.5) < 0.)
        {
            branch[numtype-1] = onesidenum;
            oneseide = r*.25;
            onesidenum = 1;
        }
        else
        {
            branch[numtype-1] = 0;
            oneseide = r*oneside*(1.-oneside);
            ++onesidenum;
        }
        otherside = r*otherside*(1.-otherside);
        for(i=0;i<numtype;i++) current[i] = 0.;
        for(i=1;i<numtype;i++)
        {
            current[i+1] += previous[i];
            current[branch[i]] += previous[i];
        }
        laps = 0.;
        for(i=1;i<numtype;i++)
    {

```

```

        laps += current[i];
        previous[i] = current[i];
    }
    topo[numtype-2] = etobin*log(laps);
}

fitnum = 32;
sxy = 0.0; sx = 0.0; sy = 0.0; sxx = 0.0;
for(i=1;i<fitnum;i++)
{
    itemp = iterations-2-i;
    sxy += itemp*topo[itemp];
    sx += itemp;
    sy += topo[itemp];
    sxx += itemp*itemp;
}
denom = fitnum*sxx - sx*sx;
topent = (fitnum*sxy - sx*sy)/denom;
printf("%1.15e,%1.15e ",r,topent);
}

```

5. Power Spectra

This is the program used to compute the power spectrum of the Couette flow signals. Needless to say, it can be used for any data. The program computes the average power spectrum using the Fourier transform library subroutines. The program's last portion sets up plotting, and will have to be modified to use the available plotting package.

```

/* fft.couette.c: Averaged Power Spectrum using      */
/*                Fast Fourier Transform             */
/*                Averages power spectrum of         */
/*                input data file                    */
/*                For Couette data (32K points):     */
/*                averages some number of 2K spectra */
/*                Requires fft.lib.o                 */
/*                up to 4K real points per transform */
/*                HP 7225A digital plotter I/O       */

#include <stdio.h>
#define LENGTH 2048
#define TOTALPTS 32768

```

```

main(argc,argv)
int argc;
char *argv[];
{
    register int i,j,k;
    float s[TOTALPTS],x[LENGTH],y[LENGTH],P[LENGTH/2],mindata,maxdata;
    double phase,pi=3.1415926535897932,twopi,etobin,temp,mintemp,maxtemp;
    double SUBTRACTDC(),atof(),pow(),log(),cos(),sin();
    char label[30];
    int forward,somepoints,numpoints>window,atoi(),rand();
    int offset,samptime,logplot,sig,numsignals,itemp;
    FILE *fp,*fopen();

    if(argc != 5)
    {
        printf("usage: fft.couette logplot window filename sampltim ");
        exit();
    }

    srand(2147976337);
    twopi = 2.*pi;
    etobin = 1./log(2.);

    logplot    = atoi(argv[1]);
    window     = atoi(argv[2]);
    samptime   = atoi(argv[4]);
    numsignals = TOTALPTS/LENGTH/samptime;
    numpoints  = LENGTH;

    for(i=0;i<numpoints/2;i++) P[i] = 0.;
    fp = fopen(argv[3],"r");
    for(i=0;i<TOTALPTS;i++) fscanf(fp,"%f",s+i);
    printf("%d points read in ",TOTALPTS);
    for(sig=0;sig<numsignals;sig++)
        for(offset=0;offset<samptime;offset++)
        {
            printf("signal %d ",sig*samptime+offset);
            itemp = offset+sig*numpoints*samptime;
            for(i=0;i<numpoints;i++) x[i] = s[itemp+i*samptime];
            printf("          read in, ");
            SUBTRACTDC(x,numpoints); /* returns dc component */
            WINDOW(x,numpoints>window);
            printf("          dc subtracted, windowed, ");
            forward = 0;
            for(i=0;i<numpoints;i++) y[i] = 0.;
            COMPLEXFFT(x,y,numpoints,forward);
            for(i=0;i<numpoints/2;i++) P[i] += x[i]*x[i] + y[i]*y[i];
            printf("          and transformed ");
        }
    fclose(fp);
    for(i=0;i<numpoints/2;i++) P[i] /= (float)numsignals;

```

```

if(logplot == 1)
{
  mindata = -20.;
  mintemp = pow(2.,mindata);
  maxdata = 5.;
  maxtemp = pow(2.,maxdata);
  for(i=0;i<numpoints/2;i++)
  {
    if(P[i] < mintemp)
      P[i] = etobin*log(mintemp);
    else if(P[i] > maxtemp)
      P[i] = etobin*log(maxtemp);
    else
      P[i] = etobin*log(P[i]);
  }
}
else
  DATARANGE(P,numpoints/2,&mindata,&maxdata);

for(i=0;i<numpoints/2;i++) P[i] = (P[i]-mindata)/(maxdata-mindata);

INITIALIZE();
SQRBNDY(4.,3.,14.);
SCALE(0.,1.,0.,1.);
AXES(0.,0.,.2,.2,0,2);
BORDER();
MOVE(0.,P[0]);
ON();
for(i=0;i<=numpoints/2;i++) MOVE(2.*(float)i/(float)numpoints,P[i]);
OFF();

MOVE(-.19,-.02);
sprintf(label,"%1.f",mindata);
LABEL(label);
MOVE(-.19,0.48);
if(logplot == 1)
{
  sprintf(label,"log P");
  LABEL(label);
  MOVE(-.19,0.44);
  sprintf(label," 2");
  LABEL(label);
}
else
{
  sprintf(label,"P(w)");
  LABEL(label);
}
MOVE(-.19,.98);
sprintf(label,"%1.1f",maxdata);
LABEL(label);

```

```

MOVE(-.01,-.1);
sprintf(label,"0");
LABEL(label);
MOVE(.44,-.1);
sprintf(label,"w (Hz)");
LABEL(label);
MOVE(.95,-.1);
sprintf(label,"%2.1f",1./(2.*.006*sampletime));
LABEL(label);

MOVE(.22,1.1);
sprintf(label,"    Couette Flow");
LABEL(label);
MOVE(.22,1.05);
sprintf(label,"Power Spectrum (DFT)");
LABEL(label);

MOVE(1.05,1.);
sprintf(label,"%d points",numpoints);
LABEL(label);
sprintf(label,"signal %s",argv[3]);
LABEL(label);
sprintf(label,"window %d",window);
LABEL(label);
sprintf(label,"%d averages",sampletime*numsignals);
LABEL(label);

EXIT();
}

```

```

/* fft.lib.c:   Fast Fourier Transform Library   */
/*             SUBTRACTDC                       */
/*             DATARANGE                         */
/*             WINDOW                           */
/*             REALFFT                           */
/*             COMPLEXFFT                       */

```

```

double SUBTRACTDC(x,numpoints)
float *x;
int numpoints;
{
    double temp;
    register int i;
    temp = 0.;
    for(i=0;i<numpoints;i++) temp += x[i];
    temp /= (float)numpoints;
    for(i=0;i<numpoints;i++) x[i] -= temp;
}

```

```

    return(temp);
}

WINDOW(x,numpoints>window)
float *x;
int numpoints>window;
{
    register int i,somepoints;
    double temp,sin(),cos(),pi=3.1415926535897932;
    switch(window)
    {
        case 0: break;
        case 1: somepoints = (float)numpoints/10.; /* Cosine-Bell */
                for(i=0;i<somepoints;i++)
                {
                    temp = .5 + .5*cos(pi*(float)(somepoints-1-i)
                               /(float)(somepoints-1));
                    x[i] *= temp;
                    x[numpoints-1-i] *= temp;
                }
                break;
        case 2: somepoints = (float)numpoints/10.; /* Experimental */
                for(i=0;i<somepoints;i++)
                {
                    temp=sin(pi/2.*(float)i/(float)(somepoints-1.));
                    temp *= temp;
                    x[i] *= temp;
                    x[numpoints-1-i] *= temp;
                }
                break;
        case 3: for(i=0;i<numpoints;i++) /* Hanning */
                {
                    temp = .5 + .5*cos(pi*(float)(i-numpoints/2-1)
                               /(float)(numpoints/2-1));
                    x[i] *= temp;
                }
                break;
        case 4: for(i=0;i<numpoints;i++) /* Hamming */
                {
                    temp = .54 + .46*cos(pi*(float)(i-numpoints/2-1)
                               /(float)(numpoints/2-1));
                    x[i] *= temp;
                }
                break;
    }
    return;
}

DATARANGE(x,num,min,max)
float *x,*min,*max;
int num;

```

```

{
register int i;
float temp;
*min = x[0];
*max = *min;
for(i=0;i<num;i++)
{
temp = x[i];
if(*min > temp) *min = temp;
if(*max < temp) *max = temp;
}
return;
}

COMPLEXFFT(x,y,numpoints,forward)
int forward,numpoints;
float *x,*y;
{
double twopi=2.*3.1415926535897932;
double sin(),cos(),log(),pow();
float cs,sn,sumx,diffx,sumy,diffy,temp,twiddledum,twiddledee;
register int i,j,k;
int l,level,index,lognum;

lognum = (int)(log((float)numpoints)/log(2.));

for(l=0;l<lognum;l++)
{
level = (int)pow(2.,(float)lognum-1);
twiddledum = 1.;
twiddledee = 0.;
cs = cos(twopi/(float)level);
sn = sin(twopi/(float)level);
if(forward == 0) sn = -sn;
for(j=0;j<level/2;j++)
{
for(i=j;i<numpoints;i+=level)
{
index = i + level/2;
sumx = x[i] + x[index];
diffx = x[i] - x[index];
sumy = y[i] + y[index];
diffy = y[i] - y[index];
x[index] = diffx*twiddledum - diffy*twiddledee;
y[index] = diffy*twiddledum + diffx*twiddledee;
x[i] = sumx;
y[i] = sumy;
}

temp = twiddledum*cs - twiddledee*sn;
twiddledee = twiddledee*cs + twiddledum*sn;
twiddledum = temp;
}
}
}

```

```
        }  
    }  
  
    j = 1;  
    for(i=1;i<numpoints;i++)  
    {  
        if(i < j)  
        {  
            temp = x[j-1];  
            x[j-1] = x[i-1];  
            x[i-1] = temp;  
            temp = y[j-1];  
            y[j-1] = y[i-1];  
            y[i-1] = temp;  
        }  
        k = numpoints/2;  
        while(k < j)  
        {  
            j -= k;  
            k /= 2;  
        }  
        j += k;  
    }  
    if(forward == 0)  
        for(i=0;i<numpoints;i++)  
        {  
            x[i] /= (double)numpoints;  
            y[i] /= (double)numpoints;  
        }  
    return;  
}
```

APPENDIX B

Chaotic Attractors of Driven Oscillators: The Movie

Chaotic attractors exist in abstract state spaces of any dimension. As their global structure is not derivable from their evolution equations, analog and digital computer simulations are necessary to reveal their shapes. Actually visualizing them requires sophisticated computer graphics, even for those in three dimensions. This is unfortunate because their global features are essential to understanding how they are chaotic. Furthermore, the manner in which they can be chaotic depends on how many directions they have to move in. That is, their structure can get more complicated in higher dimensions.

There are various techniques to see chaotic attractors in three and four dimensions. The oldest and simplest for three dimensions is stereoscopic projection. Rössler pioneered this method and it was used here in the analysis of hydrodynamic chaotic attractors. Rössler's analog computer automatically displays simulations in real-time stereoscopic projection. He urges caution with extended viewing of evolving chaotic simulations. This technique was also implemented by myself in our laboratory with no ill effects.

Animation is another, potentially more useful, technique that can be used in combination with stereoscopic projection to see into four dimensions. As a first exercise in using animation to visualize chaotic attractors in three dimensions, the movie "Chaotic Attractors of Driven

B.2

Oscillators" studies a series of classic nonlinear oscillators. The technique used is that of animated Poincare sections. This is simply the temporal animation of cross sections through an attractor. A single Poincare section is made by collecting the oscillator's position and velocity at a fixed phase of the driving force. The animation then plays back in time successive sections as the driving phase advances. The technique allows one to easily see and study the folding and stretching geometry around the attractors.

In making the movie, a microcomputer sampled voltages from analog computer simulations of the oscillator, taking data points at specified driving phases. The collected sections were then played back in succession onto a large screen storage scope and photographed with a 16mm animation camera under computer control.

The movie presents five chaotic attractors taken from three different nonlinear oscillators. The first three examples come from Shaw's variant of the driven van der Pol oscillator:

$$\dot{x} = y + F\cos(\omega t)$$

$$\dot{y} = -kx - u(a-x^2)y .$$

The control parameters for the attractors are listed in Table B in order of their appearance in the movie.

For the "Full" section the movie illustrates some of its symmetries by superposing sections.

Table B

Parameters for van der Pol Attractors

Parameter	Full	2-Band	Leafy
a	.10	.11	.07
k	.72	.72	.37
u	10.0	10.0	7.3
F	.245	.11	.56
w	1.58	1.33	.194

The fourth example comes from Duffing's oscillator

$$\dot{x} = y$$

$$\dot{y} = -gy + ax - bx^3 + F\cos(wt)$$

with $a = 1.0$, $b = 10.0$, $g = .12$, $F = .56$, and $w = .93$. The final example is the driven damped pendulum

$$\dot{x} = y$$

$$\dot{y} = -gy + a\sin(x) + F\cos(wt)$$

with $g = 1.0$, $a = 10.0$, $F = .48$, and $w = 2.03$.

The movie "Chaotic Attractors of Driven Oscillators" was filmed during the fall of 1981 and premiered at Dynamics Day La Jolla, 4 - 6 January 1982, La Jolla, California. Copies are available from the author.

Facts are simple and facts are straight
Facts are lazy and facts are late
Facts all come with points of view
Facts don't do what I want them to
Facts just twist the truth around
Facts are living turned inside out
Facts are getting the best of them
Facts are nothing on the face of things
Facts don't stain the furniture
Facts go out and slam the door
Facts are written all over your face
Facts continue to change their shape

Talking Heads,

Remain In Light,

Sire Records, New York, 1980